

ABSTRACT

Title of Dissertation: ENHANCING THE COMBUSTION
CHARACTERISTICS OF ENERGETIC
NANOCOMPOSITES THROUGH
CONTROLLED MICROSTRUCTURES

Rohit Jiji Jacob, Doctor of Philosophy in
Mechanical Engineering, 2018

Dissertation directed by: Dr. Michael R. Zachariah, Patrick and
Marguerite Sung Distinguished Professor,
Departments of Chemical Engineering and
Chemistry, University of Maryland.

Metastable Intermolecular Composites (MIC's) are a relatively new class of reactive materials which, through the incorporation of nanoscale metallic fuel and oxidizer, have exhibited multiple orders of magnitude improvement in reactivity. Although considerable research has been undertaken, their reaction mechanism is still poorly understood, primarily due to the complex interplay between chemical, fluid mechanic and thermodynamic processes that happen rapidly at nanoscale. For my dissertation, I have attempted to tackle this problem by employing controlled nanomaterial synthesis routes and optical diagnostics to identify the dominant underlying mechanisms. I begin my investigation by examining the nature of metal nanoparticle combustion wherein, I employed laser ablation to generate size-controlled aggregates of titanium and zirconium nanoparticles and studied their

combustion behavior in a hot oxidizing environment. The experiments revealed the dominant role of rapid nanoparticle coalescence, before significant reaction could occur, resulting in a drastic loss of nanostructure. The large-scale effects of sintering on MIC combustion was explored through a forensic analysis of reaction products. Electron microscopy was employed to evaluate the product particle size distributions and focused ion beam milling was used to expose the interior composition of the product particles. The experiments established the predominance of condensed phase reaction at nanoscale and the interior composition revealed the poor extent of reaction due to rapid reactant coalescence before attaining completion. In light of such limitations, the final part of my dissertation proposes a solution to counteract rapid, premature coalescence through the synthesis of smart nanocomposites containing gas generating (GG) polymers. The GG acts as a binder as well as a dispersant, which disintegrates the composite into smaller clusters prior to ignition, thereby avoiding large scale loss of nanostructure. High speed optical diagnostics including an emission spectrometer and a high-speed color camera pyrometer were developed to quantify the enhanced combustion characteristics which indicate an order of magnitude improvement in reactivity over counterparts using commercial nanomaterials. Moreover, thermal pretreatment as a possible bulk processing strategy to improve nanoaluminum reactivity in a MIC is examined, where a 1000% increase in reactivity was observed compared to the untreated case. Finally, composites of nanoaluminum and reactive fluoropolymers (PVDF) are examined as a possible candidate for energetic material additive manufacturing (EMAM) and its viability is demonstrated by 3D printing and characterizing reactive multilayer films.

ENHANCING THE COMBUSTION CHARACTERISTICS OF ENERGETIC
NANOCOMPOSITES THROUGH CONTROLLED MICROSTRUCTURES

by

Rohit Jiji Jacob

Dissertation submitted to the Faculty of the Graduate School of the
University of Maryland, College Park, in partial fulfillment
of the requirements for the degree of
Doctor of Philosophy
2018

Advisory Committee:

Professor Michael R. Zachariah, Chair
Professor Christopher Cadou, Dean's Representative
Professor Johan Larsson
Professor Kenneth T. Kiger
Professor Peter B. Sunderland

© Copyright by
Rohit Jiji Jacob
2018

Dedication

To my parents for their patience and support during the course of this graduate work.

Acknowledgements

I am extremely grateful for everyone who helped make this dissertation a possibility. I would like to first thank Dr. Michael Zachariah for his guidance, support and patience throughout my studies. I would also like to thank my current and former lab mates, Dr. Yichen Zong, Dr. Garth Egan, Dr. Yonggang Yao, Dr. Guoqiang Jian, Dr. Phillip Guerieri, Dr. Kyle Overdeep, Elliot Wainwright, Xizheng Wang, Tao Wu, Haiyang Wang, Dylan Kline and Miles Rehwoldt for the discussions and assistance. In addition, I want to thank my collaborators, Dr. Liangbing Hu, Dr. Diana Ortiz-Montalvo, Dr. Michelle Pantoya, Dr. Edward Dreizin, Dr. Timothy Weihs, Dr. Gregory Young and Dr. Sz-Chian Liou and Dr. Wen-An Chiou of the UMD AIM Lab. This work would not have been possible without funding from our sponsors, the Army Research Office, the Office of Naval Research and the Defense Threat Reduction Agency. Finally, I would like to acknowledge my advisory committee, Professor Zachariah, Professor Kenneth Kiger, Professor Peter Sunderland, Professor Christopher Cadou and Professor Johan Larsson for their valuable input. I must particularly thank Dr. Sunderland for his guidance in setting up the high-speed color camera diagnostics, which has been one of the cornerstones of my dissertation.

Table of Contents

Dedication.....	ii
Acknowledgements.....	iii
Table of Contents.....	iv
List of Tables.....	viii
List of Figures.....	ix
List of Abbreviations.....	xvi
Chapter 1 Introduction.....	1
1.1 Background on Energetic Materials.....	1
1.2 Nanoscale Energetic Materials.....	2
1.3 Mechanistic understanding of metal nanoparticle combustion.....	6
1.3.1 Mechanism of nanoaluminum combustion.....	9
1.4 Mechanistic understanding of nanocomposite reactions.....	11
1.4.1 Gas-Condensed Heterogeneous reactions.....	13
1.4.2 Condensed phase interfacial reactions.....	15
1.4.3 Mechanochemical Melt Dispersion Mechanism (MDM).....	18
Motivation and Research Outline.....	19
Chapter 2 High Heating Rate Experimental Methods.....	22
2.1 Temperature measurements through multiwavelength pyrometry.....	23
2.2 High Speed 32 channel Spectrometer.....	26
2.3 Calibration of High-Speed Spectrometer.....	28
2.4 High speed color camera pyrometry.....	31
2.5 Operation principle.....	33
2.6 Color Camera Calibration.....	35
2.7 Video Processing.....	37
Chapter 3 Size Resolved High Temperature Oxidation Kinetics of Nano-Sized Titanium and Zirconium Particles.....	38
3.1 Introduction.....	39
3.2 Experimental Methods.....	42
3.2.1 Laser ablation for nanoparticle generation.....	43
3.2.2 Differential Mobility Analyzer (DMA) for NP size selection.....	43
3.2.3 Flat flame Burner and burn time measurements.....	46
3.3 Results and Discussion.....	48
3.3.1 Size selection of particles.....	48
3.3.2 Combustion characteristics of the particles.....	50
3.3.3 Size dependent burn time.....	53
3.4 Mechanistic consideration through single particle combustion modelling.....	58
3.5 Conclusions.....	64
3.6 Acknowledgements.....	65
Chapter 4 Energy release pathways in nanothermites follow through condensed state.....	66
4.1 Introduction.....	67
4.2 Experimental Approach.....	69
4.2.1 Material choice and Properties.....	69

4.2.2	Material Preparation.....	71
4.2.3	Temperature-Jump Wire Ignition and Particle Collection.....	72
4.3	Results.....	74
4.3.1	Electron Microscopy of Post-combustion Products.....	74
4.3.2	Elemental Analysis of Post-combustion Products	77
4.4	Discussion.....	80
4.4.1	Large vs. Small Particle Products and its Significance.....	80
4.4.2	Particle Growth Analysis	82
4.4.3	Phenomenological Mechanism	86
4.5	Conclusion	89
4.6	Acknowledgement	90
Chapter 5	Incomplete reactions in nanothermite composites.....	91
5.1	Introduction.....	92
5.2	Experimental.....	95
5.2.1	Materials and Preparation	95
5.2.2	Wire Ignition Experimental Setup and Product Collection	96
5.2.3	Dual Beam FIB/SEM.....	97
5.2.4	Bomb Calorimetry	99
5.2.5	Spectroscopy and Temperature Measurement	101
5.3	Results.....	101
5.3.1	Stoichiometric Al/CuO Reaction Product Cross-Section	101
5.3.2	Non-Stoichiometric Al/CuO Reaction Product Cross-section.....	106
5.3.3	Stoichiometric Al/WO ₃ and Al/Bi ₂ O ₃ Nanothermite Mixtures	108
5.3.4	Bomb Calorimetry Results.....	110
5.3.5	Reaction Temperature.....	111
5.4	Discussion.....	112
5.5	Conclusion	118
5.6	Acknowledgements.....	119
Chapter 6	High speed 2-Dimensional temperature measurements of nanothermite composites: Probing Thermal vs. Gas generation effects.....	121
6.1	Introduction.....	122
6.2	Experimental.....	125
6.2.1	Materials and Sample Preparation	125
6.2.2	Constant volume combustion cell.....	126
6.2.3	Hot-Wire ignition tests for spatiotemporal Temperature maps	128
6.3	Results.....	130
6.3.1	Al/CuO nanothermite tests in pressure cell	130
6.3.2	Al/Fe ₂ O ₃ and Al/WO ₃ nanothermite tests in Pressure cell	135
6.3.3	Qualitative Observation of Reaction Dynamics with Camera.....	139
6.4	Mechanism.....	141
6.5	Conclusions.....	146
6.6	Acknowledgements.....	147
Chapter 7	Quantifying the enhanced combustion characteristics of electrospray assembled aluminum mesoparticles.....	148
7.1	Introduction.....	149
7.2	Experimental.....	154

7.2.1	Materials	154
7.2.2	Flat flame Diffusion Burner.....	154
7.2.3	Precursor Preparation for meso particles	156
7.2.4	Electrospray Setup and Aerosolization.....	156
7.2.5	Nano particle aerosolizer	158
7.2.6	Particle Size Distribution, High-speed videography and Electron Microscopy	160
7.3	Results.....	160
7.3.1	Morphology of Commercial Aluminum nano particles.....	160
7.3.2	Morphology of Electrospray generated meso particles	162
7.3.3	Combustion characteristics of commercial NPs vs meso particles...	165
7.4	Discussion	171
7.5	Conclusions.....	175
7.6	Acknowledgements.....	176
Chapter 8	Quantifying the effect of micro-structure on reactivity in electrospray assembled nanothermite composites.....	177
8.1	Introduction.....	178
8.2	Experimental	181
8.2.1	Materials and Sample Preparation	181
8.2.2	High speed 32 channel Spectrometer coupled combustion cell.....	185
8.2.3	High sensitivity closed bomb calorimetry	185
8.3	Results.....	185
8.3.1	Constant Volume Combustion cell tests	185
8.3.2	Bomb calorimetry results	188
8.4	Discussion and Conclusion	188
8.5	Acknowledgements.....	190
Chapter 9	Pre-stressing aluminum nanoparticles as a strategy to enhance reactivity of nanocomposite thermites	191
9.1	Introduction.....	192
9.2	Experimental	196
9.2.1	Materials and Preparation	196
9.2.2	Constant volume pressure cell and High speed 32 channel emission spectrometer	198
9.2.3	In-situ high heating rate electron microscopy.....	199
9.3	Results.....	199
9.3.1	High speed pressure and temperature measurements	199
9.3.2	Hot stage, High heating rate in-situ microscopy.....	203
9.4	Discussion	205
9.5	Conclusions.....	211
9.6	Acknowledgements.....	212
Chapter 10	Microscopic visualization of the reaction zone in 3D printed nanoaluminum PVDF composites	213
10.1	Introduction.....	213
10.2	Experimental	216
10.2.1	Sample Preparation	216
10.2.2	Temperature Diagnostics	217

10.3	Preliminary Results	219
10.4	Discussion and Future work.....	222
10.5	Conclusions.....	224
10.6	Acknowledgements.....	225
Chapter 11	Summary.....	226
11.1	Conclusions.....	226
11.2	Recommendation for future work.....	234
11.2.1	Characterizing the applicability of nEM composites as nanofuel additives	234
11.2.2	High resolution imaging of planar reaction fronts.....	236
Appendix A:	Matlab Script for Pressure Cell Spectroscopy	238
Appendix B:	Matlab Script for single particle modelling.....	260
Appendix C:	Matlab Script for Color Camera Pyrometry	266
Bibliography	282

List of Tables

Table 3-1: Results of power law fit: $t=aD^b$ for the size dependent burn time for titanium and zirconium nanoparticles.....	54
Table 4-1: Thermo-Physical properties of the nanothermite mixtures	71
Table 4-2: Image processing results for the determination of the ratio of micron and nanoparticles in combustion products.....	82
Table 5-1: Atomic % values (from normalized k-ratios) obtained for the cross-section for different nanothermite systems along with their standard deviations. Equivalence ratio of 1 implies stoichiometrically mixed.	104
Table 5-2: Bomb calorimetry results for nanothermite reactions along with standard deviations.	111
Table 7-1: Oxidation zone properties for different flame stoichiometries.	156
Table 6-2: Average burn time measurements for commercial nano aluminum powder.	168
Table 6-3: Average burn time/ standard deviation measurements for aluminum meso particles.	170
Table 8-1: Bomb Calorimetry results for nanothermite composites.....	188

List of Figures

Figure 1-1: Volumetric and gravimetric heat of reaction of Thermite formulations compared to monomolecular explosives.....	3
Figure 1-2: Effect of going to nanoscale on interparticle mixing.	4
Figure 1-3: (a) Alumina shell on commercial aluminum nanoparticles; (b) Dependence of burn time with particle size for metal particles.....	8
Figure 1-4: Schematic of the proposed heterogenous oxidation of aluminum nanoparticles. Reprinted from [27,28].....	10
Figure 1-5: Hot stage TEM images showing the microstructural evolution of nanoaluminum with temperature. (a) 300C, (b) 600C, (c) 750C, and (d) 750C 15 min after taking (c). (b1) and (c1) magnify the dotted regions in (b) and (c), respectively. Reprinted from [29]	11
Figure 1-6: (a) Time of Flight Mass Spectrometry (TOFMS) results of Al/CuO reaction highlighting simultaneous Oxygen and Aluminum release; (b) Ignition temperature vs O ₂ release temperature from pure oxidizer.	14
Figure 1-7: (a) Aggregated state of commercial aluminum nanoparticles; (b) Proposed Reactive Sintering mechanism; (c) Change in the morphology during the exothermic reaction. Reprinted from [42]	18
Figure 1-8: (a) Proposed mechanism of composite particle of nanoscale energetic material (EM) and nitrocellulose. The nitrocellulose acts as a gasifying agent, dispersing the aggregate into smaller clusters; (b) Schematic of how an aggregate of nanoenergetic material reacts, which involves sintering into a much larger particle before significant reaction.....	21
Figure 2-1: Setup of high speed emission spectrometer	27
Figure 2-2: Calibration for the MC-PMT a. Evaluating the linearity of the detector by attenuating broadband signal using ND filters. Horizontal lines represent expected attenuation. b Spectral response calibration using a high temperature Tungsten-Halogen lamp.	29
Figure 2-3: (a) Raw spectra from a reaction showing the various molecular emission peaks. (b) The channels corresponding to the red circles were removed during straight line fitting of the parameter Z to wavelength.....	31

Figure 2-4: (a) Spectral response curve of Vision Research Phantom Miro M110 high speed camera. Figure adapted from Vision Research.[67]; (b) theoretical calibration ratio profiles as a function of temperature for the three colors in CFA.	35
Figure 2-5: Calibration for the Color camera pyrometer: (a) Spectral response calibration using a Black body and high temperature Tungsten-Halogen lamp. (b) Evaluating the linearity of the camera sensor by attenuating broadband signal using ND filters. Dark line represents the expected attenuation	36
Figure 3-1: Conceptual figure showing experimentally determined diameter dependence on burn time[19].....	42
Figure 3-2: Schematic of the experimental setup showing the atmospheric pressure laser ablation system connected with the DMA and a flat flame burner.	42
Figure 3-3: Schematic of a DMA showing the various gas flows.[103]	45
Figure 3-4: Temperature profiles for different stoichiometries along the burner centerline as a function of the height above the burner.	47
Figure 3-5: Measured peak size of the particles after size selection by DMA. The line represents the theoretically estimated mobility size.	49
Figure 3-6: Particle size distributions obtained for different DMA voltages.	50
Figure 3-7: TEM micrographs of the Ti particles before combustion (a) and TiO ₂ particles after combustion.	52
Figure 3-8: Burn time for titanium particles as the function of the particle size. (a) is based on the peak DMA selected particle size, (b) is based on the estimated diameter after sintering.	54
Figure 3-9: Burn time for zirconium particles as the function of the particle size. (a) is based on the peak DMA selected particle size, (b) is based on the estimated diameter after sintering.	55
Figure 3-10: Activation Energy determined via Arrhenius plots of burn time vs. temperature for titanium and zirconium.	57
Figure 3-11: Broadband Emission Profile of a 40 nm Ti Particle.	58
Figure 3-12: Model simulations for 40 nm particle. Emission plots with: (a) TAC = 0.005, (b) TAC = 0.3.....	62
Figure 4-1: SEM image of dry, unreacted Al/Bi ₂ O ₃ showing the intimate mixing and the elemental contrast owing to the mass of the different reactant species	72

Figure 4-2: Experimental setup for rapid quench collection for nanothermite reaction products..... 73

Figure 4-3: Temporal video snapshots of Al/CuO nanothermite combustion on a 76 μm Pt wire, Heating rate = $\sim 2 \times 10^5$ K/s, time(μs) measured from the start of ignition. The red dashed line represents the wire location and the arrow shows the location of the TEM grid..... 74

Figure 4-4: Post-combustion SEM images of Al/CuO nanothermite collected at various distances. a.) Time for impingement = 90 μs . Separation of the collecting substrate: 1 mm. b.) Time for impingement = 350 μs . Separation of the collecting substrate: 3 mm. 76

Figure 4-5: Post Combustion high magnification SEM images showing surface morphology at the various separation distances for Al/CuO. a.) BSE Image Time for impingement = 90 μs . Separation of the collecting substrate: 1 mm. b.) Time for impingement = 350 μs . Separation of the collecting substrate: 3 mm..... 76

Figure 4-6: Post-Combustion TEM images (Al/CuO Nanothermite) of the smaller particles collected on a Nickel TEM grid. Time for impingement: 150 μs 76

Figure 4-7: Typical particle sizes for the two Nano Thermites Al/WO₃ and Al/Bi₂O₃. a.) Al/WO₃, Time for impingement = 300 μs , Separation of the collecting substrate: 1 mm. b.) Al/Bi₂O₃, Time for impingement = 250 μs , Separation of the collecting substrate: 1 mm. 77

Figure 4-8: High magnification SEM images of the two Nano Thermites Al/WO₃ and Al/Bi₂O₃. a.) Al/WO₃, Time for impingement = 300 μs , Separation of the collecting substrate: 1 mm. b.) Al/Bi₂O₃, Time for impingement = 100 μs , Separation of the collecting substrate: 1 mm 79

Figure 4-9 a.) High Magnification image of Al/WO₃ products showing the faceted structure and b.) showing the presence of spherical particles. c.) Al/Bi₂O₃ case showing the spherical nano-particles 80

Figure 4-10: Image processing example for combustion products of Al/CuO. The image threshold was adjusted to single out the larger particles from the background. 81

Figure 4-11: Copper particle growth using Equation (1), and assuming Cu vapor in supersaturated state with no nucleation barrier to condensation – i.e. maximum growth rate. 85

Figure 5-1: (a) Representative SEM image of products collected for the Al/CuO case; (b) a 20 μm particle sliced using high intensity gallium ion beam. 99

Figure 5-2: (a-c) Schematic of the micro-calorimeter (reproduced, with permission, from K. R. Overdeep, PhD Thesis); (d) Temperature change of the oil bath measured using a thermocouple. 100

Figure 5-3: Cross-section SEM image of a $\approx 2 \mu\text{m}$ product particle (Al/CuO, $\phi = 1$) with the EDX area scans of the associated elements: aluminum (pink), copper (blue), and oxygen (green). Electron beam conditions are 20 keV and 0.62 nA. 102

Figure 5-4: Cross-section SEM image of a $10 \mu\text{m}$ product particle (Al/CuO, $\phi = 1$) with the EDX area scans of the associated elements: aluminum (blue), copper (pink), and oxygen (green). Electron beam conditions are 20 keV and 0.62 nA. 106

Figure 5-5: (a) Cross-section SEM image and elemental maps of a $10 \mu\text{m}$ product particle (Al/CuO, $\phi = 0.5$); (b) Cross-section SEM image and elemental maps of a $7 \mu\text{m}$ product particle (Al/CuO, $\phi = 1.5$). Electron beam conditions are 20 keV and 0.62 nA. 107

Figure 5-6: (a) Cross-section SEM image and elemental maps of a $3 \mu\text{m}$ product particle (Al/ Bi₂O₃, $\phi = 1$); (b) Cross-section SEM image and elemental maps of a $2 \mu\text{m}$ product particle (Al/ WO₃, $\phi = 1$). Electron beam conditions are 20 keV and 0.62 nA. 110

Figure 5-7: Temperature profiles in inert environments for (a) Al/CuO, (b) Al/WO₃ and (c) Al/Bi₂O₃; (d) High speed snapshots of Al/CuO reaction on wire shown in (a). 112

Figure 5-8: Morphological changes to a 500 nm aggregate of Al/CuO heated by a 12 ns heating laser pulse characterized in a DTEM. (a) Aggregate prior to heating; (b) Resulting morphology after heating; (c) High speed temporal snapshots of the evolution of the aggregate morphology. Reprinted from [98]. 113

Figure 5-9: Combustion cloud of Al/Bi₂O₃ 116

Figure 6-1: Schematic of the experiment consisting of pressure cell and attached diagnostics. The pressure cell is shown on the left. The spectrometer is coupled to the pressure cell via an optical fiber. The light from the fiber is spectrally dispersed by the selected grating on the turret which is subsequently imaged on the 32 channel PMT and digitized using the Data Acquisition system (DAQ). The digitized data is processed to produce time resolved spectra. 128

Figure 6-2: Experimental rig for visualizing nanothermite reaction using high speed color camera. 130

Figure 6-3: Al/CuO nanothermite in pressure cell. a. Pressure-Normalized-Integrated Intensity profile, and b. Temporal reaction temperature profile. Region 1-2: temperature rise and pressure drop; 2-3: temperature drop and peak pressure; 3-4:

rapid rise in integrated intensity at a constant temperature with decreasing pressure; 4-6: broadly represents increase temperature; 6-7: region with temperature plateau, decreasing integrated intensity and pressure..... 132

Figure 6-4: Temperature measurement of Al/CuO nanothermite in pressure cell over extended durations measured without ND2 filter. The initial parts of the reaction is truncated due to saturated emission on the MC-PMT 134

Figure 6-5: Temporal Pressure-Temperature profiles for a. Al-Fe₂O₃, b. Al-Fe₂O₃-20WO₃, c. Al-Fe₂O₃-60WO₃, d. Al-Fe₂O₃-70WO₃, e. Al-Fe₂O₃-90WO₃, f. Al-WO₃ in pressure cell. The grey region is the error bound of the measurement. 136

Figure 6-6: Pressure-Temperature profiles for a. Effect of composition on temperature, b. Effect of composition on pressure and pressurization rate (Al/CuO: P_{max} = 572 kPa and Press. Rate = 41 kPa/μs) and c. Effect of composition on Burn time. 138

Figure 6-7: High speed pyrometry frames of a. Al/Fe₂O₃, b. Al/Fe₂O₃/70% WO₃ and c. Al/WO₃ samples ignited on a hot wire at 1 atm. argon environment highlighting the gas production and enhanced reaction. In the Al/WO₃ case, the reaction propagated up the wire over a longer time scale due to lack of gas release from the oxidizer. In each figure, the top image is a gain-adjusted raw image and the bottom image is the 2-D temperature map. 141

Figure 6-8: Proposed reaction mechanism..... 144

Figure 7-1: Multi element diffusion flat flame burner: a) Burner centerline along which particles are injected into the high temperature, oxidizing zone; b) Temperature profiles along the burner centerline for different flame stoichiometries. 155

Figure 7-2: Electro spray generated meso particle aerosolizer..... 158

Figure 7-3: Experimental setup: a) nanopowder aerosolizer; b) Experimental run showing the observed streaks for nano aluminum powders. 159

Figure 7-4: Morphology and size distribution of commercial aluminum nanopowder: a) nanopowder agglomerate with high magnification TEM image (inset); b) Size distribution of the aerosolized nanoaluminum powder..... 161

Figure 7-5: a) SEM image of electro spray assembled Al/NC (10 wt%) mesoparticles using ethanol/ether = 3:1 mixture as the solvent, with a high magnification TEM image of a single particle as inset; b) measured size distribution and comparison with self-preserving distribution. 164

Figure 7-6: TEM images of the aluminum meso particles formed using different solvents for electro spray precursor: a) ethanol/ether=3:1 mixture; b) Acetone; c) DMF/ether=1:1 mixture; d) DMF/ether=1:2 mixture; e) DMF/ether=1:3 mixture. . 164

Figure 7-7: Combustion images: a) Nanoaluminum at exposure of 0.05 sec; b) nanoaluminum at exposure of 100 μ s; c) Aluminum meso particles at exposure of 83 μ s; d) Aluminum meso particle at exposure of 0.5 sec; images shown with individual scale bars owing to the differences in magnification during the separate experiments. 166

Figure 7-8: Burn time plots for nanoaluminum for Flame 3 condition: a) All data points for nanoaluminum; b) Selected burn times below 1000 μ s for nanoaluminum. Horizontal line representing the average burn time. 168

Figure 7-9: Burn time scatter plot for aluminum meso particles in Flame 3. Horizontal line representing the average burn time. 169

Figure 7-10: SEM images of the products collected post combustion: a) Commercial nanoaluminum with an inset of an individual particle at high magnification; b) Aluminum meso particles with an inset of an individual particle at high magnification. 171

Figure 7-11: Pictorial representation of the events leading to combustion of: a) Aluminum meso particles; b) Commercial aluminum nanoparticles 173

Figure 8-1: ES assembly of nanocomposite thermites, adapted from Wang et. al [163]. (a) Experimental setup for ES synthesis, (b) Al/CuO nanocomposites prepared by electro spray and (c) backscattered electron image highlighting the intimate mixing of Aluminum (red) and Copper Oxide (green). 184

Figure 8-2: Effect of precursor loading on ES assembled mesosphere morphology (Reprinted from Wang et al.[205]). The sample tested in the current study were prepared using 80mg/ml and 205mg/ml solids loading..... 185

Figure 8-3: Combustion cell results showing pressure performance (a-c) and reaction temperature (d-e) for the nanocomposite thermites..... 186

Figure 8-4: Burn time of the composite measured as the FWHM (Full-Width-Half-Max) of the integrated emission from the constant volume pressure cell tests. 187

Figure 9-1: (a) Untreated nanoaluminum particles and (b) magnified image showing the oxide shell. 197

Figure 9-2: Pressure Cell data showing effect of prestressing (a) on Pressure and Pressurization Rate; (b) on Temperature; and (c) on Burn Time..... 202

Figure 9-3: High heating rate TEM results for Untreated nAl (a) prior to heating, (b) after RT- 1473K ramp @ 5e5 K/s, (c) after RT- 1473K second ramp @ 5e5 K/s and hold for 1s; and for 300C Exp nAl (a) prior to heating, (b) after RT- 1473K ramp @ 5e5 K/s, (c) magnified image of (b) showing the shell structure.....	205
Figure 9-4: Pressure-Temperature and Emission data for (a) Untreated nAl and (b) 300C Linear nAl; NIR vs AIO channel profile for (c) Untreated nAl and (d) 300C Linear nAl.	207
Figure 10-1: 3D printing setup with Hyrel 30 M.....	217
Figure 10-2: Optical assembly for high resolution imaging	219
Figure 10-3: Pre-ignition images of fuel rich Al-PVDF film ($\phi=3$): a. 7 Layers and b. 14 Layers.....	220
Figure 10-4: Combustion of Al-PVDF thin film, visualized using high speed microscopy (6200 fps, 161 μ s exposure).....	221
Figure 10-5: High speed pyrometry showing flame propagation	222
Figure 10-6: Phenomenological reaction mechanism for Al-PVDF composites doped with Silica mesospheres.[235]	224
Figure 11-1: (a) Toluene control sample (Top): color camera pyrometry is used to measure the flame temperature, (bottom) which is spatially averaged and temporally plotted. (b) 810 mM of TiBAI in toluene. The spatially average temperature is plotted (blue dots) along with the baseline temperature of the pure toluene (red line) from (a). The black dots are regions of heightened AIO emission as obtained from the spectrometer which was run simultaneously with the color camera to track the droplet. Droplet leaves spectrometer view at 65 ms. Disruptions at 35, 55 and 73 ms.	236

List of Abbreviations

ESD	Electro Static Discharge
NPs	Nanoparticles
ALEX	Aluminum nanoparticles from Exploding wire
Z_P	Particle mobility
Q_{sh}	DMA sheath flow rate
V	applied voltage
L	length of the DMA
R_2	Outer diameter of the DMA
R_1	Inner diameter of the DMA
e	Total charge on particle
C	Cunningham Slip correction
d_m	Mobility equivalent spherical diameter
μ	gas viscosity
d_P	Primary particle size
N	Number of particles in an aggregate
D^*	Estimated particle size after sintering (based on volume conservation)
α	Conversion factor
X_{Ti}	Volume fraction of Titanium/ Zirconium core left
τ	Burn time [s]
T	Particle Temperature [K]

m_g	Air molecular weight ($4.8 \cdot 10^{-26}$ Kg)
K	Boltzmann Constant ($1.38 \cdot 10^{-23}$ m ² Kg s ⁻² K ⁻¹)
P_g	Gas Pressure (1 atm)
γ	Adiabatic expansion factor (=1.3 at 1500 K)
T_g	Gas Temperature (1750 K)
σ	Stefan Boltzmann constant ($5.67 \cdot 10^{-8}$ W/m ² K ⁴)
a_p	Surface area of particle (m ²)
N_{av}	Avogadro's constant
d_p	Particle size (used in model)
nEM	nanoscale energetic material

Chapter 1 Introduction

1.1 Background on Energetic Materials

“Energetic material” is a term used to classify compounds that have large stored chemical potential energy with a propensity to rapidly release the energy on a short time scale. This latter characteristic of rapid energy release is what distinguishes a cookie from an explosive like TNT, in spite of the cookie containing about eight times the specific energy compared to that of TNT.[1] Energetic materials can be further subdivided into 3 categories: Propellants, Explosives and Pyrotechnics. The premise for this characterization is again the rate of energy release, with explosives releasing their energy via fast detonation processes whereas propellants and pyrotechnics doing so via slow deflagration.[2] Traditional energetic materials (RDX, TNT, Nitrocellulose etc.) consist of incorporating the fuel and oxidizer constituents into a single molecule (monomolecular materials), which greatly increases their reactivity owing to the lack of any mass transfer limitations. Another method involves physically mixing powders of fuel and oxidizer to produce energetic composites, for example, gunpowder. Such composites suffer from poor reaction rate when the particle sizes in the reactant powders are in the $>100 \mu\text{m}$ range owing to mass transfer limitations. With the energy content of conventional explosives plateauing,

significant effort has been laid into the development of new energetic composites whose reactivity could be tuned to the needs of the application.

1.2 Nanoscale Energetic Materials

An advert used as the motivation for nanoscale energetic material research is shown in Figure 1-1. As depicted, the gravimetric (per mass) and volumetric (per vol.) heats of reaction of several state of the art explosives are compared with that of metal-based composites, in this case, aluminum being the metallic fuel. The drastic improvement in the volumetric enthalpy for aluminum based composites compared to explosives is particularly noteworthy and is of critical importance in space applications where storage comes at a premium. In spite of the vastly superior reaction enthalpy, these composites are greatly limited by their inferior reaction rate which stifles their employment as energetic materials, the most prominent example being the utilization of the Al/Fe₂O₃ thermite system to weld rails since the turn of the 20th century.[3] Given the limitations, an ideal scenario would be the development of a composite energetic material that has the reaction enthalpy of a metalized systems and the energy release rate of a monomolecular explosive. With the advent of nanotechnology, which allows precise control of materials at the nanoscale, realizing this ideal has been the major motivation behind the near two decade long research on nanoscale energetic materials.[4] The ability to manufacture and tune materials at the nanoscale has greatly increased the availability of

nanomaterials for commercial use and has led to the advancement of metallic composites as energetic materials

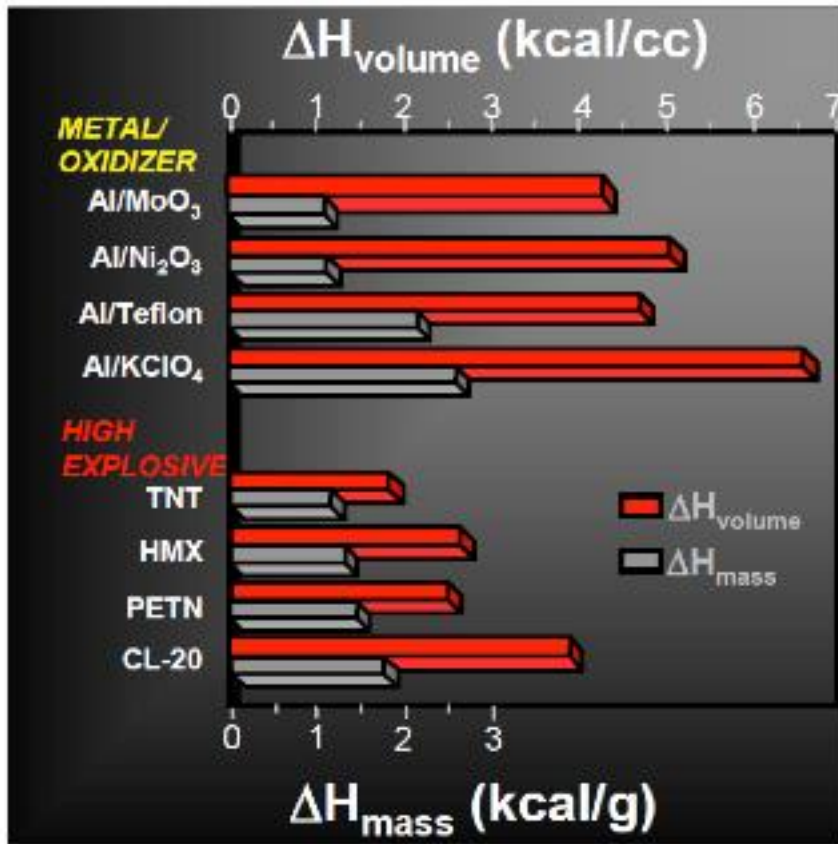


Figure 1-1: Volumetric and gravimetric heat of reaction of Thermitic formulations compared to monomolecular explosives

Nanomaterials are characterized by at least one dimension being on the order of 100 nm. A simple illustration is shown Figure 1-2, where a composite material with 1 μm primary particles is compared volumetrically to the same composite with 100 nm particles. It can be readily seen that with an order of magnitude reduction in primary size, there is a significant increase in contact points, increase in surface area

and improved intermixing. In addition, for particles at the nanoscale, a significant percentage of the constituent atoms are on the surface which due to their lower coordination number, have reduced cohesive energy. This diminishes the energy required to free a surface atom from the bulk, leading to a depression in melting point, as exemplified by the Gibbs Thomson Equation. These advantages directly contribute to the increase in reactivity of nanoparticles.[5]

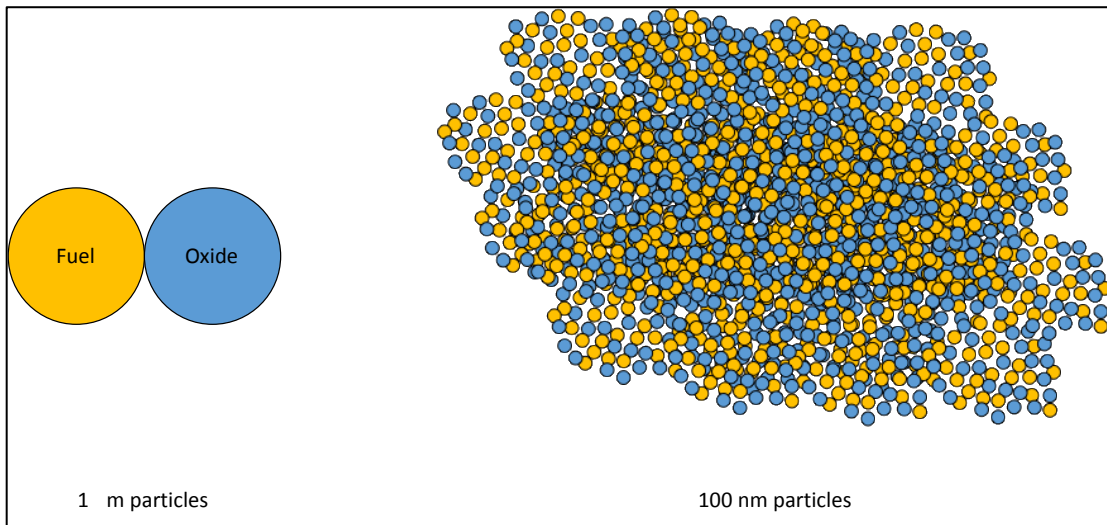


Figure 1-2: Effect of going to nanoscale on interparticle mixing.

Armstrong et al.,[6] showed that replacing conventional micron sized (10-100 μm) aluminum powder in gun propellant with aluminum nanopowders resulted in 2 order of magnitude increase in the burn rate (1 mm/s to >100 mm/s) in closed vessel experiments. The increase in burn rate is attributed to the enhanced interfacial contact area for reaction at the nanoscale. Similar work done by Dokhan et. al[7] showed an increase in solid rocket propellant burn rate with the addition of moderate amounts of nano aluminum. Apart from their use as rate augmenting additives, nanoparticles

have been utilized in the development of a relatively new class of energetic materials called Metastable Interstitial composites (MIC),[8] whose mechanistic understanding is the theme of this dissertation. MIC consists of fuel and oxidizer moieties mixed at the nanoscale, which greatly reduce the diffusion length scales and can be considered as an intermediate class of materials between the monomolecular energetics (mixed at atomic scale) and the traditional, coarsely mixed composites. MICs offer the unique advantage of nanoscale mixing, achieving the fast reaction time scales, as well as the tunability and high enthalpy of metalized composites. Nanothermite mixtures, consisting of metallic fuel (ex. Al) and metal-oxide oxidizer (ex. CuO, WO₃, Bi₂O₃ etc.), have been one of the most intensely investigated class of MIC's owing to their high energy density on both gravimetric and volumetric basis, as highlighted in Figure 1-1, and constitutes the major focus of this study. Nanothermite MICs have shown tremendous improvement in reaction rate by providing a low activation energy pathway for the reaction[9] and with sufficient tuning of the microstructure and composition, reaction propagation rates as high as 2500 m/s have been achieved.[10] One of the most attractive aspects of nanothermites is the tunability that allows the use of different Metal/Metal Oxide combinations,[11] custom nanostructures[12–14] and production techniques.[15–17] The high reaction rate exhibited by nanothermite composites has potential applications in green primers, initiators, detonators, improved rocket propellants, explosives, microthrusters, thermal batteries, in situ welding, biocidal and other biological applications.[4]

1.3 Mechanistic understanding of metal nanoparticle combustion

In spite of the several years of research, the mechanistic features of the reaction of nanoscale energetic materials remain poorly understood. Understanding the mechanism of nanoenergetic combustion would require an understanding of how nanoscale fuel particles behave. Since this work is primarily aimed at nanocomposites that use aluminum particles as fuel, a brief summary of the combustion behavior of aluminum particles in different size regimes is warranted. Most commercially available fuel particles develop an oxide shell upon exposure to atmospheric conditions (Figure 1-3a). This shell, made of high melting alumina, has a profound influence on the combustion characteristics of the fuel particles. There are two major, widely accepted modes of reaction in particle combustion. The first mode, called diffusion-limited regime, occurs when the mass flux of the oxidizer is limiting the reaction. The chemical kinetics of the reaction in this regime is considered infinitely fast. The second mode is called kinetic limited regime, where the diffusion is considered infinitely fast and the reaction kinetics limit the overall progress of reaction. In a simplified illustration, adapted from,[18] the generic reaction rate of a particle reacting with gaseous oxidizer can be expressed as:

$$\dot{\omega} = A \left(\frac{\beta k}{\beta + k} \right) C_0$$

Eq. 1-1

where, $\dot{\omega}$ is the reaction rate at the surface of the particle, β is the mass flux of oxidizer, k is the reaction rate and C_o is oxidizer concentration away from the reaction surface. This leads to explicit forms of the two aforementioned regimes. For diffusion limited, $k \gg \beta$, which reduces the reaction rate to $\dot{\omega} = A\beta C_o$. Whereas for kinetic limited case, $\beta \gg k$, which results in $\dot{\omega} = AkC_o$.

Furthermore, the mass flux can be related to the mass diffusivity via the Sherwood number, expressed as:

$$Sh = \frac{\beta}{D/d}$$

Eq. 1-2

where, D is the mass diffusivity and d is the diameter of the particle. Defining burn time as the ratio of mass to reaction rate, I can get qualitative equations that can relate the burn time to the particle dimensions.

$$\tau_{diff} = \frac{m}{\dot{\omega}} \approx \frac{d^3}{A\beta C_o} \approx \frac{d^3}{d^2 \left(\frac{Sh D}{d}\right) C_o} \approx \frac{d^2}{Sh DC_o}$$

Eq. 1-3

$$\tau_{kinetic} = \frac{m}{\dot{\omega}} \approx \frac{d^3}{AkC_o} \approx \frac{d^3}{d^2 k C_o} \approx \frac{d}{kC_o}$$

Eq. 1-4

As can be seen in Eq. 1-3 and Eq. 1-4, burn times of diffusion limited reactions scale with the square of the particle diameter whereas for kinetic limited scenario, it scales with the diameter. Experimental data correlate with the

aforementioned simplistic model where, as outlined in,[19] large solid aluminum particles (30-100 μm) are observed to burn in a diffusion controlled regime with a detached vapor phase flame surrounding the burning particle (Figure 1-3b). The burn times (of the form $t = ad^b$) have been observed to correlate with a $d^{1.8}$ power law, with d being the particle diameter. The exponent value being lesser than the theoretically expected value of $b = 2$ is considered to be a byproduct of the interference from oxide lobe that form on the particle during. As the particle sizes reduce to about $\sim 10\mu\text{m}$, the faster diffusion rates result in a transition to a kinetic limited combustion regime. The flame is observed to approach the particle surface and the diameter dependence approaches unity.[20] In this regime, the effect of the oxidizing atmosphere starts to play a crucial role in the observed combustion. As the particle sizes are further reduced below $\sim 10 \mu\text{m}$, a fractional diameter dependence is observed with the exponent approaching values as small as $b = 0.3$ or lesser,[5] which cannot be explained by any standard theory (Figure 1-3b).

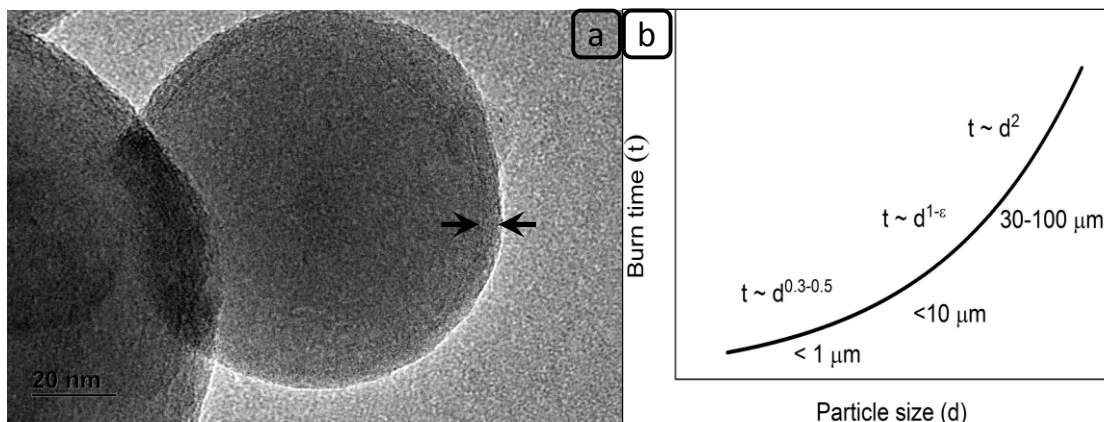


Figure 1-3: (a) Alumina shell on commercial aluminum nanoparticles; (b) Dependence of burn time with particle size for metal particles.

1.3.1 Mechanism of nanoaluminum combustion

Aluminum is the popular fuel of choice for nanoscale energetic composite owing to its high enthalpy and ease of availability. Commercial aluminum is prepared through electrical wire explosion method [21] where an large amount of current is driven through an aluminum wire, instantly vaporizing it due to joule heating. The nanoparticles subsequently nucleate and grow from the gas phase as the system cools. Upon exposure to atmospheric conditions, the NPs develop a 2-5 nm thick alumina shell (Figure 1-3b), [22] which given the primary particle size, could account for a significant mass percentage. Since alumina melts at a higher temperature (2345K) than the ignition temperature of nanoaluminum or nanoaluminum based composites,[11] understanding the nature of aluminum transport through the shell has been subjected to intense debate over the years. A starting point at understanding how the aluminum could be exposed from the shell can be found in the simple diffusion model where Al⁺ diffuse out and O⁻ diffuse in. If oxygen diffused faster than the aluminum, this would produce a “shrinking core” scenario with the shell thickening inward, which overtime leads to a diminishing metallic core.[23–25] Alternatively, if the outward diffusion of metallic ions is faster, then hollow oxide structures could result.[26] However, the low self-diffusion coefficient of alumina pose a significant hurdle to viability of this mechanism to sustain the fast reactivity observed in nanoaluminum based composites.

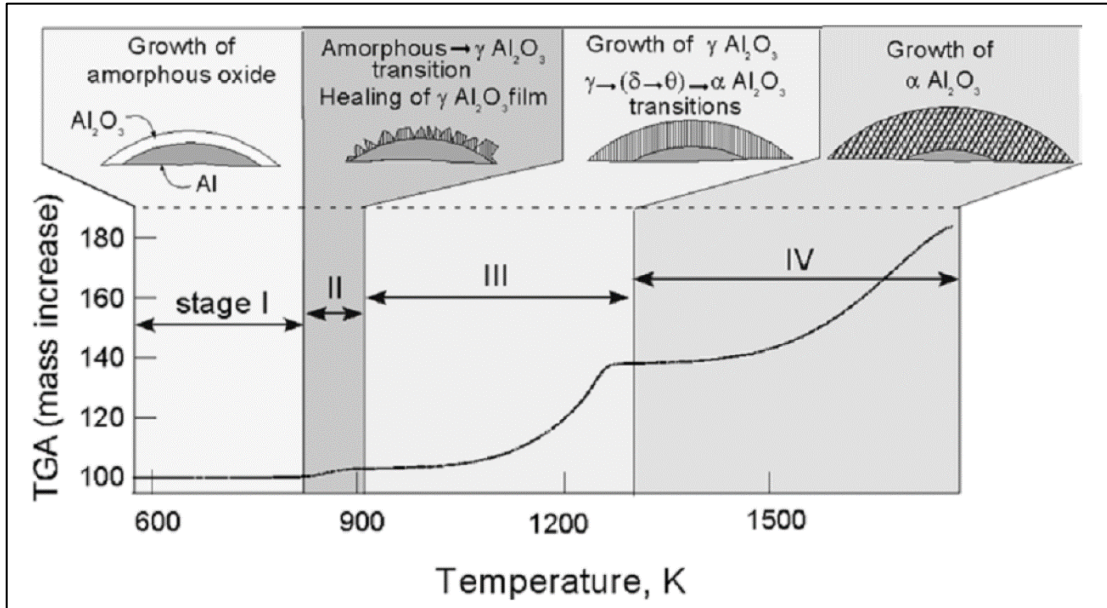


Figure 1-4: Schematic of the proposed heterogeneous oxidation of aluminum nanoparticles. Reprinted from [27,28]

A modification to this model, as developed by Dreizin and coworkers [27] incorporating slow heating rate calorimetry, suggested that the phase transition of the alumina shell into various polymorphs at high temperatures could lead to the development of cracks/ discontinuities in the shell that could rapidly expose the underlying aluminum to the oxidizer, as shown in Figure 1-4. Experimental validation of such a diffusion based mechanism was provided by Firmansyah and coworkers,[29] using high resolution transmission electron microscopy (TEM), where they found a freely expanding aluminum core when the sample was heated above 300°C, which was aided in part due to: (a) The reduction in hardness of the aluminum core due to grain growth from thermal annealing[30] and (b) due to imperfections in the shell which allowed the aluminum to freely flow out, as depicted by the TEM images

in Figure 1-5, where a clear loss of the nanoscale boundary could be observed for the nanoaluminum particles heated to several elevated temperatures. In Chapter 9 of this dissertation, the role of the oxide shell is further examined with the objective of weakening it so as to improve reactivity.

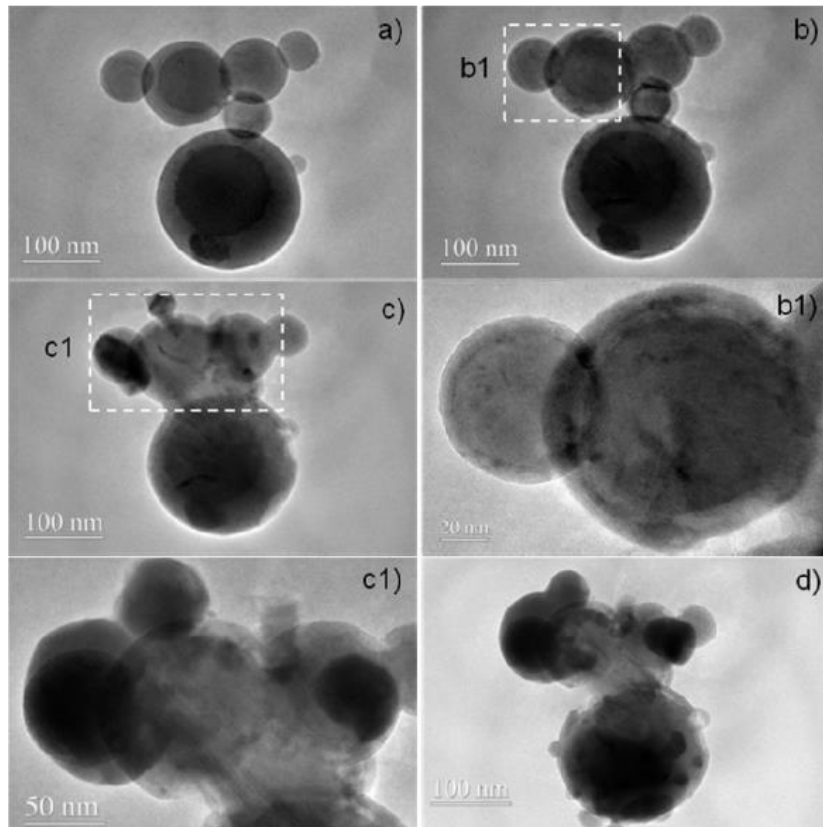


Figure 1-5: Hot stage TEM images showing the microstructural evolution of nanoaluminum with temperature. (a) 300C, (b) 600C, (c) 750C, and (d) 750C 15 min after taking (c). (b1) and (c1) magnify the dotted regions in (b) and (c), respectively. Reprinted from [29]

1.4 Mechanistic understanding of nanocomposite reactions

Moving onto energetic composites, especially propellant mixtures containing aluminum as additives, the size dependence on the burn speeds are considerably

scattered. Aforementioned results by Armstrong et al. [6] showed a d^{-2} dependence of burn speed for gun propellants containing aluminum particles in the size range of 10 μm to < 100 nm. Similarly, results from Dokhan et al. [7] showed a diameter dependence of $d^{-0.28}$ for aluminum additives in solid rocket propellant with aluminum particle dimensions ranging from 30 μm to 100 nm. On the other hand, exploring the burn speeds of nanothermite MIC's show a similar scatter in the reported diameter dependence. Sullivan et al. [31] recently observed that for nanothermite materials consisting of nano scale copper oxide as the oxidizer, the burn speeds correlated to a $d^{-0.56}$ dependence, d being the diameter of the aluminum particles used as fuel. The range of sizes considered in that study was from 100 μm to 3.5 μm . The study also reported that going to smaller aluminum particle sizes (upto 80 nm) had a detrimental effect on the burn speeds. Another study by Weismiller et al.[32] found contradictory results and stated that an improvement in burn speeds can be attained by using nanoaluminum instead of micron aluminum particles.

A large body of work has been undertaken to mechanistically probe the behavior of nanothermites in combustion environments.[33,34] Owing to the lack of a general consensus, the proposed mechanisms are briefly discussed in the following sections.

1.4.1 Gas-Condensed Heterogeneous reactions

This reaction mechanism was developed primarily based on the early investigations, which observed that several oxidizers decomposing into their suboxides, releasing gas phase oxygen (e.g., $\text{CuO} \rightarrow \text{Cu}_2\text{O} + \text{O}_2$, $\text{Fe}_2\text{O}_3 \rightarrow \text{Fe}_3\text{O}_4 + \text{O}_2$, $\text{Co}_3\text{O}_4 \rightarrow \text{CoO} + \text{O}_2$ etc.). High heating rate mass spectrometry of these oxides and the corresponding thermites has shown that this reduction process often occurs at temperatures comparable to ignition and that significant gaseous oxygen is present during reaction, as shown in Figure 1-6a, where aluminum and oxygen ions were simultaneously detected upon Al/CuO nanothermite ignition. [11,35] This is all in accordance with the gas-condensed heterogeneous reaction mechanism, where the fuel is postulated to burn in a pressurized O_2 environment created by the decomposition of these oxides. Part of the attraction of this mechanism is its relative simplicity, as it can be treated as almost a one component system with the reaction limited either by the decomposition step of the oxidizer to liberate oxygen or the reaction of fuel particle with the oxygen. This allows for the direct incorporation of the extensive combustion models that have already been developed for the combustion of metal particles in pressurized, oxygenated environments.[36–38]

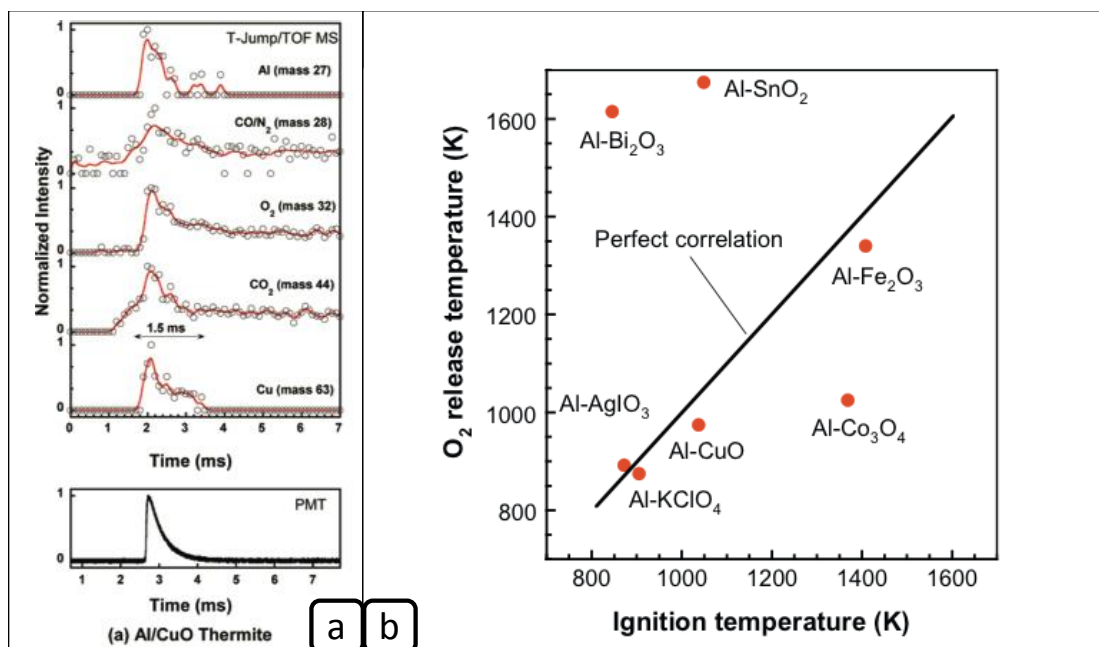


Figure 1-6: (a) Time of Flight Mass Spectrometry (TOFMS) results of Al/CuO reaction highlighting simultaneous Oxygen and Aluminum release; (b) Ignition temperature vs O₂ release temperature from pure oxidizer.

The apparent simplicity comes at the cost of a lack of widespread consensus regarding this mechanism. Nanoaluminum combustion in shock tube experiments reveal that the shortest observed burn times were on the order of 50-500 μs in pressurized, high-temperature, oxygenated environments.[39] On the other hand, constant volume combustion tests have revealed that the pressure generation during nanothermite reactions occur on a time scale of $\sim 10 \mu\text{s}$,[40] which is shorter than the shortest burn times reported for nanoaluminum. The optical signal in these constant volume tests doesn't reach its maximum until $\sim 100 \mu\text{s}$ and has a full width at half maximum (FWHM) value of more than twice that, which matches up with the reported burn times of nanoaluminum particles. Similarly, nanothermite reaction in

extended burn tube studies revealed that the reaction continued to occur for ~3 ms after initial expansion.[41] This order of magnitude difference in time scales suggests a two-step process that could be indicative of initial reaction, which heats up and reduces the oxidizer followed by heterogeneous burning in the released O₂. Further conflict with this mechanism arises from the experimental results presented in Figure 1-6b (from Ref.[11]) where the ignition temperature of various nanothermite systems were correlated with the oxygen release temperature from neat oxidizers. The results indicate that there are some oxidizers (e.g., CuO, Fe₂O₃, AgIO₃) that show a correlation between the release of O₂ and the ignition with Al. However, there are many more (e.g., Bi₂O₃, WO₃, MoO₃, and SnO₂), which ignites in the absence of gaseous O₂. This suggests that for many cases, a gas-condensed heterogeneous reaction is not responsible for ignition but may have a contribution in the long term burning of these nanothermite systems.

1.4.2 Condensed phase interfacial reactions

An alternative mechanism, which involves the reaction at the material interface owing to condensed phase species transport, has been recently suggested. Nanoparticles, owing to their high surface energy exist in a highly aggregated state (Figure 1-7a), which promotes significant interfacial contact. Sullivan et al.,[34,42] conducted high heating rate experiments in a Transmission Electron Microscope (TEM) to gauge the microstructural changes that happen during the nanothermite

reaction. Their results highlighted the dramatic loss of nanostructure during the reaction, forming large spherical melts. They proposed a mechanism called ‘Reactive Sintering’ where a condensed phase reaction at the interface between fuel and oxidizer aggregates was the impetus for the initiation, as shown in Figure 1-7b. The mechanism is predicated on either of the reactant components gaining sufficient mobility so as to coalesce with the other, which could dramatically increase the contact surface area. Once the interface reaction gets underway, the heat liberated by the exothermic reaction is conducted away from the interface and results in the melting of the adjacent particle aggregates. As material is melted during this process, capillary forces/surface tension serve to rapidly deliver the newly melted material towards the interface, where the reaction continues. Their experiments, which were done on three different MIC compositions (Al-CuO, Al-Fe₂O₃ and Al-WO₃), showed similar products morphologies, suggesting a common underlying mechanism.

One of the attributes of such a reaction mechanism is that the initial nanoscale morphology is lost before/during the reaction and the resulting product morphologies resemble large molten clusters, as seen in Figure 1-7c. Moreover, X-Ray phase contrast imaging of these reaction led to the finding that these larger, sintered masses were forming on the order of microseconds after ignition, i.e., much faster than the millisecond long combustion time scales for these systems.[41] What these results inherently imply is that the loss of nanostructure could occur rapidly during the reaction and would suggest that there could be diminished performance enhancements

as the particle size is reduced through to the nano-regime. Recent results in burn tube studies highlight this point where the researchers have noticed a reduction in burn speeds when the size of the aluminum in Al-CuO nanothermite was reduced below $3.5\ \mu\text{m}$. [31] Such an interfacial mechanism could also account for the low diameter dependencies that were observed in nanoparticle burn times. In both these cases, the diminished returns on further reduction in size can be explained by the loss of nanostructure, with the small initial particles coalescing into large particles. If this happens prior to significant combustion, the material will have the kinetics of the larger particles as opposed to the nanosized starting material. Recent Molecular Dynamics simulations in Ref. [19] highlight this point by evaluating the characteristic sintering time of nanoaluminum aggregates, found to be on the order of $\sim 50\ \text{ns}$ which is much faster than the reported burn times of nanoaluminum [39] or nanocomposites, [43] both of whom are on the order of microseconds to milliseconds.

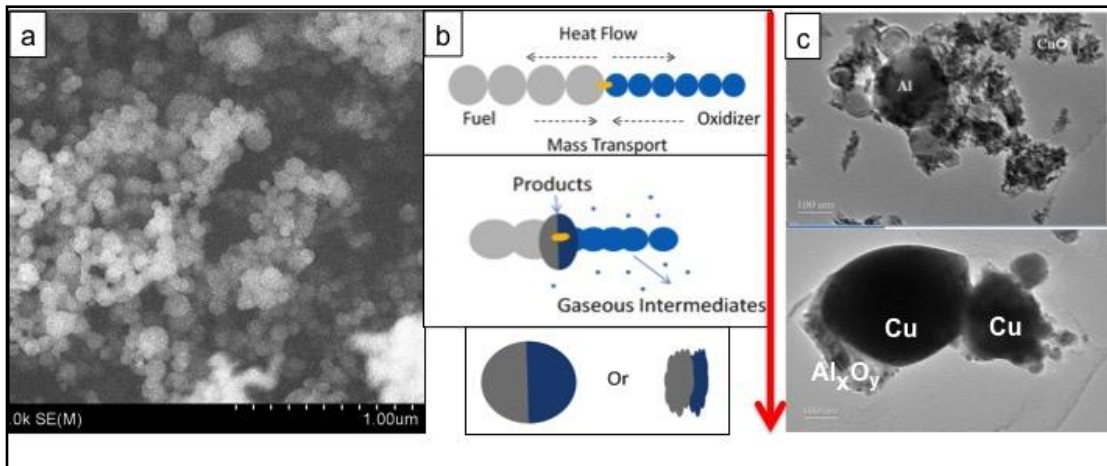


Figure 1-7: (a) Aggregated state of commercial aluminum nanoparticles; (b) Proposed Reactive Sintering mechanism; (c) Change in the morphology during the exothermic reaction. Reprinted from [42]

1.4.3 Mechanochemical Melt Dispersion Mechanism (MDM)

A third possible mechanism discussed in literature to explain the fast reactivity of nanoscale energetic composites is the Melt Dispersion Mechanism (MDM) that was postulated on the mechanochemistry of the metal nanoparticles under very high heating rates ($>10^6$ K/s).[44,45] The proponents of this work argued that the diffusion of reactants were too slow to sustain a reaction that occurred on the microsecond scale. The reaction mechanism is predicated on the differences in the thermal expansion coefficient of the aluminum core and the alumina shell which results in the development of compressive (core) and tensile stresses (shell) upon particle heating. As the stress exerted by the expanding core exceeds the yield strength of the shell, the shell is proposed to violently rupture, releasing the molten core as a mist of aluminum clusters that can react readily with the oxidizer, as limited by the reaction kinetics. Considerable calculation and modelling efforts have been undertaken to prove the applicability of this model extending from oxidation to fluorination reactions of nanoaluminum particles.[46] While this mechanism is fundamentally very different from the condensed phase discussed above, the two are not necessarily mutually exclusive. It is possible that one occurs when one set of experimental parameters are met and the other occurs under others, with MDM it could still be significant because of the high burn rate suggested by the theory.

Motivation and Research Outline

The objective of this work is to perform critical experiments so as to understand the controlling mechanism of nanoparticle/ nanocomposite reactivity and subsequently tune out the inherent limitations of the identified reaction mechanism by altering the nanostructure. The first part of this dissertation attempts to identify the reasons for the observed low diameter dependence of the burn time in nanoparticle combustion. In this part, nanoparticle aggregates of Titanium and Zirconium are synthesized via pulsed laser ablation. The advantage of this procedure is that the nanoparticle aggregates can be created in a highly controlled environment with good control on their sizes. The size-selected particles are subsequently burnt in the post flame region of a methane-oxygen diffusion burner and their burn times are measured using high-speed videography. By selecting a range of aggregate sizes in the nano regime and correlating it to the burn time, I attempt to devise scaling laws that can relate burn times to the effective diameters. The novelty of this work being that aerosol based growth models for nanoparticles are incorporated to deduce effective particle size and is further correlated to combustion mechanism by fitting the emission profiles to kinetic models.

The second part of this dissertation aims at mechanistically probing nanothermite reactions in order to provide concrete evidence regarding the predominant reaction mechanism. Results from the laser ablation experiments are used qualitatively to highlight the predominance of ultra-fast, condensed phase

interfacial reactions, which drastically altered the starting nanostructure of the composite. This part focuses on evaluating and quantifying the relative contribution of the competing reaction mechanisms i.e., gas-condensed heterogenous vs. interfacial oxidation. The probable role of either mechanisms were evaluated through a post-combustion analysis of rapidly quenched product particles of three different nanothermites systems. The three systems were chosen owing to their very different ignition and burning characteristics so as to provide sufficient breadth to the analysis.

The third part of this dissertation consists of engineering a reactive composite that counters the extent of this early interfacial reactions and enforce the composite to burn as smaller clusters. Since the reaction in these systems have been shown produce large clusters due to rapid sintering very early in the reaction, the diffusion length scales for the reactants could play a major role in the overall reactivity. By dispersing the reactants into smaller clusters, the reduction in the effective diffusion length scales could consequently attain a more complete reaction. The principle behind these custom composites is to pack nanoscale material (nano aluminum or nanothermites) using a low temperature gas generator (nitrocellulose) as a binder. The nitrocellulose acts as a binder, maintaining the integrity of the composite particle, and also as an insitu gas generator, dissociating at ca. 450 K. Since most of these nanoenergetic materials ignite above 450 K, our strategy could lead to the break up of these composites, before reaction, into smaller clusters, as shown schematically in Figure 1-8a. Also shown for comparison in Figure 1-8b is a schematic of how a nanoscale

energetic material, synthesized via powder mixing, reacts. An aggregate of the energetic material (pure nanoscale metal powder or a nanocomposite) could first sinter into a large lump and subsequently react over longer timescales. Other novel methods to improve nanoenergetic reactivity such as doping the composites with different oxidizers or tuning the characteristics of the shell are also discussed in this section. Finally, additive manufacturing techniques such as 3D printing is used to successfully demonstrate the viability of nanoaluminum-polymer/binder based energetic material.

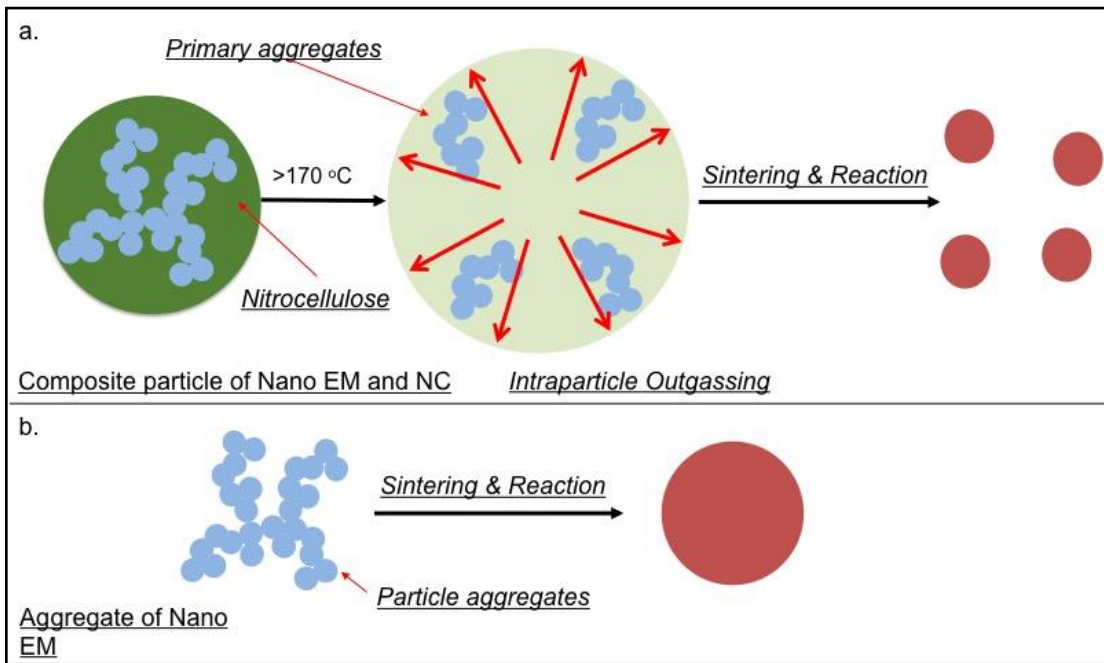


Figure 1-8: (a) Proposed mechanism of composite particle of nanoscale energetic material (EM) and nitrocellulose. The nitrocellulose acts as a gasifying agent, dispersing the aggregate into smaller clusters; (b) Schematic of how an aggregate of nanoenergetic material reacts, which involves sintering into a much larger particle before significant reaction.

Chapter 2 High Heating Rate Experimental Methods

Summary

Characterizing the ultra-fast reactions in energetic materials require the development of advanced diagnostics capable of resolving the sub millisecond reaction time scales. Conventional techniques for temperature measurements such as thermocouples and thin filaments lack response time and the high flame temperatures (>3000K) preclude the use of such invasive techniques. In this chapter, two high speed diagnostics characterizing the light emission from the energetic material reactions are introduced. A high-speed 32 channel spectrometer, capable of $\sim 2.5 \mu\text{s}$ temporal resolution, is developed to quantify the light emission from the reactions. The resulting spectra is analyzed for atomic and molecular emission and the continuum is fit to Planck's law to calculate condensed phase temperature. One of the limitations of the spectrometer setup is the lack of spatial resolution which skews the collected spectra to the brightest spots in the reaction zone. In order to resolve the spatial variations in the flame front, as is expected from a complex reaction front, a high-speed color camera pyrometer is developed as a complementary diagnostic to the spectrometer. The advantages and the limitations of the systems are detailed in this chapter along with necessary calibration steps.

2.1 *Temperature measurements through multiwavelength pyrometry*

Temperature is a fundamental, intensive property of the system and is characterized by the chemical reaction and heat transfer experienced by the system. Over the past three centuries, beginning with the work of Daniel Fahrenheit in 1714 on liquid-in glass thermometers, several methods with varying complexities have been devised to measure temperature, all of which can be classified into three categories: invasive, semi-invasive and non-invasive.[47,48] For the case of energetic materials (EM), their high reaction temperatures preclude the use of conventional invasive measurement methods such as thermocouples, thin filament pyrometers [49] that are routinely used in soot measurements. Semi-invasive methods involve doping the EM with salts that leave a thermal signature when heated. The resulting molecular emission spectra can be resolved using a grating and fit to the known spectra of the salt from which the temperature can be calculated. Barium Nitrate ($\text{Ba}(\text{NO}_3)_2$) has been used to measure apparent temperatures of RDX doped with aluminum nanoparticles, where flame temperatures as high as 4500K were obtained. [50,51] The obvious limitations for this setup is that a high-resolution spectrometer, capable of ~ 0.1 nm or better resolution is required to resolve the emission. Moreover, the calculated temperature is the temperature of the gas phase that is in equilibrium with the dopant ions. Given the condensed nature of the reactants in this study, methods using the continuum emission are needed.

The third category involves noninvasive techniques where the emission from the reaction is characterized at a standoff distance. This method is particularly useful for energetic materials owing to their bright flames and with the advent of photodetectors with very fast sampling rates, resolving the microsecond combustion time scales of explosives have been routinely attempted.[52,53] The basis of such characterization is the utilization of the Planck's law, derived in 1900's by Max Planck using quantization of energy, which defined the electromagnetic emission spectrum of a black body as a function of temperature, as shown in [54]

$$L(\lambda, T) = \frac{\epsilon * 2\pi hc^2}{\lambda^5 \left\{ \exp\left(\frac{hc}{\lambda kT}\right) - 1 \right\}}$$

Eq. 2-1

Where, L is the spectral radiance ($W/(m^2\text{-sr}\cdot\mu m)$), λ is the wavelength, h is Planck's constant ($6.626 \text{ e}(-34) \text{ J}\cdot\text{s}$), k is Boltzmann constant ($1.38 \text{ e}(-23) \text{ J/K}$) and T is the temperature. An additional parameter ϵ called emissivity is added to correct for gray bodies that emit only a fraction of that of an ideal black body at the same temperature.

The earliest forms of non-invasive pyrometers involved the disappearing filament technique, where the 'brightness' temperature was measured by visually comparing the emission from the flame with that of a controlled filament in the background and adjusting the temperature of the filament till it disappeared in the flame. The eye of the operator was soon replaced as the detector by solid state photodetectors, which used the ratio of discrete filtered emission from the flame as a

measure of the temperature. Soon two, four and six wavelength pyrometers in the visible and IR wavelengths were developed and extensively used in characterizing combustion systems.[55–57] Another form of multiwavelength pyrometry involves using a high resolution spectrometer to resolve the emission spectra over multiple wavelengths to which the Planck's law from Eq. 2-1 is fit with temperature as a free parameter. Implicit in this fit is the assumption of a reasonable model for the wavelength dependence of emissivity. For soot, $\epsilon \sim \lambda^{-1.36}$ whereas for optically thick flames a grey body assumption can be used. [58] Some authors have employed the $\epsilon \sim \lambda^{-1}$ dependence[59,60] which is derived from the spectral dependence of the absorption efficiency in the Rayleigh limit, while neglecting the spectral dependence of the absorption index. Others have corrected this correlation by incorporating the inverse wavelength dependence of the absorptive index, resulting in a $\epsilon \sim \lambda^{-2}$ dependence owing to significant absorption effects.[52] Depending on the choice of the emissivity function, the final calculated temperatures could fluctuate by as much as 1000K. [58] Other forms of non-invasive techniques involve characterizing the molecular emission of inherent species (such as Al and AlO in aluminized composites) from which the flame temperature could also be calculated.[61,62] In this work, I developed a couple of non-invasive diagnostics, one based on a high speed spectrometer and the other based on a commercial high speed camera with the objective of calculating the reaction temperature from the nanoenergetic composites.

2.2 High Speed 32 channel Spectrometer

The high-speed emission spectrometer was developed to quantify the emission spectra from the nanocomposite reaction so as to characterize its reaction temperature as well as identify dominant molecular/atomic species in emission. A constant volume combustion vessel was used to burn the sample, which is described in further detail in Chapter 6. The optical assembly interfacing the spectrometer with the pressure cell consists of a Sapphire window, a Plano Convex lens 1F from the inner edge of the vessel, a Neutral Density filter (ND2) and a 455 nm color glass filter for order sorting. The optical components are assembled inside a 0.5" lens tube and the end of the tube is closed with a SMA fiber optic adapter. The Plano Convex lens collimates the light from the inner edge of the vessel which is subsequently attenuated by a factor of 100 by the ND2 filter. The choice of the ND filter was empirical with the ND2 used for measurements at high irradiances and ND1 for low irradiance measurements. A 1mm diameter optical fiber (Princeton Instruments) transfers the emission into a 500mm, triple grating, Czerny-Turner Imaging spectrometer (Acton), as shown in Figure 2-1. A 150 groove/mm grating and a slit width of 100 μ m was chosen for this work, which gave a dispersion of 13 nm/mm at the focal plane and a spectral range of 464-867 nm. The primary objective of this work was to detect reaction temperature, hence a low-resolution grating was chosen so as to obtain the widest spectrum.

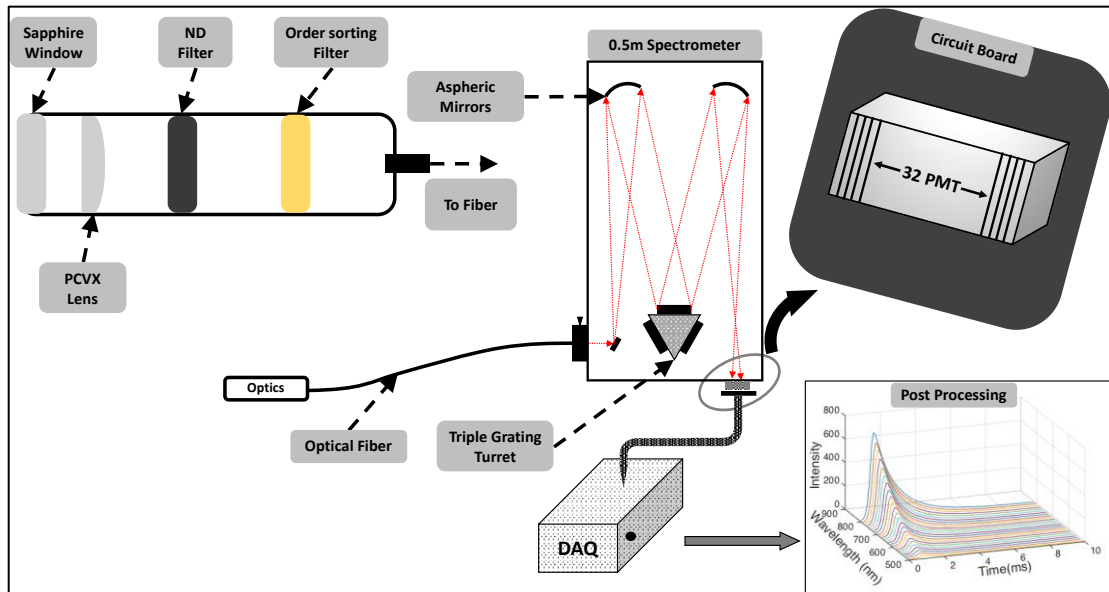


Figure 2-1: Setup of high speed emission spectrometer

The spectrometer outlet was coupled with a 32 channel PMT module (Hamamatsu, H7260) with each channel having a dimension of 0.8mm x 7mm (WxH), implying a spectral resolution of ~ 10 nm/channel. A PMT based detector was preferred in this work, owing to their fast rise times (0.6ns), tunable supply voltage (400-900V) and single photon efficiency. The multichannel PMT (MC-PMT) is interfaced with a high-speed data acquisition system (Vertilon IQSP580) which terminates the MC-PMT to 50Ω and measures the current output at the anode with 14-bit resolution. The system is capable of sampling at a maximum rate of ~ 390 kHz with an onboard storage for 5×10^5 32 channel events and has a versatile suite of triggering options. Although faster multichannel pyrometers have been recently developed for shock physics and detonation experiments[63,64] with time resolutions ranging from 800ps-10ns, their total recording time is a significant limitation. At \sim

400kHz, the spectrometer discussed herein offers a good compromise between time resolution and total recording time especially for the combustion of nanothermites which are not only much slower than traditional explosives but also has a wide range of combustion time scales. Other advantages include the ability to set the cathode voltage of the MC-PMT, which is particularly useful for samples with moderate to poor reactivity. The triple grating turret assembly allows the selection of sample specific spectral ranges along with the ability to increase the spectral resolution by switching to a higher density grating. One of the significant limitations of the setup is the 20 μ A linearity limit of the MC-PMT, which limits the dynamic range of detection. This is offset by running multiple experiments where a ND2 filter was used for characterizing the emission at peak irradiances and was replaced with an ND1 for the cooler phases of the reaction.

2.3 Calibration of High-Speed Spectrometer

The linearity of the MC-PMT was tested by illuminating the collector optics with a high temperature black body source at 1273 K and subsequently attenuating the signal using neutral density filters (OD 0.4, OD 1). Neutral Density filters corresponding to OD 0.4 and OD 1 attenuates the broadband light to 40% and 10% respectively. The results of the calibration test are shown in Figure 2-2a for the selected MC-PMT voltage of 600V. As can be seen, the detector is fairly linear although at low light intensities with OD1 some nonlinearities were observed. The

wavelength calibration for the spectrometer was done using a HgNe pencil lamp (Newport) and the spectral response calibration was done using a calibrated tungsten halogen lamp (Avantes HAL CAL) operated at 2440 K. Figure 2-2b shows the RAW counts corresponding to the intensity profile of the calibration lamp, measured at a cathode voltage of 600V on the MC-PMT. The spectral response of the entire assembly was determined by placing the calibration lamp at the inlet of the collection lens assembly for obtaining the RAW data counts at the PMT voltage of interest and computing the correction factor by taking the ratio of the RAW counts to that of the calibration curve as shown in Fig 2b. Thus, a single correction factor accounts for the detector spectral response, the grating efficiency and the transmission efficiency of the various optics.

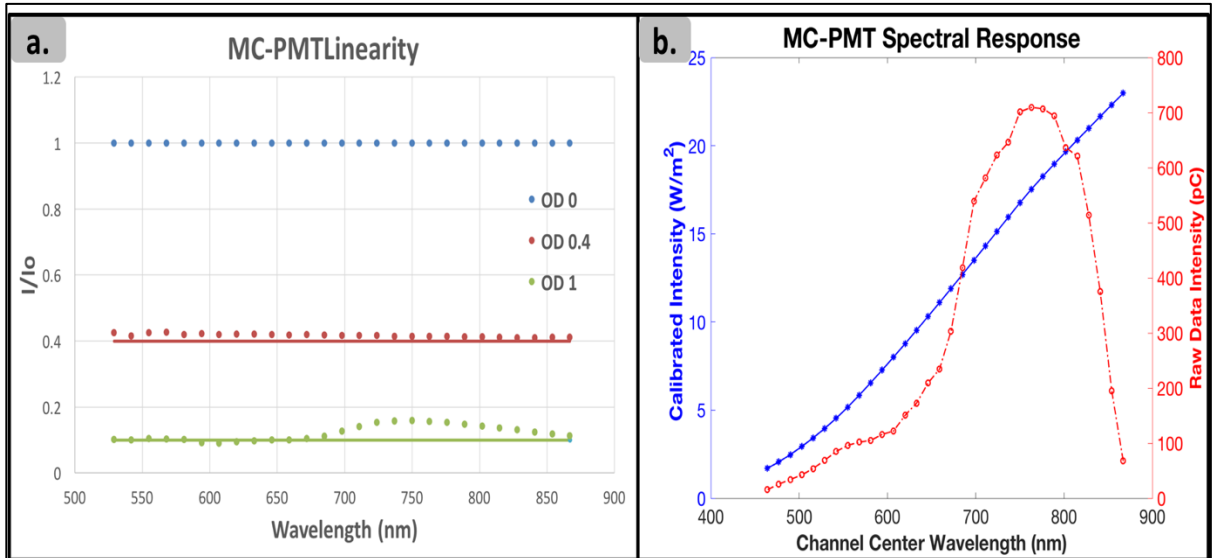


Figure 2-2: Calibration for the MC-PMT a. Evaluating the linearity of the detector by attenuating broadband signal using ND filters. Horizontal lines represent expected attenuation. b Spectral response calibration using a high temperature Tungsten-Halogen lamp.

In order to make quantitative temperature measurements, the intensity corrected data from the MC-PMT was linearized[65–67] according to Wein’s law as shown in Eq. 2. Wein’s Law is a derivative of Planck’s Law (Eq. 2-1) and is applicable when the product $\lambda T < 3000 \mu\text{mK}$, [66] satisfied by most energetic material emission in the visible spectrum. Upon linearization, an equation of the form Eq. 2-2 is derived from which the parameter Z is calculated and is plotted against the wavelength to calculate the temperature from the reciprocal of the intercept obtained from the straight line fit.

$$Z = \frac{\lambda}{C_2} \log \left(\frac{C_1}{\lambda^5 L} \right) = -\frac{\lambda}{C_2} \log \varepsilon + \frac{1}{T}$$

Eq. 2-2

Implicit in the above linearization is the grey body assumption for the flame cloud generated by the reaction, of which there has been considerable debate in the community. Recent efforts by Lynch et. al have suggested that under conditions where the high temperature flame front is optically thick, which presumably would be the case for a confined reaction in an enclosed vessel, the gray body assumption could be valid, and hence is used in this study. During the temperature fitting procedure, channels with spectral bandpass that overlapped prominent molecular emission, such as a Na doublet (588.95nm and 589.59nm) and AlO band ($\Delta v = -1, 0, +1$, 464nm – 530 nm), were removed so as to improve the fit fidelity (Figure 2-3). Built-in MATLAB fitting routines were employed to estimate the final temperature (Appendix A).

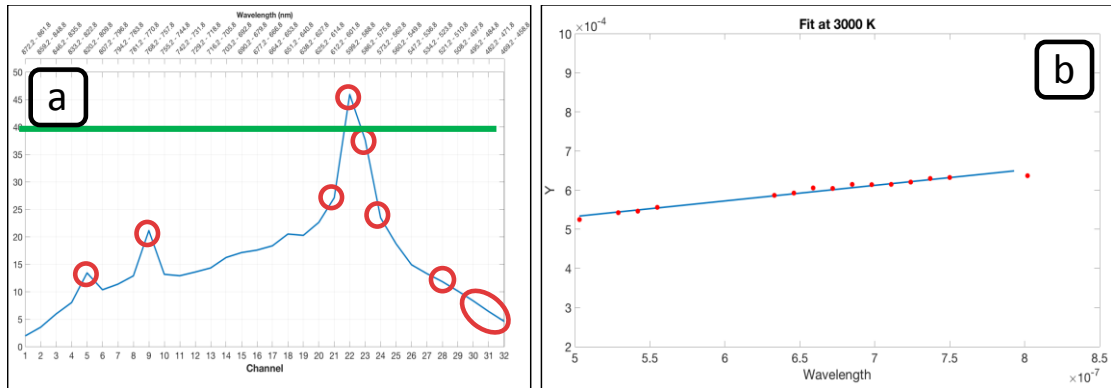


Figure 2-3: (a) Raw spectra from a reaction showing the various molecular emission peaks. (b) The channels corresponding to the red circles were removed during straight line fitting of the parameter Z to wavelength.

2.4 High speed color camera pyrometry

While the experimental setup including the spectrometer described above can accurately measure the temperature of radiating particles using multi-wavelength integration techniques, its ability to measure the spatial dynamics of the combustion process is limited by its means of data acquisition. Since the spectrometer takes in information to a small fiber optic cable, two possibilities exist for the origin of the data – focusing of a large area onto a smaller one using a lens, or a small point light source being focused directly into the cable. In either scenario, for probing of energetic nanomaterial combustion, the use of a spectrometer falls short in large volume studies for it is averaging the entire cross-sectional area that is being observed rather than having multiple point measurements to account for spatial resolution.

As a complementary technology to the spectrometer, high speed color cameras (such as the Vision Research Phantom Miro M110) capable of recording high definition videos at a resolution of 1280x800 at a frame rate of 1,630 fps (with

maximum framerate of 400,000 fps at reduced resolution),[68] is used as a spatially resolving pyrometer. The use of a high-speed color camera allows for the temperature probing capabilities at the rate of a spectrometer, but can do so over an entire image that is captured by the sensor and post-processed with camera-specific spectral response curves.[49,69–71] In the case of the particles generated by the combustion of energetic nanomaterials, the gray body assumption regarding wavelength-independent emissivity can be applied and the temperature of an object can be calculated using the ratios of intensities between two color camera channels.[69,72]

Numerous experiments have demonstrated the ability for color ratio pyrometry to effectively characterize thermally radiating particles. Color ratio pyrometry was first reported in 1994 using an infrared-sensitive pixel array to spatially resolve temperature profiles of thin filaments.[73,74] In 2001, Tsyba et al. demonstrated the capability for a consumer color camera to be used for temperature measurements between 800C and 2500C with an error within 50C.[75] Development of high-speed digital color cameras has since led to widespread research on the temperature characterization of flames, thin filaments, soot, and direct injection spark ignition (DISI) engines.[49,70,71,76–78] A paper by Densmore et al. detailed the setup for a color ratio pyrometer that was successfully used to characterize the temperature of an exploded C-4 charge at the U.S. Army Research Laboratory, which served as the basis for the experiments performed in this study.[69] The setup described by Densmore was later applied to other applications to probe the burn

characteristics of other high explosive fireballs, impact combustion, and thermites.[79–81]

2.5 *Operation principle*

In digital color cameras, the sensor used to capture light is sensitive to wavelengths extending from the ultraviolet to infrared, with a mosaic color filter array (CFA) placed in front of the sensor to serve as a bandpass of extraneous wavelengths for later reproduction of color via a demosaicing algorithm (Figure 2-4a).[69] The most common filter array used in color cameras is of the Bayer pattern, which has filters with peak sensitivities corresponding to the red, green, and blue portions of the visible color spectrum [69]. The intensity of the signal captured by the sensors is dependent on the channel gain, pixel area, solid angle, exposure time, lens transmission, spectral power density of the source, and the spectral sensitivity of the filter array integrated over the entire spectrum of sensitivity for the camera.[69] As a result, solving for temperature based on intensity of a single channel becomes inherently difficult as the level of knowledge required for accurate estimations of temperature is prone to error. Alternatively, provided that the aforementioned variables (excluding filter sensitivity) remain constant for adjacent pixels being sampled, a ratio of the channel intensities recorded by the camera can be used to back-solve for temperature as shown below, where χ_i is the normalized spectral response of the camera and ψ_i is the gain of channel i .[69] In the case of a

gray body radiating source, the emissivity is assumed constant and independent of wavelength and therefore need not be accounted for in calculation.[69,77]

$$\frac{I_i}{I_{j_{sensor}}} = \frac{\psi_i \int L(\epsilon, \lambda, T) \chi_i(\lambda) d\lambda}{\psi_j \int L(\epsilon, \lambda, T) \chi_j(\lambda) d\lambda}$$

Eq. 2-3

By performing this calculation at different temperatures, theoretical values for intensity ratios between channels can be then used to determine a “calibration factor” ($C_{ij} = \psi_i/\psi_j$) for the specific camera components by comparing the expected ratios of intensity to those collected from a standardized radiating temperature source. Calculations of temperatures is then reduced to matching of the calibration factor-corrected ratio of the channels to the theoretical ratios predetermined for the apparatus, as shown in Eq. 2-4 and Figure 2-4b.

$$\left(\frac{I_i}{I_j}\right)_{sensor} = C_{ij} \left(\frac{I_i}{I_j}\right)_{theor}$$

Eq. 2-4

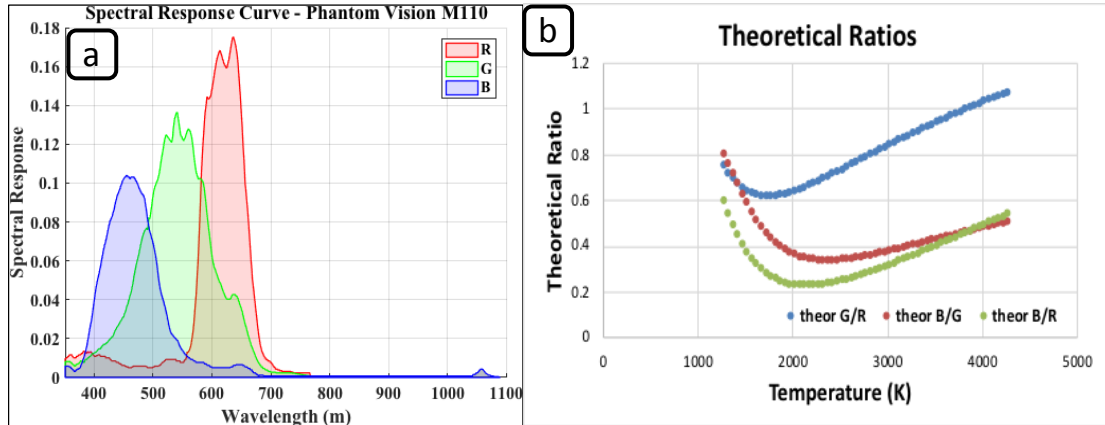


Figure 2-4: (a) Spectral response curve of Vision Research Phantom Miro M110 high speed camera. Figure adapted from Vision Research.[68]; (b) theoretical calibration ratio profiles as a function of temperature for the three colors in CFA.

2.6 Color Camera Calibration

Using the theoretical channel ratios as calculated by Eq. 2-4, calibration factors for the camera's channels ($C_{ij} = \psi_i/\psi_j$) were determined by taking videos of a blackbody light source and extracting observed channel ratios.[69] As can be seen in Figure 2-5a, the black body temperature was adjusted between 1273 and 1473 K with 50 K increments. The theoretical estimate from Eq. 2-3 is plotted as the red line with the overlaid black markers being the calculated ratios for the Green to Red channels. The calibration was extended beyond the inflection point by using a high temperature tungsten halogen lamp operated at 2440K which was factory calibrated. The calibration data was integrated with the spectral response of the camera detector (Figure 2-4a) to obtain the experimental G/R ratio. The linearity of the camera sensor was calibrated with various Neutral density filters (OD 0.1, 0.4, 0.5, 1) and the result is plotted in Figure 2-5b, along with the expected correlation, confirming the linear response of the CMOS array. For the setup used in this dissertation, the calibration factors (C_{gr} , C_{bg} , and C_{br}) for the camera equipped with a macro lens were determined to be 0.952, 0.888, and 0.847, respectively. These calibrations are expected to be valid from a low temperature of 773 K and calculations have been extended up to 4773 K.

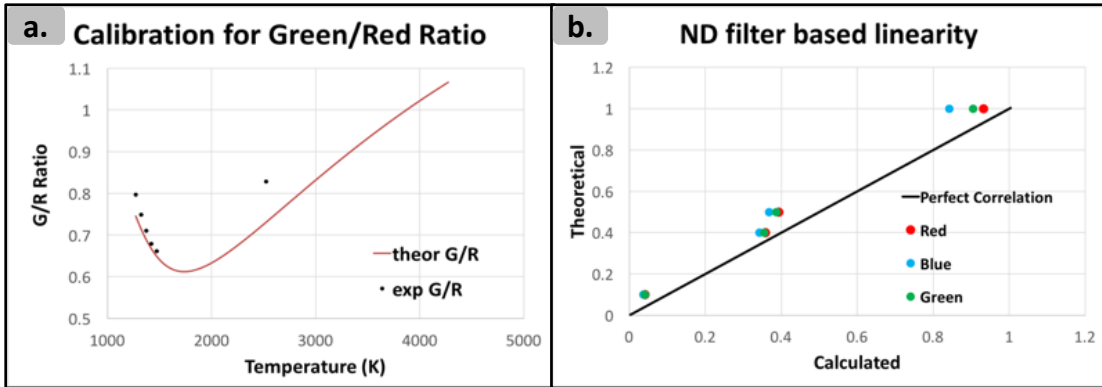


Figure 2-5: Calibration for the Color camera pyrometer: (a) Spectral response calibration using a Black body and high temperature Tungsten-Halogen lamp. (b) Evaluating the linearity of the camera sensor by attenuating broadband signal using ND filters. Dark line represents the expected attenuation

While color camera pyrometry does allow for spatiotemporal measurements of temperature, limitations in the method by which raw data is collected are a strong source of error in calculations that are performed, which ultimately lead to deviations in temperature measurement from those reported by the spectrometer. Of the many elements that emit in the visible region of light during thermal relaxation, sodium is often the most noticeable with strong, persistent lines seen as a doublet at 588.95nm and 589.59nm.[82] Such emission contributes to the red and green channel intensities owing to their high spectral response at these wavelengths (Figure 2-4a), therefore leading to error in temperature calculations. Other elements that have strong emission and are possible sources of contaminants in the experiments performed include potassium and copper. Furthermore, the calculations detailed above fail to account for light scattering from small particulates that may be generated throughout the course of the reaction, leading to another possible error within the color camera pyrometry

method for estimating temperature. Hence, in order to maintain fidelity, the error minimization algorithm used to calculate temperature is error thresholded to $\sim 100\text{K}$ and the pixels that report higher errors are browned out in the final false-color images.

2.7 Video Processing

Raw pixel values were extracted and temperatures calculated using MATLAB (Appendix C). Prior to performing temperature calculations, black-level pixels and saturated pixels were dilated by a factor of 3 and removed from the area of consideration. The raw image array was then passed through MATLAB's "demosaic" routine with the corresponding Bayer color filter array sensor alignment (gbrg) to recover values for the red, green, and blue channels at each pixel. To determine temperature, calibration factors were applied to three camera generated ratios (green/red, blue/green, and blue/red) and matched to the theoretical values in Figure 2-4a such that the summed error in all ratios was minimized. Lookup tables corresponding to the values presented in Figure 2-4a are generated depending on the emissivity model used and the error minimization is performed to obtain the final temperature. Once the temperature is calculated, the G/R ratio corresponding the calculated temperature is matched from Figure 2-4a and the difference between this value and the one obtained from the camera is used to estimate the error in temperature measurement.

Chapter 3 Size Resolved High Temperature Oxidation Kinetics of Nano-Sized Titanium and Zirconium Particles

Summary

While ultrafine metal particles offer the possibility of very high energy density fuels, there is considerable uncertainty in the mechanism by which metal nanoparticles burn, and few studies that have examined the size dependence to their kinetics at the nanoscale. In this work I quantify the size dependence to the burning rate of titanium and zirconium nanoparticles. Nanoparticles in the range of 20-150 nm were produced via pulsed laser ablation, and then in-flight size-selected using differential electrical mobility. The size-selected oxide free metal particles were directly injected into the post flame region of a laminar flame to create a high temperature (1700 - 2500K) oxidizing environment. The reaction was monitored using high-speed videography by tracking the emission from individual nanoparticles. I found that sintering occurs prior to significant reaction, and that once sintering is accounted for, the rate of combustion follows a near $\sim (\text{diameter})^1$ power-law dependence. Additionally, Arrhenius parameters for the combustion of these nanoparticles were evaluated by measuring the burn times at different ambient temperatures. The optical emission from combustion was also used to model the oxidation process, which can be reasonably described with a kinetically controlled shrinking core model.

3.1 Introduction

Metal particles are commonly used in energetic materials such as rocket propellants and explosives, due to their high energy density and reactivity. While aluminum is the most commonly used metallic fuel, other metals are also of interest. In particular, titanium (Ti) and zirconium (Zr) have been studied for their application in pyrotechnics, fire safety and flame synthesis.[83–85] Recent interest is also based on the potential of both metals in forming special energetic alloys and formulations.[86,87] Compared with aluminum (Al), which is the most important metallic fuel, both Ti and Zr have much higher melting points, and are less reactive with oxygen. Nano-sized Ti and Zr particles provide the added advantage of higher reactivity and energy release rates owing to the higher surface area to volume ratio.

So far, almost all the studies on Ti and Zr combustion are focused on micron-sized particles.[86–90] Generally, the combustion of both metals are classified as heterogenous, which means surface reactions dominate the burning process, rather than gas phase reactions. This is because the boiling points of these metals (Ti: 3560 K, Zr: 4650K), are close to/higher than their corresponding oxide, according to Glassman's criterion.[5] For micron-sized particles, Badiola and Dreizin[89] recently measured the combustion temperature of the particles, to be 3343 K for Ti and 3683 K for Zr, which are close to their adiabatic flame temperatures. Micro explosions were also observed in their study, similar to the burning of bulk size metals. In terms of nano-sized particle burning, some recent studies on aluminum (Al) and boron (B)

combustion show that the oxidation rates of the metals are significantly increased, that is, shorter burn time and lower ignition temperature than micro-sized particles.[91–93] However, complexities associated with the nature of the oxide shell,[94] and the roles of aggregates are as yet unresolved.[19] Most significantly the nature of the size dependence on the reaction rate for sub-micron particles are poorly described.[38,95–97] In this paper, I am interested in addressing the nature of the latter lack of clarity for the oxidation of oxide free metal nanoparticles.

The burn time for large metal particles ($> 30 \mu\text{m}$) has long been known to obey the “ d^2 law”, where d is the particle diameter, and the overall rate is known to be gas-phase diffusion controlled.[27] When the particle becomes smaller, the oxidation is no longer limited by gas-phase species diffusion, and transitions to a surface reaction controlled mechanism which should follow a “ d^1 law”.[98] This behavior is depicted in Figure 3-1.[20] For particles smaller than $1 \mu\text{m}$, the relationship between burn time and particle diameter is currently unclear. The very limited experimental studies indicate a power law with the exponent as 0.3-0.5.[92,96] Some studies on Al, Ti and Zr in the 1-10 μm range have shown that it’s an even weaker function of particle size.[38,89] What is unclear however is the mechanistic reason for the small power exponent. Chakraborty and Zachariah recently argued through a molecular simulation study that small aggregated particles do not necessarily remain nano-sized during oxidation due to rapid sintering, with the characteristic reaction time comparable to the characteristic sintering time.[19] More recently in-situ dynamic

TEM studies have provided experimental proof on the rapid loss of nano structure and concluded that significant morphological changes may occur very early in the reaction process, implying that the bulk of the energy release chemistry occurs in effectively larger particles.[99,100]

In this study, nano-sized metal particles of Ti and Zr were generated through laser ablation in an inert environment. The particles were then ion-mobility size selected using a differential mobility analyzer (DMA). The oxidation rate of the size-selected particles was measured by injecting them into the post flame region of a 1-D flame where the temperature could be varied from 1700 K to 2500 K by tuning the reactant stoichiometry. Finally, the size dependence of the high temperature oxidation rate for sub-micron particles were examined and theoretically interpreted, elucidating the role of aggregate sintering.

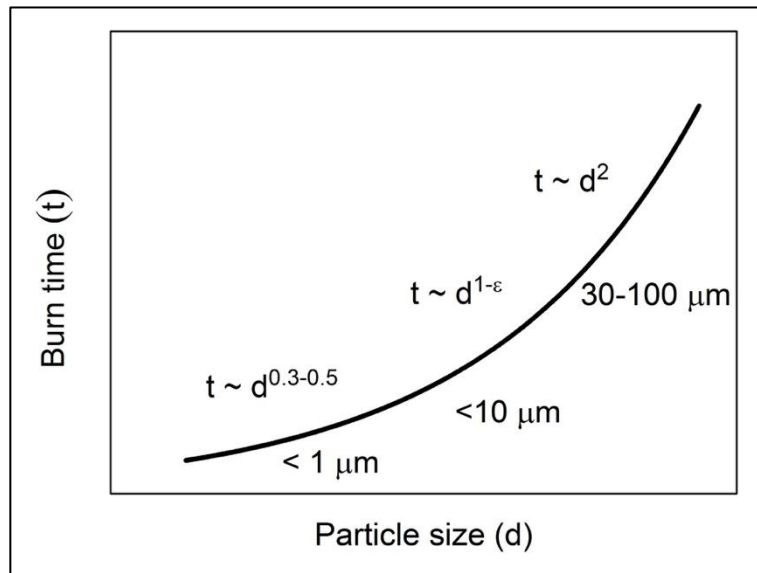


Figure 3-1: Conceptual figure showing experimentally determined diameter dependence on burn time[19]

3.2 Experimental Methods

Oxide free metal particles were generated by laser ablation and size selected in the aerosol phase. A schematic of the experimental system for size-selected metal particle production and oxidation rate is shown in Figure 3-2. The apparatus consists of two parts: An atmospheric pressure laser ablation system, with an integrated differential mobility analyzer (DMA) for particle size selection, and a multi-element diffusion flat flame burner where particles are oxidized.

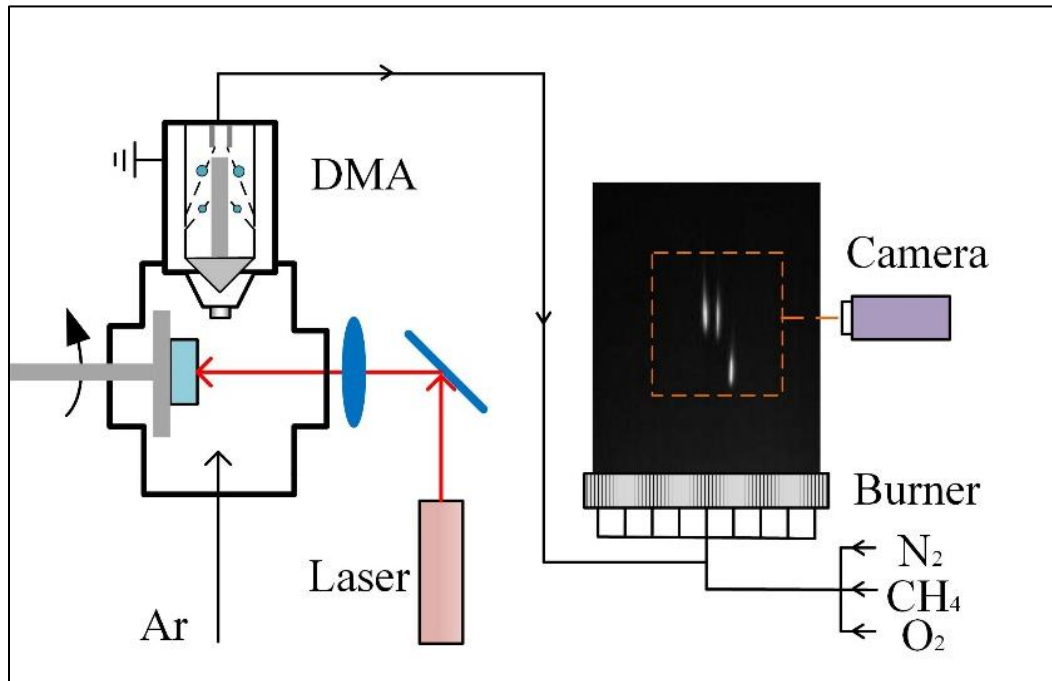


Figure 3-2: Schematic of the experimental setup showing the atmospheric pressure laser ablation system connected with the DMA and a flat flame burner.

3.2.1 Laser ablation for nanoparticle generation

In our experiments, a Q-switched Nd:YAG pulsed laser (Brilliant, Quantel) was operated at 1064 nm, with a pulse energy of 120 mJ at 20 Hz and a pulse width of ~5 ns. The pulsed beam was focused with a fused silica plano-convex lens (150 mm FD) to an energy density of $\sim 10^{10}$ W/cm² to create a local plasma. The target was a 1" diameter, high purity (99.995%) sputter target of the respective metals (Kurt Lesker). As shown in Figure 3-2, the metal target was mounted on the rotating shaft of a stepper motor, and the metal target surface was carefully positioned at the focal point of the lens. The laser spot is about 0.5 mm in diameter at the target surface. In the experiment, argon was flowed (99.995%) across the ablating surface at 1.5 lpm in order to carry the resulting nucleated particles to the DMA. The flow also acted as quenching gas to suppress further particle growth in the laser-induced plume, which was reported at extremely high temperature and pressure.[23,101] The laser ablation system was run continuously during the experiments and did not show any significant variation in the particle size distribution.

3.2.2 Differential Mobility Analyzer (DMA) for NP size selection

For size resolved measurements a DMA (3085, TSI) was modified and mounted upon the laser ablation chamber. The DMA has a cylindrical configuration and consists of two electrodes, as shown in Figure 3-3. The inner electrode is held at a high voltage (0-10 kV) and the outer cylinder is grounded. The electric field created

between the inner and outer electrode results in a size dependent radially inward electrical mobility for charged particles and is the basis for the size separation.[102] Every charged particle/aggregate in motion under an applied electrical field has an inherent electrical mobility which is the balance between the electrical force and Stoke's drag force and is a function of the size (mobility diameter), as shown in Eq. 3-1, where n is the charge on the NP, e is the elementary charge, C is the slip correction factor, μ is the viscosity and D is the mobility diameter of the nanoparticle.

$$Z_p = \frac{neC}{3\pi\mu D}$$

Eq. 3-1

The DMA construction parameters, on the other hand, can be correlated to a theoretical value of electrical mobility (Z_p), as shown in Eq. 3-2, where q_{sh} is the sheath gas flow, V is the applied voltage difference, L is the length between exit slit and polydisperse inlet, r_2 the outer radius and r_1 is the inner radius of the annular region. Equating the values of the electrical mobilities provide a relationship between mobility diameter and applied voltage, which forms the basis of size selection.[103,104]

$$Z_p = \frac{q_{sh}}{2\pi VL} \ln \left[\frac{r_2}{r_1} \right]$$

Eq. 3-2

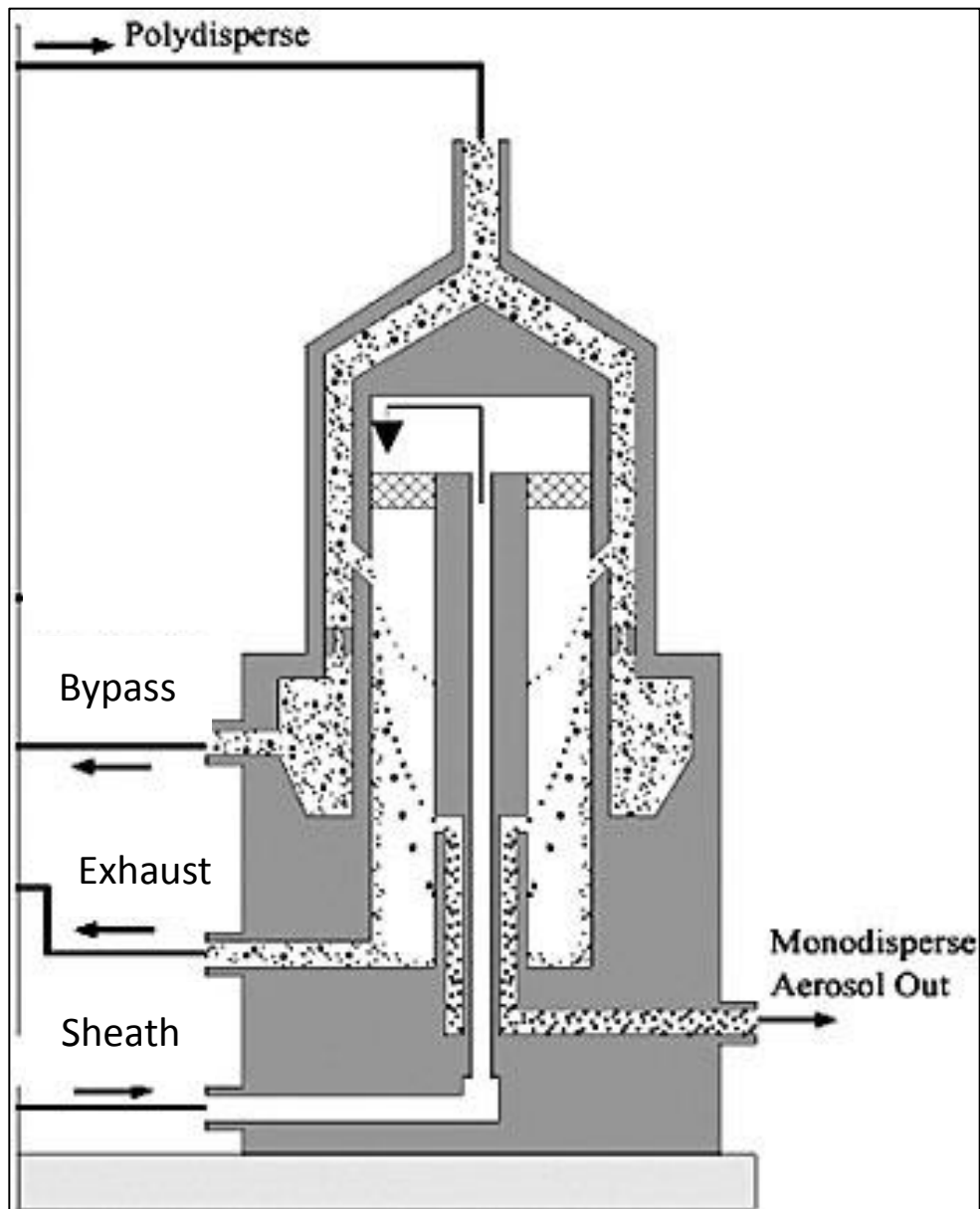


Figure 3-3: Schematic of a DMA showing the various gas flows.[104]

The metal particles generated by laser ablation are intrinsically charged owing to the high temperature in the laser-induced plasma. The generated particles were subsequently brought to Boltzmann equilibrium by neutralizing the aerosol using a

Polonium source of alpha particles, which resulted in 70% of the nanoparticles in the size range of 1-200 nm to be either neutral or have unit charge of either polarity. At a fixed voltage, the DMA operates as a band-pass filter for mobility size and can be employed as a size selection tool.[105] While argon was used in the ablation chamber I found it necessary to use N₂ (99.95%) as the sheath flow (4 lpm), owing to its higher breakdown voltage than argon. The mono-disperse particle flow was kept as 1.5 lpm, which was equivalent to the chamber inlet argon inflow. The DMA used in this work was calibrated with another DMA (3081, TSI) coupled to a condensation particle counter (CPC, 3776, TSI) to obtain the size distribution of particles emanating from the chamber.

3.2.3 Flat flame Burner and burn time measurements

A homemade multi-element diffusion flat flame burner, often referred to in the literature as a Hencken burner,[106] was used to test the ignition and combustion characteristics of the metal particles. The burner has a multi-element and non-premixed flame configuration. For these experiments, fuel lean ($\phi \sim 0.25$) methane/oxygen/nitrogen flows were used to provide an oxidizing environment in the post flame region, with an equilibrium distribution of products: oxygen = 44.3 %, nitrogen =36.5%, CO₂ =6.2% and H₂O =12.5%, The post-flame temperature at the centerline of the burner could be adjusted from 1700 K to 2500 K by increasing the methane flow rate. The flame temperature was measured by an R-type thermocouple

(Omega), which is made of platinum and platinum-rhodium alloy wires that contact each other with a 0.01-inch junction spot. After size selection, the particle-laden flow was injected into a central tube (O.D. 1/16'', I.D. 0.022'') along the centerline of the cylindrical burner as depicted in Figure 3-4.

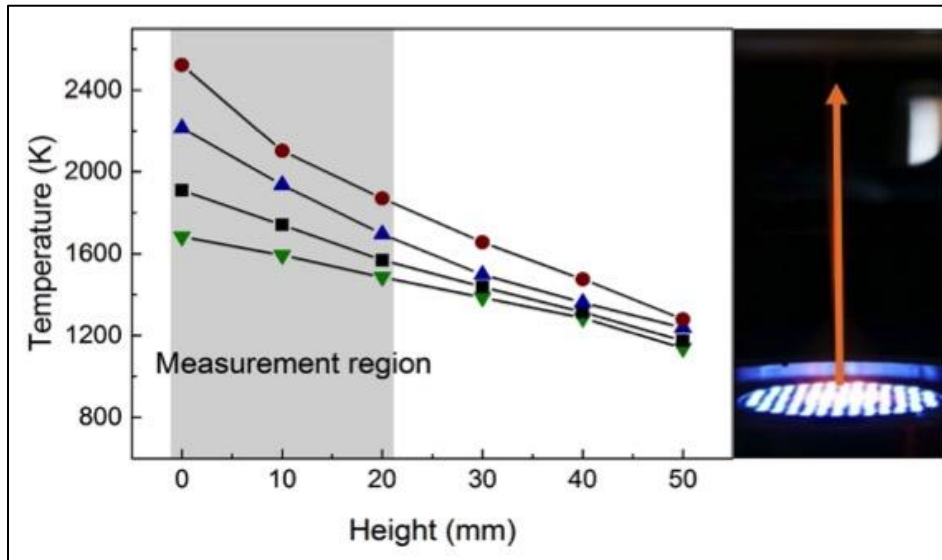


Figure 3-4: Temperature profiles for different stoichiometries along the burner centerline as a function of the height above the burner.

To evaluate the total burn time, the particle luminosity was tracked with a high-speed camera (Phantom V12.1, Vision Research) with an exposure setting of 5 ms, which is much longer than the particle burn time. Thus, the entire combustion event was recorded on a single frame as a streak, whose length could be used to extract the burn time. The velocity field above the burner was determined by tracking micro-sized seed particles of aluminum with the camera, the centerline velocity was measured as 20 ± 2 m/s within the monitored zone for particle burning. At different

heights above the burner, the metal particles were sampled by a nanometer aerosol sampler (3089, TSI) and characterized by TEM (JEM 2100, JEOL).

3.3 *Results and Discussion*

3.3.1 Size selection of particles

The size selection of the generated particles is performed by the DMA, which produces a mono-disperse aerosol of particles of the selected diameter. For a cylindrical DMA geometry, by substituting Eq. 3-1 in Eq. 3-2, the mobility particle diameter d_m as the function of applied voltage V is obtained, as depicted in Figure 3-5. Thus, with different voltage settings in the DMA, I can obtain size-selected particles from 20 nm to 150 nm. The bandwidth of the selected particle is determined by the resolution of the instrument, which is proportional to the ratio of the aerosol to the sheath flow rates used. Higher sheath flow rate will result in a higher resolution (narrowed band width of selected particles) but also a smaller number concentration exiting the device for the oxidation measurements. The settings used were chosen to provide the best compromise between these criteria. The mobility selected particle size distributions are shown in Figure 3-6, which were measured using a second homemade DMA and CPC. Another factor may affect the resolution of the size selection is the multi-charging of the particles. According to Eq. 3-1, a larger particle carrying more than one charge could have the same particle mobility as a singly charged smaller particle, which the DMA would not be able to distinguish. For the

particles generated from flame or laser ablation, multiple charging tends to occur for relatively large particles over 100 nm.[107] For this reason, I used a Polonium source to bring the charged aerosol to Boltzmann equilibrium charge distribution, as discussed in 3.2.2.

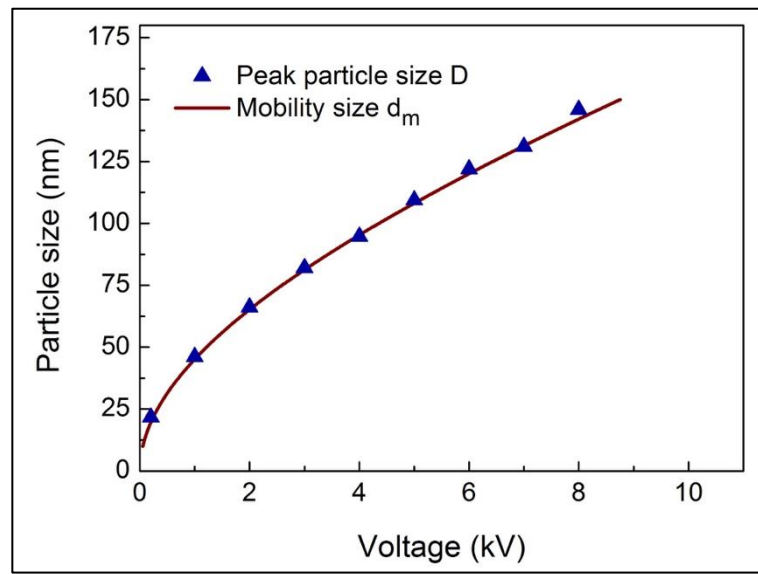


Figure 3-5: Measured peak size of the particles after size selection by DMA. The line represents the theoretically estimated mobility size.

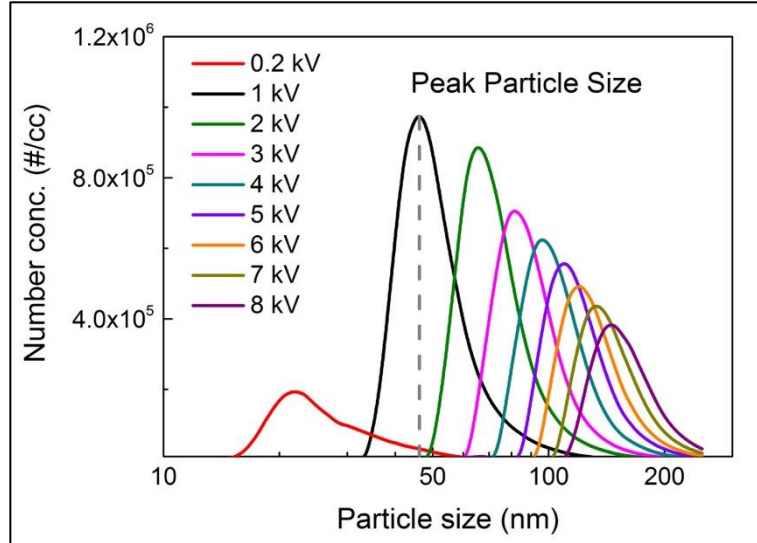


Figure 3-6: Particle size distributions obtained for different DMA voltages.

3.3.2 Combustion characteristics of the particles

The flat flame burner is adopted to provide a high temperature environment to ignite the metal particles, and an oxidizing post flame region for particles to burn. This setup allowed great flexibility in the reaction environment by tuning the stoichiometry of the reactants. The temperature profiles along the burner centerline measured using an R-type thermocouple are plotted in Figure 3-4 after radiation correction.[108] An image of the fuel-lean methane flame is also shown in Figure 3-4. The flame is flat and attached to the surface of the burner, where the temperature is the highest along the centerline. By increasing the methane flow, I can increase the temperature of the oxidizing zone from 1700 K to 2500 K. It should be noted that the melting point of Ti and Zr are 1941 K and 2128 K respectively. As the height increases, the centerline temperature decreases because of the heat loss to the

ambient. In the current experiments, the emission streaks are short (~1 mm), and usually terminate within 20 mm height from the inlet, where the average temperatures are still high enough for particle combustion. Another advantage of the current setup is that the particles experience a near isothermal ambient condition owing to their short burn times. From the temperature profile, I can estimate a temperature change of approx. 20 K over a distance of 1 mm, which is the average burn length. Furthermore, it has been recently shown that the heat loss from burning nanoparticles in the free molecular regime is not significant owing to substantially small values of the energy accommodation coefficient (EAC) for nanoparticles.[109] As shown in Figure 3-2, the particles of both Ti and Zr are observed to exhibit short emission streaks after ignition, which are quite different from those observed for micron-sized particles.[89] No micro-explosions were observed for the nano-sized particles and the emission streaks were intense and continuous. The major advantage in this study is that dilute loading of the aerosol enables us to study small agglomerates to tweeze out kinetic effects at the nano scales, as will be shown later.

I begin by examining the morphology of particle at the pre- and post-combustion zones by TEM. In Figure 3-7a, a 21.7 nm DMA selected particle is shown that was deposited after injection to the burner, but before ignition. The particles are aggregates as shown in the figure, with an average primary particle size of 10.3 ± 0.4 nm. Figure 3-7b is also a 21.7 nm DMA selected sample but deposited on a TEM grid at a height of 30 mm above the burner, where most emission streaks had

ended i.e. post combustion. These particles are seen to be isolated spheres and not agglomerates. The average particle diameter observed was 20.3 ± 1.4 nm. Figure 3-7c is a high magnification image of the particles sampled at 30 mm height, clearly showing lattice spacing, which indicates that the products are crystalline. Compared to the standard d-spacing database (PDF #21-1276, ICDD), the particle is identified as rutile phase of titania (d-spacing = 3.25 angstrom). From all three TEM images, I can say that the nanoparticles undergo both chemical and physical change through oxidation, and that the particles are fully oxidized. The morphology of the particles has changed, from aggregates to isolated spherical particles, which can be classified as a sintering process.[100] Other larger size-selected particles also show similar characteristics, i.e., from aggregates to sintered particles, and from metal to metal oxides. Similar results were also observed for the zirconium case.

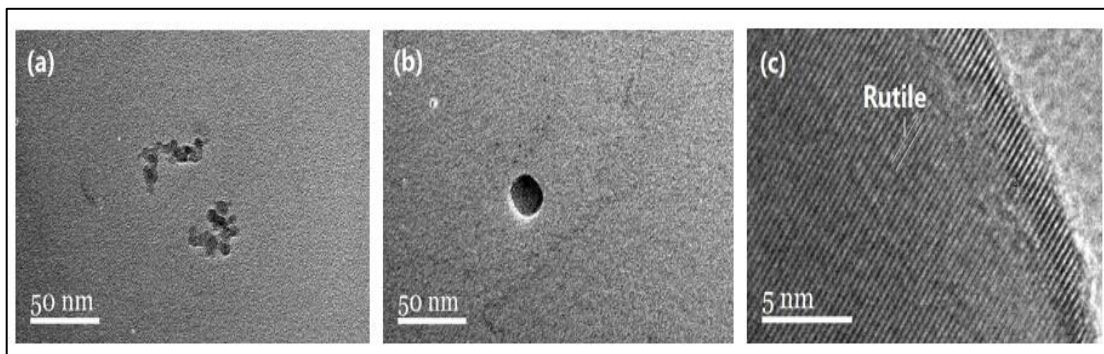


Figure 3-7: TEM micrographs of the Ti particles before combustion (a) and TiO_2 particles after combustion.

3.3.3 Size dependent burn time

Burn times were measured for size-selected particles in the range of 20 to 150 nm. For each particle size, 20 emission streaks were tracked and the average burn time was used to plot Figure 3-8a (titanium) and Figure 3-9a (zirconium) as a function of the peak particle size measured after size selection. Under the particles size range considered, the burn times of both metals increase as the particle size increases. I also note that for the size selected burn times the uncertainty bars are small (2%~9%), indicating that particles of a given size have a very narrow range of burn times suggesting they all experience an equivalent time-temperature history. For Ti, the burn time increases from 0.02 ms to 0.08 ms, which means the emission streak is four times longer for 150 nm particles than 20 nm particles. Zr, also shows a similar profile and the burn time increases from 0.02 ms to 0.06 ms under the same size range considered. The average burn time of Zr is slightly shorter than Ti, which is consistent with that found for micron-sized metals.[89] The size dependent burn time can be fit to a power law of the form: $t=aD^b$, where 't' is the measured burn time, and D is the DMA selected particle diameter. The results of the fit are shown in Table 3-1.

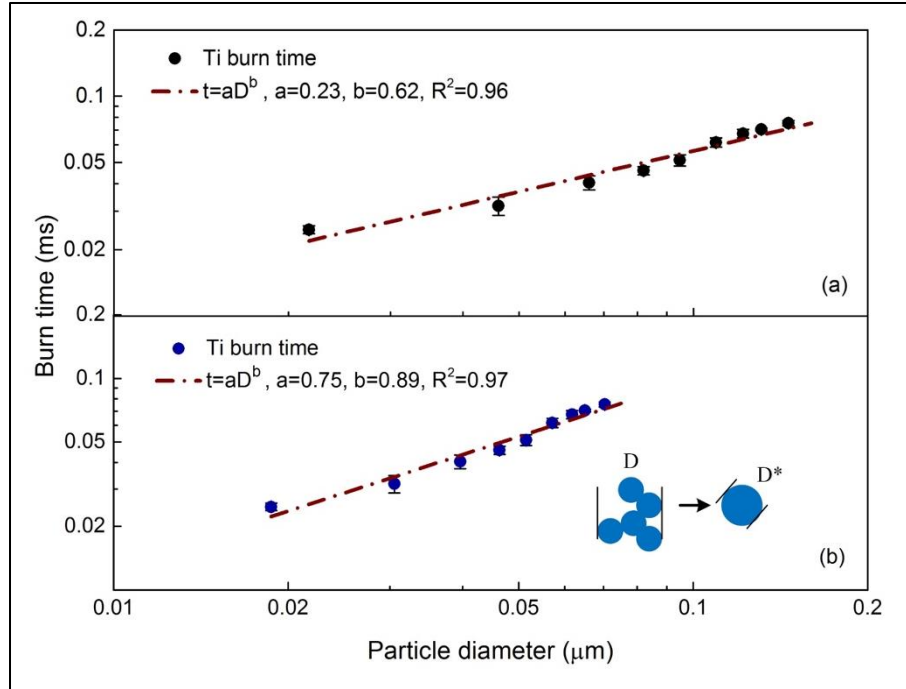


Figure 3-8: Burn time for titanium particles as the function of the particle size. (a) is based on the peak DMA selected particle size, (b) is based on the estimated diameter after sintering.

	Ti (aggregates)	Ti (sintered)	Zr (aggregates)	Zr (sintered)
a	0.23	0.75	0.16	0.45
b	0.62	0.89	0.53	0.77

Table 3-1: Results of power law fit: $t=aD^b$ for the size dependent burn time for titanium and zirconium nanoparticles.

Our measured exponents are slightly larger than the 0.3-0.5[19,96] values observed for Al and show values well below unity, which again cannot be explained by standard theory. The exponent is also larger than what was reported for micro-sized Ti and Zr particles although in that case the fractional exponent may be attributed to the significant micro explosions.

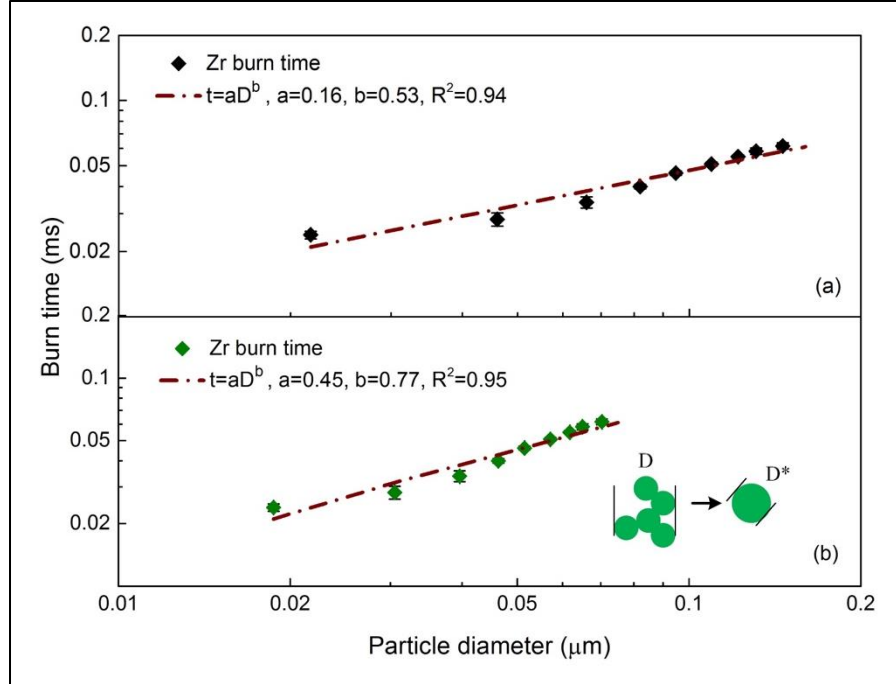


Figure 3-9: Burn time for zirconium particles as the function of the particle size. (a) is based on the peak DMA selected particle size, (b) is based on the estimated diameter after sintering.

As discussed, I have previously conjectured that particles rapidly sinter prior to the bulk of the oxidation. Thus the x-axis may not be appropriately calibrated if in fact sintering is rapid. This thinking is inspired by the TEM images presented in Figure 3-7, and our recent results on high heating rate TEM studies which observed ultra-fast loss of nanostructure for nanoparticles (on the order of 50 ns).[100] In order to determine the effect of sintering on the apparent burn time scaling law I can redefine the particle size assuming fast sintering prior to combustion. This is done by estimating the particle size of the reactant particle after sintering D^* by[110]

$$d_m = d_p N^{0.46} \quad , \quad D^* = d_p N^{1/3}$$

Eq. 3-3

where, d_m and d_p are the mobility equivalent spherical diameters of the aggregates and the average primary particle sizes measured from TEM, respectively; N represents the number of primary particles. The relationships in Eq. 3-3 are based on an understanding of the evolution of aerosol generated fractal aggregates. Sintering affects larger sized aggregates more, thus the rescaling of the size axis is most pronounced at the large size end. With this renormalization in particle size I replot our burn times in Figure 3-8b and Figure 3-9b, which I again fit using the same power law, $t=aD^b$. Based on the final size after sintering, the coefficients obtained from the fit are also shown in Table 3-1.

The exponents after correction for sintering are larger than those without the correction and now only slightly smaller than unity, which is the theoretically expected result for a purely heterogeneous reaction as depicted in Figure 3-1. Moreover, the current scaling law, when extrapolated to the size regime studied in [89], yields a burn time of approx. 3 ms for a 5 μm particle which is within the spread of the experimental results found in that study.

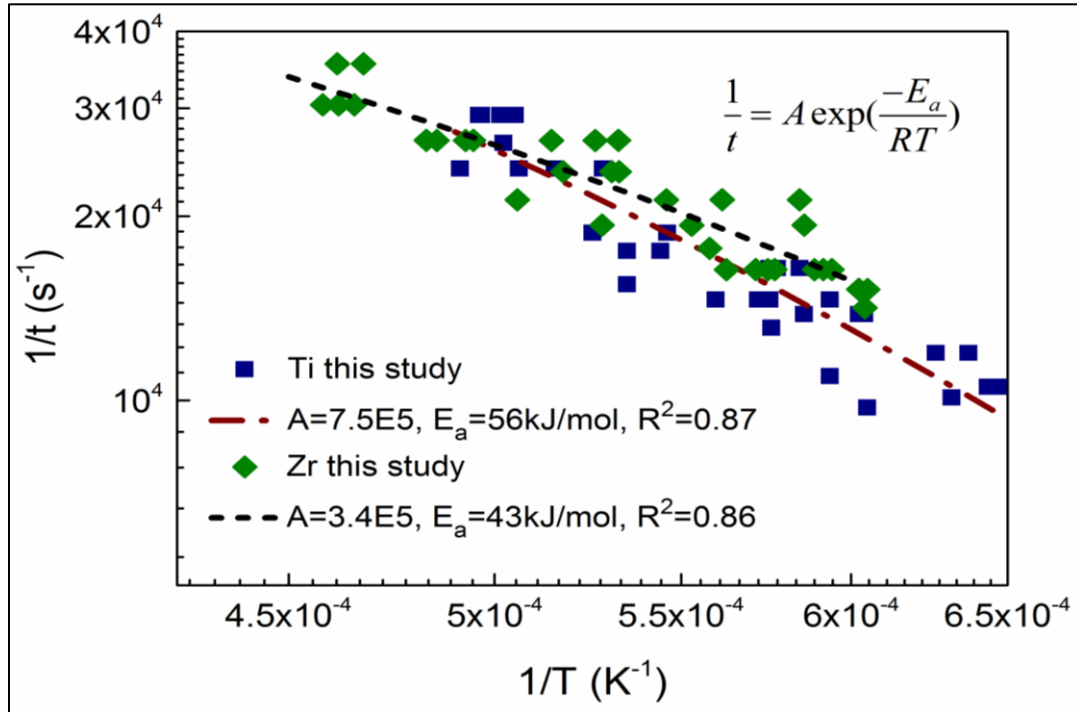


Figure 3-10: Activation Energy determined via Arrhenius plots of burn time vs. temperature for titanium and zirconium.

Finally, I consider the effect of temperature on burn time by changing the flow operating parameters as discussed previously. Owing to the short streaks, I can reasonably assume that each particle experiences a near isothermal ambience throughout oxidation. For these studies I limited the measurement to only one particle size (peak size: 145.9 nm). The starting position (height above the inlet) was evaluated for each streak and was used to estimate the temperature using the profiles shown in Figure 3-4. The result for both metals is shown in Figure 3-10 in Arrhenius plots. Burn times as expected decrease with increasing temperature. In particular for Zr, no emission streaks were observed at the lowest temperature around 1700 K. I obtain a pre-exponential factor of $7.5E5 \text{ s}^{-1}$ and an activation energy of 56 kJ/mol for

Ti; and $3.4E5 \text{ s}^{-1}$ and 43 kJ/mol , for Zr as shown in Figure 3-10. To our knowledge, there are no Arrhenius parameters for nano Ti and Zr nanoparticle oxidation.

Comparing with other metal nanoparticles, the activation energy for Al particles smaller than 50 nm was reported to be $25\text{-}32 \text{ kJ/mol}$. [23] For boron, the activation energy was reported as 33 kJ/mol for the approximate aggregates size around 200 nm . [91] Our results belong within the same order of magnitude.

3.4 Mechanistic consideration through single particle combustion modelling

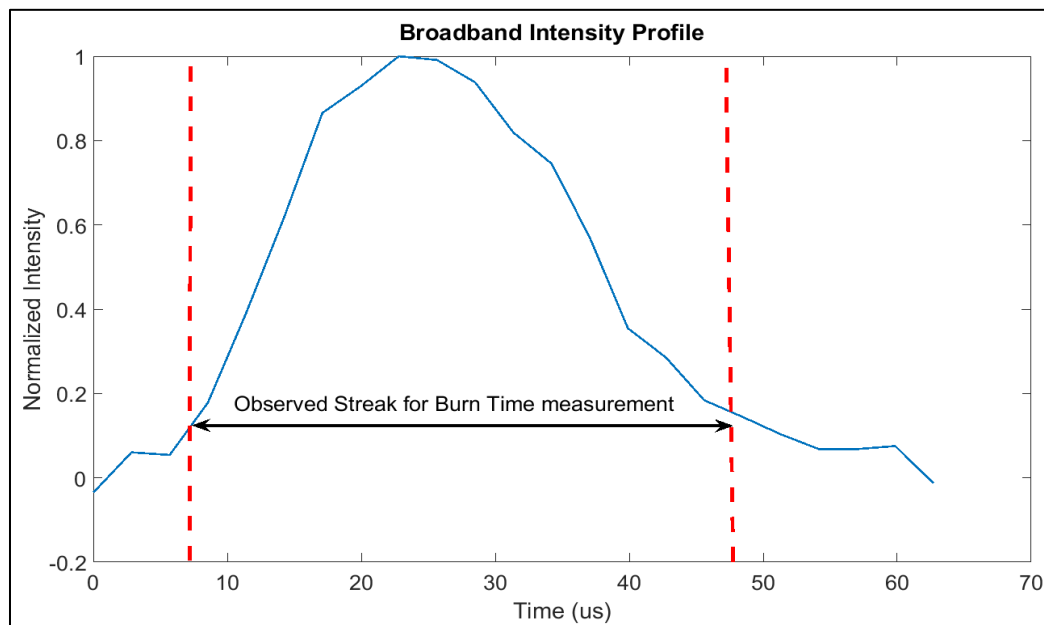


Figure 3-11: Broadband Emission Profile of a 40 nm Ti Particle.

An extension to the observed size dependence of burn time would be to use the emission profile to tweeze out the underlying reaction mechanism. The streak from a burning Ti particle in the size bin with a peak size of 40 nm is shown in Figure 3-11. As can be seen, the profile looks fairly smooth with no sudden intensity spikes

which may suggest micro explosions. This particular streak has a burn time of 40 μ s as demarcated by the dashed vertical line thresholded at 10% of peak intensity. Since the intensity of the streak can be correlated to the temperature ($I \sim T^4$), the streak profile, normalized with peak intensity, can be used as a representative of the temperature.

Since the TEM images reveal final product sizes being larger than the primary particles of the initial agglomerates, a reaction mechanism where the reactant species diffuse through the ash layer seems to be the case. Several reaction models of the form $da/dt = k(T) * f(\alpha)$ were evaluated, where, $k(T)$ is the rate constant (inverse of burn time (τ , fixed) and $f(\alpha)$ is the reaction model as a function of the conversion factor (α).[111] The three main reaction models used were (X_{Ti} represents the volume fraction of unreacted core):

Shrinking core-Kinetic mode:[112]

$$\frac{dX_{Ti}}{dt} = \frac{(-3) * X_{Ti}^{2/3}}{\tau}$$

Eq. 3-4

Shrinking core-Diffusion through Ash layer:

$$\frac{dX_{Ti}}{dt} = \frac{1}{2\tau(1 - X_{Ti}^{1/3})}$$

Eq. 3-5

Avrami-Erofeev Nucleation model (AE 4):

$$\frac{dX_{Ti}}{dt} = \frac{(-4) * X_{Ti} * (-\log(X_{Ti}))^{0.75}}{\tau}$$

Eq. 3-6

Several mass transport/reaction models were evaluated including the shrinking core model with both diffusion limited and kinetic limited regimes (Eq. 3-4, Eq. 3-5), [112] and the Avrami-Erofeev model (A4, Eq. 3-6) for nucleation and growth. [111] Nucleation mechanism was considered owing to the earlier study on micro scale titanium and zirconium particle oxidation, which identified the formation of Metal-O-N solutions and the subsequent phase change as a major constituent of the oxidation process. [88] Heats of combustion of the respective metals were used for heat generation during each step of the oxidation. It has recently been suggested that at high temperatures the thermal accommodation coefficient (TAC) becomes substantially smaller than unity [109, 113] and thus I employ a value of 0.005 for the accommodation coefficient as in ref. [109] (estimated for aluminum nanoparticles).

$$Q_{loss} = \frac{\left\{ (TAC) * \pi * \left[\frac{d_p}{2} \right]^2 * \frac{P_g}{2} * \left[\frac{8KT_g}{\pi m_g} \right]^{0.5} * \frac{(\gamma+1)}{(\gamma-1)} * \frac{(T-T_g)}{T_g} \right\}}{\text{Conduction term}} + \frac{\left\{ \epsilon_{avg} * \sigma * \pi d_p^2 * (T^4 - T_g^4) \right\}}{\text{Radiation term}} + \frac{\left\{ \frac{1 * P_S \alpha_p * \Delta H_{volatilization}}{\sqrt{2} \pi K T_p} * N_{av} \right\}}{\text{Evaporation term}}$$

Eq. 3-7

Conduction in the free molecular regime (with an accommodation coefficient of 0.005) was used along with radiative heat loss to model the heat transfer. The emissivity of the particle was calculated at each step using a molar average of the emissivity of the constituent metal and the oxide. In addition, the evaporation of oxide from the surface was evaluated from kinetic theory based on the calculation of

the heterogeneous condensation rate on particle surface at the saturation vapor pressure.[114] The complete set of constituent equations are shown in Eq. 3-7, where, d_p is particle diameter, P_g : gas pressure (1 atm), m_g : air molecular weight (4.8×10^{-26} Kg), T : particle temperature [K], T_g : gas temperature (1750 K), γ : adiabatic expansion factor (=1.3 at 1500 K), a_p : surface area of particle (m^2), ε_{avg} : molar average emissivity, N_{av} : Avogadro's constant, K : Boltzmann Constant ($1.38 \times 10^{-23} m^2 Kg s^{-2} K^{-1}$). The set of equations were solved numerically to yield temporal plots of the emission intensity (Appendix B) for the particle, along with the experimental emission profile as shown in Figure 3-12. In the application of the model I employ the experimentally determined burn time (τ) as a fixed rate parameter within all the models (see Eq. 3-4 -Eq. 3-6). Such an assumption obviously comes with a caveat that the oxidation is dominated by a single mechanism. Although such a scenario may be unlikely, in view of the simplicity of the model, and a near D^1 dependence suggesting a kinetic limit, I proceed with these caveats in mind. In addition to the aforementioned, several power law models, Prout-Tompkins model, Ginstling-Brounstein diffusion models were also evaluated.[111]

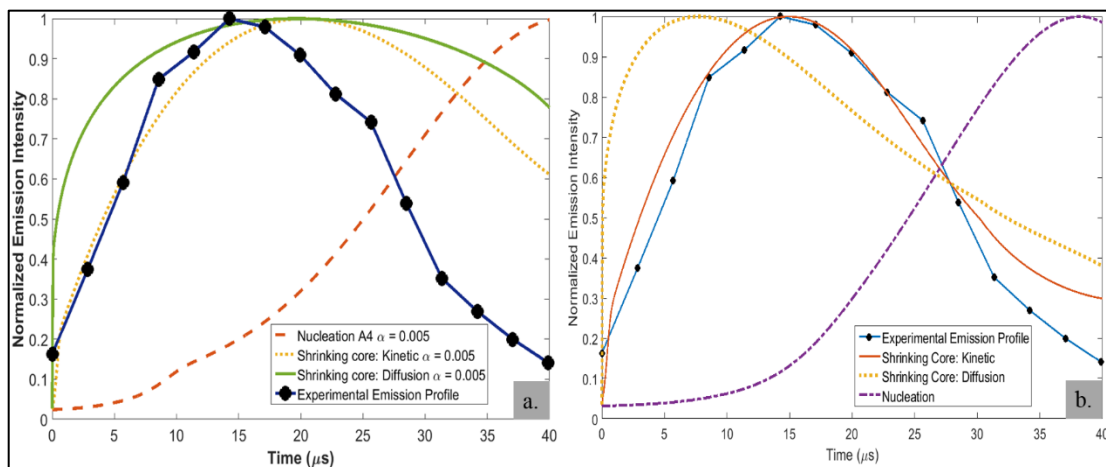


Figure 3-12: Model simulations for 40 nm particle. Emission plots with: (a) TAC = 0.005, (b) TAC = 0.3.

From Figure 3-12a I can certainly conclude that both a shrinking core diffusion model and the nucleation/ phase growth model with the accommodation coefficient of 0.005 are not reasonable descriptions. While the kinetic model could predict the shape of the emission profile to some degree, it predicted a slightly delayed peak for the reaction and the temperature did not drop quickly enough. The results for the case of zirconium were essentially similar and are not shown here.

Based on our experimental results, the burn time scaled with a nearly $(diameter)^1$ dependence. Hence it is reasonable to start the fitting procedure using a reference model whose reaction rate scaled with the diameter of the particle. From the list of condensed phase reaction models, the kinetically controlled shrinking core model incorporates a reaction rate that scales with the diameter of the particle and I chose this as our reference.[112] In order to proceed with the fitting procedure, I need to identify a free parameter. The thermal accommodation coefficient at high

temperatures has generated some recent interest owing to the results of Allen et al., [109] who's results showed small coefficients for aluminum nanoparticles at high temperature, where nominally it has been assumed to be unity. The lack of widespread confirmation led us to consider the accommodation coefficient as a free parameter. The other option, in case a single model proves insufficient, was to combine two reaction models to see if that could provide a better fit. For this consideration, I employed a kinetic shrinking core initiation followed by the subsequent reaction being controlled by sigmoidal kinetics of nucleation/ growth mechanism. A kinetic initiation was incorporated owing to the bare surface of the nanoparticle, which may present a kinetic barrier during initiation. The overall reaction was modeled such that the nucleation reaction would replace the kinetic, once its rate exceeded the rate of the kinetic reaction. The rate constants for all models considered here were taken to be the inverse of the experimentally determined burn time and thus were not free parameters.

Treating thermal accommodation as a free parameter in a kinetically controlled reaction, I obtained the best fit to the experimental emission profile with at $TAC=0.3$, as shown in Figure 3-12b. Although this value is larger than that suggested in ref. [109] (their proposed maximum value is 0.15 for alumina, but could be as low as 0.005), the model appears to predict the peak and cooling regimes fairly well, and suggests that the quantification of the thermal accommodation coefficient at high

temperatures needs further examination. I found similar behavior for other particle sizes as well.

One obvious extension, particularly since I begin with bare particles is to consider a two-stage model as a possible improvement. I find however, that while a two-stage model enabled a better approximation of the observed cooling rate late in the reaction, the improvement is too marginal to warrant further discussion, although it has been included in the supplemental. In summary, our modeling analysis implies that the combustion of nano-sized titanium and zirconium particles can be thought to follow a kinetic limited shrinking core mechanism.

3.5 Conclusions

An atmospheric pressure laser ablation system attached with a differential mobility analyzer (DMA) was used to produce size-resolved metal particles of titanium and zirconium in the range of 20-150 nm. The ignition and combustion characteristics of the metal particles were investigated in the post flame region of a flat flame burner, with the oxidizing zone temperature ranging from 1700 K to 2500 K. The particles of both Ti and Zr were observed to exhibit clear short emission streaks after ignition, which are quite different from those observed for micro-sized particles in literature. From the TEM images it was deduced that the particles coalesce during combustion and transform from aggregates to sintered spherical particles. After accounting for the effects of sintering I find the burn time obeys a

near d^1 power law. Additionally, the emission intensity profile from individual particles was used to benchmark several kinetic models. It was found that the best fit to the experimental data was obtained by using a shrinking core model that was limited by the surface oxidation kinetics as well as a Thermal Accommodation Coefficient (TAC) that was less than unity.

3.6 Acknowledgements

This work was done in collaboration with Yichen Zong (YZ), visiting scholar from Tsinghua University, who was also the co-first author of the article of which the results are presented here, reprinted with permission from Zong, Y.; Jacob, R. J.; Li, S.; Zachariah, M. R., Size Resolved High Temperature Oxidation Kinetics of Nano-Sized Titanium and Zirconium Particles. *J. Phys. Chem. A* **2015**, *119* (24), 6171–6178.[115]

Chapter 4 Energy release pathways in nanothermites follow through condensed state

Summary

Nanothermite reactions are mechanistically not well understood, due to their ultra-fast transient nature, and the complexity of probing both the vapor-phase and condensed-state chemistries. In this work I examine the combustion product particles of three nano-sized thermite systems (Al/CuO, Al/WO₃, Al/Bi₂O₃) as a probe of the underlying mechanism. Electron Microscopy (EM) and Energy-dispersive X-ray Spectroscopy (EDX) were used to evaluate the combustion product particle size distribution and composition. The results show two distinct product particle size distributions common to all three oxidizers. The larger particles are super-micron (though the precursors were nano-sized) and comprise approximately 90% of the product mass. Simple scaling arguments show that the large population cannot be formed from the vapor given the available residence time. The smaller distribution is sub-100 nm which is primarily the reduced metal formed from vapor phase condensation. This result implies that the majority of the global reaction and thus the energy release is occurring in the condensed phase. Based on these results, a phenomenological mechanism for the nanoaluminum based thermite reaction is proposed.

4.1 Introduction

Nano-scale reactive composites or metastable intermolecular composites (MIC's) are an increasingly active area of research in the field of propulsion and energetics, resulting from their high energy densities, high propagation velocities and low diffusion length scales. Aumann et al.[9] were the first to show that there is a significant difference in the reactivity of nano-sized thermite mixtures over their micron-sized counterparts. When compared to the conventional micron scale mixtures, their experimentally observed reactivity was much greater owing to the reduction in diffusion length scales. In addition to facilitating increased reactivity, use of MICs boasts higher control over energy densities compared to traditional monomolecular mixtures through the alteration of reactant stoichiometry or by changing the constituents with varying packing densities.

Of all nano-scale reactive composite fuels investigated, the combustion of nanoaluminum has been the most frequently studied. Several mechanisms for its oxidation have been proposed including pressure build-up resulting in quiescent shell rupture,[116] oxidizer diffusion into the aluminum core followed by a heterogeneous reaction at the aluminum surface,[26] or the Melt Dispersion Mechanism (violent shell rupture followed by molten core spallation).[45,117] Many researchers consider diffusion of ionic aluminum and oxygen species across the oxide shell to be the controlling process. Trunov et al.[28] have proposed a multi-stage oxidation process for aluminum particles which includes both species transport and phase changes in

the oxide shell. More recently, studies have suggested that in addition to the volumetric expansion of the core, strong electric fields induced in the oxide shell can drive cation diffusion across the shell.[118,119] Several studies have also reported the development of reaction models for mechanistic studies of these energetic composites.[93,120]

One of the outstanding issues regarding the role of the oxygen carrier in the nanothermite is whether oxygen is directly released from the oxidizer or if oxygen, in the form of an anion, is transported at the interface between the fuel and oxidizer. The latter case may be defined as a condensed state process, in which little or no aluminum-oxygen reaction occurs in the vapor phase. Lynch et. al[25] studied the combustion of nano-sized and micron-sized aluminum particles in a shock tube. Their results explicitly show that there is little Al vapor during an oxidation event of aluminum nanoparticles, which would preclude a vapor phase combustion mechanism. They also observed a sparse AlO signature in the nanoparticle oxidation at temperatures below the bulk melting point of aluminum oxide. These results, combined with those of Jian et. al[11] (where the importance of gas phase oxygen for reaction initiation was studied) suggest that a condensed phase reaction is prevalent in these systems. Another proposed mechanism is the mechanochemical Melt Dispersion Mechanism, where the aluminum core is predicted to spallate into nano-sized clusters upon the violent fracture of the alumina shell.[121,122] Other investigations such as Time-of-Flight Mass Spectrometry, pressure and optical

signature measurements[11,40,123] have also been conducted, to probe the underlying mechanism of these systems.

Fewer studies[44,124–126] have explored the reaction product distributions to obtain information about the underlying mechanism. One particular study of note is by Drew et al.[124] who studied quenched aluminum particles. I build on this work in a more quantitative manner to evaluate the probable role of condensed vs. vapor phase oxidation through a post-combustion analysis of rapidly quenched product particles. In this study, I observe three different thermite systems that show very different ignition and burning characteristics and conclude that they follow a common reaction mechanism.

4.2 *Experimental Approach*

The basic approach to this study is to ignite various nanothermite combinations on rapidly heated fine wire. By rapidly quenching product particles on a substrate, reaction products could subsequently be inspected by microscopy and surface analytics.

4.2.1 *Material choice and Properties*

In order to provide sufficient breadth to the analysis, three different nanothermite systems were chosen that have displayed very disparate reaction characteristics. The systems chosen here, exhibit varied combustion characteristics in terms of propagation speeds, pressurization rates and burn times.[11,33] These

systems were extensively studied by Sanders et al.[33] employing pressure cell, open tray, and instrumented burn tube methods to study the reaction mechanisms. They concluded the presence of vapor phase/mobile components was important to enhance the propagation velocities and proposed that a shift in the heat transfer mechanism (from convective mode to conductive) occurred when the density of the mixture increased. A particular case of interest was the performance of the Al/Bi₂O₃ mixtures at low densities which displayed a combination of both modes of heat transfer owing to a localized increase in density due to the drastic pressure rise. The adiabatic temperatures vary with the choice of the thermites, with Al/WO₃ mixtures exhibiting a very high adiabatic flame temperature compared to Al/CuO formulations. From the observed pressurization rate and temporal behavior of optical emissions, Sullivan et al.[40] showed significant differences between Al/CuO and Al/WO₃ systems regarding the relative timing of the pressure and optical peaks. Specifically, Sullivan et al. pointed out that the Al/WO₃ nanocomposite does not produce significant gaseous oxidizer species until the system temperatures are very high (~2800K). Jian et al.[11] points out that the Al/Bi₂O₃ system ignites almost 700K below its oxygen release temperature while the Al/WO₃ system does not produce any gas within the experimental temperature range. The Al/CuO mixture is observed to closely follow the expectation that ignition correlates with oxygen release from the oxidizer. Apart from these variations in their respective combustion behavior, these metal oxides

exhibit very different physical properties regarding melting and boiling temperatures as outlined in Table 4-1.

Thermite Mixture	Adiabatic Flame Temp (K)[127]	Metal Oxide decomp. Temp. (K)[11]	Reduced Metal MP (K)	Reduced Metal BP (K)
Al/CuO	2843	975	1357	2843
Al/WO ₃	3253	-	3695	5933
Al/Bi ₂ O ₃	3319	1620	545	1837

Table 4-1: Thermo-Physical properties of the nanothermite mixtures

These dissimilarities provide the motivation for choosing these three materials for the current work. All three show significantly different behavior in terms of ignition point, combustion intensity, physical properties and gas release. The question is how the nature of the product distribution varies for these disparate systems and whether analysis of the product distribution will provide insights into the reaction mechanisms.

4.2.2 *Material Preparation*

Commercially available Aluminum nanoparticles (ALEX) with an average particle size of 50 nm, procured from Argonide Corp., were used in this study. These particles had a core-shell structure with an active aluminum content of 70 % which was confirmed by thermo gravimetric measurements.[22] These ALEX nanoparticles were ultra-sonicated in hexane for approximately 20 minutes with three different metal oxide nanopowders. The metal oxide nanopowders used in this study were Copper (II) Oxide (CuO), Tungsten Oxide (WO₃), and Bismuth Trioxide (Bi₂O₃) (all

from Sigma Aldrich Corp. and $<100\text{nm}$). A representative image of the ultrasonicated mixtures (Al/ Bi_2O_3) can be seen in Figure 4-1, which highlights the intimate mixing with the brighter areas corresponding to the heavier bismuth and the darker areas corresponding to the aluminum particles (Back Scattered Electron imaging). After ultra-sonication, the intimately mixed thermite was micro pipetted onto a platinum wire of $76\ \mu\text{m}$ diameter.

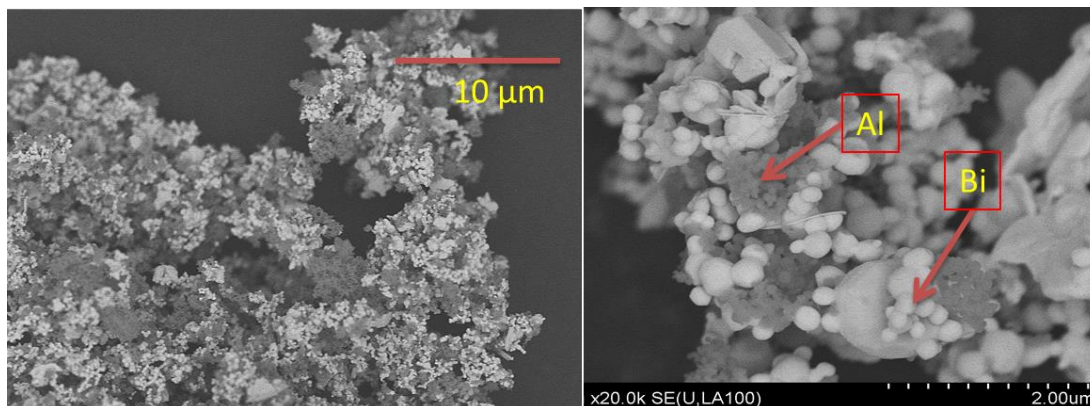


Figure 4-1: SEM image of dry, unreacted Al/ Bi_2O_3 showing the intimate mixing and the elemental contrast owing to the mass of the different reactant species

4.2.3 Temperature-Jump Wire Ignition and Particle Collection

The experiment consisted of a 12 mm long, $76\ \mu\text{m}$ diameter platinum wire (Omega Engineering Inc.) coated with the nanothermite, which was resistively heated using a high voltage electric pulser. For each run, a pulse width of 3 ms produced a heating rate of $2 \times 10^5\ \text{K/s}$ and the experiments were performed in air. The details of the wire heating system comprising the mass spectrometer and power source can be obtained in another work by Zhou et al.[128] Compared to the method of Zhou et al., the primary modification herein was the ability to reproducibly capture post-

combustion material on substrates. This entire assembly was mounted on a bi-axial linear translational stage (Newport Research Corp.). This stage had two manually controlled micrometer actuators with a resolution of 25 μm . The collecting substrate was a separately attached Scanning Electron Microscopy (SEM) stage (15 mm dia. Aluminum stage) with a layer of carbon tape on it so as to improve the conductivity of the sample, as depicted in Figure 4-2.

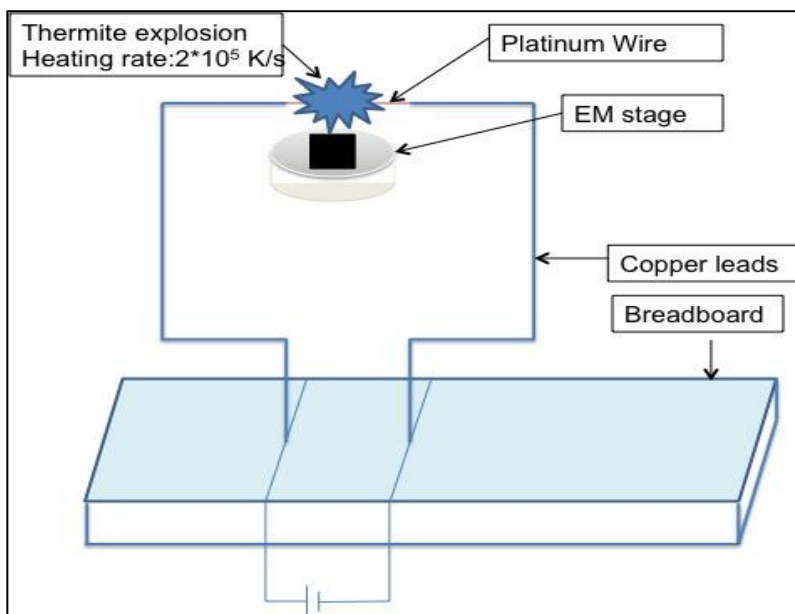


Figure 4-2: Experimental setup for rapid quench collection for nanothermite reaction products

A high speed digital camera (Phantom V12.1) was used to capture the video of the reaction from which characteristic transit times could be extracted as seen in Figure 4-3. By moving the Z direction micrometer, I could collect the product particles on the substrate at various distances on the order of several millimeters away from the wire with accuracy over several micrometers. The impingement criteria were

a separation of 1 mm for the “near” substrate condition and 3 mm for the “far” substrate condition. A similar arrangement was used for the Transmission Electron Microscopy (TEM) samples, where a Nickel TEM grid was placed on the SEM stage. The substrates were then analyzed in a Hitachi SU 70 SEM and a JEOL Field Emission Gun TEM for low and high magnification images respectively.

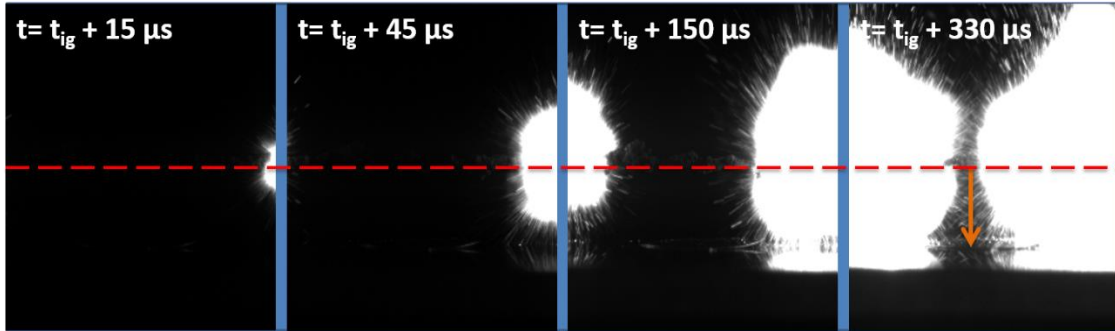


Figure 4-3: Temporal video snapshots of Al/CuO nanothermite combustion on a 76 μm Pt wire, Heating rate = $\sim 2 \times 10^5$ K/s, time(μs) measured from the start of ignition. The red dashed line represents the wire location and the arrow shows the location of the TEM grid.

4.3 Results

4.3.1 Electron Microscopy of Post-combustion Products

Combustion product particles were collected at two distinct separation distances to make a fair comparison of the particle evolution. The SEM images obtained for the three nanothermites are shown in the subsequent images with an approximate transit time to the substrate, obtained by performing high speed video imaging on the emission from individual particle trajectories.

4.3.1.1 Al/CuO Nanothermite

Figure 4-4 and Figure 4-5 show moderate and high magnification SEM images of the residue collected at the near and far substrate condition for the Al/CuO case. From these images I can see that there are a significant number of large particles (in comparison to the nanoscale starting materials) that have formed from the thermite reaction, some of which are as large as 20 μm . Figure 4-5a is a Backscattered Electron (BSE) image of the particles found for the impingement criteria of 1 mm with the bright areas depicting copper owing to its higher atomic weight. Figure 4-5b depicts the same for the far substrate case with both particles having dimensions on the order of 10 microns. Layers of small particles were also visible on the surface of the larger particles as seen in Figure 4-5b. At still higher magnifications, using a JEOL FEG TEM, I observe a layer of much finer particles as shown in Figure 4-6, which show a core-shell structure. *It is evident from these images that there are two distinct particle distributions.*

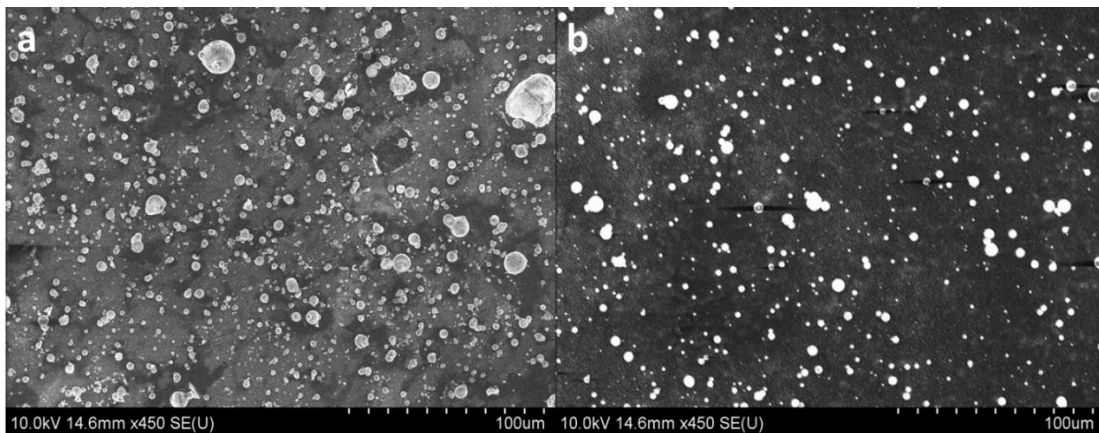


Figure 4-4: Post-combustion SEM images of Al/CuO nanothermite collected at various distances. a.) Time for impingement = 90 μ s. Separation of the collecting substrate: 1 mm. b.) Time for impingement = 350 μ s. Separation of the collecting substrate: 3 mm.

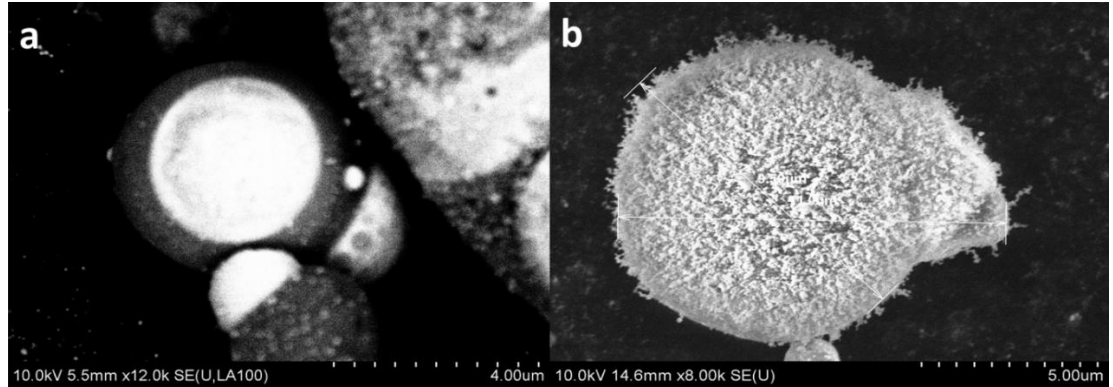


Figure 4-5: Post Combustion high magnification SEM images showing surface morphology at the various separation distances for Al/CuO. a.) BSE Image Time for impingement = 90 μ s. Separation of the collecting substrate: 1 mm. b.) Time for impingement = 350 μ s. Separation of the collecting substrate: 3 mm.

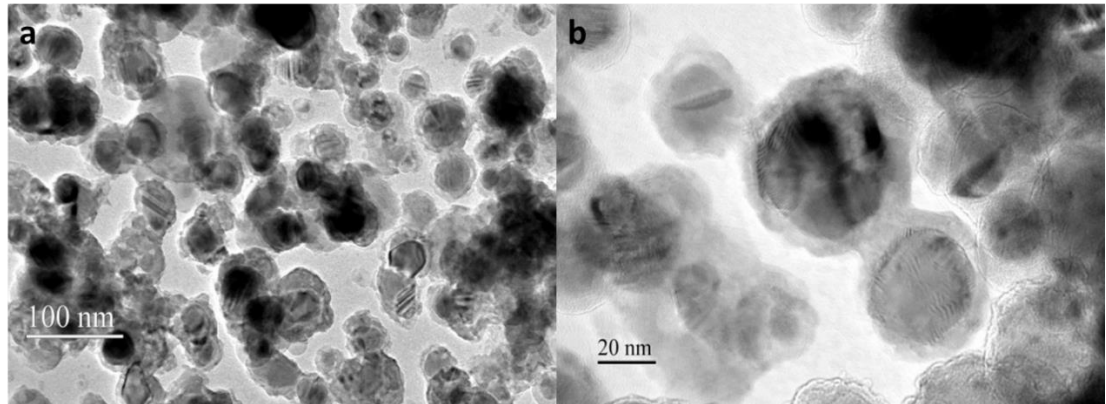


Figure 4-6: Post-Combustion TEM images (Al/CuO Nanothermite) of the smaller particles collected on a Nickel TEM grid. Time for impingement: 150 μ s.

4.3.1.2 Al/WO₃ and Al/Bi₂O₃ Nanothermites

The set of experiments was then broadened to include the Al/Bi₂O₃ and Al/WO₃. The near substrate images for both cases as well as the impingement

timescales are shown in Figure 4-7, which highlights that the key features of the product characteristics are essentially equivalent to the Al/CuO case.

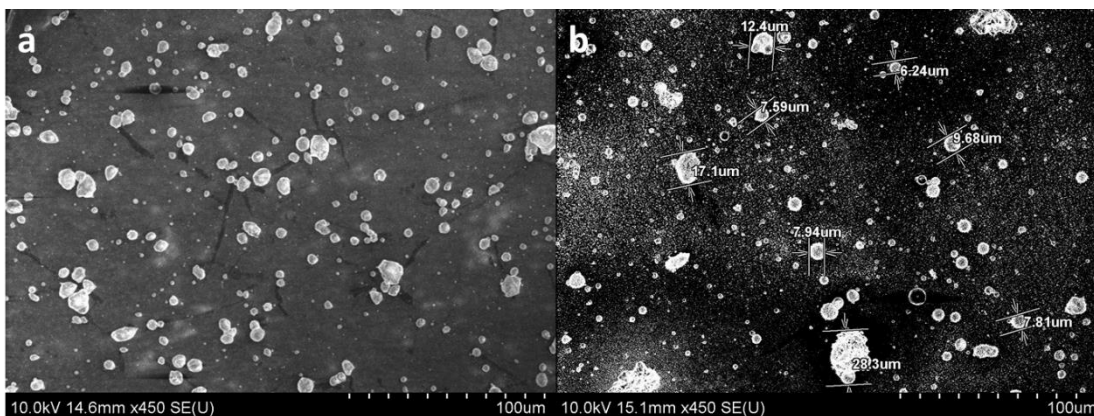


Figure 4-7: Typical particle sizes for the two Nano Thermites Al/WO₃ and Al/Bi₂O₃. a.) Al/WO₃, Time for impingement = 300 µs, Separation of the collecting substrate: 1 mm. b.) Al/Bi₂O₃, Time for impingement = 250 µs, Separation of the collecting substrate: 1 mm.

4.3.1.3 *General Conclusions of the Product Particle Distribution*

Following the preceding observations, I can conclude that the three thermite systems (Aluminum with CuO, Bi₂O₃ or WO₃) studied form characteristically large particles compared to their nano-sized reactants and would thereby follow a generic mechanism in this context. Along with the large particles, a smaller nano-sized distribution could also be observed. Assessing the relative importance of these particle distributions on the reaction mechanism constitutes the core of this study.

4.3.2 Elemental Analysis of Post-combustion Products

As seen in the near-substrate Al/CuO case (Figure 4-5a), there is a distinctive bulb formation on the large particles, which was confirmed to be metallic copper

from Energy Dispersive X-Ray Analysis (EDX). For the far-substrate case (Figure 4-5b), the larger particles were heavily decorated with nano-sized particles on their surfaces. These spherical nanoparticles were similar to those seen in the TEM images, however the structure is not believed to be core-shell as those in Figure 4-6. The surface of the large particles were identified to be an alloy of the kind $Cu_xAl_yO_z$ (for the Al/CuO case) and is conjectured to be a mixture of $CuAl_2O_4$ and Al_2O_3 based on the phase diagrams of CuO- Al_2O_3 mixtures[129] and the atomic percentages obtained from the EDX analysis. It is reasonable to assume that the rapid quenching leads to thermodynamic meta-stable states that may be far from the equilibrium phases. The relative elemental composition of the surface varies from one particle to another as the fuel/oxidizer combinations involved in the formation of each particle can be far from stoichiometric and thus different for each particle. It is important to clarify that these atomic percentages were obtained from a surface which was visually devoid of any decorations.

For the Al/ WO_3 and Al/ Bi_2O_3 cases, elemental analysis shows the surfaces of the large particles are an alloy of aluminum, oxygen and the reduced metal. As in the case of Al/CuO, surface decorations could be seen in both of these cases, but their nature differs considerably. In the case of Al/ WO_3 (Figure 4-8a) the surface decorations could be seen on fewer particles when compared to the case of Al/CuO. In the case of Al/ Bi_2O_3 (Figure 4-8b), the surface decorations formed larger bulbs of the reduced metal as opposed to the fine nanostructures in the case of Al/ WO_3 .

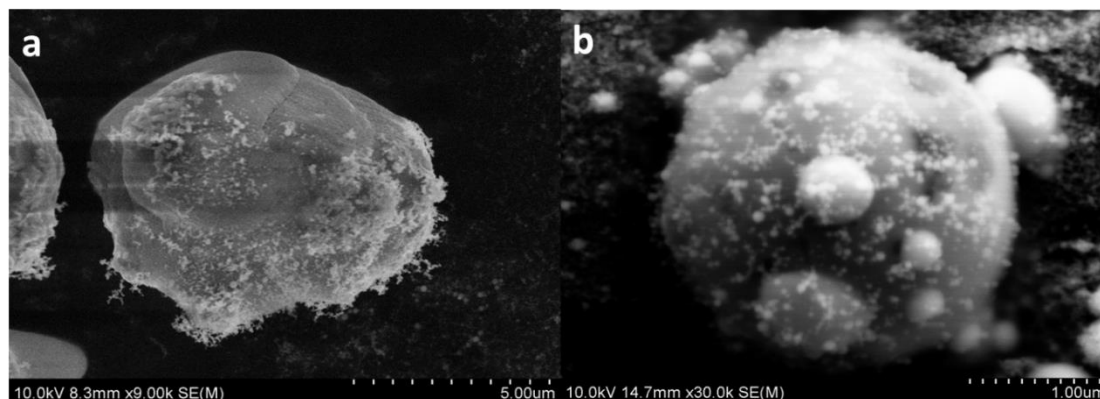


Figure 4-8: High magnification SEM images of the two Nano Thermites Al/WO₃ and Al/Bi₂O₃. a.) Al/WO₃, Time for impingement = 300 μs, Separation of the collecting substrate: 1 mm. b.) Al/Bi₂O₃, Time for impingement = 100 μs, Separation of the collecting substrate: 1 mm

Proceeding to the nanoscale population, from Figure 4-6 I can see that they are nearly spherical with an approx. size of 50 nm for the Al/CuO case. EDX analysis was performed on the core shelled structure which showed a reduced metal (Cu) core surrounded by a shell which was an alloy of aluminum, oxygen and copper. The Al/Bi₂O₃ case displayed spherical nanoparticle morphologies (50-200nm) composed of an alloy of the aluminum, oxygen and bismuth (Figure 4-9c). Similarly, for Al/WO₃, I observed faceted nanoparticles (50-100nm) entirely composed of an oxide of tungsten, WO_x, which I believe is the unreacted metal oxide or a sub oxide.[130] Additionally, spherical particles (50-200nm) could also be seen, as depicted in Figure 4-9a,b. These nuances in the nanoparticle morphology across the three systems are insignificant compared to the degree of similarity of the particle size distributions and don't contribute towards the analysis I am pursuing in this study. In order to attribute

a generic mechanism to these results, I require a better understanding of the formation of the two particle distributions common to all three thermite systems. To begin, it is imperative to know which of these particle distributions constitute the majority of the species.

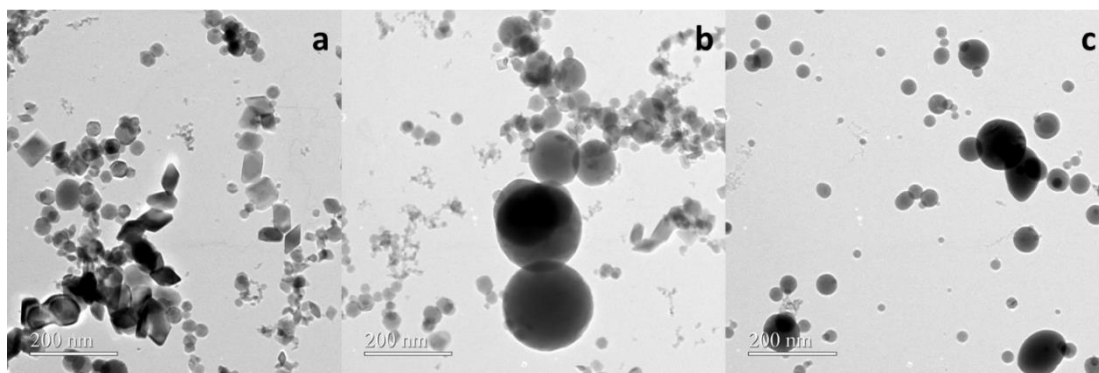


Figure 4-9 a.) High Magnification image of Al/WO₃ products showing the faceted structure and b.) showing the presence of spherical particles. c.) Al/Bi₂O₃ case showing the spherical nano-particles

4.4 Discussion

4.4.1 Large vs. Small Particle Products and its Significance

To begin our discussion, I refer to the thermo-physical properties of the thermite mixtures in Table 4-1. The previous microscopy images showed there were two distinct particle populations. Our first consideration is to understand the relative importance of these two populations in the context of a mechanism by estimating the relative mass distributions. To do this I employed digital image processing using ImageJ software. To provide an example an SEM image of the Al/CuO system is shown in Figure 4-10. The large particles are first illuminated against a dark

background by inverting the colors. By adjusting the image threshold, I can sharpen the boundaries of the large particles against the background and use the particle analyzer tool of the software to obtain the mean size of the particles. In this analysis, I assumed that the background is a uniform distribution of 50 nm particles, based on the previous TEM images. This enables us, assuming spherical geometry and total aerial coverage of the small 50 nm particles, to estimate the volume of both the small and large particle populations. Though this is a crude assumption, it is not unreasonable for the analysis I am pursuing.

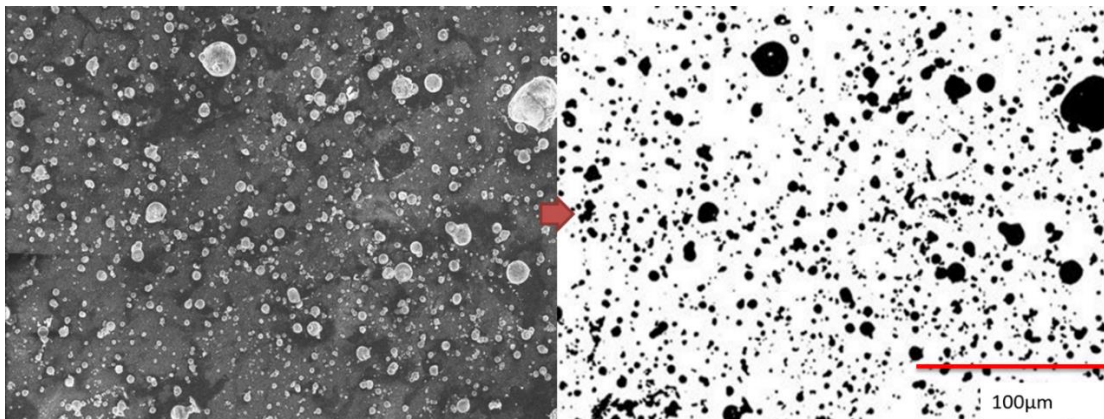


Figure 4-10: Image processing example for combustion products of Al/CuO. The image threshold was adjusted to single out the larger particles from the background.

From the image processing results, I can attribute an approximate average size of 2.5 μm to the large particles. Even though the aerial coverage of the large particles is significantly lower than that of the nano-sized particles, their larger size results in finding that 85% of the total particle volume is occupied by the large particles.

Assuming the density is roughly constant between the two particle populations, the volume ratio is also approximately the mass ratio. Similar analysis for Al/WO₃ and

Al/Bi₂O₃ yielded experimentally indistinguishable results, i.e. approximately 90% and 85% of the volume occupied by large particles respectively. These results are summarized in Table 2 and are qualitatively consistent with a very recent study by Poda et al.[126] wherein they recover product samples from the interior of a closed bomb cell. They also observed large particles in the products whose size deviates substantially from that of the nano-sized precursors. *Thus, I may conclude that the bulk of the chemistry and energy release must pass through a mechanism that leads to the larger particles as opposed to the smaller nanoparticle products.*

Thermite System	Ratio of volume of micron to nanoparticles in reaction product
Al/CuO	5.7
Al/WO ₃	9
Al/Bi ₂ O ₃	6.2

Table 4-2: Image processing results for the determination of the ratio of micron and nanoparticles in combustion products.

4.4.2 Particle Growth Analysis

I now turn our attention to how these two populations, one consisting of particles in the micron size range, and the other in the 50-200 nm range, are formed. Most of these small particles are highly spherical, implying that they were in the liquid state at some point in their history, and were rapidly quenched on the substrate. The quench time for a single suspended nanoparticle can be estimated using a lumped capacitance method outlined in Ref.[42] Under these constraints, the quench time for nanoparticles is on the order of one hundred nanoseconds for a 50 nm copper particle

cooling from its boiling point to its freezing point at an ambient temperature of 650K. Furthermore, early in the formation, the particles were clearly in a free aerosol state as molten drops (i.e. they are spherical), otherwise they would have aggregated with other smaller solid particles. These results show that the flame zone temperatures are sufficiently high to keep the nano-sized particles in the molten state.

Since the adiabatic flame temperature of copper metal is near the boiling point of the metal (Table 4-1 for the Al/CuO mixture), a suitable first approximation is that the copper metal, a product of the redox reaction, would vaporize. This is of course provides an upper limit, as the actual flame temperatures may be below the adiabatic flame temperatures due to incomplete combustion and radiation heat transfer.[60,131] This allows us to pose the question: *how large a particle can be grown from the vapor in the transit time from the wire to the substrate ?* To estimate the largest possible growth rate, I assume that the copper vapor is in a supersaturated state with no nucleation barrier. Here I conservatively assume, to maximize growth rate, the entire copper product is in the vapor phase (which is actually a factor of two higher than what equilibrium calculations with NASA CEA code predicts). The presence of copper vapor is further supported by the detection of copper peaks during the combustion of the Al/CuO nanothermite mixture in a mass spectrometer.[93] Without a nucleation barrier, nucleation and growth follows the aerosol coagulation equation in the free molecule regime.[132] The total mass of copper is estimated from the amount coated on the wire, which is approximately 0.1mg, and the stoichiometry of

the mixture. The expansion volume for the products of the thermite reaction was considered to be half the volume of the cylinder that forms between the wire and the collecting substrate, i.e. the axis of the cylinder lies along the wire. This was evaluated for the near substrate condition, as that gives the maximum initial monomer concentration, thereby giving the fastest rate of coagulation compared to the far substrate case.

To simplify the calculations, I assume a constant collision kernel, $K = 5E-10$ cc/s, so that the Smulochowski population balance is reduced to Eq. Eq. 4-1:[132]

$$\frac{dN_{\infty}(t)}{dt} = \frac{N_{\infty}(0)}{1 + K * N_{\infty}(0) * t/2}$$

Eq. 4-1

where, $N_{\infty}(0)$ is the initial monomer concentration (#/cc), $N_{\infty}(t)$ is the total particle concentration (#/cc) at time t (s). The solution for the average particle diameter as a function of time can be obtained by employing a simple volume conservation using the Van der Waals radius of copper (~0.14 nm) and assuming an initial monomer concentration equal to the maximum vapor phase concentration of Cu.

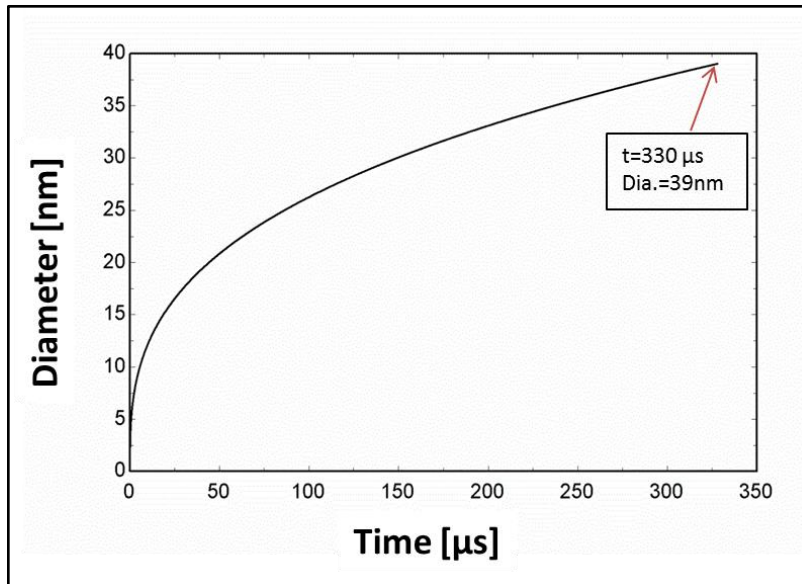


Figure 4-11: Copper particle growth using Equation (1), and assuming Cu vapor in supersaturated state with no nucleation barrier to condensation – i.e. maximum growth rate.

Figure 4-11 shows the growth of particles as a function of time at effectively the maximum collision rate. I see that at $\sim 330 \mu\text{s}$, which corresponds to the transit time of the particles from the wire to the substrate based on the high-speed video, the average particle size in the distribution should be approximately 40 nm. This is reasonably consistent, given the approximations in our calculation, with the TEM results for the small particles. *More significantly however, it says that there is no way that the large micron size particles, which can be recalled constituting the bulk of the mass, can form from the vapor.* In their work on arrested reactive milling, Schoenitz et al.[133] also found large particles in the product of micron size Al/MoO₃ combustion. In our previous work by Sullivan et al.,[42] real time X-ray phase contrast imaging was performed to substantiate the formation of sintered particles

early in the reaction. They found large particles forming rapidly and early in the reaction. Thus, I believe the large particles correspond to aluminum-metal oxide reaction that must have occurred in the condensed phase. Such particles have also been formed during flash ignition of nano aluminum thermites,[134] thus strengthening a common reaction feature irrespective of the environment, ignition mechanism or heating rate.

4.4.3 Phenomenological Mechanism

I believe these results can be attributed to a generic reaction mechanism. From the previous EDX results (for the Al/CuO case), I observed that the large particles were primarily composed of an alloy of aluminum, copper and oxygen on the surface. The vast majority of the particle products studied are at least two orders of magnitude larger in diameter than the starting nano-sized materials and, as I showed from simple calculations, cannot be formed from a vapor condensation mechanism. Thus, the bulk of the energetic heat release must come from a condensed phase reaction. The large particles are postulated to be the result of sintering hence, I can argue that their temperature would, at some point in their evolution, be above the melting point of the alloy formed due to complete/incomplete oxidation or diffusion of species. As the nanoparticles grow from the vapor phase, they would be expected to be scavenged by the larger particles by coagulation/coalescence resulting in morphologies as shown in Figure 4-5. The criterion for the metallic cap formation is that the melting point of the

coagulating nanoparticle be lower than the ambient temperature and the temperature of the large particle on which they impinge. In this case, the incident molten nanoparticles would immediately coalesce upon collision and phase separate forming the bulb. This can be confirmed from the melting points of the reduced metals: Bismuth and Copper (Cu: 1357K, Bi: 545K), which are low melting and as predicted forms such caps. Similar results involving metallic caps were observed in the study by Schoenitz et al.[133] in a pressure cell (where compressive heating is a major factor) implying that the nature of these formations from our wire heating experiment does not create an artificial condition.

From our coagulation calculation it is evident that the large particles cannot be formed from the vapor phase. In one of our previous publications, I discussed the possibility of early sintering of the reactants due to the heat released by the exothermic reaction, termed Reactive Sintering.[42] I believe that the current evidence strengthens the arguments made in that work. As outlined in the references,[34,42] the reaction initiates at the reactant contact points. The oxidation can occur with both the participating species (aluminum and oxygen) counter-diffusing in the condensed state. Here, the diffusion need not be across a solid shell. Rather, it can even be the consequence of shell rupture and the subsequent seepage of molten fuel. Once the exothermic oxidation reaction initiates, the system temperature, and consequently the vapor pressure of the reduced metal, increases resulting in significant volatilization (as per equilibrium code for the mixture, the mole fraction of

copper vapor in products is 0.4). The reduced metal in the vapor phase will subsequently nucleate and grow depending on the transit time. Lynch et al.,[25] studied nanoaluminum burning in a shock tube, and observed little or no aluminum vapor when the combustion temperature was below that of the melting point of Alumina. Consistent with those results, I observed in a prior study mass spectrometrically Al vapor only in small concentration, and no larger Al clusters.[35] The results in this work reinforce these other studies, as product particle analysis shows aluminum-containing nanoparticles being the minor combustion product formed from the vapor. This aluminum could be the result of any metal vaporization or spallation. But the striking point is that the cumulative effect of all such events which result in aluminum going into the vapor phase is limited to only 10% of the products (recall that the product species in the nano regime also has the reduced metal) and therefore, the major part of the heat release is contributed by a condensed phase mechanism. The proponents of MDM may argue against the formation of aluminum vapor from the high energy nano-sized spalls (5-10 nm)[45] and this discussion does not preclude such a claim. Rather, I set forth that the combination of all such nano-sized dispersions from the system would contribute to only 10% of the constituent products.

In another recent work,[100] these core-shell Aluminum nanoparticles were studied in a Dynamic TEM where a pulsed laser was used to heat up these nanoparticle aggregates at rates of 10^{11} K/s, a rate far higher than that of our wire

experiments. They observed that the aggregates sintered on a time scale of 10 ns which is three orders of magnitude lower than the reaction time scales that were reported in[39] where a shock tube was employed. Similar results were also found through MD simulations[19] and thus I can safely say that there is a propensity for the nanoparticles to aggregate into larger sizes before the reaction can initiate, and I believe that the large particles seen in this study and elsewhere in other studies are formed as a result of such pre-combustion sintering.

4.5 Conclusion

The products of the combustion of three metastable intermolecular reactive composites were studied by quenching the product particles on substrates that could be analyzed by electron microscopy and elemental analysis. The results show that there are two distinct populations of particles. The larger super-micron sized particles comprised and estimated 85%-90% of the total product particle mass. The large particles are primarily composed of aluminum, oxygen, and reduced metal on the surface while the nano-sized particle population was composed of reduced metal/metal oxide. Simple scaling arguments show that such large particles cannot be formed from vapor phase condensation during the available transit time to the substrate and thus must be formed in the condensed state as molten material. This result also suggests a possible reason why nanostructured particles may not react as

fast as might be expect based on simple surface area arguments due to the rapid sintering during the reaction process.

4.6 Acknowledgement

The results presented in this work is reprinted with permission from Jacob, R. J.; Jian, G.; Guerieri, P. M.; Zachariah, M. R., Energy Release Pathways in Nanothermites Follow through the Condensed State. *Combust. Flame* **2015**, *162* (1), 258–264.[135]

Chapter 5 Incomplete reactions in nanothermite composites

Summary

Exothermic reactions between oxophilic metals and transition/ post transition metal-oxides have been well documented owing to their fast reaction time scales ($\approx 10 \mu\text{s}$). This article examines the extent of reaction in nano-aluminum based thermite systems through a forensic inspection of the products formed during reaction. Three nanothermite systems (Al/CuO, Al/Bi₂O₃ and Al/WO₃) were selected owing to their diverse combustion characteristics thereby providing sufficient generality and breadth to the analysis. Microgram quantities of the sample were coated onto a fine platinum wire, which was resistively heated at high heating rates ($\approx 10^5 \text{ K/s}$) to ignite the sample. The subsequent products were captured/quenched very rapidly ($\approx 500 \mu\text{s}$) in order to preserve the chemistry/morphology during initiation and subsequent reaction and were quantitatively analyzed using electron microscopy (EM), focused ion beam (FIB) cross-sectioning followed by energy dispersive X-ray spectroscopy (EDX). Elemental examination of the cross-section of the quenched particles show oxygen predominantly localized in the regions containing aluminum, implying the occurrence of redox reaction. The Al/CuO system, which has simultaneous gaseous oxygen release and ignition ($T_{\text{Ignition}} \approx T_{\text{Oxygen Release}}$), shows substantially lower oxygen content within the product particles as opposed to Al/Bi₂O₃ and Al/WO₃ thermites, which are postulated to undergo a condensed phase reaction ($T_{\text{Ignition}} \ll T_{\text{Oxygen Release}}$).

An effective Al:O composition for the interior section was obtained for all the mixtures, with the smaller particles generally showing higher oxygen content than the larger ones. The observed results were further corroborated with the reaction temperature, obtained using a high-speed spectro-pyrometer, and bomb calorimetry conducted on larger samples (≈ 15 mg). The results suggest that thermites that produce sufficient amounts of gaseous products generate smaller product particles and achieve higher extents of completion.

5.1 Introduction

Thermite reactions are exothermic, redox reactions between a metallic fuel and a metal oxide and are known to have high energy density on both gravimetric and volumetric basis.[136,137] Traditional thermite mixtures, with fuel and oxidizer moieties mixed at the micrometer scale, suffer from significant ignition delay times and poor reaction rates arising from large diffusion length scales and slow conductive heat transfer.[138,139] With the advent of nanotechnology and the subsequent improvement of control at the nanoscale, researchers showed two decades ago that an enhanced reactivity could be observed when the fuel and oxidizer were mixed at the nanoscale[8] and coined the term metastable intermolecular composites (MIC) for such systems. MICs have shown tremendous improvement in reaction rate[9] and with sufficient tuning of the microstructure and composition, have been shown to approach propagation rates as high as 2500 m/s in burn tube measurements.[10,140]

One of the most attractive aspects of MICs is the tunability that allows the use of different metal/ metal-oxide combinations, custom nanostructures[141,142] and production techniques.[13,15,16] Several studies have been undertaken to mechanistically explain the combustion of MICs.[33,42] Heat transfer is considered to be dominated by convection and molten particle advection,[143,144] corroborated by the observation of peak reactivity in cases with highest gas production. The initiation may undergo a condensed phase mechanism where the fuel and oxygen ions are transported across the reaction interface[34,93] or it may undergo a heterogeneous mechanism where the oxygen released from the oxidizer would subsequently react with fuel particles.[35,145,146] It has also been suggested that the fuel nanoparticles can have a more violent response under very high heating rates leading to a catastrophic failure of the protective oxide shell and subsequent spallation of the molten fuel.[44,46] Egan et. al[99] recently conducted experiments of nanoscale Al/CuO composites in a high heating rate transmission electron microscope (Dynamic TEM) and observed the rapid loss of nanostructure to occur about two orders of magnitude faster than a heterogeneous reaction, highlighting the dominance of condensed phase reactions at the nanoscale. Other studies, which combine high heating rates and microscopy, have shown, for Al/WO₃[34] and Al/Bi₂O₃,[147] that the loss of nanostructure and the ensuing reaction is limited to regions where there is sufficient contact between the fuel and oxidizer, suggesting a condensed phase initiation. Another recent study[135] that looked at the reaction products of three

nanoscale thermite systems highlighted the morphological similarities between the products collected from high heating rate experiments under atmospheric conditions with that of those observed in the Dynamic TEM.[99] The study concluded, through the inspection of the product distribution, that the major contribution to the exothermic reaction occurs through the condensed phase as opposed to a gas phase reaction (Chapter 4).

Recent work studying flame propagation of nanothermites[41] has revealed a specialized condition termed ‘reactive entrainment’ which highlights the prolonged combustion of nanothermites which extend over time scales on the order of milliseconds (≈ 3 ms), displaying a gradual release of energy. This combined with the confined pressure cell data showing initial pressure rise times on the order of 10 μ s[40] suggests the possibility of a two-stage combustion where the fast initiation is followed by a slow burning. As the majority of the applications of nanothermites are contingent upon the rapid release of energy feeding the initial pressurization, a quantification of the extent of reaction during the first stage of combustion seems necessary for the development of smart energetics that could be appropriately tuned for maximizing the power output.

The current work is an extension of the previous work on product analysis wherein I tried to identify the predominant energy release pathway in nanothermite reactions. The first part of this work consists of igniting microgram quantities of nanothermites on a resistively heated fine wire followed by rapid quenching and

collection of the combustion products, within $\approx 500 \mu\text{s}$. This allows us to look at the products formed exclusively during the rapid, first stage of combustion. The extent of oxidation is evaluated by employing the focused ion beam (FIB) technique to cross-section the collected product particles, which are subsequently subjected to quantitative elemental analysis using energy dispersive X-Ray spectroscopy (EDX). Three different nanothermite compositions (Al/CuO, Al/WO₃ and Al/Bi₂O₃) are analyzed owing to their diverse combustion characteristics, as discussed in the experimental section. The result obtained from the cross-section analysis is corroborated with the macroscopic heats of reaction for these systems, found using bomb calorimetry. Furthermore, temperature measurements using a spectropyrrometer were also made to augment the analysis on the extent of reaction.

5.2 Experimental

5.2.1 Materials and Preparation

The composites were chosen to be consistent with those in the previous chapter (Chapter 4.2.1) and all three composites exhibit distinctive combustion properties. Al/CuO nanothermite shows concurrent oxygen release and ignition temperatures in high heating rate experiments, which may entail a gas phase ignition whereas Al/Bi₂O₃ nanothermite ignites almost 700 K below the oxygen release temperature from the bare oxidizer and it has been subsequently verified that its initiation proceeds through the condensed phase. It is also the most gas producing/

energetic nanothermite of the three studied.[148] Al/WO₃ is believed to undergo a completely condensed phase initiation/ reaction as WO₃ does not release any gas phase oxygen, although it decomposes into gas phase sub-oxides (WO_x) at ≈ 2800 K.[40] The nanothermite composites were prepared through physical mixing by ultrasonication, as outlined in Chapter 4.2.2. Commercially available aluminum nanoparticles (Argonide Corp.) with an average particle size of 50 nm were used as the fuel. These particles had a core-shell structure with an active aluminum content of 64.5 %, which was confirmed by thermo-gravimetric measurements. The nanoparticles were ultra-sonicated in hexane for approximately 20 min. with three different metal oxide nanopowders. The metal oxide nanopowders used in this study were copper oxide (CuO), tungsten oxide (WO₃), and bismuth trioxide (Bi₂O₃) (all from Sigma Aldrich Corp. and <100 nm) in particle size. After ultra-sonication, the intimately mixed nanothermite slurries were micro pipetted onto fine platinum wires for ignition.

5.2.2 Wire Ignition Experimental Setup and Product Collection

The wire ignition experiment consisted of a platinum wire, ≈ 12 mm length, 76 μm diameter (Omega Engineering Inc.) onto which a slurry of thoroughly mixed nanothermite is coated. The wire is then resistively heated at $\approx 10^5$ K/s using a tunable voltage pulse generated by a custom-built power source. The details of the setup is presented in Chapter 4.2.3. The combustion event was monitored using a high-speed

camera (Phantom Miro) from which the approximate transit time for the products before quenching on the stub was calculated. For the current work, the collection stub was placed such that it allowed $\approx 500 \mu\text{s}$ of transit time for the products before being quenched on the substrate.

5.2.3 *Dual Beam FIB/SEM*

The substrates were subsequently analyzed with focused ion beam scanning electron microscopy (FIB/SEM). The instrument used was a FEI Nova NanoLab 600 DualBeam (Gallium ion source and a Schottky field-emission electron gun) coupled with an 80 mm² Oxford X-Max silicon drift detector to do EDX analysis. The primary advantage of the FIB/SEM instrument is the ability to image embedded phases,[149] where the high-energy ion beam, upon elastic interaction with the sample, mills the material, revealing the cross-section of the sample. The dual beam system has a vertical electron beam column and a gallium ion beam column tilted at an angle of 52° , both focusing at the same point on the sample. The stage with the sample is first tilted at 52° so as to make it perpendicular to the ion beam and the specimen is subsequently milled. Once the milling is complete, the electron beam is used to image the milled surface as well as obtain elemental spectra (EDX). Obtaining the EDX spectra from a tilted surface has its advantages in that the electron beam enters the sample at an oblique angle, which results in the sample surface absorbing a larger portion of the incident electrons when compared to normal

incidence, thereby improving the X-ray emission. However, the stage was not rotated to optimize the take-off angle of X-rays toward the EDX detector from the milled surface and thus the X-ray photon collection was not optimized and longer acquisition times were needed for the analysis. Dual beam FIB/SEM has been extensively used in the semiconductor industry[150] and has found other applications in biological sciences,[151] fuel cells, optical coatings, atmospheric chemistry[149] and primarily TEM sample preparation.[152] Applications of FIB milling in energetics have been limited. FIB assisted nanotomography is a technique that has been used to characterize microstructure and porosity of high explosives to shed more light on the pore collapse mechanism.[153] It has also been used to study intermetallic reactions,[154] synthesis of high explosive composites,[155] as well as examining the extent of oxidation in fine aluminum particles.[30] In this work, I employ the FIB/SEM to mill the product particles of nanothermite reactions so that their interiors can be subjected to quantitative elemental measurements. A representative image of the products on the substrate is shown Figure 5-1a. Selected particles are then cross-sectioned using the gallium ion beam, as can be seen in Figure 2b. The cross-section of the sample is subsequently analyzed using the electron beam and the silicon drift detector for elemental quantification.

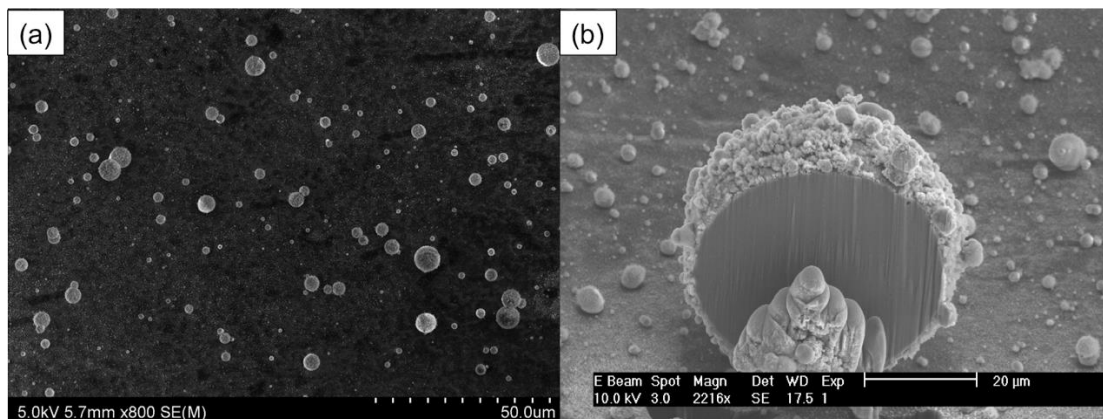


Figure 5-1: (a) Representative SEM image of products collected for the Al/CuO case; (b) a 20 μm particle sliced using high intensity gallium ion beam.

5.2.4 Bomb Calorimetry

The micro-calorimeter used in this study is a low heat capacity instrument specially designed for making measurements of small amounts of reactive materials at 1 atm pressure with a choice of ambient gas. The bomb calorimeter is made from titanium and has an inlet valve to adjust the environment and two electrical feed-through pins. Within the bomb, a thin nichrome filament bridges the two electrical pins and is bent to a point and lowered into the sample that is held in a small ceramic crucible (Figure 5-2). The bomb is sealed, vacuum purged twice and filled with 1 atm of argon to ensure a highly inert environment. The bomb is then suspended in a low heat capacity silicone oil that is constantly stirred. To react the sample, a 10 V potential is applied between the electrical pins, causing the filament to heat and ignite the powder in the crucible. The heat from the reaction disperses within the bomb and into the surrounding oil bath, causing the temperature of the entire system to increase by a small amount, as shown in Figure 5-2d.

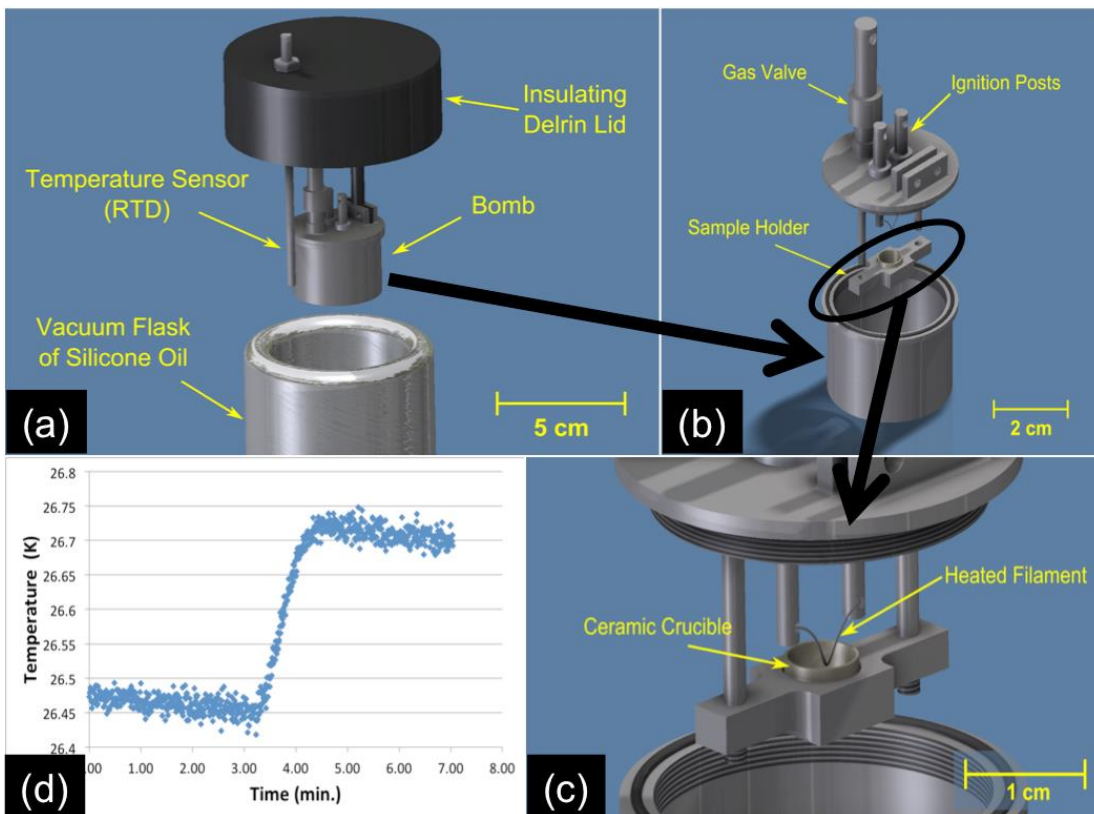


Figure 5-2: (a-c) Schematic of the micro-calorimeter (reproduced, with permission, from K. R. Overdeep, PhD Thesis); (d) Temperature change of the oil bath measured using a thermocouple.

The total test time was approx. 6 min, with 2 minutes each for three regions of temperature measurement: pre-reaction baseline, temperature rise after ignition, and the post-reaction baseline. The heat of reaction is calculated from the product of the calorimeter constant measured during calibrations (135 J/K) and the temperature rise of the oil bath measured during the experiment. The electrical power from ignition is very small and is subtracted from the calculated heat of reaction. More information about this system can be found in a recently published article.[156]

5.2.5 *Spectroscopy and Temperature Measurement*

In addition to calorimetry and elemental quantification, temperature measurements during combustion of these nanothermite composites augment the analysis since a reaction temperature closer to the adiabatic flame temperature would suggest a more complete reaction. Given the transient nature of the event, the diagnostics used require sub millisecond temporal resolution, which precluded the use of conventional techniques such as thermocouples as well as infrared (IR) cameras. The setup and calibration of the high-speed spectrometer is presented in Chapter 2.2. PMT based systems have the advantage of extremely fast rise times (≈ 1 ns) along with high dynamic range and sensitivity, which allowed for extremely fast data acquisition. The data was acquired over the wavelength range of 513 nm to 858 nm (incorporating 27 channels of the PMT). The sampling rate on the acquisition system was set at 50 kHz, which produced a sample every 20 μ s, sufficient to resolve the sub millisecond reactions. The spectrum was subsequently fit to Planck's law, assuming grey body behavior with temperature as a free parameter, to obtain the time-resolved temperature profile.[65]

5.3 *Results*

5.3.1 *Stoichiometric Al/CuO Reaction Product Cross-Section*

As can be seen in **Error! Reference source not found.**, the collected product particle sizes have a wide distribution. However, almost all the product particles seen

in the SEM micrograph are two orders of magnitude larger than the nanoscale reactants (50 to 100 nm primaries). Such large products are a direct consequence of coalescence during the rapid exothermic reaction.[42,99] In addition to these large particles, nanosized product populations were also observed on the substrate, which are a result of nucleation from the gas phase, although their contribution to the net product mass was previously determined in Chapter 4.4.1 to only be ≈ 10 %.[135,157] In order to provide sufficient breadth to the analysis, a range of particle sizes ($> 1 \mu\text{m}$) are considered for ion beam cross-sectioning. Figure 5-3 shows the cross-sectional view of a $\approx 2 \mu\text{m}$ diameter product particle, quenched during the combustion of a stoichiometric Al/CuO thermite mixture (ignition temperature: $(1040 \pm 50) \text{ K}$),[11] accompanied by the area scans. As I can see, there are no visible phase separations within the interior of the particle and the oxygen seems to be evenly distributed throughout the sample.

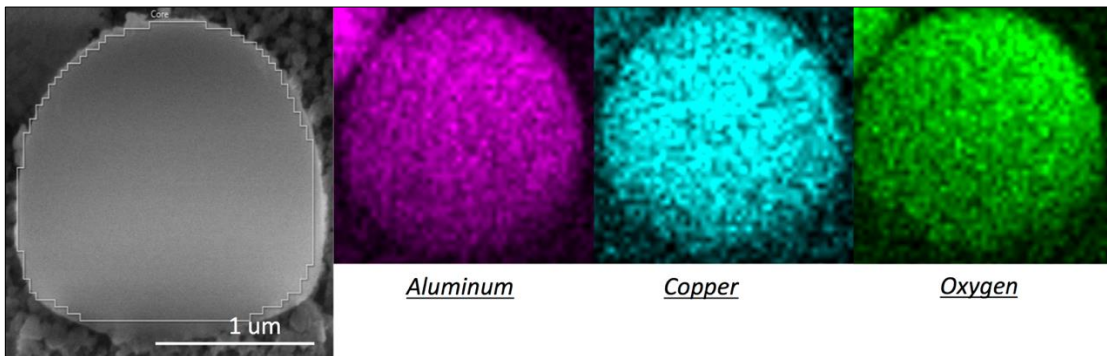


Figure 5-3: Cross-section SEM image of a $\approx 2 \mu\text{m}$ product particle (Al/CuO, $\phi = 1$) with the EDX area scans of the associated elements: aluminum (pink), copper (blue), and oxygen (green). Electron beam conditions are 20 keV and 0.62 nA.

Prior to obtaining quantitative data from the EDX spectra, the instrument's calibration was checked using pure, micrometer scale alumina powder (100 μm , Sigma-Aldrich), for which the EDX system quantified the Al:O atomic ratio as 0.64:1 which is close to the expected value of 0.66:1 for pure alumina, implying an accuracy within 3 %. The elemental composition obtained for the sample in Figure 5-3 is shown in Table 5-1 along with an average composition obtained for particles of a similar size range (2 to 3 μm). The aluminum to oxygen ratio corresponds to an effective $\text{Al}_2\text{O}_{2.7}$ composition, which is close to the expected Al_2O_3 from complete oxidation of the fuel. However, several points regarding this conclusion must be clarified. Firstly, since Al_2O_3 is the only known oxide of aluminum in the condensed phase, an effective value of $x = 3$ in Al_2O_x would imply either a composition of $(\text{M} + \text{Al}_2\text{O}_3)$, where M is the reduced metal (Cu in this case) or a mixture of alumina, MO_y and Aluminum, with the Al and MO_y being mixed such that an effective Al_2O_3 composition is obtained. Similarly, if $x > 3$, it would imply that the Al_2O_3 in the product is mixed with another oxide (MO_y) and a $x < 3$ would imply the Al_2O_3 in the product is mixed with some residual aluminum. Secondly, it can be seen from the Al:Cu ratio in Table 5-1 that the system is significantly aluminum-rich even though the reactants were stoichiometrically mixed.

Al/CuO	Eq. Ratio	Al (at %)	Cu (at %)	O (at %)	x in Al ₂ O _x	Al:Cu
Particle in Figure 5-3	1	32	26	42	2.7	1.2
Avg. <5 μm particles (total 5)	1	38 ± 3	21 ± 4	41 ± 3	2.2 ± 0.3	1.9 ± 0.5
Avg. >5 μm (total 3)	1	34 ± 4	36 ± 5	30 ± 1	1.8 ± 0.1	1 ± 0.3
Fuel-rich (Figure 5-5b)	1.5	49	14	37	1.5	3.5
Al/WO ₃	Eq. Ratio	Al (at %)	W (at %)	O (at %)	x in Al ₂ O _x	Al:W
Avg. <5 μm particles (total 2)	1	32 ± 0	13 ± 1	55 ± 1	3.4 ± 0	2.4 ± 0.2
Avg. >5 μm (total 2)	1	40 ± 2	13 ± 3	47 ± 1	2.3 ± 0.1	3.2 ± 0.8
Al/Bi ₂ O ₃	Eq. Ratio	Al (at %)	Bi (at %)	O (at %)	x in Al ₂ O _x	Al:Bi
Avg. <5 μm particles (total 2)	1	42 ± 1	7 ± 3	51 ± 4	2.4 ± 0.2	7 ± 2.4
Avg. >5 μm (total 2)	1	17 ± 1	46 ± 4	37 ± 4	4.4 ± 0.2	0.4 ± 0.1
Theor. Complete Rxn.	Eq. Ratio	Al	Red. metal	O	x in Al ₂ O _x	Al:M
Al/CuO	1	27.3	31.7	41	3	0.86
Al/WO ₃	1	34.6	13.4	52	3	2.58
Al/Bi ₂ O ₃	1	30.5	23.7	45.8	3	1.29

Table 5-1: Atomic % values (from normalized k-ratios) obtained for the cross-section for different nanothermite systems along with their standard deviations. Equivalence ratio of 1 implies stoichiometrically mixed.

Incorporating the 35.5% weight of the protective oxide shell (estimated via Thermogravimetric Analysis) and assuming complete reduction of copper oxide, the exothermic reaction can be written as $2Al+3CuO+0.29Al_2O_3 \rightarrow 1.29Al_2O_3+3Cu$. This corresponds to an Al:Cu ratio of 0.86 in products, which means that the interior of the particle in Figure 5-3 contains substantially less copper (1.2 vs. 0.86).

Calculation of reaction products using the NASA CEA[158] equilibrium code gives an adiabatic flame temperature of ≈ 2840 K for the Al/CuO system which is at the boiling point of elemental copper. The calculation predicts a copper vapor mole fraction of 0.29, which theoretically leads to an Al:Cu ratio of 1.41 in the condensed phase, in qualitative agreement with the results in Table 5-1 that the reaction products should be aluminum-rich. The vapor phase copper would subsequently nucleate into nanosized particles, but their capture efficiency in our experiment is expected to be low.

A similar analysis is extended to larger particles on the order of $10\ \mu\text{m}$ as shown in Figure 5-4. There is substantial phase separation in the cross-section of these larger particles. Moreover, several cracks and holes can be seen in the copper-rich region, which suggests the production of gaseous species during sintering. The elemental maps show that oxygen is exclusively found in regions containing aluminum and the effective oxidation in this case is $\text{Al}_2\text{O}_{1.8}$ as outlined in Table 5-1. This does not imply that the reaction is producing condensed phase AlO, but rather that the product Al_2O_3 is mixed with some residual aluminum from the reactant, leading to an effective Al:O composition that implies fuel rich, in spite of the reactants being mixed stoichiometrically. What it also means is that at the upper limit, the effective oxidation of the fuel is approximately only 50 % complete in these large particles.

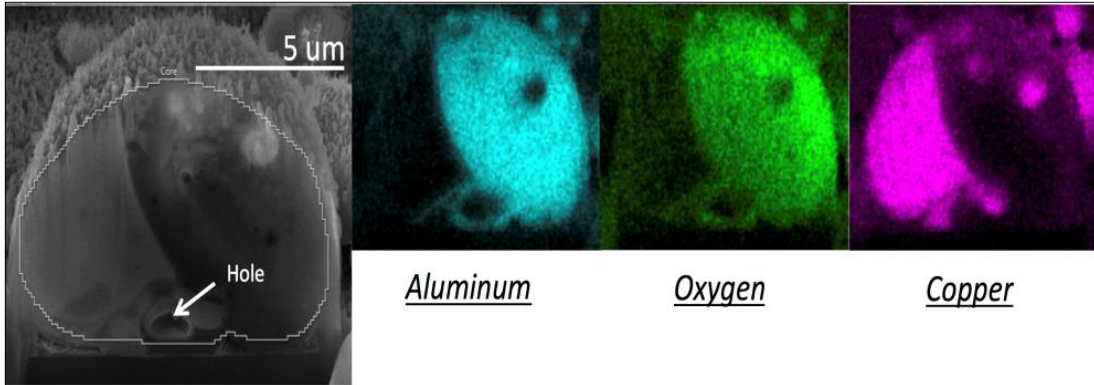


Figure 5-4: Cross-section SEM image of a 10 μm product particle (Al/CuO, $\phi = 1$) with the EDX area scans of the associated elements: aluminum (blue), copper (pink), and oxygen (green). Electron beam conditions are 20 keV and 0.62 nA.

5.3.2 Non-Stoichiometric Al/CuO Reaction Product Cross-section

Similar analysis is extended to Al/CuO thermite mixtures. Two cases were analyzed here: a fuel-lean case with Equivalence ratio (ϕ) = 0.5 and a fuel-rich case with $\phi = 1.5$. Figure 5-5 shows the product cross-sections of non-stoichiometric reactants along with the elemental maps. For the fuel-rich case (Figure 5-5b), I can see that there is a substantial volume of aluminum with oxygen distributed uniformly throughout the particle. For the aluminum-rich region, an effective composition of $\text{Al}_2\text{O}_{1.55}$ is obtained which reiterates poor oxidation. This implies that the improved combustion behavior commonly observed at slightly fuel-rich conditions may not be a direct consequence of enhanced oxidation but merely because of the larger amount fuel in the reactants and the improved thermal conductivity which aluminum provides to the reactant mixture.[159] For the case of fuel-lean mixtures, large voids were found within the product cross-sections (Figure 5-5a) and the elemental maps

confirmed that the voids were found in regions with excess copper. The presence of such voids made getting effective Al:O ratio pointless and subsequently I focused more on examining the compositional gradients within the particle. A possible mechanism for the creation of voids could be the un-reduced or partially reduced CuO losing its oxygen during sintering. Given the fuel-lean compositions and the lack of aluminum in the elemental maps, it would be reasonable to assume that the temperature of this particle would have been quite low, thereby making the evaporation of the copper less likely. The presence of oxygen throughout the particle (even in aluminum-lean areas) suggests that some of the oxygen is indeed bonded with copper, which may subsequently be released into the gas phase leading to void formation.

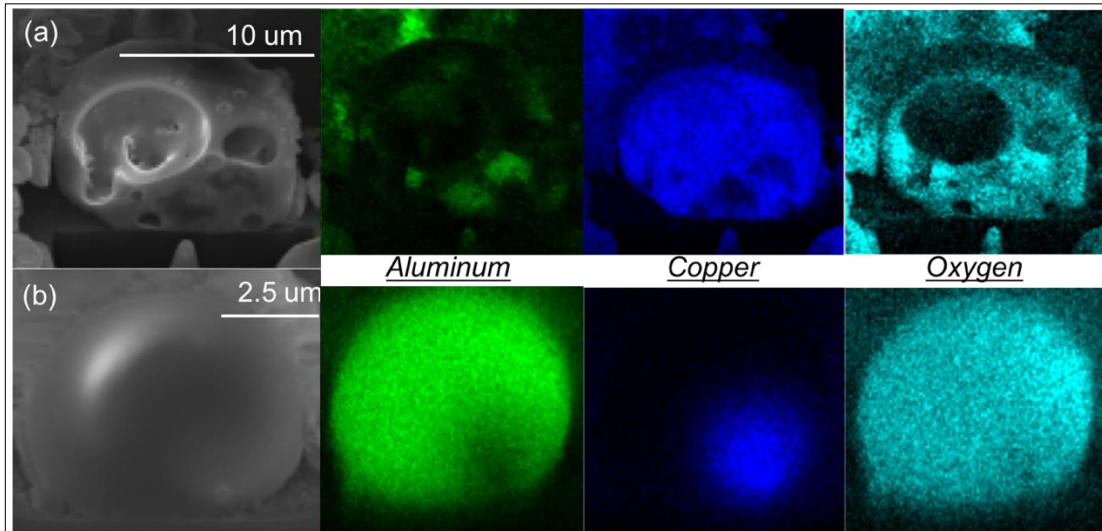


Figure 5-5: (a) Cross-section SEM image and elemental maps of a 10 μm product particle (Al/CuO, $\phi = 0.5$); (b) Cross-section SEM image and elemental maps of a 7 μm product particle (Al/CuO, $\phi = 1.5$). Electron beam conditions are 20 keV and 0.62 nA.

5.3.3 Stoichiometric Al/WO₃ and Al/Bi₂O₃ Nanothermite Mixtures

Experiments on Al/CuO nanothermite mixtures revealed an enhanced effective oxidation at the smaller product length scales. Copper oxide nanopowder has a high propensity to release gas phase oxygen upon heating,[11] whereas oxidizers like bismuth trioxide and tungsten trioxide show no traces of gas phase oxygen release at temperatures at or below the ignition temperature. Thus, it can be expected that upon reaction with aluminum, Bi₂O₃ and WO₃ must show even higher traces of oxygen within the product particles as they are speculated to react solely through the condensed phase. The images for the tungsten and bismuth cases are shown in Figure 5-6 and the quantitative data shown in Table 5-1 reveal higher oxygen content for both cases. Although only a limited amount of data could be obtained for these two thermite systems, the results are in qualitative agreement with the predicted reaction mechanism. For the Al/Bi₂O₃ system, four particles (two per size regime) were analyzed and the proportion of oxygen atoms in Al₂O_x was found to be 2.4 for < 5 μm and 4.4 for > 5 μm particles. The expected Al:Bi ratio for a stoichiometric reaction is 1.29 which implies the smaller particles are substantially low in bismuth whereas the larger particles seem to be bismuth-rich. Equilibrium calculations predict that most bismuth in the reaction products is in the vapor phase, owing to its low boiling point (1837 K) which could explain the lack of bismuth in the smaller particles. The larger particles, which show substantial amounts of bismuth, need a more comprehensive examination since they cannot be formed from

the vapor phase coagulation.[135] A visual inspection of the collected products for Al/Bi₂O₃ revealed that the majority of the particles were on the order of a few micrometers. I tried to confirm this observation by performing the image processing routine outlined in Ref. [135] on the electron micrographs of the collected particles. From this analysis, outlined in Chapter 4.4.1, I obtained a qualitative comparison between the product sizes of the three systems. Al//Bi₂O₃ products were the smallest with average particle diameters ranging from 600 nm to 1 μm. This suggests that the large particles found for the Al/Bi₂O₃ case are probably from a region of poor mixing with excessive Bi₂O₃, which might subsequently decompose due to the heat from the adjacent reaction zones. This would also lead to the scenario where $x > 3$ in Al₂O_x which would imply the mixing of aluminum oxide in the reaction product with excess, unreacted/ partially reacted oxide from the reactants.

Similarly, for the Al//WO₃ case, the proportion of oxygen atoms in Al₂O_x was found to vary between 2.3 and 3.4 (Table 5-1) for different particle sizes, which is near the expected value of 3. In both cases the amount of oxygen in the interior was higher than the case of copper oxide and the oxygen was predominantly localized to regions with aluminum. The Al:W ratio vary between 2.4 to 3.2 which is near the predicted value of 2.58, a consequence of barely any gasification. Also, like the copper oxide case, the larger particles contained less oxygen than the smaller ones.

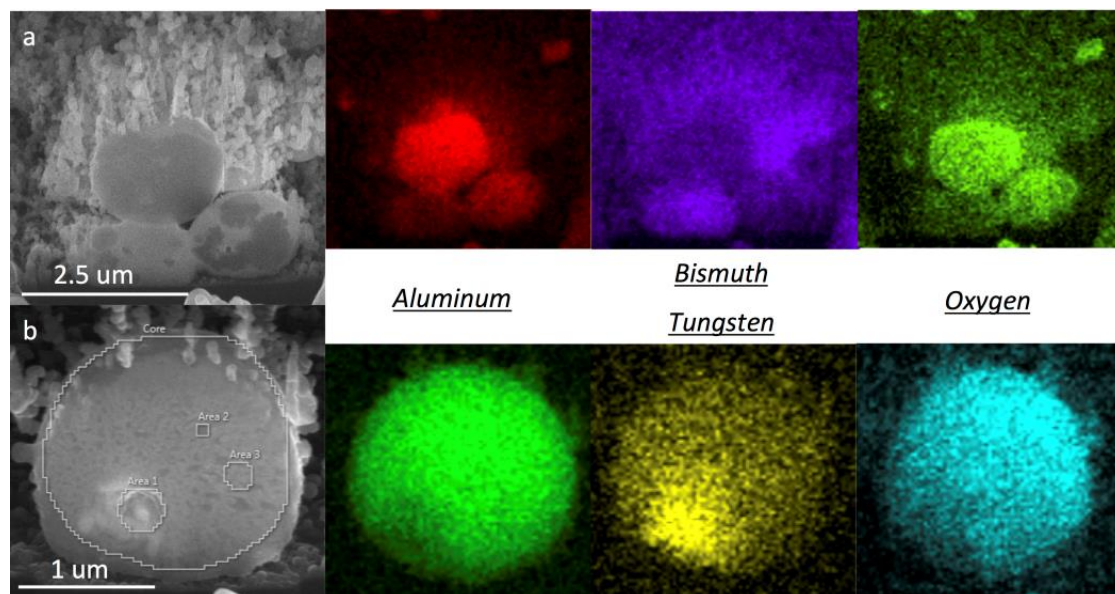


Figure 5-6: (a) Cross-section SEM image and elemental maps of a 3 μm product particle (Al/ Bi_2O_3 , $\phi = 1$); (b) Cross-section SEM image and elemental maps of a 2 μm product particle (Al/ WO_3 , $\phi = 1$). Electron beam conditions are 20 keV and 0.62 nA.

5.3.4 Bomb Calorimetry Results

Bomb calorimetry measurements were conducted under argon to prevent any secondary reaction with air. The measured heat of reaction (ΔH_{Rx}), for the three nanothermite systems (stoichiometric), are shown in Table 5-2 along with an estimated percentage of completion. The reported average values were obtained from 5 runs of Al/CuO, which helped ensure the repeatability of the experiment and were subsequently extended to Al/ WO_3 and Al/ Bi_2O_3 (2 runs each). The standard deviations were within 10%, which precluded the need for additional runs for the latter cases. Nanothermite systems reacting via condensed phase mechanism (Al/ Bi_2O_3 and Al/ WO_3) show higher completion than those having a gas phase

reaction component. Literature values for the theoretical gas production, adiabatic flame temperature (T_{ad}) and pressurization rate in constant volume cell tests are also tabulated for further discussion.

Thermite (phy.mix)	Exp. ΔH_{Rx} (J/g)	Theo. ΔH_{Rx} (J/g)[136]	% Complete	Gas Prod. @ 1 atm (g of gas/g of mix)[160]	Press. Rate (kPa/us)[40,147]	T_{ad} (K)[136]
Al/CuO	2479 \pm 334	4071	61	0.343	76.6	2843
Al/WO ₃	2192 \pm 176	2910	75	0.146	0.2	3253
Al/Bi ₂ O ₃	2141 \pm 54	2115	\approx 100	0.894	108.3	3253

Table 5-2: Bomb calorimetry results for nanothermite reactions along with standard deviations.

5.3.5 Reaction Temperature

Reaction temperature was also measured for these nanothermite systems in inert environments (Ar, 1 atm) and the results are shown in Figure 5-7 along with the adiabatic flame temperature for comparison. Figure 5-7d shows high-speed temporal snapshots of the Al/CuO nanothermite reaction, with the time elapsed from trigger shown as insets. The snapshot at 2.882 ms corresponds to the peak temperature observed in Figure 5-7a. Except for the Al/CuO system, the other two nanothermites produce temperatures that are at or below their respective adiabatic flame temperature.

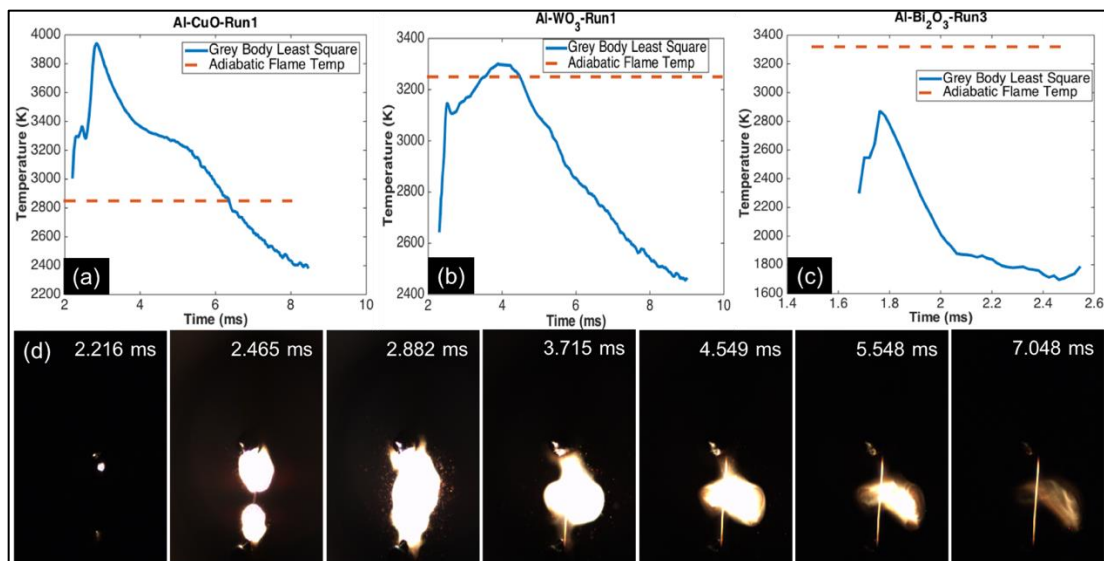


Figure 5-7: Temperature profiles in inert environments for (a) Al/CuO, (b) Al/WO₃ and (c) Al/Bi₂O₃; (d) High speed snapshots of Al/CuO reaction on wire shown in (a).

5.4 Discussion

The results from the previous section show that the dimensions of the final nanothermite reaction products are on the micrometer scale in spite of the reactants being nanoscale. Molecular dynamics simulations done by Chakraborty et. al[19] have shown that nanoscale aluminum aggregates can lose their surface area and sinter into characteristically larger particles in nanoseconds. Since most nanopowders exist in an agglomerated state, this rapid loss of surface area could be substantial.

Experimental validation of this postulate was recently published where temporal snapshots of nanoaluminum aggregates subjected to high heating rates, were taken in a Dynamic Transmission Electron Microscope (DTEM).[100] The results indicated that the loss of nanostructure was complete on the order of ~ 50 ns which is 3-4

orders of magnitude faster than the what is observed for nanoaluminum (~0.5ms).[161]

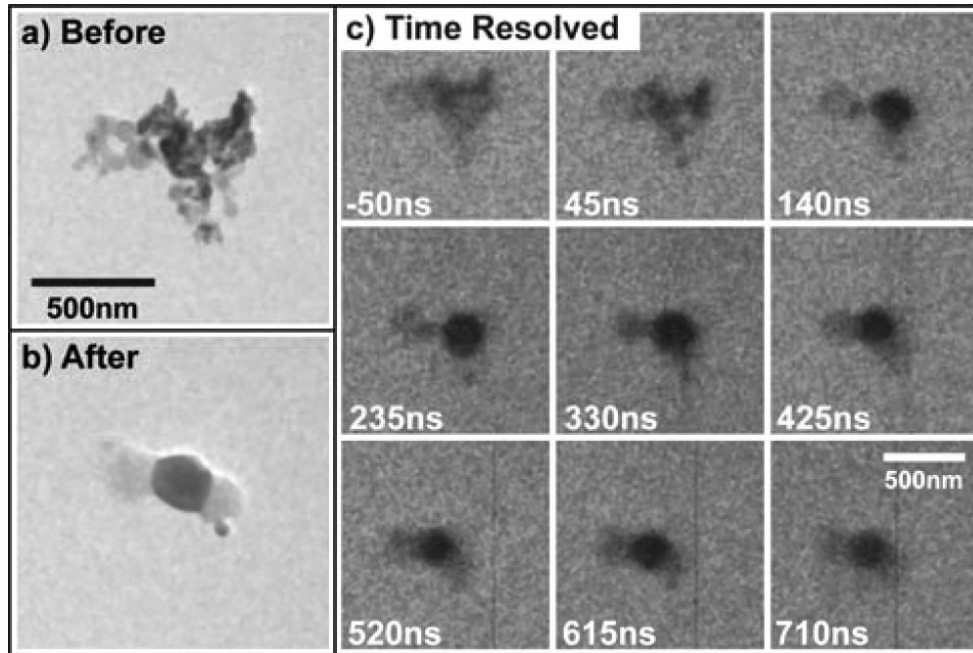


Figure 5-8: Morphological changes to a 500 nm aggregate of Al/CuO heated by a 12ns heating laser pulse characterized in a DTEM. (a) Aggregate prior to heating; (b) Resulting morphology after heating; (c) High speed temporal snapshots of the evolution of the aggregate morphology. Reprinted from [99].

The same experiment, extended to Al/CuO nanothermite,[99] also showed this rapid loss of nanostructure, occurring on a slightly longer time scale of ~ 300 ns, as shown in Figure 5-8, which is still much faster than the combustion of these composites (~1ms).[43] A direct consequence of this loss of nanostructure is the formation of large, condensed phase products which greatly increase the diffusion length scales for the reactants, leading to slow afterburning,[41,81] thereby defeating the purpose of using nanoscale material for rapid reaction. With this work, I try to

examine the detrimental effects of such sintering by quantifying the energy release as well as the internal composition.

The biggest difference between the three nanothermite systems studied here is that in reactions where condensed phase chemistry is predominant (Al/WO₃ and Al/Bi₂O₃), the elemental compositions from the interior revealed a higher oxygen content, implying a higher extent of reaction. This is directly observed on the macroscopic scale as well, in the bomb calorimetry experiments, where larger sample mass and longer sampling duration was employed. The aforementioned nanothermite systems (Al/WO₃ and Al/Bi₂O₃) were observed to approach their theoretical heats of reaction to a greater extent than Al/CuO. Moreover, from Table 5-2, it can be seen that the Al/Bi₂O₃ system is expected to produce the most gas phase products upon reaction. This is primarily due to the low boiling point of the bismuth product compared to the other two reduced metals, copper and tungsten. Such excessive gas production could significantly influence the heat of reaction. Firstly, higher gas production could mean a stronger pressure wave emanating from the ignition point which could help in de-aggregating the adjacent reactant particles into smaller clusters, thereby preventing large-scale sintering. Since condensed phase reactions rely on species diffusion, these smaller clusters of fuel and oxidizer would react much faster, owing to their shorter diffusion length scales. This could also lead to the prevention of a two-stage combustion, as outlined earlier, where sintered particles would undergo slow burning in ambient atmosphere.

The influence of gas production on the product sizes was examined further following the procedure in Chapter 4.4.1, where image processing, using ImageJ, was performed on the electron micrographs of the collected product to estimate their average sizes. Al/Bi₂O₃ products were the smallest with particle diameters ranging from 600 nm to 1 μm. Al/CuO product sizes were approximately 1 μm to 2 μm and Al/WO₃ had product sizes in the 3 μm to 4 μm range. Correlating this observation with that of the gas production, one can see the influence quite clearly with gas production scaling as Al/Bi₂O₃ > Al/CuO > Al/WO₃ leading to product sizes Al/Bi₂O₃ < Al/CuO < Al/WO₃ and reaction completion being Al/Bi₂O₃ > Al/WO₃ > Al/CuO.

The latter correlation for reaction completion does not strictly align with theory of smaller products leading to higher completion. A possible reason for this would be the gas phase oxygen release from copper oxide nanopowder, which has been shown to be concurrent with ignition of the Al/CuO nanothermite.[11] This release of oxygen could result in diminished local availability of condensed phase oxidizer to the fuel particles, leading to poor reactivity. This is indeed observed in the spectrometric temperature measurements shown in Figure 5-7, where the initial spike in temperature for the Al/CuO case is near the micrometer aluminum flame temperatures/ alumina volatilization temperatures.[162,163] Since the flame temperatures were measured in an inert environment, the high initial temperature can be explained to be a consequence of a sintered aluminum particle reacting with the

gas phase oxygen released from the bare CuO. Such large sintered aluminum aggregates may not completely combust, leading to a drop off in heat of reaction. Moreover, the flame cloud shown in Figure 5-7d at 2.882 ms (at the peak temperature shown in Figure 5-7a) need not have a homogenous temperature distribution since the spectrometer would be biased to the highest temperature within the cloud (due to intensity being a function of T^4). Hence isolated events of aluminum combustion with ambient oxidizer could be responsible for the high temperature. It should be noted that the measured temperatures for Al/Bi₂O₃ are substantially lower than the adiabatic flame temperature in spite of the reaction going to near completion. A possible reason for this could be that the grey body assumption for temperature calculation fails for this particular reaction due to the highly dilute flame cloud. Recent studies on the effect of emissivity of aluminized flame clouds have suggested that in case of dense particle clouds, multiple scattering could result in an effective grey body behavior.[58] High speed video of the Al/Bi₂O₃ reaction, shown in Figure 5-9, reveals that the flame cloud produced for this system looks less dense compared to those produced for the other two thermites.

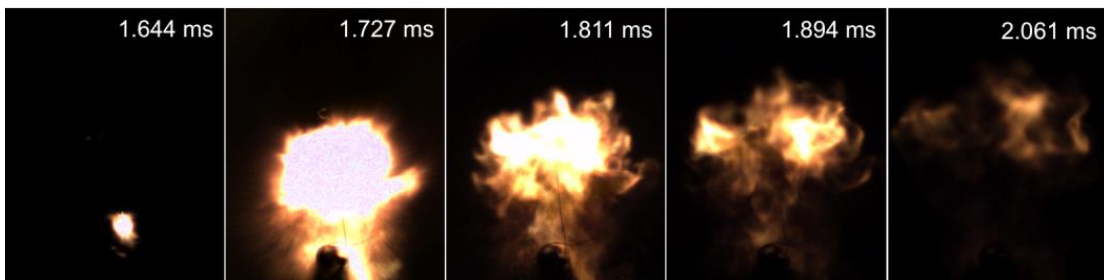


Figure 5-9: Combustion cloud of Al/Bi₂O₃

Experimental evidence of cracks and voids in the cross-section of the collected products of the oxygen releasing thermites like Al/CuO, suggest that the sintering might be occurring on a time scale much shorter than the gas release. This could be particularly detrimental as the released oxygen would neither support condensed phase nor gas phase oxidation of the fuel. Moreover, this was observed only in large particle cross-sections (Figure 5-4) and in fuel-lean Al/CuO systems (Figure 5-5a), further supporting the claim that smaller products must lead to a more efficient combustion. Several recent experiments have been directed at reducing the product particle size[125,164] owing to the higher reactivity that has been observed in cases where there is less coalescence of reactants. Results of Wang et al.[164] showed an increase in the pressurization rate and peak pressure for nanothermite composites that were designed to reduce the coalescence of the reactants through internal gas generation, thereby allowing greater exposure for the fuel to react. Another recent study,[142] which looked at the reactivity of nano aluminum based composites containing gas generators, showed an order of magnitude improvement in reactivity owing to a smaller sized reactant matrix. The underlying principle for all such observations could be explained, based on the current results, as a consequence of reducing the effective diffusion length scales for reactants as well as dispersing the reactants, which would ensure faster reaction and also prevent the unreacted material from getting arrested within a coalesced particle, as seen in Figure 5-4 and Figure 5-5a.

5.5 Conclusion

Quenched reaction products of thermite systems were analyzed to understand the extent of reaction and energy yield. The product particles were quenched immediately (within 500 μs) upon ignition so as to prevent any adulteration from subsequent reaction with the ambient. The elemental analysis of the product particle cross section revealed that nanothermite compositions where condensed phase reactions are predominant (Al/WO₃ and Al/Bi₂O₃), the elemental compositions from the interior revealed a higher oxygen content, implying a higher extent of reaction. This was correlated on the macroscopic scale as well, in the bomb calorimetry experiments, where the aforementioned nanothermite systems (Al/WO₃ and Al/Bi₂O₃) were observed to approach their theoretical heats of reaction to a greater extent than Al/CuO. The product particle sizes were estimated from the SEM images via image processing and were found to be in the order: Al/Bi₂O₃ < Al/CuO < Al/WO₃. Which correlated with the total gas release from each nanothermite system (from pressure cell tests) Al/Bi₂O₃ > Al/CuO > Al/WO₃. This implies that strong gas generation during thermite reaction could have a significant effect on inhibiting sintering in the reactants, thereby reducing the length scale that the reactants have to diffuse for reaction in the condensed phase.

The reaction completion, found using bomb calorimetry scaled as Al/Bi₂O₃ > Al/WO₃ > Al/CuO. The lack of correlation between reaction completion and gas generation for the Al/CuO case was interpreted as a consequence of gas phase oxygen

release from the bare oxidizer which has been experimentally found to match the ignition temperature. Such release of oxygen gas led to limited oxidizer being present in the condensed phase, which results in poor reactivity observed in calorimetry results as well as lower oxygen content in the elemental maps from cross section. This could also imply that condensed phase reactions are more efficient when it comes overall reactivity since gas phase reactions often occur over longer durations and are plagued by sintering. Furthermore, the results were corroborated with reaction temperature in inert environments where for Al/CuO, significant gas phase reaction between Al and oxygen (released from CuO) was observed ~ 1 ms after ignition. The measured reaction temperatures were at and below the adiabatic flame temperatures for Al/WO₃ and Al/Bi₂O₃ respectively.

The elemental maps revealed that in all cases, the oxygen was predominantly localized in the regions containing aluminum, although in the case of non-gas-generating thermites, some oxygen could be seen with the reduced metal too. These results imply that the thermite reaction are not be achieving completion even though the constituents are mixed on the nanoscale, owing to severe sintering of the reactants before the reaction can go to completion.

5.6 Acknowledgements

The findings presented in this work were the result of a collaboration with Dr. Diana Ortiz-Montalvo, Staff Scientist at the National Bureau of Standards and

Technology and Dr. Kyle Overdeep from Dr. Tim Weihs' Lab at Johns Hopkins University Baltimore. The results are reprinted with permission from Jacob, R. J.; Ortiz-Montalvo, D. L.; Overdeep, K. R.; Weihs, T. P.; Zachariah, M. R. Incomplete Reactions in Nanothermite Composites. *J. Appl. Phys.* **2017**, *121* (5).[165]

Chapter 6 High speed 2-Dimensional temperature

measurements of nanothermite composites: Probing

Thermal vs. Gas generation effects

Summary

This work investigates the reaction dynamics of metastable intermolecular composites through high speed spectrometry, pressure measurements, and high-speed color camera pyrometry. Eight mixtures including Al/CuO and Al/Fe₂O₃/xWO₃ (x being the oxidizer mol. %) were reacted in a constant volume pressure cell as means of tuning gas release and adiabatic temperature. A direct correlation between gas release, peak pressure and pressurization rate was observed, but it did not correlate with temperature. When WO₃ was varied as part of the stoichiometric oxidizer content, it was found that Al/Fe₂O₃/70% WO₃ achieved the highest pressures and shortest burn time despite a fairly constant temperature between mixtures, suggesting an interplay between the endothermic Fe₂O₃ decomposition and the higher adiabatic flame temperature sustained by the Al/WO₃ reaction in the composite. It is proposed that lower ignition temperature of Al/WO₃ leads to the initiation of the composite and its higher flame temperature enhances the gasification of Fe₂O₃, thus improving advection and propagation as part of a feedback loop that drives the reaction. Direct evidence of such gas release promoting reactivity was obtained through high speed

pyrometry videos of the reaction. These results set the stage for nanoenergetic materials that can be tuned for specific applications through carefully chosen oxidizer mixtures.

6.1 Introduction

Research in nanoscience, as in many fields, has permeated the development of energetic materials where the demand for improved reactivity may be achieved with increased intimacy between reactants. Traditional monomolecular CHNO systems represent optimal reactant proximity, with mixing achieved at the molecular scale. However, the gaseous nature of their reaction products allow limited enhancements in their energy content.[166,167] As a result, much recent research has been directed towards nanoscale composite energetic materials incorporating metal nanoparticles as the fuel so as to enhance energy content and release rate.[168] One of the primary advantages of using metallic fuels is their high volumetric energy density leading to some metal based energetic materials having heats of reaction larger than state of the art CHNO systems.[166] However, using non-molecular, fuel-oxidizer systems implies a diffusion-limited process. It has been demonstrated repeatedly that the use of nanoparticles, with its decreased length scale, leads to a metastable system with orders of magnitude improvement in reactivity compared to their counterparts mixed at coarser scales.[9] A large body of recent research has been directed at exploring the underlying mechanism responsible for the fast reaction rates observed in such

Metastable Intermolecular Composites (MIC)/nanothermite combustion, with the general consensus being that the dominant energy transfer mechanism in MIC powder is convection and molten particle advection[143] and the primary mode of ignition/reaction is via the condensed phase diffusion of reactant moieties.[42,135]

A significant benefit of MIC systems is their tunability, which stems from the extensive permutations in the selections of fuels, oxidizers,[11,169] gas generators[170] and architecture[171,172], with the state of the art systems showing flame speeds as high as 4000 m/s.[140] Several methods have been developed to quantify their reaction dynamics with, ignition temperature and speciation measurements,[11,35] thermo-analytical methods,[145] flame speeds,[173] thermo-equilibrium software (CEA, Cheetah)[137] and constant volume combustion[33] being the most common. Although these methods do help in quantifying the combustion characteristics of MIC's, the flame speed and pressure measurements are significantly affected by variations in their experimental design. Temperature, on the other hand, is a fundamental thermodynamic property and is directly related to energy release, although its measurement in energetic materials research is not as prevalent as one might suppose. Primarily, the wide range of reaction times (10 μ s - 100ms), temperature range (800K – over 4000K) and spatial inhomogeneity make robust temperature measurements a challenge. Moreover, MIC's have significant emission interference from atomic and molecular species that participate in the high

temperature reaction, thereby reducing the applicability of broadband measurement techniques.

Despite these limitations and challenges, the non-invasiveness and relative simplicity of emission measurements as compared to other optical methods and the artifacts introduced by traditional invasive methods mean that optical emission is preferred for MIC characterization. Weismiller et al.[60] studied three different nanothermite compositions in an unconfined pile, and confined burn tube using multi-wavelength pyrometry. Kappagantula et al.[174] also examined several Al/CuO and Al/PTFE based composites with metal additives using an IR camera as a means to optically measure performance. Despite the assortment of temperature measurement methods used to observe these energetic compounds, a common theme in each experiment was the inability for the compound to achieve its adiabatic flame temperature. The similarity across different composite mixtures has supported the conclusion that the systems under study were limited by the melting and decomposition of the oxide. Through such insight into the reaction dynamics, it might be possible to tune the reactivity of composite materials by altering the participation of competing reactions through mixture content variation. Prior work by Sullivan et. al[40] first explored this possibility by incrementally adding nanoscale WO_3 to an Al/ Fe_2O_3 nanothermite to demonstrate an increase in pressurization rate under constant volume combustion environment. The result was counterintuitive as gas generation was observed to increase with the reduction of gas generating species

(Fe₂O₃) in the composite. The Al/Fe₂O₃ nanothermite was postulated to be rate limited by oxidizer decomposition, and the performance improvement was attributed to efficient decomposition of Fe₂O₃ induced by the heightened flame temperature at higher WO₃ concentrations. While the results were corroborated with equilibrium calculations, no direct temperature measurement was made to support the claims regarding the interplay of reaction mechanisms. The purpose of this work is to extend the results of Sullivan et. al[40] through high-speed, multi-wavelength pyrometry to probe the tunable reactivity of a nanothermite composite in a closed pressure vessel. Moreover, the effects of enhanced gas production on reactivity is visualized under unconfined conditions with high spatial and temporal resolution using high speed color camera pyrometry.

6.2 *Experimental*

6.2.1 Materials and Sample Preparation

Commercially available aluminum nanoparticles (ALEX, Argonide Corp.) with an active content of 68.7 wt. % (from thermogravimetric analysis) and an average particle size of 50 nm were used in this study. The oxide nanopowders (CuO, WO₃ and Fe₂O₃) were procured from Sigma Aldrich and all had average diameters < 100 nm. The samples were prepared by dispersing a known amount of oxide in 10 mL of hexane and sonicating in an ultrasonic bath for an hour. This was done in order to break down the soft aggregates, ensuring better mixing with the fuel. A stoichiometric

amount of aluminum was then added to this slurry and further sonicated for an hour. The slurry was left overnight to dry. The dry sample was gently scraped off the vial and broken up using a grounded spatula until powder consistency was achieved. Samples prepared included stoichiometric blends of Al/CuO, Al/Fe₂O₃ and Al/WO₃. Additionally, a set of 5 samples were made where I systematically adjusted the oxidizer composition by adding 20, 60, 70, 80 and 90% by mole of WO₃ to Fe₂O₃ system, while maintaining the overall stoichiometry of the blend as outlined in the prior work by Sullivan et al.[40] For experiments involving high-speed videography, the slurry was kept as is for drop casting on a fine platinum wire for rapid heating, as discussed in the forthcoming sections.

6.2.2 Constant volume combustion cell

The constant volume pressure cell used is described in detail elsewhere.[40,175] Briefly, the cell is a closed reaction vessel with a free volume of ~20 cm³, equipped with 3 ports (as shown in Figure 6-1). One port houses a high frequency pressure transducer (PCB Piezoelectronics) for measuring the pressure signal generated during sample ignition and combustion. The second port is connected to an optical assembly used for collecting broadband emission from the inner edge of the vessel. The optical assembly consists of a plano convex lens (Thorlabs) which collects and focuses the light from the vessel into a 2 meter long fiber optic cable (Dia. 1mm, Thorlabs Inc.) coupled to photomultiplier tube (PMT)

(Hamamatsu). An optional neutral density filter (Thorlabs Inc.) is placed between the lens and the fiber for significantly brighter samples so as to prevent saturation of the detector. Both the PMT and the pressure transducer outputs are connected to a digital oscilloscope (Teledyne LeCroy Wavesurfer 3000) sampled at 5 MHz. The PMT's cathode voltage is selected empirically by monitoring the output current during trial tests. The third port houses another optical assembly which collects and relays the emission to a spectrometer, which is detailed in Chapter 2.2. The cell was placed inside an artificial environment bag which was purged with argon to mitigate the influence of atmospheric oxygen on the reaction.

Each sample (25 mg) was tested in triplicate by ignition with a resistively heated nichrome wire connected to a DC power supply. A custom square wave generator was built in-house to simultaneously trigger the spectrometer, oscilloscope and the power supply for the nichrome wire. Owing to the high temperatures and significant production of gas and condensed species, a sapphire window was used to protect the optical assembly and was cleaned periodically so as to ensure accurate measurement of the emission.

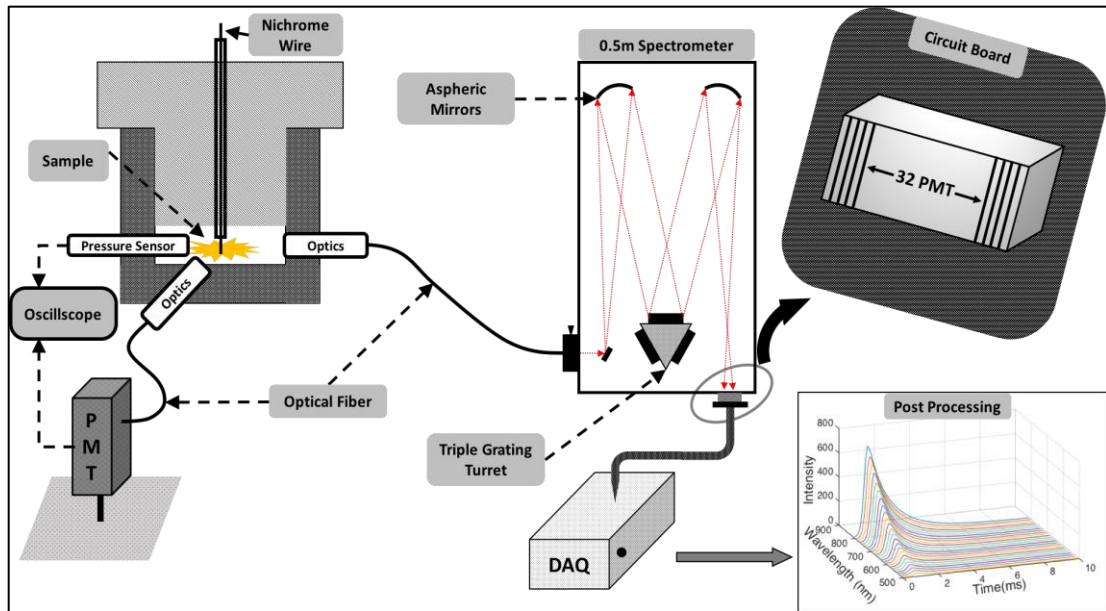


Figure 6-1: Schematic of the experiment consisting of pressure cell and attached diagnostics. The pressure cell is shown on the left. The spectrometer is coupled to the pressure cell via an optical fiber. The light from the fiber is spectrally dispersed by the selected grating on the turret which is subsequently imaged on the 32 channel PMT and digitized using the Data Acquisition system (DAQ). The digitized data is processed to produce time resolved spectra.

6.2.3 *Hot-Wire ignition tests for spatiotemporal Temperature maps*

While the experimental setup including the spectrometer described above can measure the temperature of radiating particles using multi-wavelength techniques, its ability to measure the spatial dynamics of the combustion process is limited by means of its data acquisition. Owing to the nature of light collection through an optical fiber, the spectrometer would be biased to the brightest/hottest spots within the flame due to the exponential scaling of light intensity with temperature as per Stefan-Boltzmann Law. Furthermore, due to the spatially dynamic nature of the flame front, point light sources could constantly move in and out of the field of view, affecting the

temperature measurement. As a complementary diagnostic to the spectrometer, a high-speed color camera based pyrometer, as described in Chapter 2, is used to record videos of the combustion event so as to probe the highly dynamic flame front.

Although color camera pyrometry does allow for spatiotemporal measurements of temperature, limitations in the method by which raw data is collected are a strong source of error ultimately leading to deviations in temperature measurement from those reported by the spectrometer. Of the many elements that emit in the visible region during thermal relaxation, sodium is often the most noticeable with strong, persistent lines seen as a doublet at 588.95nm and 589.59nm.[82] Such emission contributes to the red and green channel intensities, due to their high spectral response at these wavelengths, leading to error in temperature calculations. Other elements that have strong emission and are possible sources of contaminants in the experiments performed include potassium and copper. Furthermore, the calculations detailed above fails to account for light scattering from small particulates that may be generated throughout the course of the reaction. Hence, in order to maintain fidelity, the error minimization algorithm used to calculate temperature is error thresholded to $\sim 100\text{K}$ and the pixels that report higher errors are excluded from the final false-color images.

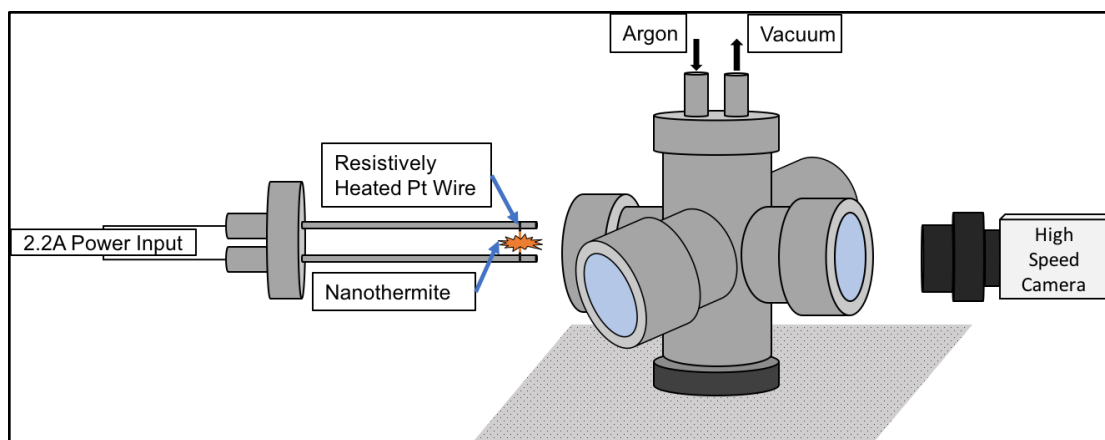


Figure 6-2: Experimental rig for visualizing nanothermite reaction using high speed color camera

Wire ignition experiments were conducted in a stainless steel 6-way cross, with windows to visualize the combustion with the high-speed camera (Figure 6-2). The interior of the chamber was painted black in order to minimize light reflections. A premixed slurry of thermite sample were coated onto a 76 μm -diameter platinum wire and resistively heated in a 1 atm argon environment for 4ms at a rate of $\approx 10^5$ K/s using the T-Jump apparatus detailed by Zhou et al.[35] Two videos were recorded per sample at a framerate of 20,000 fps with the $f/\#$ and exposure times empirically chosen to provide the best signal to noise ratio.

6.3 Results

6.3.1 Al/CuO nanothermite tests in pressure cell

As a control system, I begin with the most studied thermite system Al/CuO. Figure 6-3 shows the temporal pressure response, normalized-integrated radiance across all PMT channels (Figure 6-3a) and the temperature fit (Figure 6-3b) for the

Al/CuO reaction in the pressure cell. The peak pressure of the system is ~ 741 kPa and the pressurization rate is ~ 118 kPa/ μ s, calculated based on the rise time of the first pressure peak. The temporal temperature profile shown in Figure 6-3b is recorded using the ND2 Neutral density filter in order to quantify the emission at peak light intensity. The custom fitting algorithm enabled the simultaneous calculation of temperature, and the error associated with the fit which was thresholded to ± 400 K before plotting the profile shown in Figure 6-3b. The missing data points at longer durations correspond to such cases where the calculated error was higher than the threshold value. The figure is horizontally sectioned by gridlines so as to qualitatively analyze the different regimes.

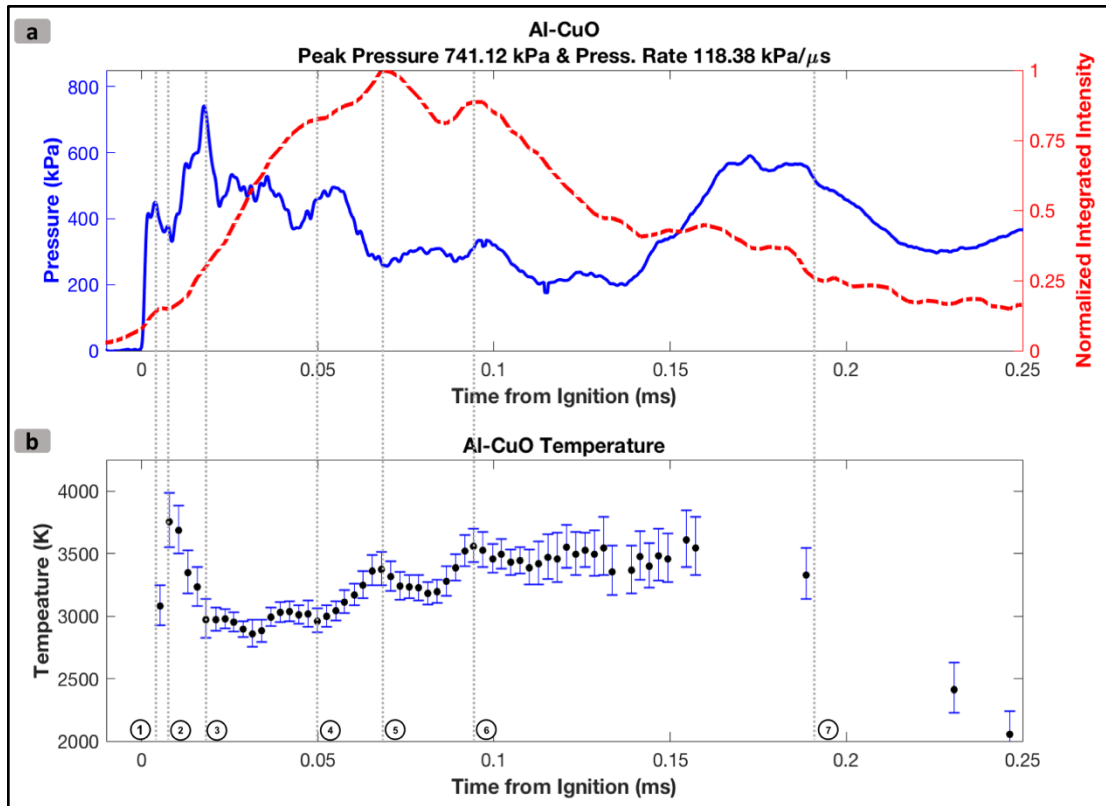


Figure 6-3: Al/CuO nanothermite in pressure cell. a. Pressure-Normalized-Integrated Intensity profile, and b. Temporal reaction temperature profile. Region 1-2: temperature rise and pressure drop; 2-3: temperature drop and peak pressure; 3-4: rapid rise in integrated intensity at a constant temperature with decreasing pressure; 4-6: broadly represents increase temperature; 6-7: region with temperature plateau, decreasing integrated intensity and pressure.

Owing to the error thresholding, the first temperature data point was obtained at ~ 0.005 ms from ignition, where the integrated emission is approx. 15% of the peak integrated intensity. The pressure trace at this point corresponds to the first local maxima, as highlighted by the vertical line 1. Region 1-2 corresponds to a reduction in pressure accompanied by a temperature rise to ~ 3600 K which is followed by a sharp drop to ~ 2800 K in region 2-3. This coincides with an increase in pressure to its

maximum value at ~ 0.017 ms (location 3) and the emission intensity is observed to have a sharp positive slope from point 2 onwards. At the instant of peak pressure, the normalized emission is $\sim 30\%$ and the temperature is near the adiabatic flame temperature for Al+CuO (2837 K).[40] Region 3-4 corresponds to the most substantial increase in integrated intensity as it rises from 30 to 80% at 0.05ms (location 4) although the temperature in this region is observed to plateau at ~ 3000 K. The pressure profile, on the other hand, shows a steady decline in this region. Region 4-6 broadly corresponds to an increase in temperature to ~ 3500 K (location 6) and the emission intensity is observed to first increase in the region 4-5 by $\sim 20\%$, attaining its peak at location 5. Region 5-6 continues the increasing trend of temperature although the integrated intensity is observed to drop by $\sim 25\%$, achieving a local maximum at location 6, corroborated with an increase in temperature. In region 6-7, the emission intensity is observed to decline although the temperature profile is essentially plateaued at ~ 3500 K. Measurements beyond this point resulted in high errors due to low signal and were thresholded at ± 400 K. The pressure signal is observed to continue its decline, although at 0.17 ms, a spike is observed which is the reflected pressure wave from the initial pressure spike. Such damped reflections were observed over a period of ~ 150 μ s, approximately the time it takes a sound wave to traverse twice the diameter of the cell. A lack of deviation in the measured temperature suggest the same, as a change in combustion mechanism would have manifested in the measured temperatures. Qualitatively similar profiles were observed for repeat

runs as well and the significance of each regime is discussed in more detail in the mechanism section. For measuring temperatures at longer durations, where the emission intensity is lower, a complementary test without employing the ND2 filter was done and the result is shown in Figure 6-4.

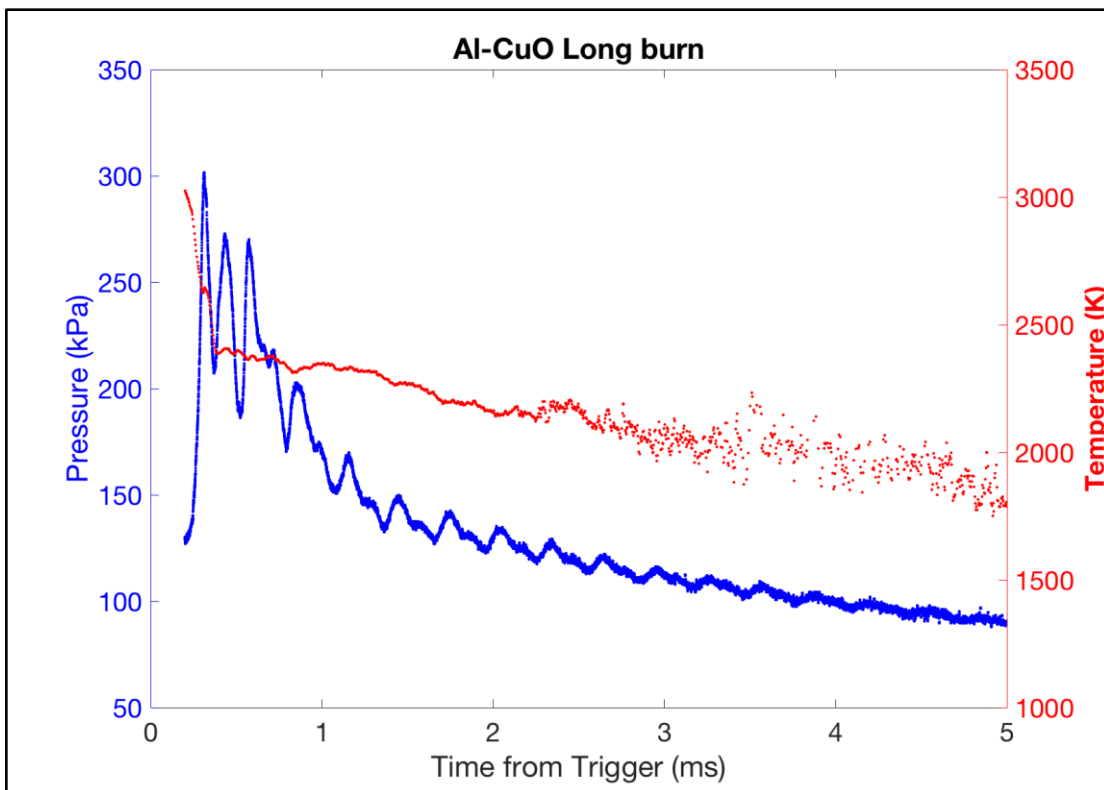


Figure 6-4: Temperature measurement of Al/CuO nanothermite in pressure cell over extended durations measured without ND2 filter. The initial parts of the reaction is truncated due to saturated emission on the MC-PMT

Curiously, the integrated intensity (as shown in section 5-7 of Figure 6-3a) is observed to decline gradually after reaching the maximum, although the recorded temperature is still observed to increase/plateau. A possible explanation for this observation could be that the flame cloud could have disintegrated into individual

emitters which subsequently attenuate the net emission from the reaction due to the reduction in the emission area. Since the lens assembly is focused at the inner edge of the cell, and given that the temperature is seen to rise, I believe the spectrometer is observing the combustion of such individual emitters which could be sintered reactants scattered by the initial pressure pulse.

6.3.2 Al/Fe₂O₃ and Al/WO₃ nanothermite tests in Pressure cell

The principal focus of this work is to infer the role of temperature in the tunable reactivity of nanothermites, specifically for Al/Fe₂O₃ nanocomposite doped systematically with WO₃ nanoparticles. The pressure-temperature profiles for select samples are shown in Figure 6-5, and quantitative comparison for the full suite of samples are shown in Figure 6-6. As can be seen in Figure 6-5a for the Al/Fe₂O₃ sample, the pressure profile is characterized by slow buildup which achieves the peak pressure ~10ms after ignition. Such poor performance is again highlighted in Figure 6-6c, where the average Full Width Half-Max (FWHM) burn time is plotted against the composition, with Al/Fe₂O₃ being the slowest burning composite at 5.5 ms. With incremental addition of WO₃, the performance of the composite improves significantly, exemplified by the faster pressure buildup (Figure 6-5), higher pressurization rate (Figure 6-6b), and much shorter burn time, as shown in Figure 6-6c. With the increase of WO₃ concentration in the composite, the pressure and pressurization rates are observed to increase till it reaches an optimum value at ~70%

WO₃ (Figure 6-6b) beyond which any addition of WO₃ resulted in the detriment of the reactivity. For Al/WO₃, the observed pressure buildup was slower than that of the composites with mixed oxides although it is still faster than Al/Fe₂O₃, suggestive of higher reactivity as demonstrated by its shorter burn time compared to Al/Fe₂O₃ (2.5 ms vs 5.5 ms). The lack of any gas phase products for the Al/WO₃ reaction[11] explains its poor pressure metrics among all the composites. The qualitative difference between the respective plots would be analyzed in more detail from a mechanistic standpoint in a later section.

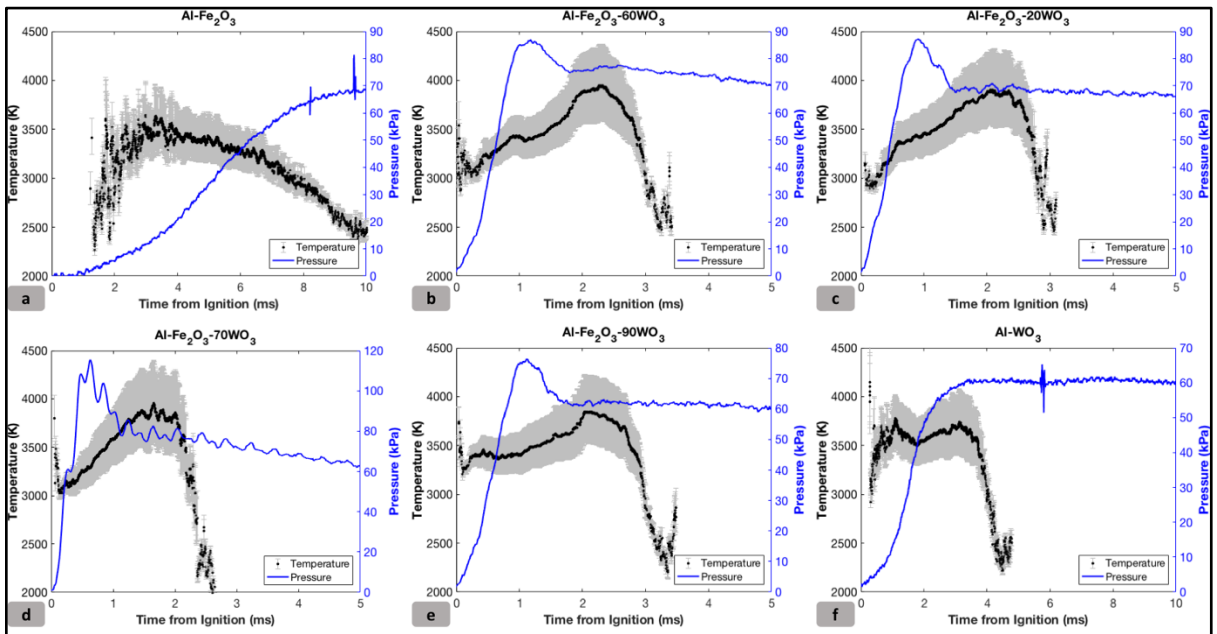


Figure 6-5: Temporal Pressure-Temperature profiles for a. Al-Fe₂O₃, b. Al-Fe₂O₃-20WO₃, c. Al-Fe₂O₃-60WO₃, d. Al-Fe₂O₃-70WO₃, e. Al-Fe₂O₃-90WO₃, f. Al-WO₃ in pressure cell. The grey region is the error bound of the measurement.

The quantitative metrics for the full suite of samples tested in this study, averaged over 3 runs, is presented in Figure 6-6. Theoretical estimates of the

temperature and pressure under constant volume conditions, calculated using NASA CEA, are also presented for comparison. Figure 6-6a highlights the effect of composition on temperature thresholded to a standard error of ± 400 K, as it was the maximum error allowed in these measurements. With the addition of minimal amounts of WO_3 the average temperatures are seen to rise and plateau at around 3400K which corresponds to the adiabatic flame temperature of Al/WO_3 (3447 K),[40] and is slightly higher than the temperature for full Fe_2O_3 decomposition. The peak temperatures, on the other hand, is seen to rise gradually with added WO_3 until it reaches a local maximum at 70% WO_3 , although the high errors associated with peak temperatures preclude further discussion. Figure 6-6c compares the average FWHM burn times for all composites, with $\text{Al}/\text{Fe}_2\text{O}_3$ not surprisingly being the slowest (~ 5.5 ms) and Al/CuO the fastest (~ 150 μs). The other composites show a steady burn time of ~ 2 ms. $\text{Al}/\text{Fe}_2\text{O}_3/70\text{WO}_3$ had the shortest burn time in the pressure cell tests, although it is difficult to distinguish on the logarithmic scale. The error bars associated with the burn time measurements were, in some cases, smaller than the marker themselves. Al/CuO pressure data is not shown in Figure 6-6b owing to its large magnitude ($P_{max} = 572$ kPa and Press. Rate = 41 kPa/ μs) which skews the pressure profile, inhibiting visual comparison.

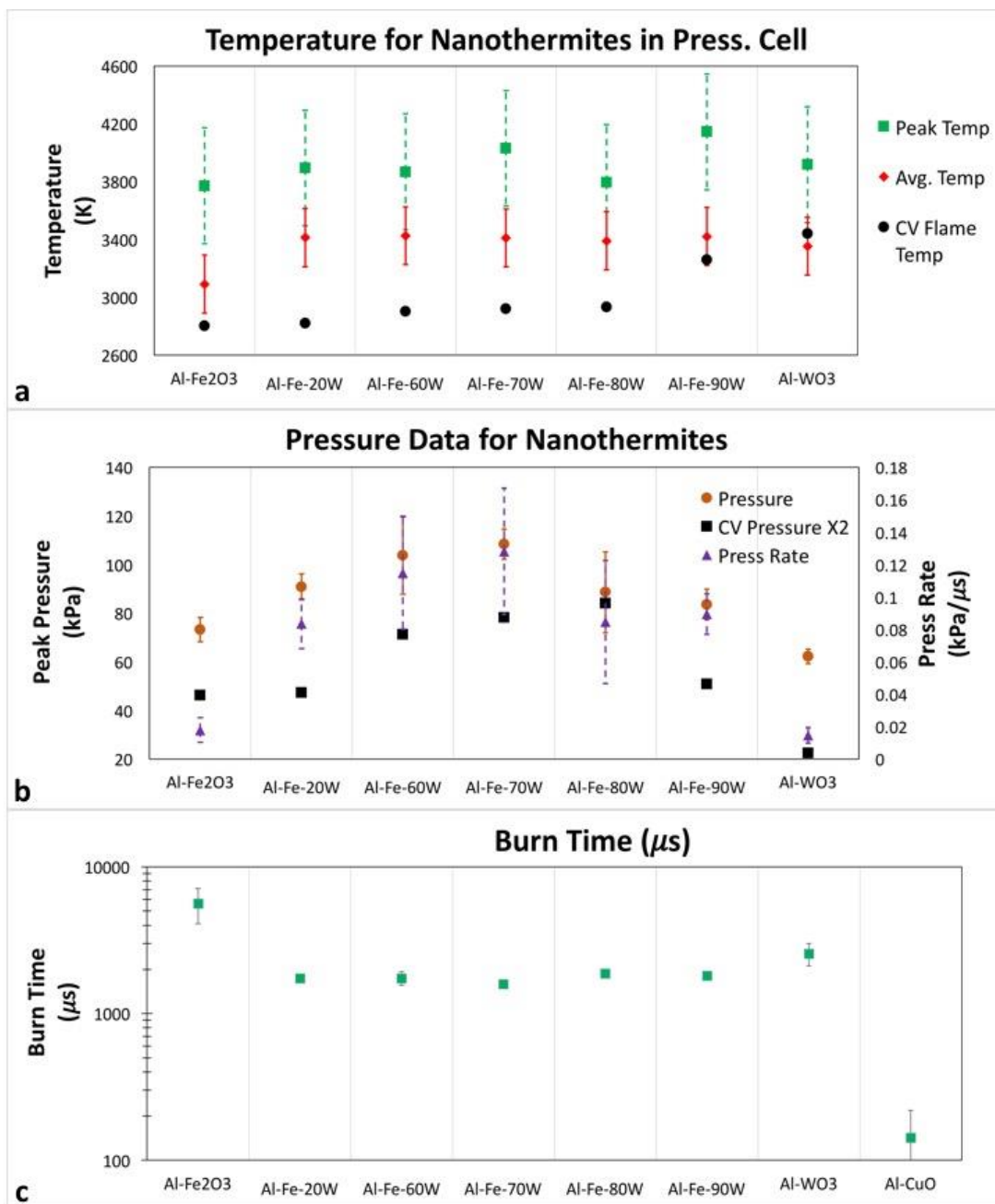


Figure 6-6: Pressure-Temperature profiles for a. Effect of composition on temperature, b. Effect of composition on pressure and pressurization rate (Al/CuO: $P_{\max} = 572$ kPa and Press. Rate = 41 kPa/ μ s) and c. Effect of composition on Burn time.

6.3.3 Qualitative Observation of Reaction Dynamics with Camera

High speed color camera pyrometry videos enabled the identification of the different mechanisms of the Al/Fe₂O₃, the Al/Fe₂O₃/xWO₃ and Al/WO₃ reactions due to distinct features that appeared throughout the reaction. For the Al/Fe₂O₃ mixture, the gas release from the thermite mixture produced a cloud of reacted material and little unreacted material was left as it propagated down the wire (Figure 6-7a). The Al/Fe₂O₃ reaction is believed to be limited by the oxidizer decomposition, and is characterized by the slow reaction of the aluminum with gas phase oxygen released from the oxidizer, as exemplified by its longer burn durations and slow rising pressure profile.[11,40] In comparison, the Al/WO₃ reaction is expected to occur in the condensed phase due to the lack of oxygen release from WO₃. [11] Upon observing the videos of the Al/WO₃ reaction, the condensed phase nature of this reaction was evident by the absence of a reactive cloud, as the reaction seemingly occurred on the wire and continued on to the ends after melting the wire (Figure 6-7c). In line with the observations from the pressure cell, the Al/Fe₂O₃/70% WO₃ sample (Figure 6-7b) shows both higher peak temperature, and a larger combustion zone which I attribute to higher gas release. The use of a color camera to measure temperature allows for the direct observation of the disaggregating role that the oxidizer gas release plays during reaction since the reaction cloud exhibits higher temperatures than the material remaining on the wire.

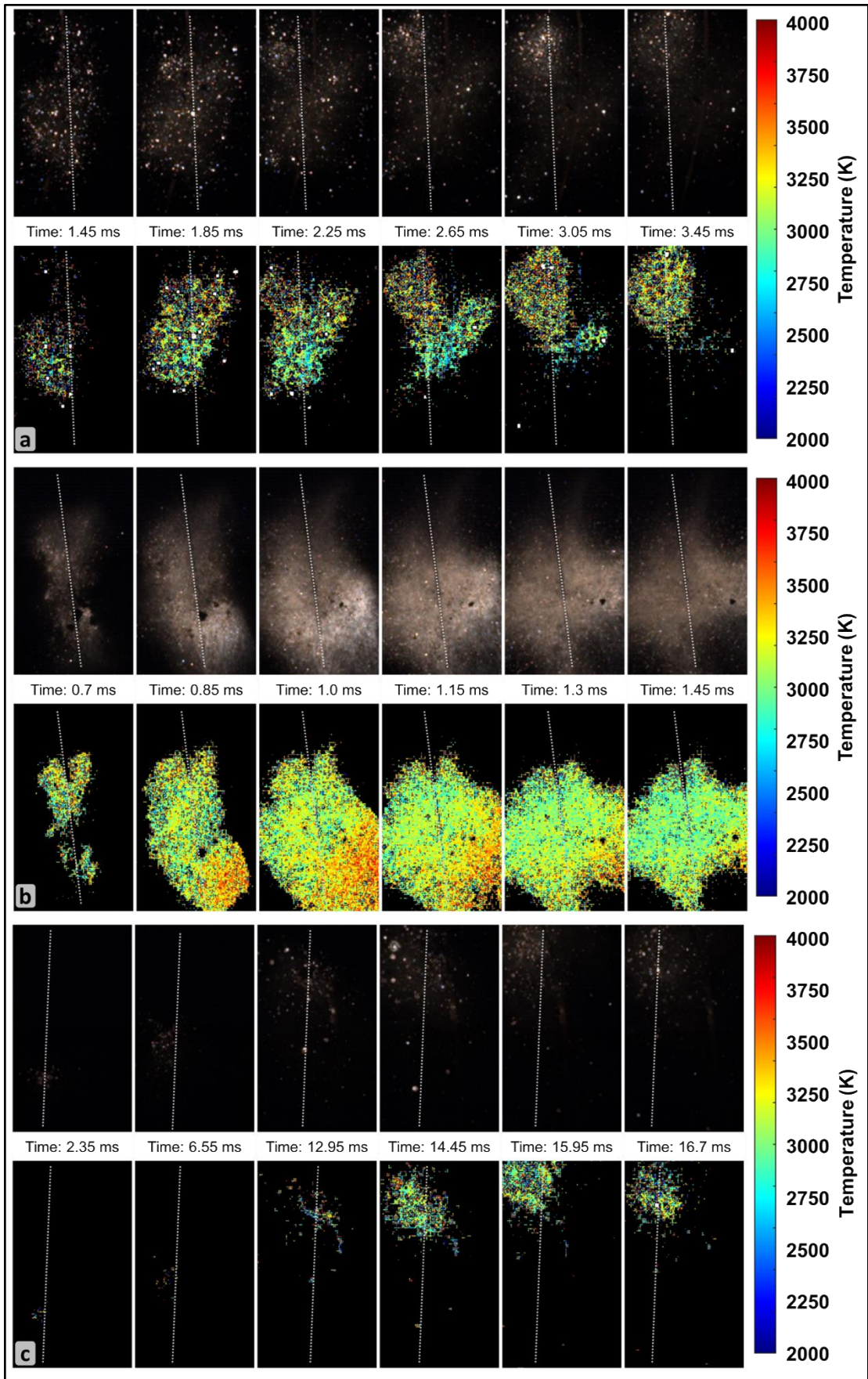


Figure 6-7: High speed pyrometry frames of a. Al/Fe₂O₃, b. Al/Fe₂O₃/70% WO₃ and c. Al/WO₃ samples ignited on a hot wire at 1 atm. argon environment highlighting the gas production and enhanced reaction. In the Al/WO₃ case, the reaction propagated up the wire over a longer time scale due to lack of gas release from the oxidizer. In each figure, the top image is a gain-adjusted raw image and the bottom image is the 2-D temperature map.

6.4 Mechanism

A large body of previous work has been devoted to the mechanistic examination of Al/CuO system and is only briefly described here. It has been shown through high resolution microscopy that the Al/CuO system initiates in the condensed phase[99] where the reactants are postulated to undergo reactive sintering. Based on the observed pressure, emission and temperature profile, I propose the following mechanism for the Al/CuO system. Upon ignition, the temperature observed in Figure 6-3b is close to the adiabatic flame temperature (T_{ad}) of Al/CuO (2837 K)[40] and rises as the pressure wave unloads (region 1-2), with gas phase reactions between aluminum and oxygen, from the decomposition of CuO, dominating the combustion (region 1-2). Due to this spike in temperature, the unreacted copper oxide would undergo endothermic decomposition (as highlighted by the reduction in temperature in region 2-3), producing gaseous oxygen and a rise in pressure. This promotes advection which ignites the bulk sample and continues to burn in the region 3-4, where temperatures measured are close to the T_{ad} . The gas generation and unreacted material ignition is a symbiotic process and leads to bulk overall combustion as exemplified by the sharp increase in the emission intensity in the region 3-4.

I believe that the dominant reaction pathway in this region is in the condensed phase through reactive sintering[42,135] as evidenced by large reaction products that are known to form.[42] The rising temperature in region 4-6 results from oxygen released from the decomposition of CuO reacting with Al. The most clear evidence for this is that the observed temperatures at ~3500 K exceeds the adiabatic flame temperature of Al/CuO and thus implies that aluminum, which has sintered into super-micron particles, is behaving like micron aluminum burning in oxygen.[176] Region 6-7 is characterized by a temperature plateau at ~ 3500 K which could be attributed to the combustion of such aggregates, similar to that observed in extended length burn tube tests.[41] The maximum achievable spectral resolution of this instrument is 1 nm/channel (using a 1800l/mm grating) which is low for resolving the AlO emission band, a common signature of gas phase combustion of aluminum particles, and hence was not adopted in this study.[25]

In comparison to Al/CuO, the Al/Fe₂O₃ reaction is limited by the slow decomposition of the iron oxide into gas phase oxygen, which leads to prolonged emission traces and slow pressurization rates. The Al/WO₃ reaction is expected to occur entirely in the condensed phase as the WO₃ produces no gas phase decomposition products. Such qualitative differences can be readily seen in Figure 6-5 upon initiation, the reaction temperature is ~2400K and has a significant delay of ~1.5ms. The temperature is seen to rise gradually over ~2ms, reaching a peak at ~3500K, and dropping gradually thereafter for over 6 ms. The burn time observed for

Al/Fe₂O₃ was the longest of the samples studied with average FWHM burn time being approx. 6 ms, as shown in Figure 6-6c. Gaseous oxygen is initially released by Fe₂O₃ at approximately 1400K[40] and the combustion of the nanothermite is believed to be limited by the oxidizer decomposition, since complete decomposition to Fe occurs at (~ 3300K).[40]

With addition of WO₃, the initial reaction temperature of the sample rises by approximately 500K to ~3000K and is observed for all compositions containing WO₃. I believe the similarities in temperature is due to the aluminum initiating with WO₃, as it has a lower ignition temperature (1030K vs. 1410K),[11] leading to a higher ‘initiation spot’ temperature comparable with that of pure Al/WO₃. This initial enhancement in temperature could significantly improve the gasification of Fe₂O₃, which could help in disaggregating the sample as highlighted by the increase in pressure and pressurization rate in Figure 6-6b. Although the initial temperatures are higher, the concentration of WO₃ in the blend could be too low to influence the entire composite, hence only limited improvement in pressure was noticed. With further addition of WO₃, the temperature does not change significantly, although the pressure metrics show improvement. The average temperatures in Figure 6-6a are observed to plateau at ~3400K, close to the adiabatic flame temperature of Al/WO₃ (3447K) and above the complete decomposition point, shown thermodynamically, of Fe₂O₃. [40]

Comparing the measured temperatures to that of the theoretical estimates, it is observed that the predicted temperature profile rises slowly with incremental addition

of WO_3 until a sharp rise at $\text{AlFe}_2\text{O}_3/90\text{WO}_3$, as opposed to the measured data which more or less plateaus at $\sim 3400\text{ K}$ with addition of WO_3 . The observed temperatures were also higher than the theoretical estimates as well as the average temperatures for $\text{Al/Fe}_2\text{O}_3$ ($\sim 3100\text{ K}$) suggesting heightened oxidizer decomposition. The lack of direct correlation between theoretical and measured values highlight the competing dynamics of the condensed phase reaction between Al-WO_3 and gas phase reaction between $\text{Al-Fe}_2\text{O}_3$. Recent work from our group[165] suggested that nanothermite reactions with a larger amount of gas release tend toward a more complete reaction due to disaggregation of the material, preventing active reactants from coalescing. The enhanced gas release observed in this work for the $\text{Al/Fe}_2\text{O}_3/x\text{WO}_3$ composite would suggest that the composite is achieving a higher extent of reaction, resulting in shorter combustion time. Thus, the enhanced gas release could create a feedback loop where the composite disaggregation and convective heat transfer is promoted thereby increasing reactivity, as pictorially represented in Figure 6-8.

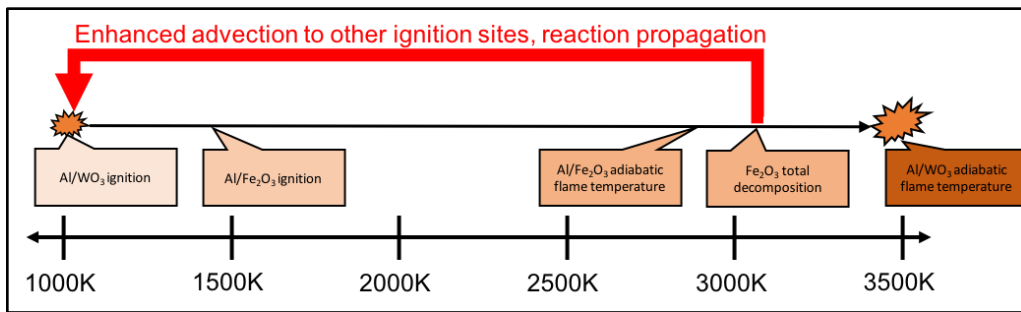


Figure 6-8: Proposed reaction mechanism.

As suggested in Figure 6-8, ignition of Al/WO_3 (which occurs at 1030 K) brings the mixture to a temperature at which oxygen release in Fe_2O_3 is initially

observed (1400K).[11] The subsequent disaggregation of material due to oxygen release then contributes to a more complete combustion of the Al/WO₃ that approaches the adiabatic flame temperature of the mixture at 3447K, at which point the temperature exceeds the total decomposition point of Fe₂O₃[40]. The Fe₂O₃ decomposition into its suboxides (Fe₃O₄, FeO, Fe)[35] then releases more gaseous oxygen, leading to further disaggregation of material and propagation of the cycle. This is exemplified by the color camera pyrometry videos in Figure 6-7, where the Al/Fe₂O₃/70% WO₃ composites exhibit a larger flame cloud with a higher temperature. Moreover, the reaction is observed to occur away from the wire highlighting the disaggregation effects of gas release.

As the temperatures exceeds full decomposition temperatures of Fe₂O₃ (~3300K),[40] a cloud of oxygen gas could be generated in which any residual aluminum, which could have coalesced into larger particle sizes, could now react. The high temperatures, observed for the doped composites approaching ~3800K, similar to that of micron aluminum combustion in oxygen,[176] could be suggestive of such a mechanism. The resulting figure of temperature and pressure as a function of oxidizer composition (Figure 6-6) therefore illustrates a complex interplay between WO₃ content (which elevates the temperature) and Fe₂O₃ (which elevates pressure through release of gaseous oxygen). This trend continues until a tipping point near 80% WO₃, where the disaggregation through oxygen release from the Al/Fe₂O₃ reaction is not able to influence the bulk of the composite, owing to Fe₂O₃ now being

the minor component, suggesting a deviation from the optimal composition, in spite of the temperature profile showing similar features. When the composite is entirely WO_3 , the high temperature regions ($\sim 3800\text{K}$), observed for the doped composites, are no longer observed and the temperature is close to the adiabatic flame temperature of the Al/WO_3 reaction (3447K).[40]

6.5 Conclusions

The reactivity of metastable intermolecular composites were investigated through high speed spectrometry, pressure measurements, and color camera pyrometry, culminating in a proposed reaction mechanism for tunable thermite reaction. Seven mixtures of $\text{Al}/\text{Fe}_2\text{O}_3$ were doped with varying amounts of WO_3 to manipulate the primary reaction mechanism from gas-generating (Fe_2O_3) to condensed-phase (WO_3). While pressure, pressurization rate and burn time correlate with mixture fraction, temperature was relatively insensitive once a threshold addition of WO_3 was achieved. Pyrometry videos capture the interplay of reaction mechanisms of the doped thermite mixtures as evidenced by an enlarged reactive cloud size and faster reaction times with increasing amounts of WO_3 up to the 70% mark. It is proposed that initiation by Al/WO_3 reactions leads to a greater degree of reduction of Fe_2O_3 . The high oxygen release also results in flame temperatures in excess of the $\text{Al}/\text{Fe}_2\text{O}_3$ adiabatic flame temperature and reflects the burning of Al in an oxygen environment. The relative interplay between condensed and gas phase combustion

suggests that performance of nanoenergetic materials can be tuned for specific applications by means of complementary reaction mechanisms.

6.6 Acknowledgements

The findings presented in this work were reproduced with permission from: Jacob, R. J.; Kline, D. J.; Zachariah, M. R. High Speed 2-Dimensional Temperature Measurements of Nanothermite Composites: Probing Thermal vs. Gas Generation Effects. *J. Appl. Phys.* **2018**, *123* (11), 115902.[177]

Chapter 7 Quantifying the enhanced combustion characteristics of electrospray assembled aluminum mesoparticles

Summary

Aluminum particles have been extensively used to enhance the combustion characteristics of propellant, pyrotechnic and explosive formulations. Unfortunately, the relatively high ignition temperatures of aluminum result in severe sintering prior to combustion, leading to early loss of nanostructure and thus a smaller power law exponent for size dependent burning than expected. One such scheme I explore, to defeat sintering, is to create low temperature gas-generation, which helps in breaking up the soft agglomerates before/during combustion. In this article, I characterize the combustion characteristics of electrospray assembled micron scale particles composed of commercial nano-aluminum (ALEX), bound in an energetic polymer matrix composed of nitrocellulose. The nitrocellulose not only acts as a binder for the nanoparticles but also as a dispersant owing to its dissociation at low temperatures (ca. 450K). Combustion characteristics were measured by direct injection of the electrospray assembled particles into the post flame region of a CH_4/O_2 diffusion flame. I find that the composite meso particles show an order of magnitude reduction in average burn times when compared to that of the commercial nano aluminum (ALEX), and are as fast as the smallest nanoparticle burn time. Scanning electron microscopy of quenched post-combustion particles clearly shows smaller sized

products in the combustion of electrospray generated composite particles when compared to ALEX powder. This latter point should also lead to a more complete reaction and certainly demonstrates that the concept of using a two-stage reacting system: one at low temperatures to generate gas to separate particles followed by the nominal oxidation reaction is at the least a strategy that is worthy of further exploration.

7.1 Introduction

Addition of reactive metals to energetic formulations have been extensively studied and practiced over the past five decades.[135,138,178] Aluminum owing to its low cost, availability, safety and higher energy density has been the focal point of this research. A large body of work has already been undertaken to gauge the benefits of the addition of aluminum particles to energetic formulations and the general consensus is that the addition of aluminum to propellant mixtures improves the combustion stability, energy density and impulse performance.[179] Although the benefits are unambiguous, practical systems have been unable to unlock the maximum potential of aluminum additives. Traditional propellant systems incorporate fine aluminum particles in the range of 10-100 μm , which are protected by an alumina shell (3–5 nm) with a substantially higher melting point (2350 K) compared to the aluminum core (933 K). Such a high melting shell delays the ignition until the temperature rises to the range of 1000 – 2300 K for particles in the transition

regime (10 -100 μm) and above 2350 K for larger aluminum particles,[180] which correspond to the melting of the shell. Such a delay results in agglomerate formation within the pockets of the oxidizer grains in the propellant and ultimately much larger aluminum droplets, which burn farther from the propellant surface thus reducing the heat feedback and performance. In addition, such large agglomerates increase the slag weight in the combustion products leading to two-phase flow losses.

Much effort has been expended at the mechanistic understanding of the burning of aluminum particles.[36,181,182] Large aluminum particles ($>200 \mu\text{m}$) are observed to burn in a diffusion-limited regime, following a $D^{1.8}$ dependence. The slightly lower exponent than the expected D^2 is attributed to the presence of oxide caps on the burning particle and violent fragmentation of the same towards the end of the burn. For finer particles, the data is much more scattered and the conclusions consequently more ambiguous. The diameter power dependence for fine particles in the range of 10-14 μm vary from 0.3-1,[183] whereas for ultra-fine particles (nano scale), recent results report a diameter dependency of ~ 0.3 .[161] Such scatter makes it impossible to model the behavior of a burning aluminum particle across a wide size range[96,184] and raises questions regarding the mechanistic features that would lead to such low power dependence. Several postulates have been proposed for resolving this conflict. Allen and co-workers[109] have suggested that the thermal accommodation coefficient at high temperatures is lower than the assumed value of unity implying that burning nanoparticles might be hotter than expected. This

possibility enhances the prospects posited[34] that nanoparticles which are normally in the form of fractal aggregates sinter rapidly, resulting in a larger effective particle size. Recent MD simulations[19,118] of nanoscale energetics provided a theoretical validation of the rapid sintering concept. The authors argued that upon heating, strong electrical fields generated within the particles lead to enhanced migration of aluminum ions into the protective shell resulting in the transformation of the shell into an aluminum rich, low melting alloy. This transformation led to enhanced coalescence at lower temperatures than the melting point of the protective alumina shell. The authors concluded that for a 100 particle aggregate of 50 nm diameter primaries, the effective coalescence time is ~ 50 ns which is orders of magnitude smaller than the characteristic reaction time (~ 10 μ s). More recently, experimental validation for this theoretical postulate was presented by Egan et. al,[100] where the aggregates of aluminum nanoparticles were rapidly heated within a Dynamic Transmission Electron Microscope (DTEM) which provided high temporal and spatial resolution of the sintering event. Based on their results, sintering of aluminum nanoparticle aggregates were found to be complete on a time scale of <50 ns. Very recent work by our group on the combustion of size selected nano particles of Titanium and Zirconium suggests that once the effects of sintering are accounted for, the diameter dependence of the particle burn time approaches the $\sim D^1$ dependence suggesting that the combustion at the nanoscale is predominantly limited by heterogeneous reactions as expected[115,185] and that sintering must occur very

early in the reaction. What I may conclude is that despite the uncertainty in burning mechanisms, and the diminished power in the scaling law, there appears to be a preponderance of evidence that there is definitely an improvement in going to the nanoscale in terms of burn rate and ignition delay.

Despite the overall improvement in going to the nanoscale, the fact that the scaling law for burning has a low power dependence suggests that many of the advantages of small scale are not being completely exploited. Combating sintering of metal additives has been a focal point of several recent works owing to the benefits of shorter ignition delays resulting in enhanced heat feedback to the propellant surface and reduced two-phase flow losses.[186,187] Although the usage of nano aluminum does increase the burn rate of composite propellants, there are significant difficulties in processing the propellant formulation leading to less than optimal aluminum content, lower friction and impact thresholds and shorter shelf life. Another option, which could circumvent the disadvantages of nano scale material, would be to develop functionalized micron sized materials, which are modified such that they contribute to the reaction at a much faster time scale than the parent particle. This could be done by modifying the surface of conventional micron sized particles with halides,[188,189] which weakens the shell, or as discussed in this study, bottom up approaches may also be used to package nano-material into micron scale structures.[12,164] Recent studies in this direction use mechanical activation (Top down) by milling micron sized aluminum particles with gas generators (LDPE),

oxidizers (PTFE)[190–192] or with other metals such as Nickel[193] or Magnesium.[194]

Bottom up assembly offers clear advantages with a more direct control of assembly.[195,196] Recent work by our group in employing electro spray assembly/ synthesis has found interesting, and in some cases, unexpected benefits in producing energetic fibers and nanothermite composites.[197] In this work, I employ electro spray assembly to generate micron-sized particles (hereon meso particles) composed of nano-sized commercial aluminum powder (ALEX) assembled into a meso structure using nitrocellulose as a binder. The benefits of such architecture are multifold whereby in addition to creating a highly accessible, porous structure with a high surface area for reaction (nanoscale characteristic), the generated particles are bound together using an energetic binder, which has a low dissociation temperature. This leads to intra-particle outgassing at the early stages of particle heat up thereby reducing the sintering during combustion. In addition, the generated composite particles are micron sized which should offer processing and handling advantages of the micron scale. Previous works on such meso scale composites have shown interesting behavior such as lower ignition delay times, greater reactivity, and high fuel loading capabilities.[198] The basic concept behind this structure is that the addition of low temperature gas-generator (nitrocellulose) should promote primary particle separation and thus decrease sintering. The current work expands these results more quantitatively, gauging the reactivity of such meso particles by measuring

their burn time in a hot, oxidizing environment. Direct comparisons with that of the parent nanoparticles highlight the de-agglomeration effects of the meso particles.

7.2 *Experimental*

7.2.1 *Materials*

Commercial aluminum nano powder (ALEX) prepared via exploding wire technique was procured from Argonide Corp. The particles had a core-shelled structure and the primary particle sizes were 50 nm with an active aluminum content of 70 %, measured using Thermo Gravimetric Analysis (TGA). Collodion solution was procured from Sigma Aldrich and contained 4-8 wt.% nitrocellulose in an ethanol/diethyl ether mix. The solvent was evaporated off to get the polymer (NC), which was further cut to the required mass.

7.2.2 *Flat flame Diffusion Burner*

The burner setup is described in detail in Chapter 3.2.3. In the current study, the central tube carrying the aerosol was larger to avoid clogging, hence the temperature field above the burner is slightly different, as shown in Figure 7-1. The flat diffusion flame on the Hencken burner was fuel lean ($\phi \sim 0.3$) so as to keep oxygen as a major constituent in the post flame environment. As shown in Figure 7-1a, the particles are injected along the centerline of the burner directly into the products of the flat diffusion flame. The temperature of the oxidizing zone could be

varied by changing the reaction stoichiometry and was varied between 900K and 1500K as can be seen in Figure 7-1b. The major product compositions, predicted by constant enthalpy-pressure calculations in NASA CEA, for each of these flame conditions are outlined in Table 7-1. Temperature along the burner centerline was mapped using a B-type thermocouple (Omega) consisting of platinum rhodium alloy wires (Pt30Rh and Pt6Rh) with a 0.01 inch junction spot and is plotted in Figure 7-1b after correcting for radiation from the junction spot.[108] Three readings were recorded per position in the oxidizing zone and the average was taken to reduce the error associated with carbon deposition on the fine wire.

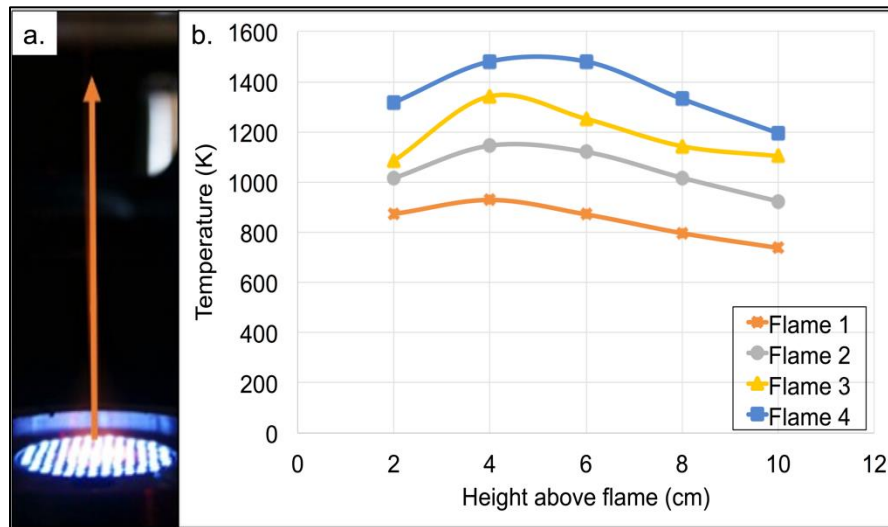


Figure 7-1: Multi element diffusion flat flame burner: a) Burner centerline along which particles are injected into the high temperature, oxidizing zone; b) Temperature profiles along the burner centerline for different flame stoichiometries.

Flame condition	Eq. Ratio (Tad, K)	Product fraction: O2	Product fraction: CO2	Product fraction: H2O	Product fraction: N2
Flame 1	0.21 (1770)	0.49	0.067	0.13	0.30
Flame 2	0.3 (2174)	0.42	0.091	0.18	0.29
Flame 3	0.33 (2212)	0.37	0.094	0.18	0.33
Flame 4	0.41 (2328)	0.29	0.101	0.20	0.38

Table 7-1: Oxidation zone properties for different flame stoichiometries.

7.2.3 Precursor Preparation for meso particles

The typical precursor preparation entailed weighing out 185.6 mg of aluminum nanopowder (containing 70% of active aluminum particles and pouring into 1.5ml of ethanol (99.8 %). The mixture is then ultra-sonicated for an hour to form a homogenous suspension. After ultra-sonication, 14.4 mg (for 10 wt. % NC case) of nitrocellulose was added into the system along with 0.5 ml of ether. The suspension was further magnetically stirred for 24 hours to form the final precursor for the electrospray synthesis. Two more precursors compositions were also considered containing 5 and 15 wt. % NC respectively so as to gauge the effect of nitrocellulose on the combustion characteristics. Subsequent TEM analysis of the meso particles did not show any discernable changes to the oxide shell of the nanoaluminum.

7.2.4 Electrospray Setup and Aerosolization

After stirring for 24 hours, the precursor was electrosprayed through 23-gauge nozzle (McMaster, I.D. 0.017”) connected to a high voltage source at (+) 10 kV to create the electric field required to drive the electrospray process (Figure 7-2). The

liquid flow rate was controlled with a syringe pump at a feed rate of 4.5 ml/hr (7.5 mg/min of meso particles). The feed rate and the voltage were empirically selected to provide a stable Taylor cone for droplet generation. In our previous works the mesoparticles were deposited on a substrate where macroscopic harvesting enabled powder sample combustion studies.[164] However for evaluating single mesoparticle combustion and its comparison with nanoaluminum, it was necessary to inject the electropray stream of mesoparticles directly into the burner. In order to do so, the needle, connected to the high voltage supply, was housed within a chamber with a grounded outlet so as to generate the electric field required to drive the electropray. The length of the chamber was designed so as to provide sufficient residence time for solvent evaporation in the generated droplets (~ 15 s in the current setup). Sheath airflow of 1.5 lpm was used as carrier gas to aerosolize the generated droplets and carry them to the combustion zone. A polonium source was incorporated within the chamber, as depicted in Figure 7-2, to bring the highly charged droplets to Boltzmann equilibrium charge distribution so as to reduce the losses during transit within the chamber and tubes.

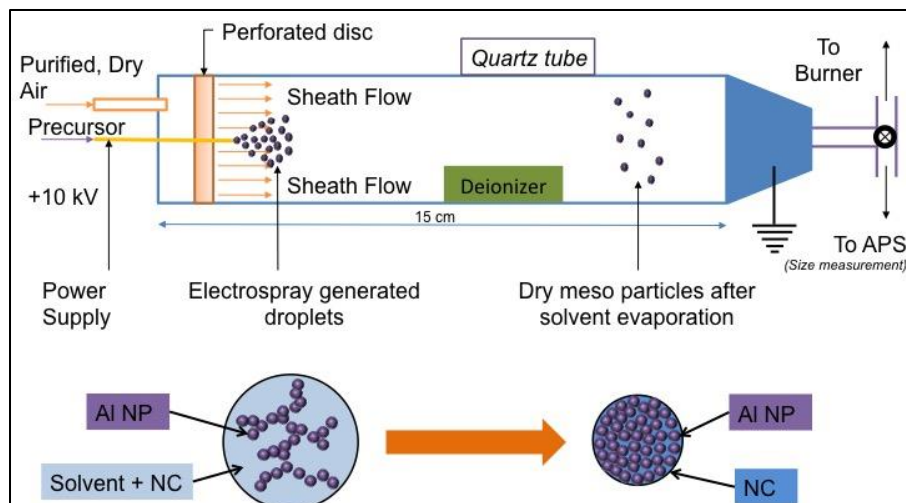


Figure 7-2: Electro spray generated meso particle aerosolizer.

7.2.5 Nano particle aerosolizer

The meso particles are a structural assembly composed of commercial nano particles as primaries. So, to gauge any enhancement, a direct comparison of the combustion characteristics needs to be made between the meso particles and the commercial nano particles. In order to do so, a powder aerosol generator was built as shown in Figure 7-3a.

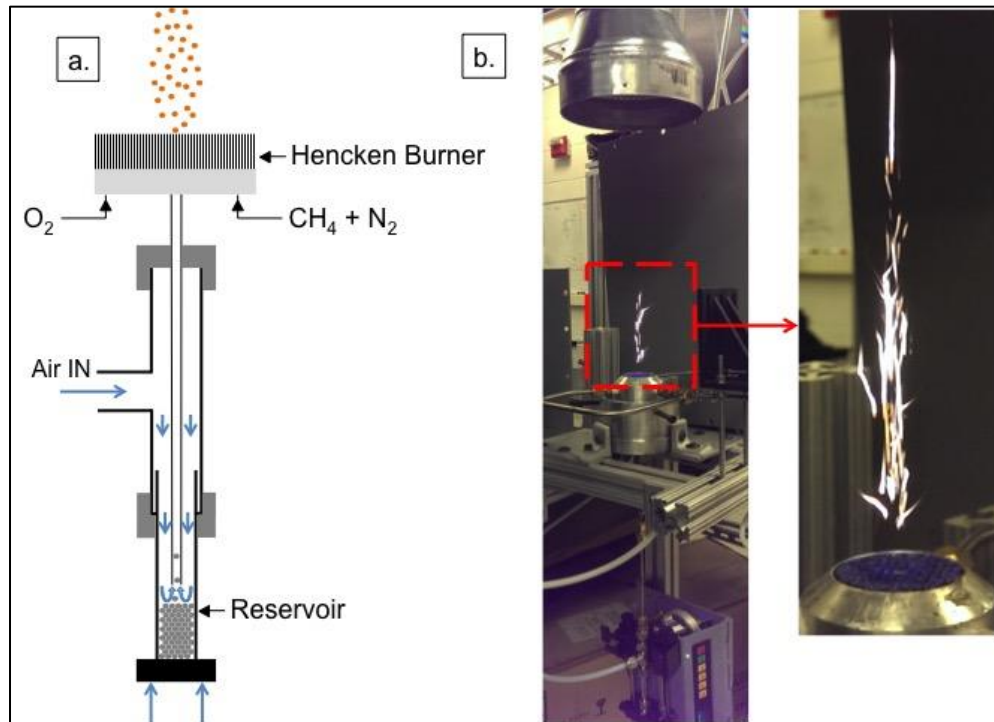


Figure 7-3: Experimental setup: a) nanopowder aerosolizer; b) Experimental run showing the observed streaks for nano aluminum powders.

The design for the feeder was inspired from the work on coal combustion by Quann et. al.[199] The feeder consisted of a cylindrical powder reservoir (0.18” ID x 2” length), which was mounted upon a screw feeder connected to a stepper motor. 100 mg of aluminum nanopowder was weighed and vigorously shaken using a vortex mixer to break up large agglomerates before adding into the reservoir. The sheath air (1.5 lpm) entrains the particles from the upper surface of the powder and subsequently enters a 1/8” tube which delivers it into the high temperature oxidizing environment. Adjusting the speed of the stepper motor allowed the control of the powder feed rate and was set at 5 mg/min, which offered the steadiest burn at 1.5 lpm.

7.2.6 Particle Size Distribution, High-speed videography and Electron Microscopy

The size distribution of the aerosol before feeding into the burner was measured using an Aerodynamic Particle Sizer Spectrometer (TSI model 3321). The spectrometer uses scattered light from the particles in the aerosol and has an operation range of 0.5 – 20 μm . Combustion of the particles was observed using a Phantom high-speed camera (V12.1) focused directly at the burner centerline. Owing to the extremely small sizes of the particles being studied, I found it necessary to employ a macro lens (Nikon, 105 mm) to get the best resolution while tracking the burning particles. The frame rate used was 10000-13000 fps at an exposure of 100-77 μs respectively an aperture of f/2.4. The burn time was calculated by tracking individual particles frame to frame so that the total burn time could be obtained by taking the product of the number of frames and the interval between the frames. The combustion products were quench collected onto metallic stubs and were subsequently analyzed in a Scanning Electron Microscope (Hitachi SU-70 SEM) for final product characterization.

7.3 Results

7.3.1 Morphology of Commercial Aluminum nano particles

Commercial aluminum nanopowder is composed of primary particles with a mean diameter of 50 nm. Although the individual particles have a nanoscale dimension, the powder is heavily agglomerated owing to weak Van-der Waals

interactions, which leads to characteristically larger agglomerates. A SEM image of the nanopowder is shown in Figure 7-4a, which shows an agglomerate composed of fine nanoparticles as primaries. The inset shows a high magnification TEM image of the 50 nm primary particles within the agglomerate. When the powder is aerosolized, the generated aerosol would contain such agglomerates rather than individual primary particles as exemplified by Figure 7-4b, which shows the size distribution of the aerosol that is generated using the commercial aluminum powder. The lower detection limit of the instrument was limited to 0.5 μm and hence the complete size distribution down to the nanoscale could not be determined. Even with this limitation, it can be concluded that the commercial powder contains a very wide size distribution with at least two peaks: one at the submicron range and other at approx. 2-3 μm .

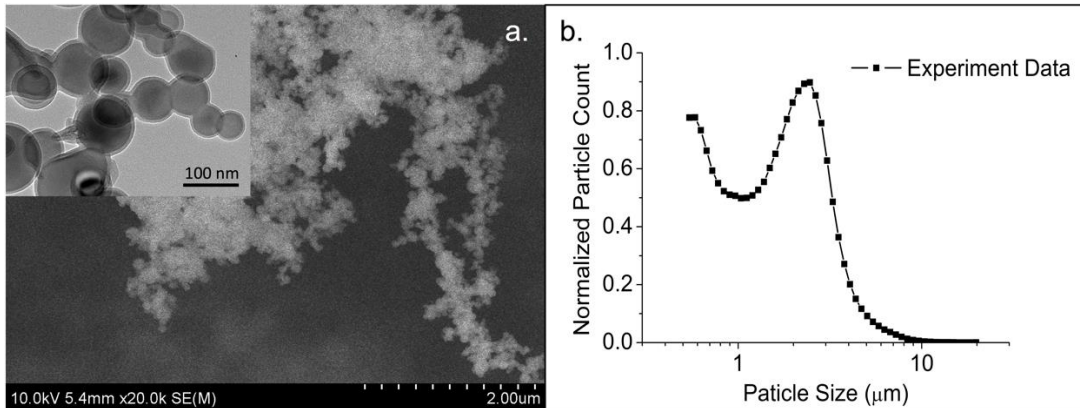


Figure 7-4: Morphology and size distribution of commercial aluminum nanopowder: a) nanopowder agglomerate with high magnification TEM image (inset); b) Size distribution of the aerosolized nanoaluminum powder.

7.3.2 *Morphology of Electrospray generated meso particles*

Electrospray generation is a simple one step process in which the liquid precursor is subjected to an electro-hydrodynamic electrical stress, which leads to its breakup into small droplets. Such disintegration is contingent upon the applied electrical stress overcoming the surface tension and viscous stress that try to maintain the integrity of the jet. Depending on the competition between the various stresses, different spraying modes can be produced varying from simple dripping to multiple cone spraying.[200] In this work I employed the cone jet spraying mode owing to the monodisperse nature of the droplets that are generated.[201] The choice of solvent has a significant impact on the structure of the generated particles. The electrospray process generates droplets containing the precursor solution from which the solvent subsequently evaporates leading to the formation of composite meso structures. As outlined in a recent review by Xie et al.,[200] solvents with low vapor pressure have longer evaporation times and therefore lead to particles that have smoother surface morphologies whereas, solvents with high vapor pressure have higher evaporation rates which leads to the formation of particles that exhibit highly porous or textured surface morphologies owing to the lack of rearrangement time for the polymer chains within the droplets. Our objective was to create meso structures that demonstrated a significantly high surface area, on the same order as that of nanoparticles, but packaged into a micron scale composite. Hence several volatile solvents such as ethanol-ether (3:1), acetone and DMF were tested for the electrospray generation.

The particles generated using ethanol ether mix (3:1) demonstrated a highly spherical structure (Figure 7-5a) when compared to the other solvents used (Figure 7-6). A closer look at the individual particles for the aforementioned case shows a highly textured surface as shown in the inset of Figure 7-5a. The key advantage of such a ground up synthesis is that the generated micron sized particles possess approximately the same specific surface area as the primaries comprising the mesoparticles. This implies that the whole mesoparticle structure has the same effective reaction surface area as the nanoparticles, as is also evidenced in the cross-sectional SEM images in ref. [12]. In Figure 7-5b I present the measured size distribution of the electrospray generated nanoparticles, along with a log-normal fit. The resulting size distribution, with a mean size of 1.6 μm , is quite narrow with a standard deviation of 0.37. This is one of the main advantages of using electrospray technique as it generates a near monodisperse aerosol of particles. For comparison I also plot the corresponding self-preserving size distribution (centered at the same peak size) that would be obtained if a normal spray were employed to generate the meso particles i.e., without an electric bias.[132]

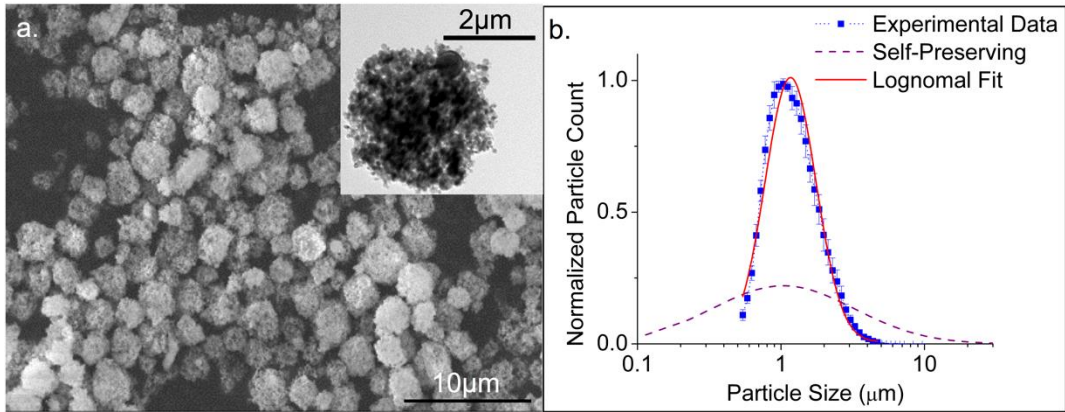


Figure 7-5: a) SEM image of electrospay assembled Al/NC (10 wt%) mesoparticles using ethanol/ether = 3:1 mixture as the solvent, with a high magnification TEM image of a single particle as inset; b) measured size distribution and comparison with self-preserving distribution.

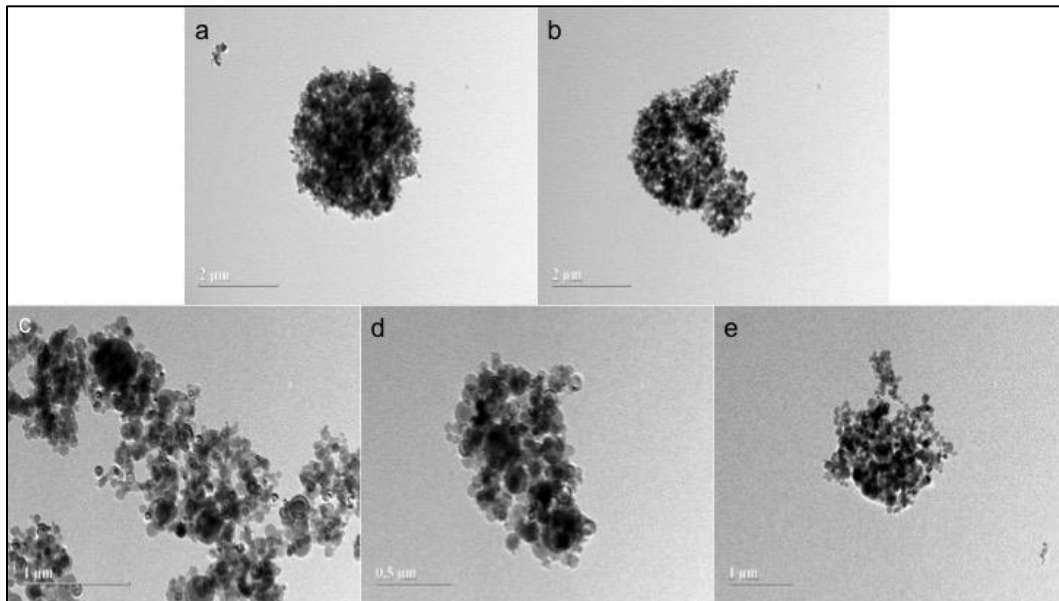


Figure 7-6: TEM images of the aluminum meso particles formed using different solvents for electrospay precursor: a) ethanol/ether=3:1 mixture; b) Acetone; c) DMF/ether=1:1 mixture; d) DMF/ether=1:2 mixture; e) DMF/ether=1:3 mixture.

7.3.3 Combustion characteristics of commercial NPs vs meso particles

7.3.3.1 Visual inspection of the combustion behavior

The representative images of the combustion of both sets of particles are shown in Figure 7-7. Figure 7-7a shows a long exposure (1/20 s) image of the combustion of nanoaluminum, whereas Figure 7-7b represents a similar event recorded at 10000 fps or 100 μ s exposure. As can be seen from Figure 7-7a, combustion of nanoaluminum particles shows a wide range of streak lengths (i.e. burn times). Some very short streaks occurring close to the aerosol outlet at the base of the burner probably represents the population of particles that belong to a much finer size scale, as their ignition temperatures and ignition delays are substantially lower than that of larger particles.[184] This latter point also is consistent with sintering, since one expects ignition to be characteristic of the primary particle size and not the size of the aggregate, unless sintering is rapid. In comparison, the electrospray assembled meso particles (Figure 7-7c,d) show a much smaller burn time and are also observed to ignite sooner than the bulk of nanoaluminum particles. Figure 7-7d represents an image taken at a longer exposure for the mesoparticles from which the narrow flame shape confirms the narrow range of burn times, certainly much narrower than that found for the nanoaluminum.

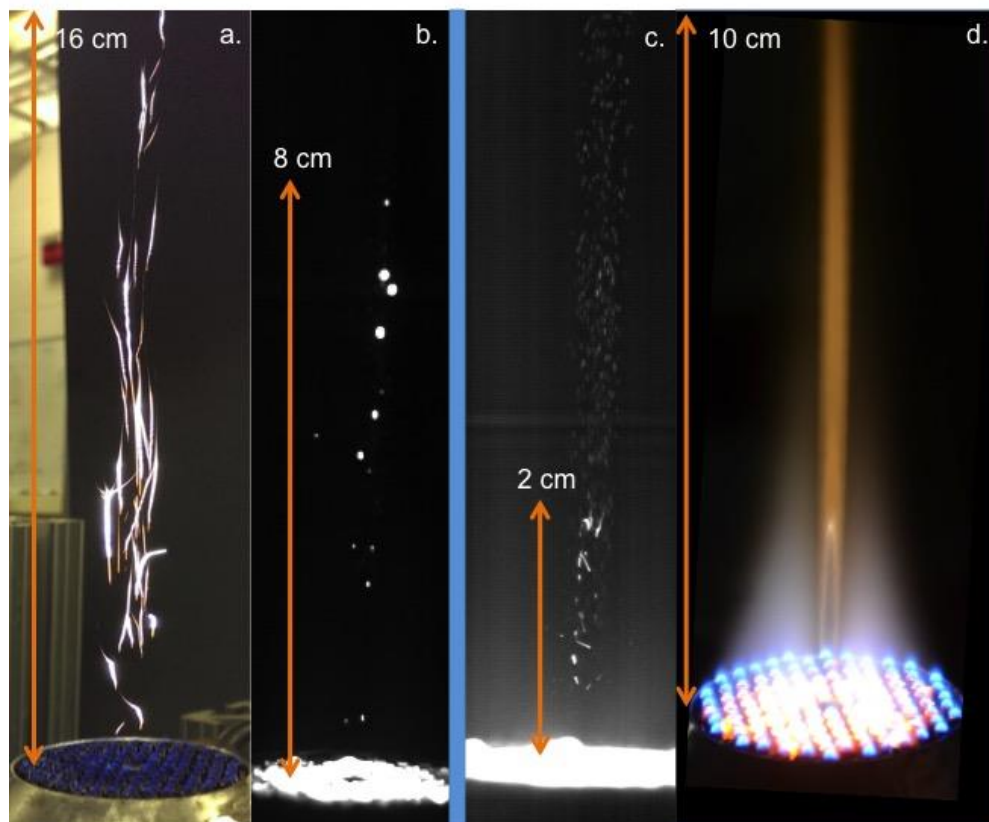


Figure 7-7: Combustion images: a) Nanoaluminum at exposure of 0.05 sec; b) nanoaluminum at exposure of 100 μ s; c) Aluminum meso particles at exposure of 83 μ s; d) Aluminum meso particle at exposure of 0.5 sec; images shown with individual scale bars owing to the differences in magnification during the separate experiments.

7.3.3.2 *Quantifying the burn time of nanoaluminum*

From the high-speed images, as shown in Figure 7-7b, individual particles were tracked throughout its burn and the frame number was used to quantify the burn time. Approximately 100 particles were tracked for each ambient temperature condition corresponding to those outlined in Table 7-1 and Figure 7-1. A histogram plot representing the distribution of burn times for nanoaluminum at Flame 3 condition is shown in Figure 7-8a. As can be seen, the burn time measurements are

spread over a wide range of values and have a standard deviation of 6000 μs , with an average of around 4500 μs . From the figure, it is also evident that the majority of burn time measurements are within the 1000 μs bin. Owing to the polydisperse nature of the powder resulting from agglomeration, particle burn times as large as 35000 μs were observed which skewed the average to a higher value. At this point I note that these measurements of average burn time of ALEX nanoparticles ($\sim 4500 \mu\text{s}$) are consistent with the values published by other researchers on the combustion of nanoaluminum at atmospheric conditions.[106,161] In order to sieve out the outliers, all the values exceeding 1000 μs were discarded from the burn time measurements and the results are plotted in Figure 7-8b. With this filtering, the measurements all lie within a narrow range of values with a standard deviation of 150 μs as opposed to 6000 μs when the entire range was considered. The average value of the selected data is found to be $\sim 570 \mu\text{s}$ and represents the shortest burn times observed for nanoaluminum combustion. Experimental findings by Bazyn et. al[39] have shown that nanoaluminum burn times are on the order of $\sim 500 \mu\text{s}$ in a shock tube at 8 atm pressure, 1400 K and 50% O_2 environment. Due to the shock induced breakup of the large agglomerates, the shock tube results should reflect the combustion of the smallest aggregates in the aerosol.

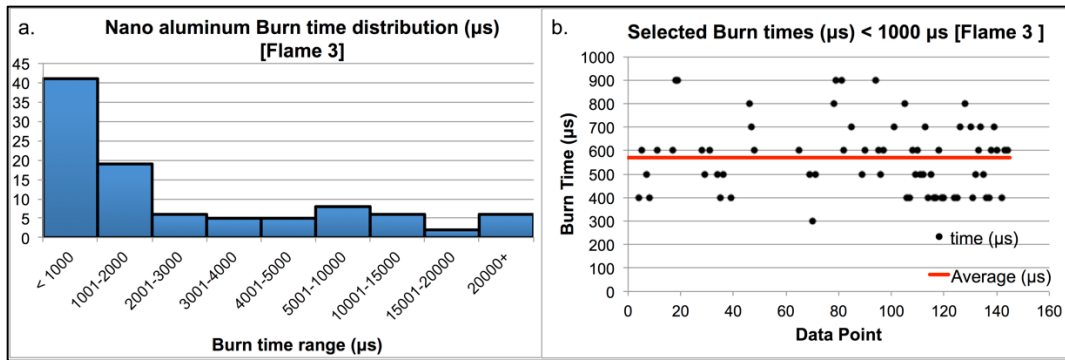


Figure 7-8: Burn time plots for nanoaluminum for Flame 3 condition: a) All data points for nanoaluminum; b) Selected burn times below 1000 μs for nanoaluminum. Horizontal line representing the average burn time.

Burn time measurements for nanoaluminum are summarized in Table 7-2 with each flame condition represented by an average temperature obtained from the profile. Also shown are the average burn time estimates based on considering only sub 1000 μs measurements. Although only about 100 burn time measurements were made for each flame condition, I believe the statistical confidence in this measurement, based on the standard deviations, is sufficient to corroborate the arguments regarding the combustion enhancement of the mesoparticles.

Flame condition ->	Flame 1 (841 K)	Flame 2 (1040 K)	Flame 3 (1200 K)	Flame 4 (1360 K)
Nano Al Burn time (μs) [All data points]	2700 μs	4740 μs	4440 μs	3460 μs
Nano Al Burn time (μs) [sub 1000 μs data]	750 μs	663 μs	570 μs	594 μs

Table 7-2: Average burn time measurements for commercial nano aluminum powder.

7.3.3.3 Quantifying the burn time of aluminum meso particles

A similar procedure as that of the commercial nanoparticles were undertaken for measuring the burn times for the meso particles, and the results (all burn time data

points) are plotted in Figure 7-9. In some cases, owing to the low intensity levels during combustion, I found it necessary to digitally enhance the gain of the video to clearly demarcate the beginning and end of combustion. As can be seen, the burn times of meso particles do not display the scatter that the commercial nanoparticles have. The average burn time measured for the Flame 3 condition was measured to be 365 μs , with a standard deviation of 62 μs . I attribute this narrow range of burn times as a direct consequence of the highly monodisperse nature of the meso particles.

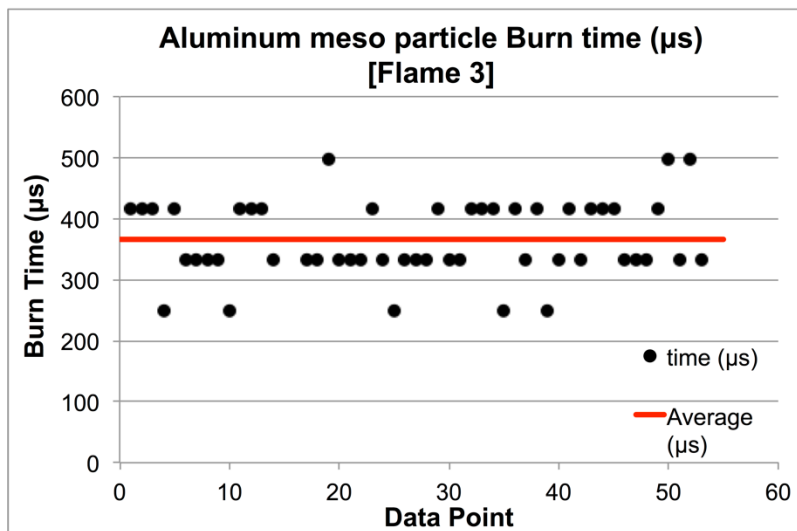


Figure 7-9: Burn time scatter plot for aluminum meso particles in Flame 3. Horizontal line representing the average burn time.

Burn times and standard deviations measured for meso particle combustion in different ambient temperatures are shown in Table 7-3. Similar measurements were also made for meso particles made from varying percentages of nitrocellulose (5% and 15% wt. NC) loading in the precursor and are also shown in Table 7-3. As can be seen, the percentage of nitrocellulose in the composite has little effect on the burn

time. In general, I see smaller burn times than the nanoparticles (compare with Table 7-2), the implications of which will be discussed later in the paper.

Flame condition ->	Flame 1 (841 K)	Flame 2 (1040 K)	Flame 3 (1200 K)	Flame 4 (1360 K)
Meso Al Burn time (μs) [10 wt. % NC]	366 μs / 72 μs	420 μs / 76 μs	365 μs / 62 μs	326 μs / 83 μs
Meso Al Burn time (μs) [5 wt. % NC]	302 μs / 48 μs	286 μs / 49 μs	357 μs / 153 μs	324 μs / 88 μs
Meso Al Burn time (μs) [15 wt. % NC]	385 μs / 63 μs	405 μs / 63 μs	380 μs / 51 μs	390 μs / 58 μs

Table 7-3: Average burn time/ standard deviation measurements for aluminum meso particles.

7.3.3.4 Product analysis:

The idea behind packing commercial nanoparticles into a meso structure using an energetic gas-generator was to ensure that the low temperature dissociation of the energetic binder (NC) would enhance the dispersion of the nanoparticles thereby reducing sintering at the onset of combustion. In order to confirm if such a phenomenological mechanism is indeed occurring, direct measurements of the particle sizes post combustion were made. For this study the products of combustion were quench collected by rapidly inserting metallic substrates into the post flame region at a height of ~10 cm above the aerosol inlet and imaged in a Scanning Electron Microscope (SEM). The results are shown in Figure 7-10 for both commercial nanoparticles and our meso particles. As can be inferred from Figure 7-10a, commercial nanoparticles do produce some very large spheres, which are a result of a large agglomerates sintering into a much larger droplet, and subsequently

burning in the oxidizing environment. Interestingly, for the case of meso particles (Figure 7-10b), no such large particles were found in the SEM images. This result implies that our approach to assemble meso particles comprised of nanoparticles offers a successful strategy to disintegrate the structure into fine components that burn individually and at a higher burn rate.

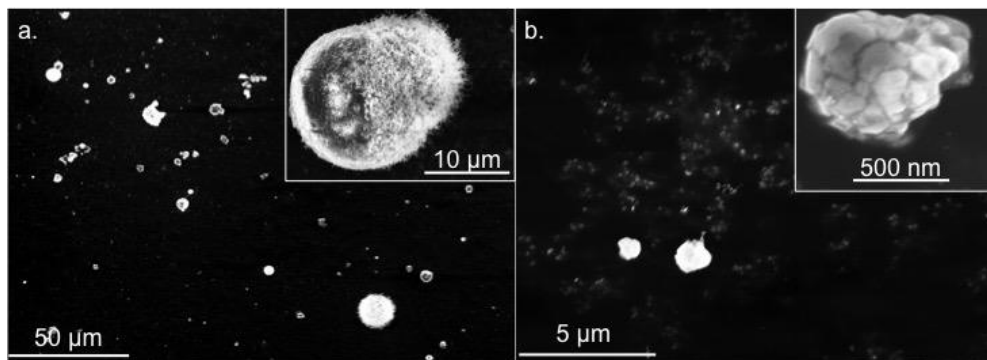


Figure 7-10: SEM images of the products collected post combustion: a) Commercial nanoaluminum with an inset of an individual particle at high magnification; b) Aluminum meso particles with an inset of an individual particle at high magnification.

7.4 Discussion

From the size distribution results in Figure 7-4, it is clear that the commercial nanopowder (ALEX) has a polydisperse size distribution owing to the weak Van der Waals interactions between the individual nanoparticles leading to the formation of agglomerates.[202] Since ALEX was synthesized using the exploding wire technique, particle collisions during coalescence lead to the formation of the so called hard agglomerates which exhibit intraparticle necking[203] as can be seen in the inset of Figure 7-4. Such hard agglomerates usually extend to approximately 10 primary

particles and are extremely difficult to break therefore any measured property of commercial nanoaluminum particles would inevitably be affected by such agglomerates. Hence the larger agglomerates that I see in the size distributions are aggregates of such hard aggregates. Recent results from high heating rate dynamic TEM experiments[100] show that once an aluminum agglomerate heats up beyond a threshold temperature of approx. 1300 K, coalescence is immediate and occurs on a time scale of tens of nanoseconds which is 3-6 *orders of magnitude* shorter than the measured burn times in this study. This result offers an interesting discussion point to our experiments, since the ambient conditions for Flame 1 and Flame 2 (Figure 7-1) are seldom above 1300 K implying that the heat required for coalescence must come from the exothermic oxidation reaction. This means that the reaction would have initiated at some localized hot spots within the agglomerates, and the heat generated from this reaction would subsequently accelerate the coalescence. This results in a characteristically much larger particle, on the order of several micrometers, (Figure 7-10) burning over a much longer duration than what would be expected from a truly nanosized material,[115] as graphically depicted in Figure 7-11b. This can be further corroborated by the measurements made for micron sized particles with reported burn times in the range of 2 – 5 ms for particles in the range of 2-20 μm . [89]

Electrospray generated meso particles on the other hand are packaged into a micron scale composite hence the surface area for heat transfer is greatly reduced although the area available for oxidation remains comparable to the parent

nanoparticles owing to the highly intricate meso structure. Owing to the low decomposition temperature of nitrocellulose (170 C), the porous structure of the meso particles would be exposed early on in the heating. The heat liberated from the oxidation from such exposed regions may contribute directly to cooperative heating of the particle rather than being lost to the surroundings. Such a mechanism would lead to an acceleration of the global reaction owing to the higher temperatures within the composite leading to intraparticle outgassing culminating in the breakup of the structural integrity of the composite, shattering into much smaller particles. These smaller fragments could further react without being in close proximity with other fragments till all the fuel is completely oxidized as depicted in Figure 7-11b.

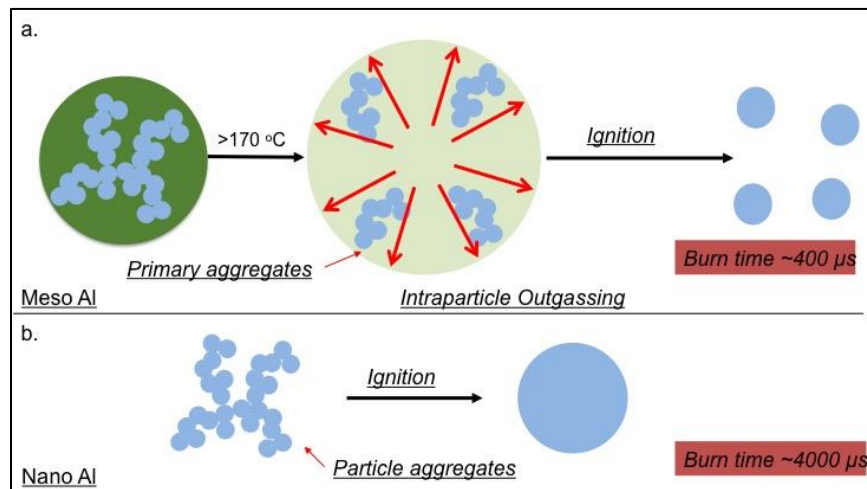


Figure 7-11: Pictorial representation of the events leading to combustion of: a) Aluminum meso particles; b) Commercial aluminum nanoparticles

From Figure 7-7, I see that some of the streaks in the case of meso particles are transverse to the carrier gas flow and this could be a result of the aforementioned outgassing that would lead to sudden impulses which change the trajectory of the

particles. The burn time measurements also corroborate such a mechanism, as the measured values for aluminum meso particles were in all cases an order of magnitude smaller than what were measured for commercial nanoaluminum. Shock tube measurements of nanoaluminum particles[39] reported a burn time of ~500 μs which are in line with what I observe for the meso particles. It must be pointed out that in a shock tube, the particles are ignited behind the reflected shock wave, which implies that the powder is dispersed by a pair of powerful shocks that could successfully break up the large agglomerates. Thus, the measurements made would be a function of the smallest aggregates in the powder, which, I believe, would be the aforementioned hard aggregates. The similarity between the shock tube result and the meso particles' result in the current study implies that the outgassing is successfully able to disperse the composite structure into smaller fragments albeit under atmospheric conditions in the absence of any shock.

The post-combustion harvesting and imaging of the products of combustion showing the product particles being significantly smaller for mesoparticles than for nanoaluminum is consistent with the conceptual model presented in Figure 7-11. Moreover, very recent results[204] incorporating these mesoparticles into composite rocket propellant formulation showed a 35% enhancement in burn rate when compared to the traditional baseline formulation containing 2-3 μm Aluminum particles. Such an improvement is attributed to a significant increase in the density and a decrease in size of burning particles on the surface of the propellant. These

results imply that the ES assembled meso particles can be successfully processed in composite propellant formulations and that the meso structure is able to successfully disintegrate into smaller fragments that have a lower barrier toward ignition. Such a mechanism subsequently improves the heat feedback to the propellant surface and more importantly the final size of the products are greatly reduced which would help in the reduction of two phase flow losses in the motor thereby improving the combustion efficiency and specific impulse.

7.5 *Conclusions*

To summarize, nanoaluminum has several advantages, over dense micron aluminum, including shorter ignition delay, burn times and lower ignition temperatures, properties that are highly desirable for the enhancement of propellant combustion. However, owing to their extremely high surface area and the highly aggregated state of the unreacted as-purchased particles, pre-reaction sintering results in characteristically much larger particles participating in the actual combustion event. In addition, processing challenges and heat transfer effects encountered for nanoparticles have led to a net detrimental effect on combustion characteristics when compared to micron particles. In this work I attempt to bridge the advantages of nanoscale (high surface area) and micron scale (ease of processing) by packaging the nanoparticles into larger *micron scale* composites using an energetic (Nitrocellulose) as a binder. The energetic binder acts as a low temperature gas generator, which helps

to disassemble the soft aggregates into smaller fragments early in the reaction process so that the nanostructure inherent in the initial starting material is more effectively utilized. I find in this work that our assembled mesoparticles burn as fast as the smallest hard aggregates in the nanopowder and has a much narrower distribution of burn times than nanoaluminum. This effectively results in the combustion of the smallest aggregates in the powder precursor leading to an order of magnitude lower burn times and substantially smaller products. This latter point should also lead to a more complete reaction and certainly demonstrates that the concept of using a two-stage reacting system, one at low temperatures to generate gas to separate particles followed by the nominal oxidation reaction, is at the least a strategy that is worthy of further exploration.

7.6 Acknowledgements

The findings presented in this work were reproduced with permission from Jacob, R. J.; Wei, B.; Zachariah, M. R., Quantifying the Enhanced Combustion Characteristics of Electrospray Assembled Aluminum Mesoparticles. *Combust. Flame* **2016**, *167*, 472–480.[142]

Chapter 8 Quantifying the effect of micro-structure on reactivity in electrospray assembled nanothermite composites

Summary

Exothermic reactions between nanoscale metal/ metal oxide systems are of importance in the field of energetics owing to their fast reaction timescale, high energy density and tunability. In this work, I attempt to tune the reactivity of nanothermites by assembling them into gelled microspheres via one step electrospray (ES) synthesis and compare their combustion performance with physically mixed counterparts. The electrosprayed composites incorporate a low temperature gas generator (nitrocellulose) as a binder, which helps in de-aggregating the composites prior to reaction, leading to reduced diffusion length scales and increased reactivity. The combustion performance was gauged by simultaneously recording the pressure and emission signal from a burning pile of the material in an inert environment inside a constant volume pressure cell. The optical emission was spectrally and temporally resolved (at ~350 kHz) using a high-speed spectrometer/ data acquisition to obtain time resolved molecular emission from intermediate species as well as temperature, by fitting to Planck's law. Moreover, the extent of reaction was also examined by performing bomb calorimetry on these samples. The results indicate that the ES

assembled composites, owing to their characteristic in situ gas generation, significantly outperform their physically mixed counterparts and achieve higher extents of completion. The nitrocellulose not only acts as a binder but also as a dispersant of the nanocomposite which reduces widespread coalescence prior to reaction. Moreover, the mesoscale composites prepared with low solids loading precursors displayed a more porous network compared to that of high loading precursors, and subsequently displayed enhanced combustion performance owing to improved convective heat transfer within the composite.

8.1 Introduction

Exothermic, metal/metal oxide redox reactions are known to have high energy density on both gravimetric and volumetric bases.[136] Previous attempts at incorporating metals in energetic formulations involved using micron scale metal particles as additives to enhance the energy content. One of the significant disadvantages of using micron scale material is the large diffusion length scales which prevent the metal particles from igniting/ reacting at the flame front in the energetic composite, resulting in prolonged combustion away from the flame zone.[41,179] Using metal nanoparticles alleviate some of the concerns owing to their lower ignition temperature and faster burn rate, which allows the metal to burn closer to the propagating flame front, thereby directly enhancing the heat feedback.[186] By reducing the reactant sizes to the nanoscale, a highly intimate mixing between the

reactants could be achieved. This new class of nanoscale energetic composites, termed metastable intermolecular composites (MIC), have shown tremendous improvement in reaction rate and with sufficient tuning of the microstructure and composition, have been shown to approach propagation rates as high as 2500 m/s in burn tube measurements.[10] A significant disadvantage of using metal nanoparticles stems from the aggregated nature of the material which leads to widespread coalescence within the composite, resulting in a drastic loss of the initial nanostructure.[205] With the advent of nanotechnology, novel formulations with the aim of accelerating the participation of metal nanoparticles in combustion have been synthesized.[12,121]

One of the most attractive aspects of MICs is the tunability that allows the use of different metal/ metal-oxide combinations, custom nanostructures and production techniques. The initiation is predicted to undergo via condensed phase reactions where the fuel and oxygen ions are transported across the reaction interface.[34,42] The detriment of such a reaction, as highlighted by Egan et. al,[99] is the rapid loss of nanostructure which happens 2-3 orders of magnitude faster than the reaction time scale. This loss of nanostructure occurs due to the reaction happening at the contact points between fuel and oxidizer with the generated heat being transferred to the nearby unreacted/ partially reacted reactants. Such a reaction mechanism, termed reactive sintering, suffers from poor reaction completion and was highlighted in a recent publication.[165] Recent research efforts have been directed at reducing the

pre-reaction coalescence of the reactants by incorporating low-temperature gas generators in the reactant matrix. The basic concept being that the low dissociation temperature of such gas generators would promote primary particle separation prior to composite ignition thereby reducing the extent of sintering. Preliminary work utilizing this concept has revealed reduced ignition delays, improved reactivity, reduced burn time as well as smaller product particle sizes, highlighting the ability to limit coalescence. [12,164,169] The current work aims to expand on these preliminary results by measuring reaction metrics such as temperature, pressure and extent of completion in these composite materials. Herein, I manufacture nanothermite composites incorporating nitrocellulose as gas generator and compare their reaction metrics with that of their physically mixed counterparts. The novel nanocomposites are manufactured via one step electrospray (ES) method which allows for versatile tuning of the reactants as well as produce a highly monodisperse distribution of composite particle sizes. The size and porosity of the final composite can be carefully tuned by selecting the appropriate precursor composition and ambient temperature. This method therefore helps in generating composite microspheres that not only have intimate mixing between the reactants but also retain the high specific surface area that are representative of nanoscale materials.[12]

Three different nanocomposite thermite compositions (Al/CuO, Al-Fe₂O₃, Al-WO₃) are examined in this study owing to their diverse characteristics, which provide sufficient breadth to the analysis. Moreover, two different morphology of the ES

assembled microsphere composites are generated for the three aforementioned systems so as to gauge the effect of the microstructure on the reactivity. The combustion performance of the samples are characterized using closed combustion cell tests equipped with high speed emission spectrometer which is used to determine reaction temperature. Moreover, the samples are also tested for extent of reaction in a closed bomb calorimeter in inert environment.

8.2 *Experimental*

8.2.1 Materials and Sample Preparation

Three different nanothermite formulations (Al-CuO, Al-Fe₂O₃, Al-WO₃) were tested in this study, primarily owing to their diverse ignition and reaction characteristics. Jian et. al.[11] highlights the salient differences between several nanocomposite thermite formulations in regard to their ignition temperatures and oxide decomposition properties. Briefly, Al-CuO and Al-Fe₂O₃ nanocomposite formulations are characterized by concurrent ignition and oxygen release temperatures, with AlCuO ignition temperature ($\sim 1050 \pm 50\text{K}$) being much lower than that of Al/Fe₂O₃ ($1400 \pm 50\text{K}$). Al/CuO is the most tested nanocomposite in literature and its reactivity is characterized by strong pressure release as opposed to Al/Fe₂O₃ where the pressure build-up is slow, primarily limited by the oxidizer decomposition.[40,177] Both oxides are characterized by decomposition into gaseous oxygen which results in significant reaction between aluminum and oxygen in the gas

phase, although both composites are dominated by condensed phase reactions during ignition. [42] Al/WO₃, on the other hand, has a completely different reaction characteristics as the oxide in this case is not prone to decomposition into gaseous oxygen. The initiation and reaction is observed to occur strictly in the condensed phase, with the ignition temperature (1030±50K) being closer to Al/CuO. Al/WO₃ composites exhibited shorter combustion duration (Full Width Half Max of emission intensity) and higher temperature than Al/Fe₂O₃ composites in constant volume pressure cell combustion tests, as presented in Chapter 6.3.2 and published in a recent study.[177] The adiabatic flame temperatures also vary with the choice of the composite, with Al/CuO and Al/Fe₂O₃ samples exhibiting lower flame temperatures (2967K and 2834K respectively) than Al/WO₃ (3447K), under conserved volume-energy (UV) calculations.

In this study, novel nanothermite composites of three aforementioned constituents are tested with the aim of gauging the effect of nanostructure on their reactivity. The baseline composites are made via ultrasonic mixing, which is the most widespread technique used in nanothermite synthesis. Preparation of physically mixed samples are presented elsewhere.[177] Briefly, a prescribed mass of oxide nanopowder (Sigma Aldrich, < 100nm) was dispersed in 10 mL of hexane and sonicated in an ultrasonic bath (Branson 2510) for an hour. This was done in order to break down the soft aggregates, ensuring better mixing with the fuel. A stoichiometric amount of aluminum NPs (ALEX, Novacentrix, 80% active, ~80nm) was then added

to this slurry and further sonicated for an hour. The slurry was left overnight to dry. The dry sample was gently scraped off the vial and broken up using a grounded spatula until powder consistency was achieved.

The strategy to prepare ES assembled nanocomposites can be found in Wang et. al. [164,206], where the clear morphological differences in the composite structure is highlighted. Briefly, stoichiometric amounts of fuel and oxidizer were sonicated in a solution of ethanol and ether in 3:1 volume ratio. Subsequently, collodion solution (5 wt. % total solids loading) was added to the mixture and stirred for 24 hours. The subsequent precursor solution was electrospayed so as to make micron sized composite particles of intimately mixed fuel and oxidizer with the nitrocellulose gas generator acting as a binder. The composite was sprayed onto a conductive foil and harvested for further tests. Electrospaying the composites provide the distinct advantage of intimate mixing as well as a highly monodisperse distribution of the composite particles as highlighted in Figure 8-1. Two different solids loading scenarios were considered in this work, following the work by Wang et. al [206] where a low loading precursor (80mg/ml total solids) resulted in a more open/ porous composite when compared to the high loading (205 mg/ml) case, which was characterized by a spherical, compact structure, as can be seen in Figure 8-2, (adapted from Wang et al.[206])

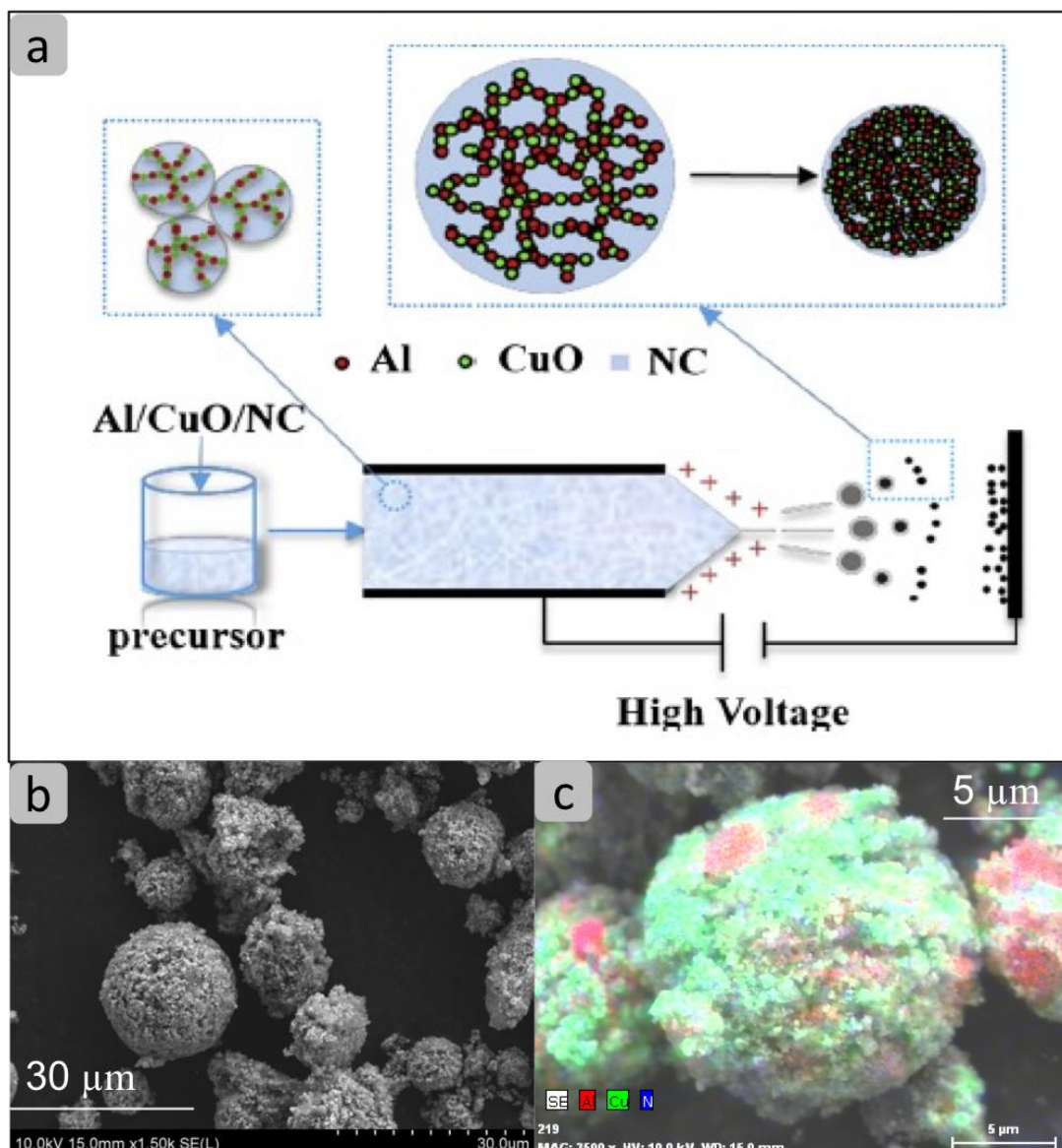


Figure 8-1: ES assembly of nanocomposite thermites, adapted from Wang et. al [164]. (a) Experimental setup for ES synthesis, (b) Al/CuO nanocomposites prepared by electrostatic spray and (c) backscattered electron image highlighting the intimate mixing of Aluminum (red) and Copper Oxide (green).

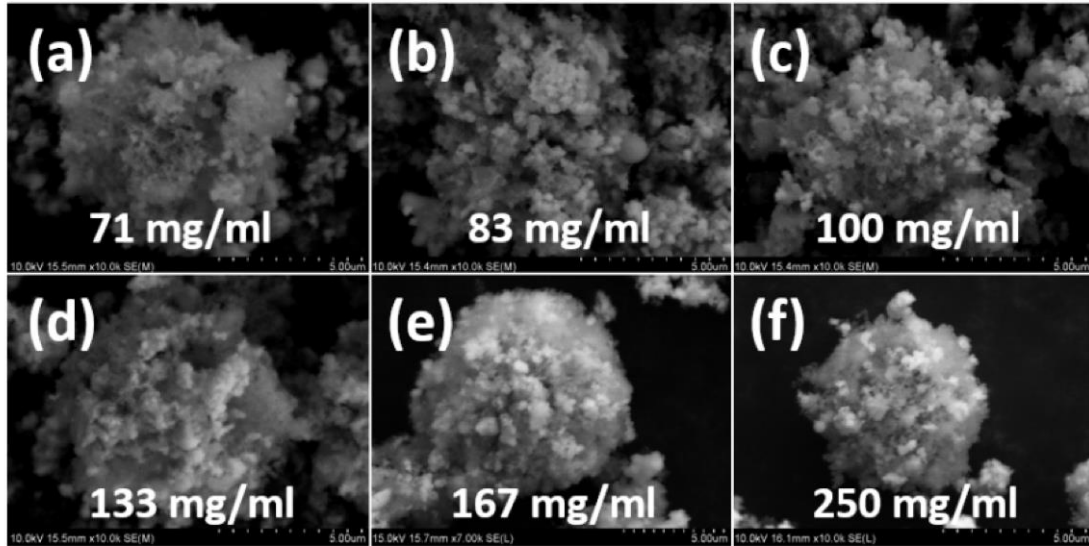


Figure 8-2: Effect of precursor loading on ES assembled mesosphere morphology (Reprinted from Wang et al.[206]). The sample tested in the current study were prepared using 80mg/ml and 205mg/ml solids loading.

8.2.2 High speed 32 channel Spectrometer coupled combustion cell

The details of this setup can be found in Chapter 2.

8.2.3 High sensitivity closed bomb calorimetry

The details of this setup can be found in Section 5.2.4

8.3 **Results**

8.3.1 Constant Volume Combustion cell tests

The results from the constant volume combustion cell tests are shown in Figure 8-3, which highlights the dependence of pressure metrics and reaction temperature on composition and morphology of the nanocomposites tested in this study.

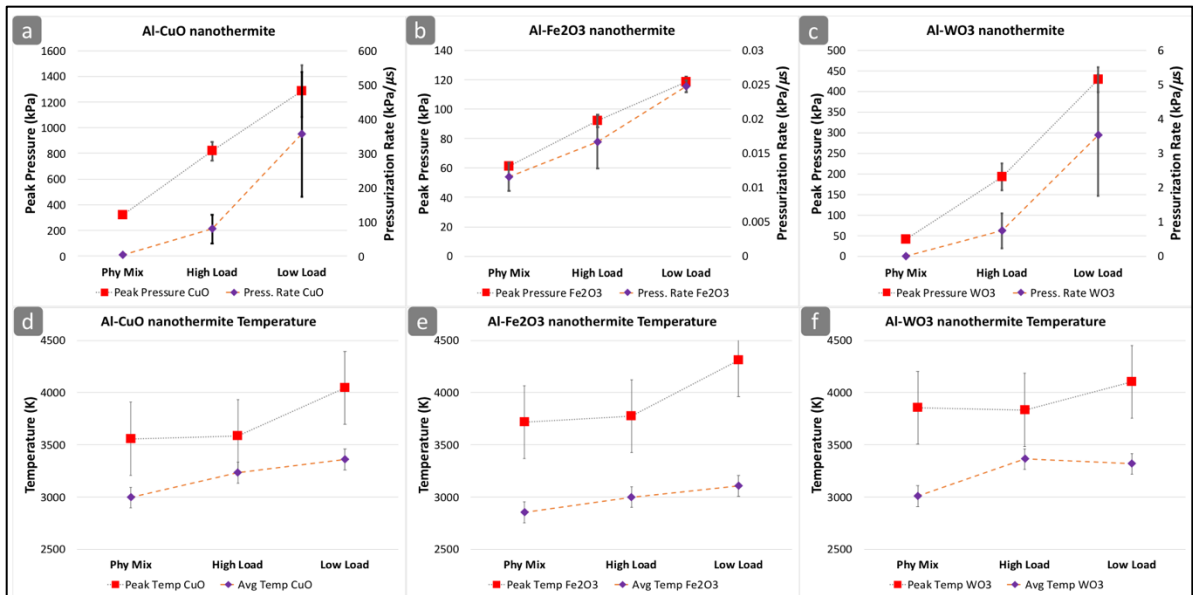


Figure 8-3: Combustion cell results showing pressure performance (a-c) and reaction temperature (d-e) for the nanocomposite thermites.

As can be clearly seen, the ES assembled composites significantly outperform their physically mixed counterparts for all the compositions examined. Al/CuO system, as expected, exhibit higher pressure and pressurization rate compared to Al/WO₃ and Al/Fe₂O₃ samples owing to the propensity of CuO to decompose into gaseous species.[11] More importantly, the nanocomposite prepared from low loading precursor performed better than other morphologies for all the compositions studied. The peak and average temperatures measured during reaction are also plotted in Figure 8-3 (d-f), which shows slight improvement (within error) in average and peak temperatures upon changes in the sample morphology.

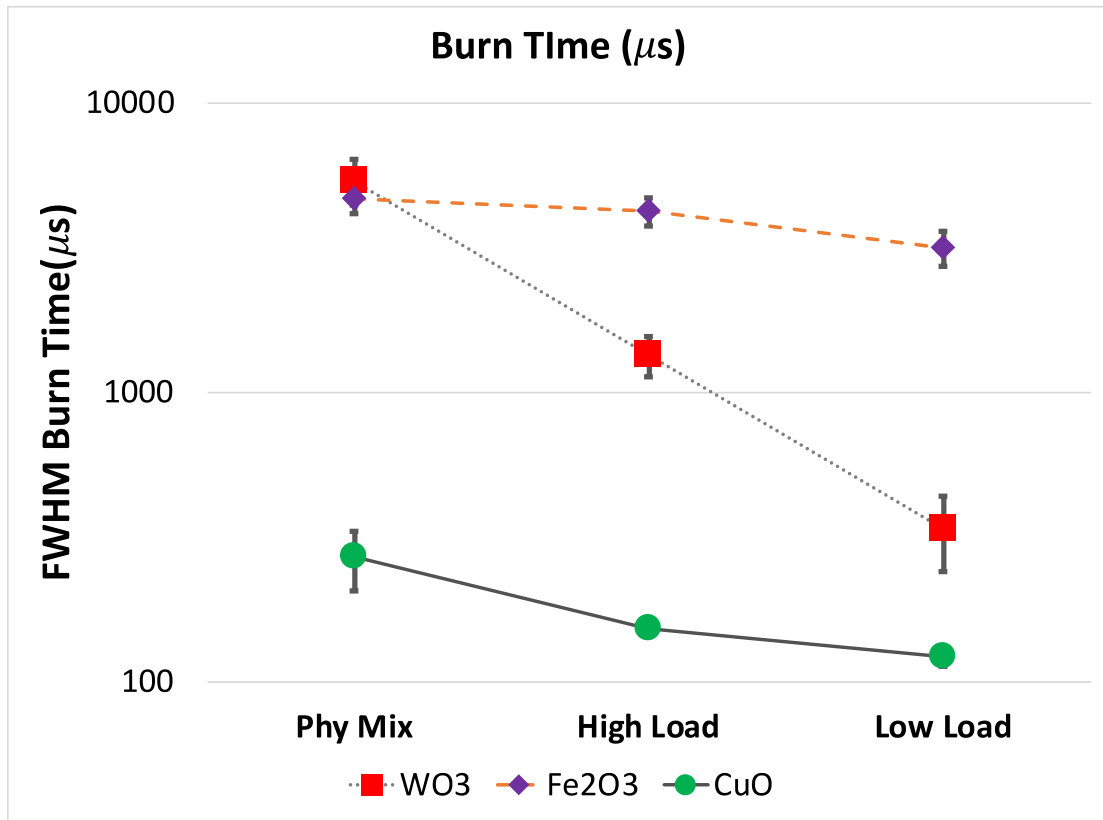


Figure 8-4: Burn time of the composite measured as the FWHM (Full-Width-Half-Max) of the integrated emission from the constant volume pressure cell tests.

The Full-Width-Half-Max (FWHM) of the integrated emission intensity from the nanocomposite reaction in the combustion vessel is used to compute the burn time, which can be used as a metric of the reaction rate of the composites. The results, plotted in Figure 8-4, shows that for all the compositions examined here, the electrospayed composites, particularly low loading case, burned significantly faster than the physically mixed counterparts. Al/WO₃ samples in particular showed an order of magnitude improvement in burn time which highlights the ability of these composite to unlock the fast reaction kinetics of the composites.

8.3.2 *Bomb calorimetry results*

Following the results in the previous section where the ES assembled composites are observed to show improved combustion performance, bomb calorimetry was performed so as to gauge the effect of microstructure on the global extent of reaction. The tests were conducted in an inert argon environment to prevent any secondary reaction with air. The measured heat of reaction (ΔH_{Rx}), for the three nanothermite compositions, in both physically mixed as well low loading configurations, are shown in Table 8-1 along with an estimated percentage of completion. The theoretical estimates of the heat of reaction was obtained from the work by Fischer and Grubelic,[136] and was modified in order to account for the inert alumina shell, as shown in Table 8-1. The reported average values were obtained from 3 runs which helped ensure the repeatability of the experiment.

Composition	Phy. Mix Theor.	Phy. Mix Exp.	% Complete	Low Load Meso Theor.	Low Load Meso Exp.	% Complete
Al/CuO	3902	2560±339	66	3817	3376±240	88
Al/Fe ₂ O ₃	3731	2614±930	70	3654	2672±356	73
Al/WO ₃	2787	1842±339	66	2758	2842±988	~100

Table 8-1: Bomb Calorimetry results for nanothermite composites

8.4 *Discussion and Conclusion*

The results presented in the previous sections clearly indicate the enhanced combustion characteristics of ES assembled nanocomposites with higher pressure,

pressurization rate, temperature and extent of reaction over physically mixed counterparts. Although intimately mixed, physically mixed samples (Figure 4-1) are composed large aggregates that immediately coalesce into super micron spheres when the reaction initiates, which results in significant quantities of unreacted material getting arrested within the coalesced mass, as described in Chapter 5. With the presence of nitrocellulose, highly monodisperse composite microspheres with controlled size can be generated which in addition to being intimately mixed, have the ability of in situ gas generation that could help disaggregate the composite prior to significant reaction. Experimental evidence of such disaggregation phenomena is presented in Figure 7-10 and in Wang et. al,[164] where an order of magnitude reduction in product size was observed for Al/CuO composite.

The advantages of using electrospray assembly are multifold in that commercial raw materials could be used and the synthesis can be scaled up for bulk production. Moreover, a variety of different metal/ metal oxide/ halide combinations can be used in the precursor and can be assembled into these microspheres.[169,207,208] More than a synthesis route, the ES assembly allows for maximizing the performance of a given nanocomposite by limiting the detrimental effects of coalescence of global reactivity. The potential advantages of assembling the nanocomposites into a porous mesosphere are: 1. enhanced mixing which reduces the diffusion length scales between reactants; 2. the closed matrix of the composite microsphere accumulates the generated heat from the reaction to a higher degree than

an open composite which results in a higher extent of reaction and 3. the presence of gas generating binder help disaggregate the composite prior to significant reaction which results smaller composite cluster reacting away from each other, thereby resulting in faster and a more complete reaction.

8.5 Acknowledgements

This work was done in collaboration with Dr. Tim Weihs' group at Johns Hopkins University. Special thanks to Elliot Wainwright and Madeline Mueller for performing the bomb calorimetry tests.

Chapter 9 Pre-stressing aluminum nanoparticles as a strategy to enhance reactivity of nanocomposite thermites

Summary

Aluminum nanoparticles (NPs) upon exposure to air develop an 3-5 nm amorphous alumina shell, which acts a diffusion barrier to the release of aluminum during reaction. Pre-annealing the aluminum NPs have been recently proposed as a viable, bulk processing, strategy to improve reactivity whereby the NPs are annealed to high temperatures so as to weaken the shell. In this work, batches of aluminum NPs annealed at 200, 300 and 400C were mixed with Copper Oxide NPs to make nanocomposite thermite and their performance was tested in a constant volume combustion cell. The combustion cell is coupled with a fast spectrometer, capable of measuring emissions spectra from the reaction pile at ~350 kHz, which was subsequently fit to Planck's law to obtain grey body temperatures. The results indicate that prestressing the Al NPs has a significant effect on the pressure metrics on the nanocomposites with the samples annealed at 300C showing a 36% improvement in pressure and 1000% improvement in pressurization rate, compared to that of the untreated samples. The Full Width Half Max (FWHM) burn time was also measured from the integrated intensity with the 300C annealed samples exhibiting the fastest combustion durations. Quench rates of the annealed samples did not exhibit a significant effect on the performance of the composites. The faster release of

aluminum in case of annealed samples was visualized using high heating rate Transmission Electron Microscopy (TEM) where, for the 300C annealed sample, the aluminum in the core was observed to diffuse out faster than for the untreated case.

9.1 Introduction

The advent nanotechnology has facilitated significant developments in the field of metalized energetic materials, which have been historically plagued by poor reactivity and incomplete combustion.[124] With the objective of approaching the high reactivity of traditional monomolecular explosives, a new class energetic material, termed 'Metastable Intermolecular Composites' (MIC's), was developed which incorporate condensed phase metal-oxidizer system. MIC's have has gained significant traction in recent years owing to their high energy density, tunability and reactivity.[168] Aluminum has been the fuel of choice owing to its availability, low cost, energy density and environmentally benign products although other metallic fuels such as boron, titanium and tantalum[168] are also being investigated.

Conventional wisdom advocates that reactivity scale inversely with particle size, owing to a reduction in the diffusion length scales for the reactants. Although this hypothesis has proven true for metallic fuel particles in the micron scale[36] to early nanoscale (100s of nm),[184] further reduction of the primary particle size in the nano-regime has produced diminished returns in terms of reactivity.[31]

Nanoaluminum (nAl) naturally develops a 3-5 nm shell[209] upon controlled

exposure to air and its contribution to the particle mass dramatically increases as the particle size is shrunk leading to reduced active content at smaller particle sizes, which is a significant contributor to the aforementioned reduction in reactivity.[210] Another reason, which has been recently postulated, is the role of inter-particle sintering whereby, at high temperatures, the highly aggregated nanoparticles coalesce rapidly into larger characteristic dimensions,[100,115] effectively reducing the advantage of employing nanoscale materials.

The role of the inert alumina layer on the reaction pathway of nAl has been subjected to intense debate over the years as it presents a diffusion barrier to the interaction of aluminum with the oxidizer.[22] Several theories have been proposed to identify the dynamics of the core shell interface and its significance to the reactivity of the nanocomposite, with the mechanochemical Melt Dispersion Mechanism (MDM)[44] and the condensed phase diffusion mechanism being the most prominent. MDM predicates on the catastrophic spallation of the molten core upon failure of the shell at very high heating rates ($\sim 10^6 - 10^8$ K/s), leading to the released aluminum clusters undergoing a kinetically limited reaction with the oxidizer. Diffusion mechanism, contrarily, proposes the condensed phase transfer of Al ions across the phase transformed alumina shell as the reason for the fast reactivity.[22,28] Recent high spatio-temporal resolution experiments on nanoscale Al-CuO reaction in a dynamic Transmission Electron Microscope (TEM) have revealed the predominance of a condensed phase diffusion mechanism where the reactant moieties were observed

to rapidly coalesce ($< 1 \mu\text{s}$) to larger characteristic dimensions resulting in an increase in diffusion length scales and thereby not achieving completion.[99,135,165]

Attempts at improving the reactivity of nanoscale energetic materials (NEMs) can be broadly classified into either altering the mesoscale architecture/assembly of fuel and oxidizer moieties (improved mixing)[169,171] or altering the performance/properties of the fuel so as to ensure rapid introduction of fuel. The latter method, the focus of this work, has burgeoned with the recent development in synthesis routes leading to the production of intermetallic fuels,[211] multi-metal fuels,[212,213] oxide free aluminum nanoparticles (Al NPs) passivated with carboxylic acids[50] and surface functionalized nanoparticles with oxidizers.[214] With the objective of accelerating the participation of aluminum in reaction, this work focuses on another strategy where commercial Al NPs are pre-annealed so as to weaken the alumina shell and expedite the release of aluminum during reaction. Prestressing involves annealing the powder sample at a fixed temperature followed by quenching it at a preset cooling rate. This fairly novel strategy affords the use of commercially available nanoparticles and has the advantage of bulk processing as opposed to the wet chemistry techniques that usually has poor yield.[215] Recent experiments have demonstrated the advantages of prestressing on micron scale aluminum powders (5 μm) where $\sim 25\%$ improvement in flame speed was observed for samples annealed at 300C. No significant dependence on cooling rate was observed in this study. Through X-Ray diffraction measurements, the heightened flame speed was correlated to a \sim

6000% increase in the dilatational strain of the aluminum core which consequentially led to larger grain sizes and reduced hardness.[216,217] Other studies on nAl samples have revealed 30% improvement in flame speed when nAl-MoO₃ composites were annealed at 105 C in argon, again corroborated to a reduction in the ultimate strength of the alumina shell due to aluminum diffusion into the shell.[118,218] For these nanoscale samples, the adopted quench regime demonstrated a noticeable effect on flame speed with a 14% improvement reported when the cooling rate was increased from 0.06 K/s to 0.13K/s. At higher cooling rates (0.33 K/s), the nAl powder was observed to spontaneously ignite, highlighting the drastic improvement in reactivity. Contrarily, high resolution hot stage TEM experiments conducted on nanoscale aluminum particles revealed that the aluminum core at room temperature exists in a pre-expanded state and that it passes through a zero-strain state at ~ 300C, with any further increase in temperature leading to an almost unconstrained expansion of the core. This was attributed to the inhomogeneous crystallization of the amorphous alumina, which prevented pressure build up from an expanding core[29] thereby aiding the aluminum to leak through imperfections in the inhomogeneous shell. The results were corroborated with high resolution images depicting the release of aluminum and loss of nanostructure with increasing temperature.

Although the results are scattered, there seems to be general merit in annealing the aluminum particles prior to combustion for enhanced performance and a systematic analysis of the combustion performance of nAl annealed to various

temperatures would be undertaken in this study. The model composition employed is that of nanoscale Al/CuO, which is the most investigated nanothermite system. Al/CuO system has been shown to produce significant quantities of gas phase oxygen due to the decomposition of CuO, leading to a proposed two stage reaction mechanism where condensed phase ion transport is responsible for the ignition followed by gas phase reaction of aluminum with the oxygen.[11] In this study, I employ high speed emission spectroscopy and pressure measurements to quantify the combustion performance of prestressed nAl composites and use high heating rate in-situ TEM to augment the combustion results.

9.2 *Experimental*

9.2.1 Materials and Preparation

Commercial aluminum nanopowder (Novacentrix) with a primary particle size of ~80 nm and active content of ~ 80% was used in this study. Upon exposure to ambient atmosphere the nanoparticles develop a ~4 nm thin oxide shell, as shown in Figure 9-1.

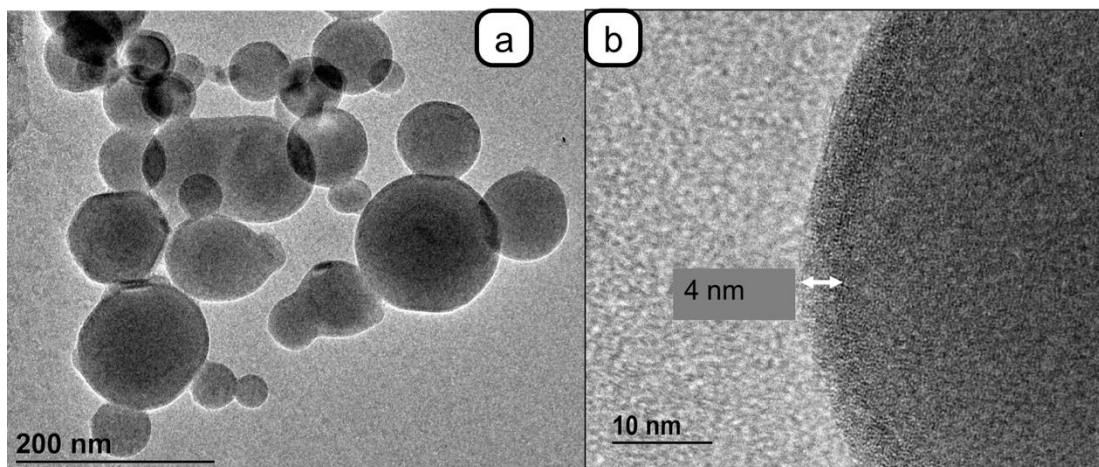


Figure 9-1: (a) Untreated nanoaluminum particles and (b) magnified image showing the oxide shell.

The as purchased aluminum was subjected to a highly controlled thermal environment using a Q800 Dynamic Mechanical Analyzer (TA instruments). Three sets of samples each annealed to 200, 300 and 400C at 10C/min and held at the prescribed temperature for 15 mins were prepared for this study. Once annealed, two different cooling routines were employed so as to gauge its effect on reactivity.[216] The sample subjected to slow cooling (termed exponential) were left within the oven to naturally cool to room temperature whereas for fast cooling, the annealed sample was placed in a refrigeration unit till it attained room temperature (termed linear).

Detailed description of the preparation of nanothermite composites can be found elsewhere.[177] Briefly, a known mass of Copper Oxide nanopowder (Sigma Aldrich, <100 nm) was dispersed in a vial containing 10 ml of Isopropyl alcohol (IPA) and was subsequently sonicated in an ultrasonic bath for 1 hr. To this mixture, a stoichiometric amount of the thermally treated aluminum powder was added, and

the slurry was further sonicated for an hour. The IPA acts as a Process Control Agent (PCA) which disperses the nanoparticles in solution to achieve intimate mixing, while also preventing accidental ignition. The sonicated samples were dried in a fume hood for 24 hours and the subsequent dry powder clumps were harvested off the vial and broken up using a grounded spatula to achieve fine consistency. The combustion performance of the samples were tested and compared to the baseline performance of untreated nAl samples so as to gauge improvement.

9.2.2 Constant volume pressure cell and High speed 32 channel emission spectrometer

Detailed description of the diagnostics used in this work can be found in a recently published article[177] and in Chapter 2.2 and Chapter 6.2.2 The pressure cell-spectrometer setup was used to measure reaction temperature from constant volume combustion of the composites. The wavelength and intensity calibration was performed as outlined in Ref.,[177] following which the corrected spectra was fit to Planck's law incorporating a grey body assumption to obtain the condensed phase flame temperatures, error thresholded to ± 350 K.[59] Channels overlapping with significant molecular emission species (such as Na doublet, AlO bands etc.) were removed from the custom-built MATLAB fitting routine. Each sample was tested in triplicate so as to ensure repeatability.

9.2.3 *In-situ high heating rate electron microscopy*

Owing to the fast reactivity of these composites, rapid heating rate diagnostics are paramount to probe the underlying initiation dynamics of these materials subjected to ignition. Accordingly, the prestressed nAl sample that demonstrated the best performance in the combustion cell tests were subsequently tested in a Transmission Electron Microscope (TEM, JEM 2100 Lab6) to afford high resolution imaging. The samples were tested in-situ using a specially designed probe (Protochips Aduro) capable of sustaining a rapid thermal pulse at very high heating rates ($\sim 5 \times 10^5$ K/s), commensurate with the dynamics of an actual reaction front.[34] The nAl slurries were drop cast onto custom made TEM grids and was subsequently subjected to a thermal ramp up to 1473K. The modularity of the probe allowed a choice of final temperatures as well as hold time and high-resolution images were taken before and after heating to compare and draw conclusions about the mechanism.

9.3 *Results*

9.3.1 *High speed pressure and temperature measurements*

The performance of the various composites in the combustion cell is presented in Figure 9-2 **Error! Reference source not found.** where the effect of prestressing on combustion performance is depicted as a function of annealing temperature and quench regime. The pressurization rate was measured by dividing the first prominent pressure peak (10% prominence) by the time elapsed from ignition. As can be clearly

seen, a significant improvement in peak pressure (36%) and pressurization rate (1000%), compared to untreated samples (baseline) was obtained when annealed to 200C, with a slight improvement in peak pressure (39%) observed at 300C. The peak pressures also exhibited a dependence on the cooling regime with faster, linear quench resulting in the composites attaining a higher peak pressure. The pressurization rate for samples annealed at 200C and 300C was nearly identical (average values within 5 %) and showed only slight improvement for faster quench rates. For the samples annealed at 400C, the pressure metrics were significantly diminished compared to 300C case with the peak pressure values being similar (~1.1x) to that of the untreated case. The pressurization rate, although lower than the 300C samples, were still ~6 times of that observed for the untreated samples. The lower pressure metrics at 400C treatment may suggest that the nAl particles must have deteriorated significantly, given that the annealing was performed in air and TGA results, in the literature on nAl reaction, have shown previously that the reaction onset could be as low as 450C.[30]

Temperature measurements made during the constant volume combustion of the composites are shown in Figure 9-2b, where the light emission from the reaction was fit to Planck's law with grey body assumption. The peak temperatures can be seen to approach ~3800K, which can be expected from gas phase combustion of aluminum and oxygen, given the proclivity of CuO to decompose into Cu₂O and Oxygen.[11] The peak temperatures were thresholded to the highest admissible error

(± 350 K), which made meaningful mechanistic interpretation difficult. The average temperatures, on the other hand, has much lower error compared to peak temperatures, and it can be seen that with prestressing, the average temperatures are slightly lower than for the untreated samples. Further discussion about the ramifications of the temperature dependence can be found in a later section. For the 400C case, the peak and average temperatures were lower than for the other samples, which in conjunction with the poor pressure metrics could reinforce the detrimental effects of thermal treatment in air at high temperatures such that the active content/shell could deteriorate significantly.

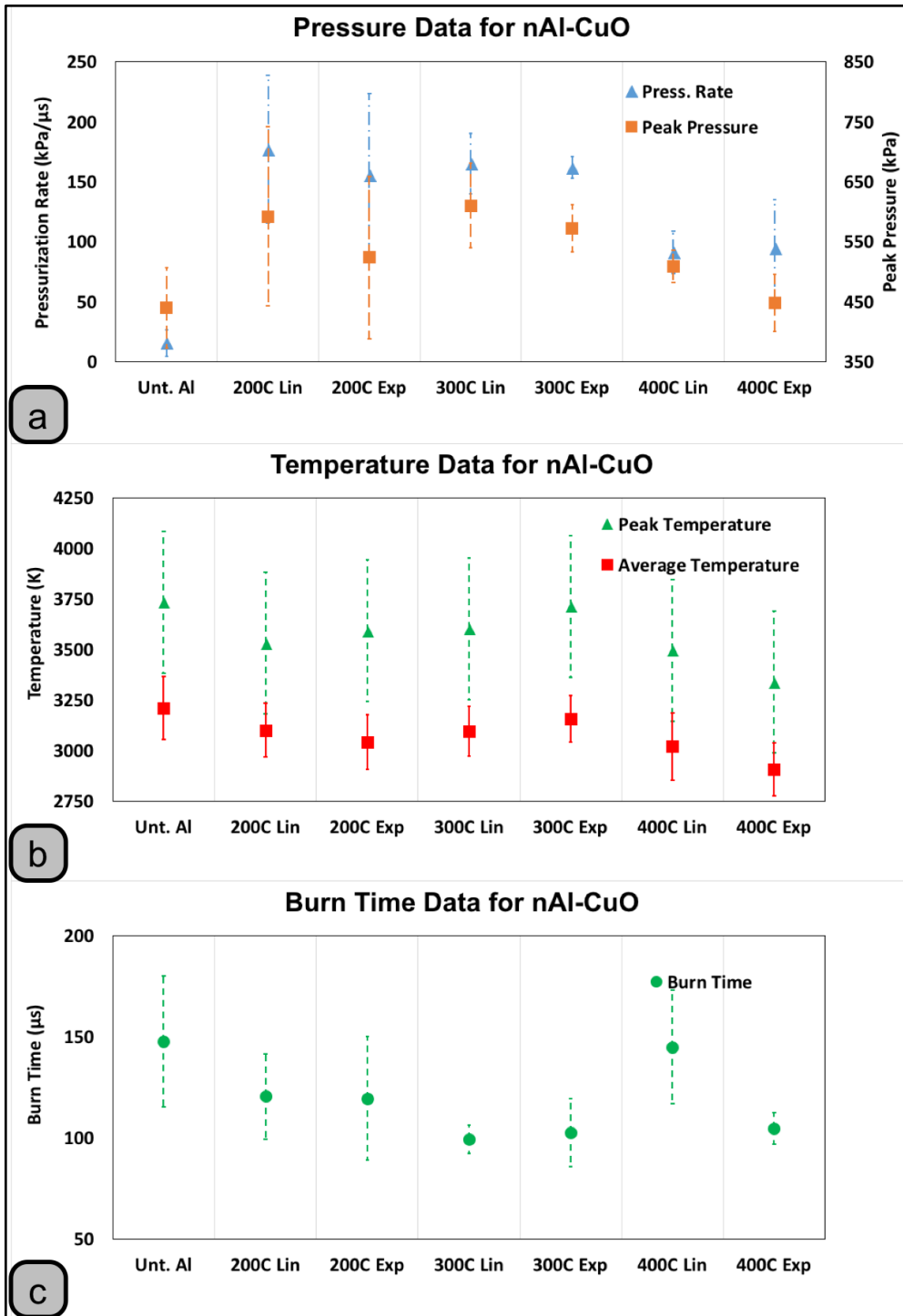


Figure 9-2: Pressure Cell data showing effect of prestressing (a) on Pressure and Pressurization Rate; (b) on Temperature; and (c) on Burn Time.

The full width half max (FWHM) burnt time obtained from the integrated emission spectra during reaction is shown in Figure 9-2c, where the samples annealed to 200 and 300C show faster burn times compared to the untreated and 400C samples. Also evident is the inverse correlation between burn time and peak pressure measurements, which would imply that the samples annealed to 200 and 300C are achieving a more complete reaction given that they are attaining higher peak pressure and faster combustion in spite of having the same composition.[209]

9.3.2 *Hot stage, High heating rate in-situ microscopy*

Select samples were tested in a high heating rate TEM where the samples were drop cast onto special microscopy grids and were subsequently ramped from room temperature (RT) to 1473K at a rate of 5×10^5 K/s. The heating rate and temperatures were so chosen so as to ensure significant differences in morphology before and after the heating pulse. The results for untreated nAl is shown in Figure 9-3a-c whereas for the nAl annealed at 300C-Exp is shown in Figure 9-3d-f. Samples prior to heating pulse, as shown in Figure 9-3a,d for nAl and 300C-Exp samples respectively, exhibit a fairly aggregated structure. Upon being subjected to the rapid heating ramp, the morphology of the 300C annealed sample (Figure 9-3e) is observed to undergo significant changes, with the aluminum in the core appearing to diffuse out of the shell, leading to a reduction in the boundaries that clearly demarcated the individual nanoparticles prior to heating. More importantly, no violent

spallation/ejection of the core material following catastrophic shell explosion is observed, as expected in the case of the Melt Dispersion Mechanism (MDM). Figure 9-3f shows a magnified image of the nanoparticles after the heating pulse where heterogeneities are observed to develop on the shell leading to a more corrugated structure.[34] Contrarily, untreated nAl is observed to undergo no significant morphological changes post the rapid heating pulse (Figure 9-3b), with some nanoparticles in the image undergoing discoloration, probably due to crystallization or healing of the defects in the shell at the high temperature. In order to force a morphological change as seen for the annealed samples, the nAl samples were subjected to a second heating ramp with a 1 second hold at 1473 K (Figure 9-3c), which resulted in significant morphological changes to the aggregate structure. These results imply that in the case of thermal pretreatment, there seems to be a greater propensity for the aluminum core to diffuse out of the shell when compared to that of the untreated samples.

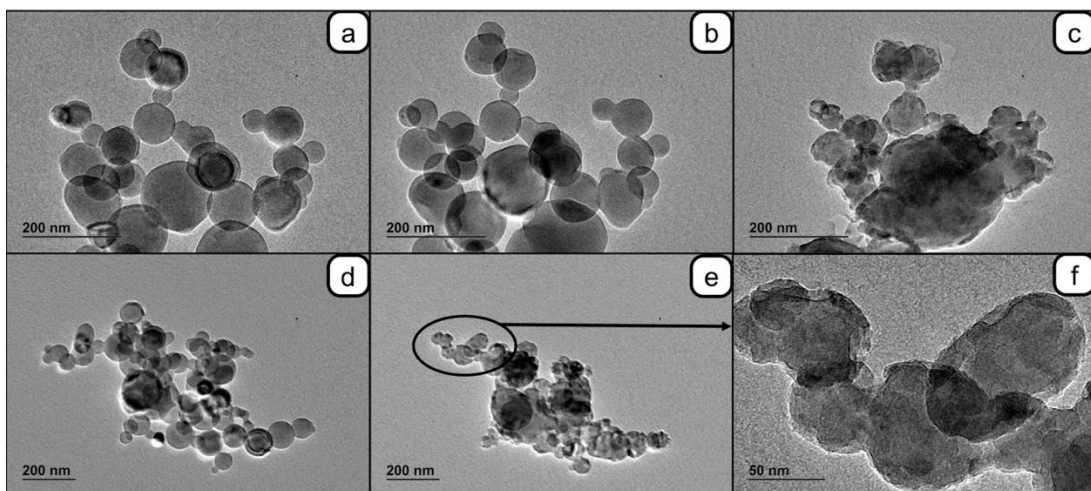


Figure 9-3: High heating rate TEM results for Untreated nAl (a) prior to heating, (b) after RT- 1473K ramp @ 5×10^5 K/s, (c) after RT- 1473K second ramp @ 5×10^5 K/s and hold for 1s; and for 300C Exp nAl (a) prior to heating, (b) after RT- 1473K ramp @ 5×10^5 K/s, (c) magnified image of (b) showing the shell structure.

9.4 Discussion

Results presented in the aforementioned sections demonstrate the benefits of prestressing nAl particles prior to combustion, with the annealed composites achieving higher pressure, pressurization rates and faster burn times compared to the untreated samples. Bachmaier et. al[217] demonstrated a significant reduction in hardness when consolidated pellets of micron aluminum particles ($1.3 \mu\text{m}$) were annealed above 200C and attributed it to the onset of grain growth, as corroborated by microscopy measurements. Recent results on prestressed micron aluminum have revealed significant increase ($\sim 6000\%$) in the measured dilatational strain in the aluminum core, which would imply that the aluminum matrix is expanding freely.[216] Similar results corroborating the freely expanding nAl core were also observed in hot stage TEM results and concluded that the aluminum core exists in a pre-expanded state at room temperature and passes through a zero stress state at $\sim 300\text{C}$, followed by an unconstrained expansion above 300C. Such an unconstrained expansion is only possible if the aluminum finds a pathway to ‘leak-out’ through the passivation shell, primarily through the inhomogeneities developed in the shell due to phase changes in alumina and/or penetration of Al ions which could modify its microstructure.[29] Molecular Dynamics simulations[19] on nanoaluminum particles

have revealed the presence of induced electric fields at the core shell interface (Cabrera Mott mechanism) that aid the transfer of aluminum ions across the shell, culminating in significantly softening the shell. The softened shell is postulated to melt at a lower temperature which combined with the softer aluminum core (due to grain growth during annealing) could lead to faster release of aluminum, as exemplified by the TEM results presented in Figure 9-3, where a significant loss of nanostructure is observed under reduced thermal load for the annealed samples as opposed to the untreated nAl samples.

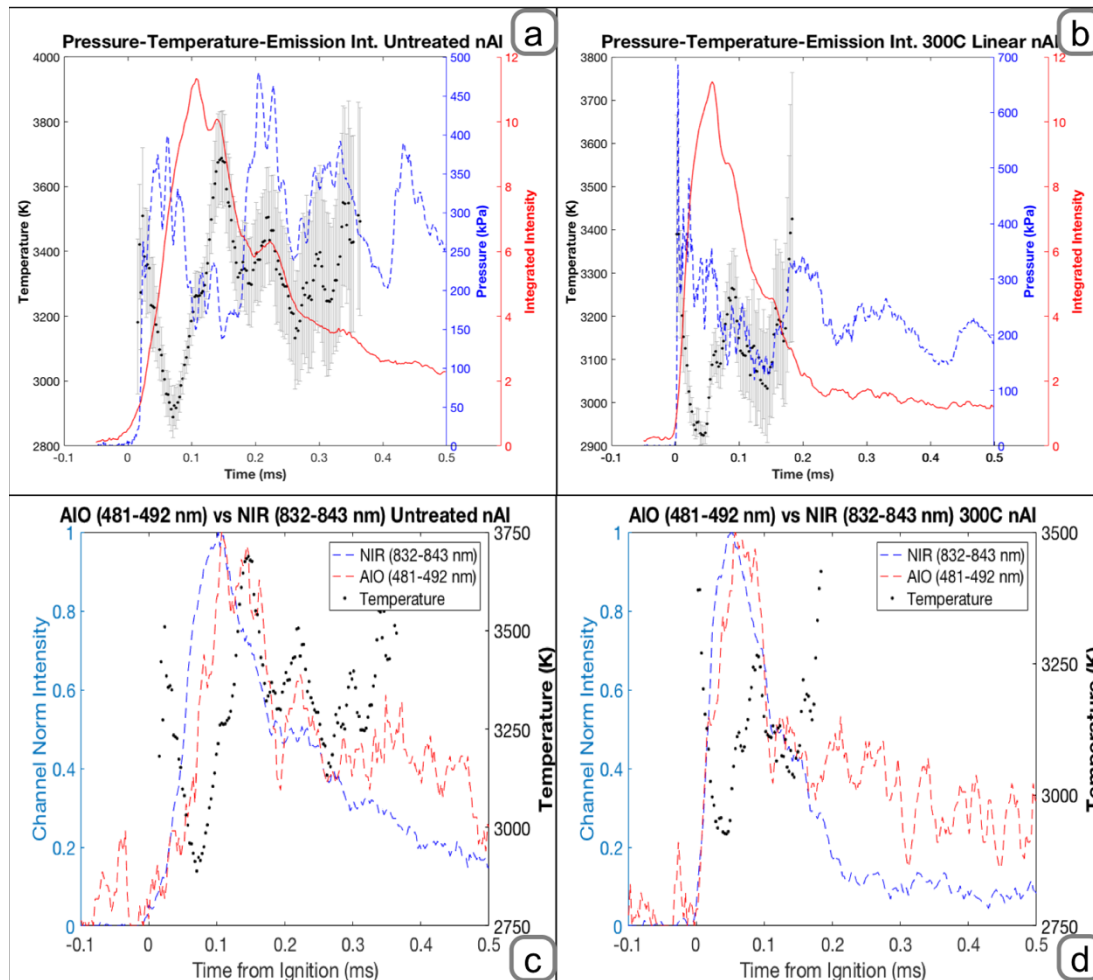


Figure 9-4: Pressure-Temperature and Emission data for (a) Untreated nAl and (b) 300C Linear nAl; NIR vs AIO channel profile for (c) Untreated nAl and (d) 300C Linear nAl.

Owing to the significant loss in nanostructure as seen in Figure 9-3, I believe the previously postulated condensed phase exothermic reactive sintering mechanism, aided by species diffusion, is dominant in these systems.[42] The mechanism is predicated on the reactant moieties attaining significant mobility in the condensed phase such that they diffuse rapidly toward each other resulting in a reaction interface. The heat generated at the interface is transmitted through the sample,

leading to further melting of the unreacted samples. The molten reactants are subsequently transferred toward the interface through capillary forces which propagates the reaction. High resolution TEM and macro scale product collection techniques have revealed the presence of such reaction interfaces within the composite. Given the faster release of aluminum for the thermally treated samples, the inherent diffusion limit in the reaction would be alleviated resulting in a larger portion of the composite reacting at ignition, as demonstrated in Figure 9-4b, where the pressure, emission and temperature from the reaction in the combustion vessel is plotted vs. time from ignition. The time axis is truncated at 0.5ms as the emission intensity is observed to drop significantly resulting in high errors in measured temperatures. As can be clearly seen in Figure 9-4a, for untreated samples, the pressure profile is cyclical with similar pressure peaks whereas for the 300C Linear sample in Figure 9-4b, the initial pressure peak significantly outperforms the subsequent ones, implying a more extensive combustion of the composite at ignition. The cyclical pressure profile is due to the pressure wave reflecting off the cell walls but such waves must have attenuate in amplitude over time. The observation for the untreated samples where the cyclical pressure peaks have similar amplitude must suggest slow pressure release/reaction. In Figure 9-4a, the temperature fits (with grey error bars) are also shown where, upon ignition the sample temperature is observed to increase followed by a rapid drop to ~2900K just before peak emission. With the adiabatic flame temperature of Al-CuO calculated to be 2967 K,[40] this region

should correspond to bulk combustion of the composite following which the temperature is observed to rise to ~3500K. The temperature profile superimposed on the normalized emission intensity of two channels of the spectrometer is shown in Figure 9-4c (Untreated nAl) and Figure 9-4d (300C Lin) respectively. The channels were specifically chosen so as to compare the thermal component of the emission with that of AIO ($B^2\Sigma^+ \rightarrow X^2\Sigma^+ \Delta\nu=0$ band).[219] For thermal component, the channel covering a band from 832 – 843 nm (NIR) was chosen, devoid of any molecular emission and for the AIO channel, a band of 481-492 nm was chosen. Owing to the low resolution of the spectra, no direct fits to the molecular emission could be made, but owing to the strength of the AIO emission, temporal comparisons can be made so as to make inferences on the reaction mechanism. For a purely thermal event, the normalized intensities on both channels must superimpose each other, the lack of which for both samples suggest significant AIO emission. For the untreated samples in Figure 9-4a, the highest temperature regions correlate with local maximas of AIO channel, deviating from the NIR channel, suggesting gas phase combustion of aluminum with the oxygen released from CuO. The fact that this happens at longer durations suggest that upon ignition and subsequent combustion, significant portions of the aluminum remain unreacted and subsequently burn as micron scale droplets in the pressurized oxygenated environment sustained by the decomposition of CuO.[11,165,177] The annealed samples on the other hand, shows only slight deviation between the AIO and NIR bands with temperatures approaching

3500K after significant reduction in emission intensity. In both cases, the AIO channel is observed to decay slower than the NIR channel. Although the noise levels in the AIO channel is significantly high, it highlights the late gas phase combustion between aluminum and oxygen with the aluminum presumably existing as large micron scale droplets.

Upon further increase in the annealing temperature to 400C, the pressure response of the sample deteriorates significantly. A possible reason for this behavior could be that the aluminum nanoparticle could lose significant active content owing to shell growth resulting from being annealed in air, as reported in,[28] where amorphous alumina is postulated to grow from 300-550C. The measured temperatures are also lower than the other samples (Figure 9-2b), which could possibly be the result of the composite being fuel lean owing to significant loss of active aluminum during annealing. Other factors that govern reactivity, apart from annealing temperature, could be the state of the native oxide shell on the nanoparticles. Given the variations in shell inhomogeneities, shell thickness and the manufacturing technique, the pre-anneal temperatures for optimum reactivity could significantly change, making *a priori* estimates of the reactivity difficult, as presented in Ref.,[220] where optimum flame speed of nAl (different manufacturer)-MoO₃ composites was observed at an anneal temperature of 105 C with a significant dependence on the ensuing cooling rate. Although direct estimation of the governing factors in combustion of prestressed nAl could not be made, there seems to be a

general merit in prestressing the nanoscale aluminum particles for improving reactivity and is suggestive to be a strategy worth exploring owing to its simplicity and ease of scale up, given that commercially manufactured material could be directly used.

9.5 Conclusions

Aluminum nanoparticles (NPs) upon exposure to air develop an 3-5 nm amorphous alumina shell, which acts a diffusion barrier to the release of aluminum during reaction. Pre-annealing the aluminum NPs have been recently proposed as a viable, bulk processing, strategy to improve reactivity whereby the NPs are annealed to high temperatures so as to weaken the shell. In this work, batches of aluminum NPs annealed at 200, 300 and 400C were mixed with Copper Oxide NPs to make nanocomposite thermite and their performance was tested in a constant volume combustion cell. The combustion cell is coupled with a fast spectrometer, capable of measuring emissions spectra from the reaction pile at ~350 kHz, which was subsequently fit to Planck's law to obtain grey body temperatures. The results indicate that prestressing the Al NPs has a significant effect on the pressure metrics of the nanocomposites with the samples annealed at 300C showing a 36% improvement in pressure and 1000% improvement in pressurization rate, compared to that of the untreated samples. The Full Width Half Max (FWHM) burn time was also measured from the integrated intensity with the 300C annealed samples exhibiting the fastest

combustion durations. Quench rates of the annealed samples did not exhibit a significant effect on the performance of the composites. The faster release of aluminum in case of annealed samples was visualized using high heating rate Transmission Electron Microscopy (TEM) where, for the 300C annealed sample, the aluminum in the core was observed to diffuse out faster than for the untreated case.

9.6 Acknowledgements

This work was done in collaboration with Dr. Michelle Pantoya's group at Texas Tech University. The samples were prepared at Texas Tech by Kevin J. Hill, PhD student in Dr. Pantoya's group and were tested at UMD.

Chapter 10 Microscopic visualization of the reaction zone in 3D printed nanoaluminum PVDF composites

Summary

Nanoaluminum based composites containing reactive polymers such as Teflon (PTFE) and polyvinylidene fluoride (PVDF) have attracted much interest owing to their high reactivity, intense gas production, biocidal properties and flexible manufacturing. In this work, energetic thin films containing commercial nanoaluminum dispersed in a reactive binder (PVDF) is prepared by 3D printing. The thin films are printed directly onto cover glass slides and the reaction front propagation is observed using a high-speed color camera. In order to extract maximum information about the flame propagation, a microscope objective is used in conjunction with the camera lens in order to record high resolution videos (1 $\mu\text{m}/\text{px}$) of passing flame fronts. The color image of the flame front is further processed to extract temperature information using the principles of color camera pyrometry. In this chapter, the setup and some preliminary results are discussed and future work is outlined.

10.1 Introduction

Metallized propellants offer several advantages including high thrust and energy density, but one of its main disadvantages is the lack of throttling ability

which prevents single stage to orbit (SSTO) operation. A new direction within the propellant research community is the development of smart propellants called Electrically-Controlled Solid Propellants (ESPs) that can be electrically activated, which allows for on/off and throttling capabilities.[221] This is particularly possible with the incorporation of fluoropolymer binders in the propellant mix, which owing to their piezoelectric properties, allow electrical pulses to tune their sensitivity.[222] Polymers such as polyvinylidene fluoride (PVDF), polystyrene etc. are known piezoelectric materials and are extensively used in smart switches, pressure sensors, smart mirrors and microphones.[223] The high fluorine content in these polymers are particularly advantageous when it comes to metallizing these polymers, since they produce significantly more gas compared to oxygen containing oxidizers., resulting in higher pressure and pressurization rates.[46] Moreover, fluorine is the most electronegative element and its fluorination reaction with nanoaluminum, resulting in AlF_3 has a specific heat of reaction of 55.7 kJ/g which is 80% higher than the oxidation reaction to Al_2O_3 (31kJ/g).[46,208] Moreover, it has been shown that fluorine significantly weakens the protective alumina shell through pre ignition reactions resulting in significant improvements in flame speeds, particularly for nanoscale aluminum, where the oxide shell constitutes to a significant portion of the nanoparticle mass.[224]

Recent efforts at exploiting the aluminum fluorine exothermicity includes coating commercial nanoparticles with fluorinated acids,[214,225] generating

composites with polymer inclusions via mechanical activation[191] and generating microspheres[226] and thin films through electrospray.[196] The results highlight the improved thermal stability and decomposition of PVDF with addition of nanoaluminum. The protective oxide shell in the case of nanoaluminum plays a significant role in the overall reaction mechanism whereby the alumina is observed to catalyze the decomposition of PVDF into gas phase HF species which subsequently etches the alumina shell and reacts with the aluminum.[227] This is in contrast to the condensed phase reaction mechanism that has been observed for oxidation reactions between nAl and metal oxides. Such Pre-Ignition-Reaction (PIR) has been observed in other halide containing systems as well and is particularly crucial when nanoscale aluminum is used.[228] The processing advantages of PVDF with it being readily soluble has seen tremendous increase in its applications, particularly in energetic thin films where films with high mechanical strength have been manufactured which could sustain self-propagating combustion.[208] Most importantly, high metal loading of metal nanoparticles can be incorporated into these films, which has been a significant limitation owing to the drastic increase in viscosity of the polymer melt upon introduction of nanoscale materials with high surface area.[229–231] More recently, electro spun mats of metallized fibers have also been manufactured which highlight the versatility of this technique and act as a prelude to 3D printing composite solid propellants with high metal loadings.[196,197]

The recent proliferation of additive manufacturing techniques, particularly 3D printing, have found significant application in the field of energetic materials owing to complexities and limitation of traditional manufacturing techniques.[232] In addition to 3D printing, Electrophoretic deposition[233] and inkjet printing[234] have also been investigated as a route to manufacture multicomponent energetic composites. In this work, multilayer composites of commercial nanoaluminum and PVDF is 3D printed onto cover glass slides and the reaction front is imaged using a high-speed color camera. Moreover, in order to resolve the microscopic nature of the flame front, a microscope objective (40x) is mounted in front of the camera and the resulting video is post processed to obtain temperature maps, following the theory of color pyrometry.

10.2 Experimental

10.2.1 Sample Preparation

Commercial aluminum nanopowder (Al-NPs) (ALEX, Argonide, 50 nm) was used in this work. The active Al was 70% by mass determined by thermogravimetric analysis (TGA). PVDF (MW 534000) and DMF (99.8 wt %) was purchased from Sigma–Aldrich and were directly used as received. In a typical experiment, 600mg mixtures of Al-NPs and PVDF powders (Al-NPs and PVDF in equal measures, resulting in a stoichiometry of 3) was mixed in 5 ml of DMF. The mixture was prepared with the objective of high fuel loadings; hence a fuel rich stoichiometry was

chosen. Moreover, from preliminary tests, samples with a stoichiometry of 3 resulted in good adhesion to the substrate during printing and was empirically chosen. The mixture was first vigorously stirred for 2 h and then sonicated for 1 h, followed by 24 h magnetic stirring. The as prepared precursor was loaded into a syringe and installed onto the print head of a Hyrel 30M 3D printer (**Error! Reference source not found.**). Commercial cover glass slides (VWR, 0.17mm thickness) was laid onto the 3D printer bed, which was heated to 80C. After careful calibration of the needle tip's position with respect to the glass slides, the print job was initiated.

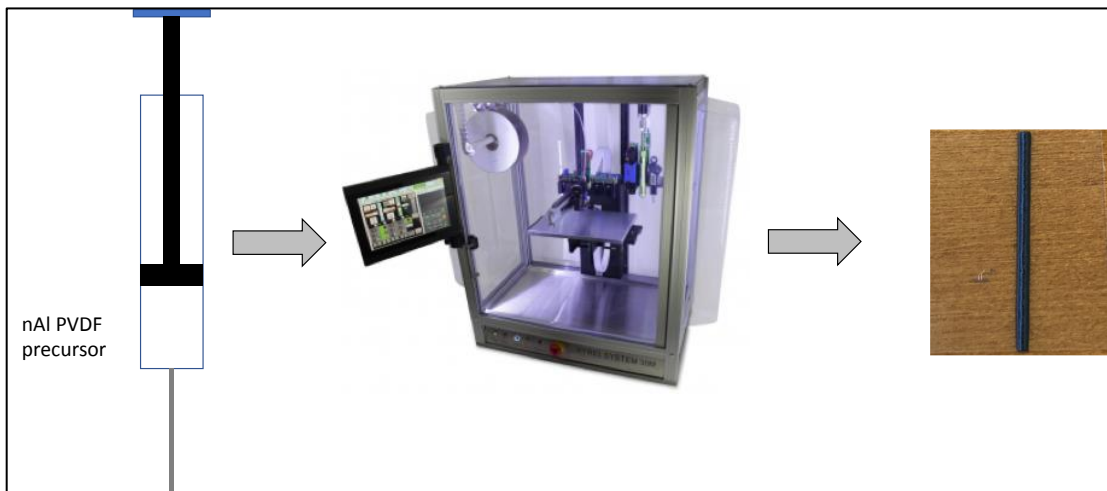


Figure 10-1: 3D printing setup with Hyrel 30 M.

10.2.2 Temperature Diagnostics

The color camera used in this study and the associated calibration for pyrometry is detailed in Chapter 2. In order to refine the highly dynamic flame front, a microscope objective was used in order to magnify the sample under observation. In this study, I used a Nikon 40x Plan Fluor objective, which has a working distance of

0.66mm and a high numerical aperture of 0.75. The microscope objective was focused on the backside of the cover glass slide on which the film was printed on, thereby allowing the visualization of the flame front without the generated products obscuring the view. A high numerical aperture is crucial since, upon magnification, the light intensity reduces significantly which subsequently increases the error in pyrometry measurements. The light collimated by the microscope passes through a beam splitter and is focused by the camera lens (Nikon 105mm Macro), focused at infinity. The third port of the beamsplitter cube houses a red LED (630 nm), which is collimated using a plano convex lens at $1f$. The collimated beam is reflected by the beam splitter and focused on the sample via the microscope and the scattered light from the sample is imaged by the camera for focusing purposes. The subsequent image of the region of interest is called 'Bright Field Image'. The camera was run at an exposure of $\sim 100\mu\text{s}$, owing to poor throughput at high magnifications, which in the current setup was $\sim 1\mu\text{m}/\text{pixel}$. A schematic of the optical assembly is shown in Figure 10-2.

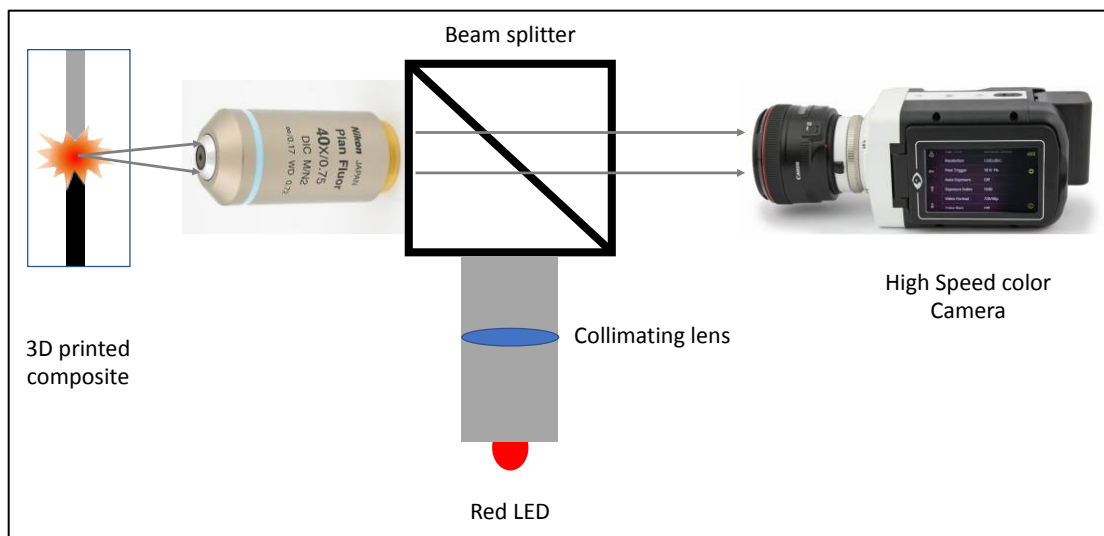


Figure 10-2: Optical assembly for high resolution imaging

10.3 Preliminary Results

High magnification image of the Al-PVDF film before ignition is shown in Figure 10-3. The film shown in Figure 10-3a was obtained using a fuel rich precursor ($\phi=3$) with 7 layers (~100 μm total thickness), where the bright spots correspond to coalesced polymer. This represents an ideal sample for videography since the composite exhibits good adhesion to the glass substrate. Figure 10-3b, shows a film with the same composition but with 14 layers. The sample exhibits poor adhesion with the glass substrate as evidenced by the interference fringe patterns which arise due to the sample being separated from the glass substrate due to excess polymer pooling up between the composite layer and the substrate. This phenomenon was observed in fuel lean and stoichiometric samples as well, where the fraction of PVDF in the precursor is high. Currently, efforts are ongoing in order to empirically choose

the ideal printing configuration to ensure satisfactory adhesion of the films to the substrate.

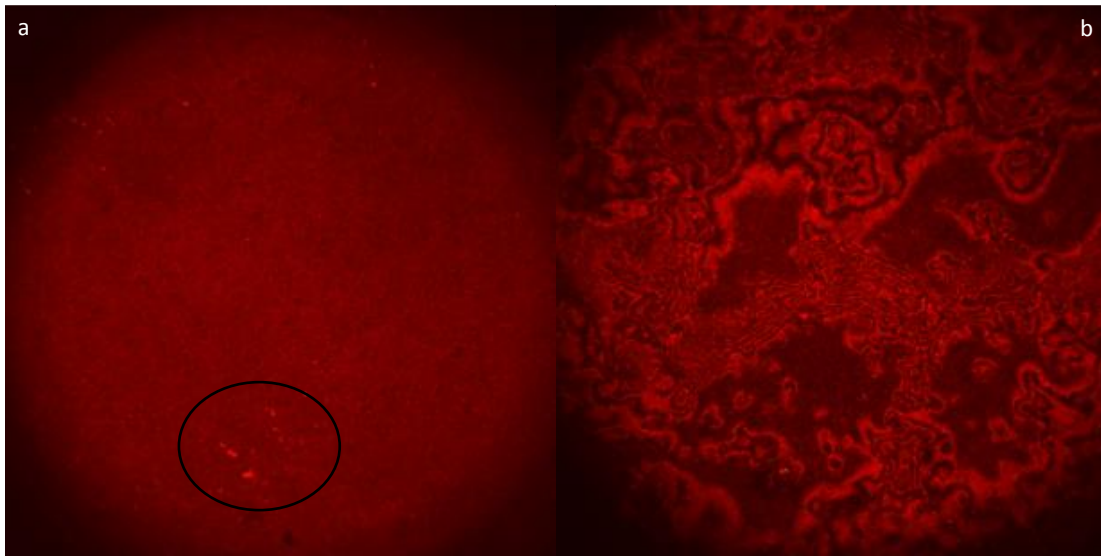


Figure 10-3: Pre-ignition images of fuel rich Al-PVDF film ($\phi=3$): a. 7 Layers and b. 14 Layers.

Figure 10-4 presents the high-speed microscopy images obtained before (Figure 10-4a) and during combustion (Figure 10-4b). The video was recorded at 6200 fps, which afforded a maximum exposure of 161 μs . As can be seen in Figure 10-4b, the flame front is highly corrugated and is characterized by a thin ($\sim 20 \mu\text{m}$) reaction front.

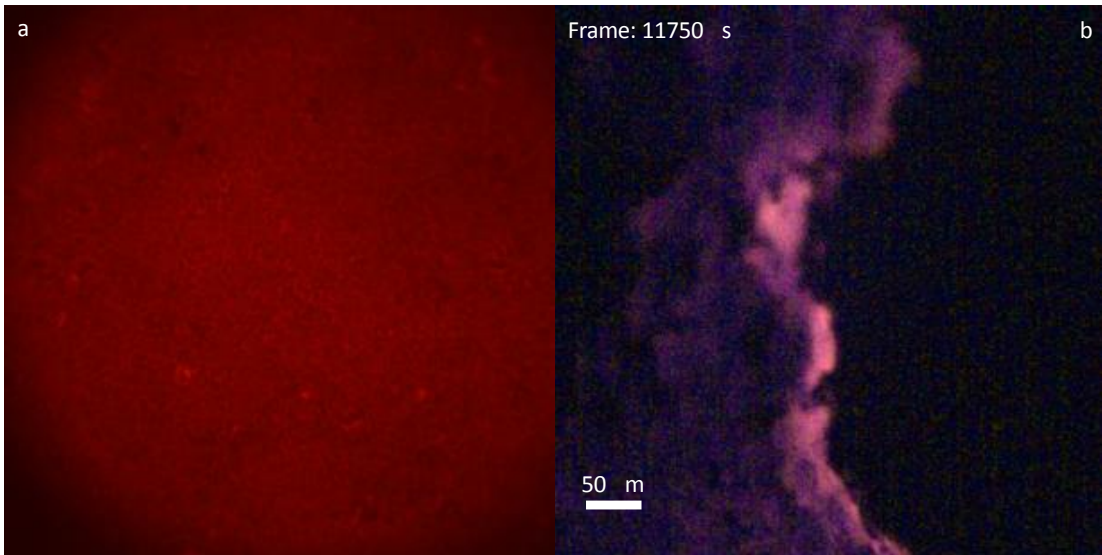


Figure 10-4: Combustion of Al-PVDF thin film, visualized using high speed microscopy (6200 fps, 161 μ s exposure).

The video was subsequently processed using color camera ratio pyrometry and the results are presented in Figure 10-5, where the RAW pixel data is presented along with the false color videos of the reaction front. As can be clearly seen, the flame front has a non-homogenous temperature distribution and is characterized by highly corrugated, fingerlike protrusions. In some cases hot spots and micro explosions could also be observed (3.5484 ms).

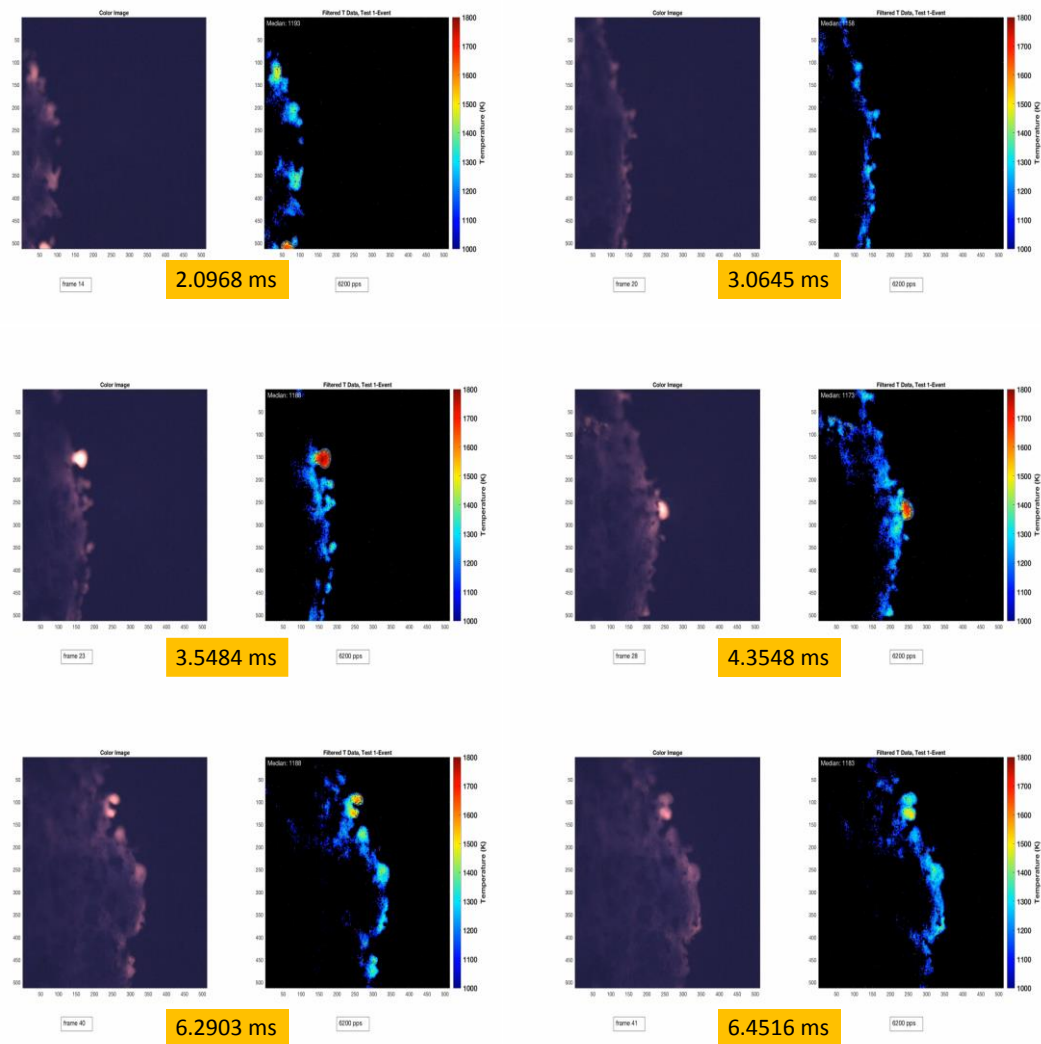


Figure 10-5: High speed pyrometry showing flame propagation

10.4 Discussion and Future work

The samples prepared in this study were directly printed onto the glass slides so as to facilitate direct imaging. A drawback of manufacturing the films in such a fashion is significant increase in the heat losses to the substrate. Since these films are postulated to propagate through the convection of hot product gases, having the film

adhered to the substrate could, to some extent hinder the global reactivity.[227] This could be one of the possible reasons for the low flame temperature of about 1800K when compared to the peak flame temperature for Al/PTFE (a fluoropolymer similar to PVDF), which was measured to be ~ 2500K.[174] Owing to the relative novelty of Al-PVDF composites, literature values on its combustion performance are sparse hence mechanistic corroborations are difficult to make based on the current results. Experiments are currently planned to probe the combustion of these composites under a variety of conditions so as to develop a more holistic mechanistic picture.

The ability to visualize the combustion along with an added layer of temperature distribution is a powerful tool to study such condensed phase systems. Experiments resolving micron scale features in composites have been previously employed in studying shock propagation, where gated CCD cameras were used to take very fast snapshots of the composite under shock loading, with the emission being quantified using emission spectroscopy.[235] The apparatus presented in this chapter allows for the quantification of emission with high temporal and spatial resolution. Future work would involve testing the effect of composition and number of layers on flame speed and temperature. Particularly, the factors that govern the development of the flame front into the highly corrugated fingers, as depicted in Figure 10-5, and its relationship to global flame propagation is of interest. Once the controlling parameters are established, new formulations incorporating dopants in the Al-PVDF matrix could be studied. A recent publication in this direction incorporated

mesoporous silica particles in the Al-PVDF matrix and the resulting composite exhibited a 3X increase in burn rate.[236] The results were phenomenologically explained based on the low thermal conductivity of mesoporous SiO_2 acting as a heat transfer barrier leading to the generation of hot spots. Such hot spots were proposed to augment the germination of multi-ignition spots which consequently increased the flame area and radiative feedback resulting in the increased flame speeds (Figure 10-6).

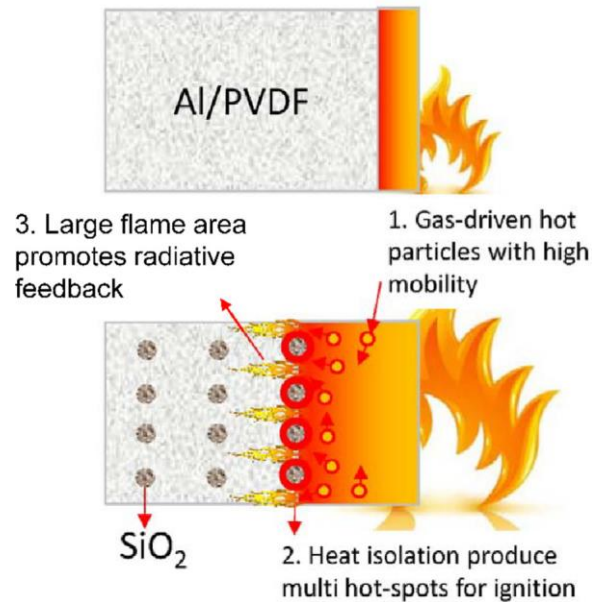


Figure 10-6: Phenomenological reaction mechanism for Al-PVDF composites doped with Silica mesopsheres.[236]

10.5 Conclusions

Fluoropolymer based nanoaluminum composites are of interest to the propulsion community owing to their piezoelectric properties which allow for throttling and on/off capabilities of such solid propellants. In this work, high metal

loading ($\phi=3$) composites containing commercial nanoaluminum and PVDF were prepared and was 3D printed as a multilayer geometry onto glass substrates. The simplicity of the additive manufacturing technique allow straightforward variations in sample composition and number of multilayers. The printed samples were subsequently ignited and the flame propagation front was recorded from the substrate end using a 40X microscope objective couple with a high speed camera. The resulting video is processed using color camera pyrometry technique, which aided in characterizing the temperature of the reaction front. The preliminary results revealed a highly corrugated flame front with average temperatures of ~ 1400 K and several instances of hot spot formation (1700 K) could also be observed. These results lay the groundwork for further experiments into 3D printed propellants so as to develop a holistic understanding of the reaction mechanisms at the microscale.

10.6 Acknowledgements

I want to thank Noah Eckman and Haiyang Wang for assistance with the sample preparation and 3D printing.

Chapter 11 Summary

11.1 Conclusions

As introduced in Chapter 1, nanocomposite energetic materials (nEM), of which nanothermites is a subset, have several advantages over their microscale counterparts and traditional organic energetic materials. However, their direct application in the fields of energetic materials provide diminished returns in terms of burn rate. Developing a detailed understanding of the limiting mechanisms in nanothermite reactions is the objective of the research presented in this dissertation. Compiling the presented results, a comprehensive picture of the dominant reaction mechanism is outlined following which, novel composites were synthesized to enhance and tune the reactive properties of the energetic composites. Also, an underlying theme of the novel synthesis routes adopted in this study reflect quick scale up abilities, which is essential for ensuring extensive applicability.

Quantifying the highly dynamic combustion domains of these nanoscale composites that burn on the sub-millisecond timescale require advanced diagnostics that can resolve temporal, spatial and molecular features in the reaction front. Accordingly, two high-speed, non-invasive diagnostics were developed to characterize and quantify the emission from the nEM reactions. A high-speed emission spectrometer, capable of spectrally resolving the visible light from the reaction, is introduced, designed and calibrated in Chapter 2. The spectrometer is

capable of a temporal resolution of $\sim 2.5 \mu\text{s}$, which is sufficient for the characterizing nEMs, whose reactivity is observed to be between fast explosives and slow deflagrations. Owing to the lack of spatial resolution of the spectrometer system, a complementary diagnostic based on a commercial high-speed color camera is also developed so as to record high speed videos of the reaction. The resulting videos are processed to account for the spectral response function of the filters, detector and the optics to output high resolution spatial temperature maps of the combustion event.

Understanding the global reaction mechanism of nEMs essentially require an adequate understanding of the reaction mechanism of metal nanoparticles. This was undertaken in Chapter 3, where an atmospheric pressure laser ablation system attached with a differential mobility analyzer (DMA) was used to produce size-resolved metal nanoparticles of titanium and zirconium in the range of 20-150 nm which were subsequently ignited and burnt in a hot, oxidizing environment. The particles of both Ti and Zr were observed to exhibit clear short emission streaks after ignition, which are quite different from those observed for micro-sized particles. From the TEM images it was deduced that the particles coalesce during combustion and transform from aggregates to sintered spherical particles. After accounting for the effects of sintering I found that the burn time obeys a near d^1 power law. Additionally, the emission intensity profile from individual particles was found to best fit a shrinking core model that was limited by the surface oxidation kinetics. This result implied that the nanoparticle aggregates coalesced rapidly when exposed to a high

temperature environment and that their subsequent reaction is characteristic of the coalesced particle as opposed to the initial nanosized material.

The global effects of nanoparticle coalescence on the reaction mechanism of nanothermites were probed in Chapter 4 and Chapter 5. Through forensic analysis of the rapidly quenched combustion products of nanothermite composites, it was found that the products were ~2 orders of magnitude larger than the nanoscale reactants. Through simple scaling arguments it was identified that the dominant reaction mechanism was that of reactive sintering, which is a byproduct of rapid nanoparticle coalescence. Although such a mechanism is detrimental to the specific surface area and the diffusion distances, it also aids in the development of enhanced interfacial contact between fuel and oxidizer. Such interfaces act as an avenue for the condensed phase reactions between fuel and oxidizer ions, resulting in heat generation. The reaction is postulated to propagate with the transfer of molten unreacted components to the reaction interface through capillary forces. The reaction mechanism thus identified was found to be universally applicable irrespective of the composition of the nanothermite used and the results were found to be consistent with those obtained from high resolution microscopy of these nanothermites, where an ultrafast loss of nanostructure (~ 300ns) was found to dominate the reaction at initiation. The collected products were further probed using focused ion beam milling in order to gauge the extent of reaction by analyzing the chemical composition of the interior. The elemental analysis of the product particle cross section revealed that for

nanothermite compositions, where the oxidizer has a low propensity to decompose into gaseous oxygen (Al/WO₃ and Al/Bi₂O₃), the interior revealed a higher oxygen content, implying a higher extent of reaction. This was correlated on the macroscopic scale with bomb calorimetry experiments, where the Al/WO₃ and Al/Bi₂O₃ nanothermite systems were observed to approach their theoretical heats of reaction to a greater extent than Al/CuO. The product particle sizes were estimated from the SEM images via image processing and were found to be in the order: Al/Bi₂O₃ < Al/CuO < Al/WO₃, which correlated with the total predicted gas release from each nanothermite system: Al/Bi₂O₃ > Al/CuO > Al/WO₃. This implies that strong gas generation during thermite reaction could have a significant effect on inhibiting sintering by breaking apart the aggregated reactant nanoparticles, thereby reducing the effective diffusion length scales for condensed phase species transport. The reaction completion, found using bomb calorimetry scaled as Al/Bi₂O₃ > Al/WO₃ > Al/CuO with the poor performance of Al/CuO system attributed to the gaseous oxygen release from the decomposition of CuO thereby limiting the availability of oxidizers in the condensed phase. The results imply that condensed phase reactions are capable and more efficient at ensuring fast reactivity since gas phase reactions often occur over longer durations.

The main takeaway from the previous chapter is the beneficial effect of in situ gas generation on reactivity. The next set of chapters aim at improving the reactivity of the nEM composite by altering, independently, the three basic constituents of a

composite: (1) Oxidizer, (2) Binder and (3) Fuel. Chapter 6 focuses on tuning reactivity of nanothermites composites by altering the composition of the oxidizers in a stoichiometric mixture of Al/Fe₂O₃/WO₃. Seven mixtures of Al/Fe₂O₃ were doped with varying amounts of WO₃ to manipulate the primary reaction mechanism from gas-generating (Fe₂O₃) to condensed-phase (WO₃). While pressure, pressurization rate and burn time correlate with mixture fraction, temperature was relatively insensitive once a threshold addition of WO₃ was achieved. It was proposed that the faster initiation of the Al/WO₃ reactions leads to a greater flame temperature and thereby leads to a greater degree of reduction of Fe₂O₃ to suboxides and O₂ (g). The high oxygen release also results in flame temperatures in excess of the Al/Fe₂O₃ adiabatic flame temperature and reflects the burning of Al in an oxygen environment. The relative interplay between the competing reaction mechanisms were captured in pyrometry videos where an enlarged reactive cloud size and faster reaction times were observed with increasing amounts of WO₃ up to the 70% mark. This work highlights the ability of tuning the nanocomposite reactivity for specific applications by means of complementary reaction mechanisms.

Chapter 7 and Chapter 8 focus on the possibility of incorporating energetic binders as a means for artificial gas generation within the nEM composite. Novel nanocomposites of commercial aluminum nanoparticles (NPs) (Chapter 7) and nanothermites (Chapter 8) that incorporate nitrocellulose as an energetic binder were manufactured via one step electrospray method. Nitrocellulose satisfies the dual role

of a binder as well as a low temperature gas generator (dissociation temp ~ 450 K), thereby aiding in the disaggregation of the composite before significant reaction and ensuring that the nanostructure inherent in the initial starting material is more effectively utilized. By packaging the nanoparticles into larger *micron scale* composites, I was able to simultaneously utilize the potential benefits of nanoscale materials, such as high surface area and reactivity, as well as the processing and heat retention benefits of micron scale composites. In Chapter 6, commercial aluminum NPs were assembled into mesoscale composites and their combustion performance was compared with parent commercial nanopowder to gauge enhancement. It was found that the mesoparticles burnt as fast as the smallest aggregates in the commercial aluminum NPs and had a much narrower distribution of burn times than nanoaluminum. This effectively implies that the dispersive effects of insitu gas generation is forcing the NPs to combust as small aggregates thereby leading to an order of magnitude reduction in burn times and substantially smaller products. This latter point should also lead to a more complete reaction, based on the results in Chapter 5. The experiments were further extended to incorporate nitrocellulose in nanothermite composite (Chapter 8) where high speed temperature and pressure measurements were made in addition to bomb calorimetry so to quantify and compare the reaction metrics of these novel composites with their traditionally mixed counterparts. The results indicate, as expected, a higher combustion performance with higher pressure and pressurization rate irrespective of the nanothermite composition.

The extent of reaction completion was also tested and was found that the ES assembled composites did attain a higher extent of reaction compared to the physically mixed baseline mixtures. Moreover, the morphology of the composite was also varied by tuning the precursor loading, and the results indicate that more open/porous composites performed better than compact versions. This can be attributed to the improved convective transport of the generated gas in porous matrices as opposed to compact counterparts.

The results presented thus far perturbed the Oxide and Binder attributes of the composite. The last component is the fuel, in this case nanoaluminum, that can be tuned to improve reactivity. In the work presented in Chapter 9, the inert oxide shell that naturally passivates commercial aluminum nanoparticles and acts as a diffusion barrier was weakened through thermal annealing. The treated aluminum was subsequently mixed with CuO to make nanothermite composite, whose combustion performance was gauged and benchmarked against untreated samples. The results indicate that annealing the Al NPs had a significant effect on the pressure metrics of the nanocomposites with the samples annealed at 300C showing a 36% improvement in pressure and 1000% improvement in pressurization rate, compared to that of the untreated samples. The Full Width Half Max (FWHM) burn time was also measured from the integrated intensity with the 300C annealed samples exhibiting the fastest combustion durations. The faster release of aluminum in case of annealed samples was visualized using high heating rate Transmission Electron Microscopy (TEM)

where, for the 300C annealed sample, the aluminum in the core was observed to diffuse out faster than for the untreated case.

The results presented in the aforementioned chapters cumulatively identified the limitations of a high speed condensed phase interfacial reaction on the overall reactivity of nanothermite composites and attempted to tune the reactivity by means of three knobs: (1) change the oxidizer composition, (2) change the microstructural assembly with binder and (3) altering the fuel properties. In the final chapter of this dissertation, a new composite based on nanoaluminum and PVDF was analyzed as a potential propellant. This novel composite ticks all the three aforementioned ‘tuning knobs’ since: (1) PVDF is a fluoropolymer whose fluorination reaction with aluminum is more exothermic than aluminum oxidation, (2) PVDF is also a gas generating polymer and fills the role of nitrocellulose in the previous studies and (3) PVDF decomposition is catalyzed by alumina therefore the alumina shell on the nanoparticles are consumed to some degree by PVDF and the resulting HF gas. Chapter 10 lays the experimental groundwork for future tests on Al-PVDF composite as a candidate for 3D printed solid rocket propellants. In this work, multilayered, fuel rich, Al-PVDF composites were 3D printed onto a glass slide and the reaction front was characterized by high speed color camera pyrometry. The highly carbonaceous products of PVDF reaction allowed the use of grey body approximation in deducing the reaction temperatures. The preliminary results revealed a highly corrugated flame front with average temperatures of ~ 1400 K and several instances of hot spot

formation (1700 K) could also be observed. These results lay the groundwork for further experiments into 3D printed propellants so as to develop a holistic understanding of the reaction mechanisms at the microscale.

11.2 Recommendation for future work

11.2.1 Characterizing the applicability of nEM composites as nanofuel additives

The high volumetric energy content and specific enthalpy of combustion of metal nanoparticles makes them attractive candidates for burn augmenting additives in liquid propellants. Historically, micron-sized metal particles have been used extensively as an additive to increase the energy content of solid and gelled propellants. Nanoparticles (with diameters between 1-100 nm), on the other hand, due to their shorter ignition delays, higher burning rates and specific surface area could be better suited to liquid propellant incorporation since they can replace traditionally non-energetic gelling agents and boast lower settling velocities than larger particles. The nanocomposites synthesized in this dissertation could be another attractive candidate for the role of burn rate enhancer in nanofuels. Preliminary work highlighting the beneficial effects of nanoaluminum based mesoparticles on the combustion characteristics of kerosene droplets were presented by Guerieri et al. [237], where a maximum 26% improvement in burn rate constant was observed with the incorporation of nAl based meso particles.

In the proposed work, the high-speed diagnostics developed as part of this dissertation could be used as a means to characterize the mechanisms underpinning the enhanced burn rate. Particularly, the role of gas generator as a source of micro explosions in the fuel droplets could be evaluated with high spatial resolution using the color camera pyrometer. Moreover, the well-developed emissivity models for soot oxidation can be readily used to obtain flame temperatures. The contribution of nanoaluminum to the overall droplet combustion could also be evaluated using emission spectroscopy, where the emission from key species such as Al vapor (394, 396 nm) and AlO (480-50 nm) could be tracked along with the droplet burn. Preliminary work in this direction was performed as part of a collaboration with Dr. Philip Guerieri, where single droplet combustion of triisobutylaluminum (TiBAI) dissolved in toluene was examined with the optical diagnostics. Highly reproducible droplets were generated in a custom-built tower and individual droplets were analyzed during free falling combustion. The combustion was recorded and processed to reveal the soot temperatures, as shown in Figure 11-1, where the effect of the disruptive behavior of TiBAI additive is clearly seen in Figure 11-1b. A significant spike in molecular AlO emission intensity could be observed concomitantly with disruptive behavior, which in this case was attributed to the participation of the additive during the combustion of toluene. Similar experiments could be done to understand the role of nitrocellulose, nanoaluminum and nanocomposite thermites as possible rate enhancing additives in liquid fuels.

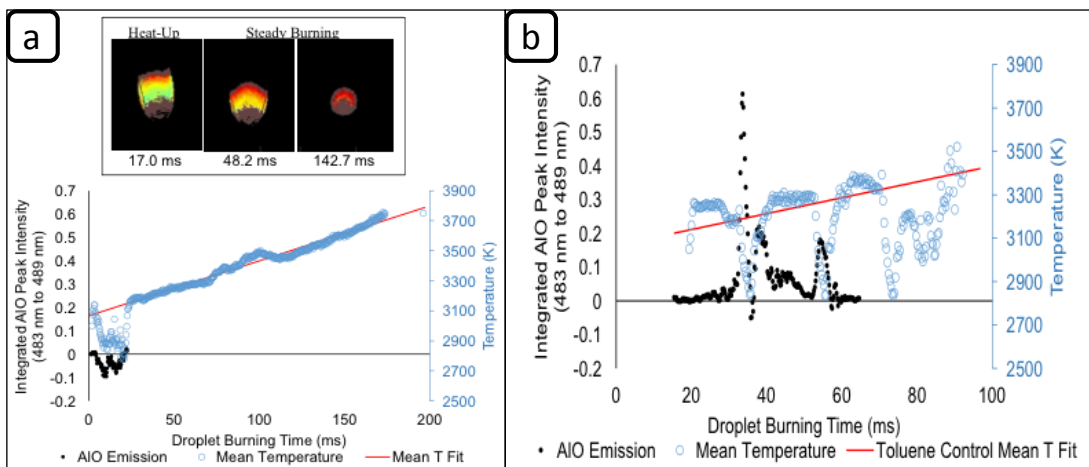


Figure 11-1: (a) Toluene control sample (Top): color camera pyrometry is used to measure the flame temperature, (bottom) which is spatially averaged and temporally plotted. (b) 810 mM of TiBAI in toluene. The spatially average temperature is plotted (blue dots) along with the baseline temperature of the pure toluene (red line) from (a). The black dots are regions of heightened AIO emission as obtained from the spectrometer which was run simultaneously with the color camera to track the droplet. Droplet leaves spectrometer view at 65 ms. Disruptions at 35, 55 and 73 ms.

11.2.2 High resolution imaging of planar reaction fronts

The results on reaction front imaging presented in Chapter 10 offer an insightful method into understanding the microscale evolution of nanocomposite reactions. The field of high resolution, high frame rate optical imaging is still in early stages of development with efforts being directed using plasmonic gratings to achieve super resolution imaging.[238] Although the preliminary results look promising, the high magnification involved significantly reduced brightness at the image plane, which limits the exposure and therefore the frame rates that can be used for videography. A workaround could be achieved by using high speed image intensifiers (HICATT, Lambert Instruments) that could directly couple with existing high-speed

camera machinery and improve the overall sensitivity of the system. The optical assembly would be significantly more complicated than the one shown in Chapter 10, with the need for monochrome camera sensor but with the commercial high-speed cameras achieving frame rates as high as 1 million fps, it could offer a completely novel perspective to analyzing reaction fronts where microsecond temporal resolution could be combined with micrometer spatial resolution at atmospheric conditions.

Appendix A: Matlab Script for Pressure Cell Spectroscopy

```
%% Temperature measurement in pressure cell based on the gains found
using Avantes lamp

% Last edited on 3/6/18- RJ
% This code is used for measurements with pressure cell.
% Derived from Tmeasure_PressureCell_PMT_edit.m
% check before run: TimeBuffer; linearity limit (default
CurrentLimit = 25 uA);
% Variables to open : DataGroup 9,name,6,8,10,7,4
% _____

clear variables;
addpath ('/Users/Rohit_Jacob/Desktop/7_Spectroscopy/Code',
'/Users/Rohit_Jacob/Desktop/7_Spectroscopy/Code/Scripts/Functions');

[chWave,chWid] = channelWavelengthGen(658,150,'09292017');
% spectrometer CW and grating (1/mm)
GainStruct = load('/Users/Rohit_Jacob/Desktop/7_Spectroscopy/Gain
calibrations/150 lmm grating/HAL CAL
AlignedSpec/658nm_100um_092917/Pressure Cell
ND2/12302017/PCF658_092917_ND2_123017_Clean.mat');
fieldName = fieldnames(GainStruct);
GainArray = GainStruct.(fieldName{1});
NumChan = 32;

Foldername = {
% '/Users/Rohit_Jacob/Desktop/8_Pressure Cell Temp/Pantoya
Samples/DAQ Data/12212017 Stoic PreStressed/Unt/Run3';...
'/Users/Rohit_Jacob/Desktop/8_Pressure Cell Temp/Pantoya
Samples/DAQ Data/12212017 Stoic PreStressed/200L/Run4';...
};

SaveFolderName = '/Users/Rohit_Jacob/Desktop/8_Pressure Cell
Temp/Pantoya Samples/Processed Data/12212017 Stoic
PreStressed/Updated Prate Params/';

%% Import Pressure, PMT & IR channel data

for fileNum = 1:size(Foldername,1)

    clearvars -except Foldername SaveFolderName fileNum chWave chWid
GainArray NumChan;
    cd(Foldername{fileNum});
    s=dir('C*.dat');
    SpecFileName = dir('*.txt');
    SpecFileName = fullfile(pwd,SpecFileName.name);
```

```

P = load(s(1).name);
ScopeSampleInt = round(diff([P(1,1),P(2,1)]),9);
% rounding off to nearest nanosecond

P(:,2) = smooth(P(:,2),1e-6/ScopeSampleInt,'moving');
% change smoothing sample (use 1us as default)
P(:,2) = P(:,2)*1000*6.9/1.01;
% mV to kPa
OrigMaxP = max(P(:,2));

D = load(s(2).name);
if D(find(abs(D(:,2))==max(abs(D(:,2))),1),2)<0
    D(:,2) = (-1)*smooth(D(:,2),1e-6/ScopeSampleInt,'moving');
else
    D(:,2) = smooth(D(:,2),1e-6/ScopeSampleInt,'moving');
end

D(:,2) = D(:,2)*1000/50;
% 50 ohm termination convert to mA; let this statement execute for
Diode cases

f1 = figure('units','normalized','outerposition',[0 0 1 1]);
plot(P(:,2));
hold on;
P_filt = medfilt1(P(:,2));
% Default medfilt 3 pt
plot(P_filt);
plot(smooth(P_filt,100,'moving'),'-k');

yyaxis right;
plot(D(:,2),':b');
hold on;
plot(smooth(D(:,2),100,'moving'),'--r');

legend('P 5 pt smooth','P medfilt','medfilt 100 pt
smooth','diode 5 pt smooth','100 pt smooth');
title('Do you want to keep 100 pt smoothing ? ');

set(gca,'FontSize',20);
checkSmooth = input('Do you want to keep 100 pt smoothing (0=
none, 1= both, 2= P only, 3= D only ? ');
if checkSmooth == 1
    P_filt = smooth(P_filt,100,'moving');
    D(:,2) = smooth(D(:,2),100,'moving');

elseif checkSmooth == 2
    P_filt = smooth(P_filt,100,'moving');

elseif checkSmooth == 3
    D(:,2) = smooth(D(:,2),100,'moving');

```

```

end
close(f1);

[ChIR,TimeStamp] = importCh(SpecFileName,3);
ChIR = medfilt1(ChIR);
% change filtering methods here
ChIR = smooth(ChIR,5,'moving');
DaqTimeStart = TimeStamp(1);
TimeStamp = TimeStamp - DaqTimeStart;

%% Selecting the start point thresholds for IR channel

[~,NoiseIndex] = max(ChIR);
ChIRThreshold =
round(1.5*max(ChIR(1:round(0.85*NoiseIndex))),2);           % 50%
higher than background noise
ChIRStart = find(ChIR>ChIRThreshold,1);

% For Fast thermites*****
ChIREnd = (ChIRStart + 1000) + find(ChIR((ChIRStart + 1000):end)
< ChIRThreshold,1) - 1;

% For Slow thermites***** since light intensity <0
before peak pressure
% ChIREnd = (ChIRStart + 100) + find(ChIR((ChIRStart +
100):(ChIRStart + 10000)) > ChIRThreshold,1,'last') - 1;

% this method is better since all data points are imported

%% Import spectra, aquisition variables and wavelength bands

par = importpar(SpecFileName);
t_int = par(1,1);
% in us
srate = par(3,2);
volt = importvolt(SpecFileName);
GainVector = GainArray(GainArray(:,1)==volt,3:34);
CalibIntTime = GainArray(GainArray(:,1)==volt,2);
% CalibIntTime in us
TimeBuffer = 5e-3;

SampleBuffer = round(TimeBuffer*srate);
% number of buffer samples to ensure all data points are imported
imp_d = importfile(SpecFileName,(ChIRStart-
SampleBuffer+18),(ChIREnd+SampleBuffer+18));
[r,c] = size(imp_d);

ChannelData(:, :) = imp_d(:,6:NumChan+5);
% 32 channels

```



```

    DaqTS = imp_d(:,38)-DaqTimeStart;
% imp_d starts from ch1Start-preTriggerSamples; keep the time from
trigger

    %% Molecular emission check

    [~,temp] = max(ChannelData(:,3));
    f1 = figure('units','normalized','outerposition',[0 0 1 1]);
%     molTestSpectra = bsxfun(@times,mean(ChannelData(temp-
10:temp+10,1:NumChan)),GainVector);

    plot(1:32,mean(ChannelData(temp-
10:temp+10,1:NumChan)), 'LineWidth',3);           % average of 21 spectrum
so as to check the presence of any molecular emission
    grid on;
    ax1=gca;
    ax1.Position = [0.1300    0.1100    0.7750    0.7150];
    ax1.XTick = 1:NumChan;
    ax1.XLim = [1,32];
    ax1.FontSize = 20;
    ax1.XLabel.String = 'Channel';
    ax1.XLabel.FontWeight = 'bold';

    T1 = (num2str((chWave(1,:)*1e9)));
    T2 = (num2str((chWave(2,:)*1e9)));
    T3 = [T1, repmat(' - ',32,1),T2];
    C = fliplr(cellstr(T3)');
    clear T1 T2 T3;

    pos = [0.1300    0.1100    0.7750    0.750];
    ax2 =
axes('Position',pos,'XAxisLocation','top','YAxisLocation','right','C
olor','none','XLim',[chWave(3,end) chWave(3,1)]*1e9);
    ax2.YTick = [];
    ax2.XTick = fliplr(chWave(3,:)*1e9);
    ax2.XDir = 'reverse';
    ax2.XTickLabel = C;
    ax2.XTickLabelRotation = 45;
    ax2.FontSize = 15;
    ax2.XLabel.String = 'Wavelength (nm)';
    ax2.XLabel.FontWeight = 'bold';

    checkMol = input('Are there any sharp peaks/ broken points that
are prominent in the spectra ? Enter the X axis positions as an
array ([1,5,z])');
    close(f1);

    %% Smoothing Data and Baseline Selection
% using 20 uA as the limiting pulsed current for linear range

```

```

    CurrentLimit = 25;
% in uA
    ChargeLimit = CurrentLimit*t_int;
% in pC

    CD = zeros(size(ChannelData));

    testCh = input('Enter 3 Channels to test Smoothing..');
% [5,15,22] for Bi, [5,22,30] for Cu,W and Fe

    f1 = figure('units','normalized','outerposition',[0 0 1 1]);
    h1 =
plot(1:r,ChannelData(:,testCh(1)),1:r,ChannelData(:,testCh(2)),1:r,C
hannelData(:,testCh(3)));
    hold on;
    title('Smoothing');
    check = 1;
    while check
        Smoother = input('Enter smoothing paramter (1-50). 1 for no
change...');
        for i = 1:NumChan
            CD(:,i) =
smoothdata(ChannelData(:,i),'movmean',Smoother);
        end
        h2 =
plot(1:r,CD(:,testCh(1)),1:r,CD(:,testCh(2)),1:r,CD(:,testCh(3)),'Li
neWidth',2);

        check = input('Improve Smoothing ?...');
        if check
            delete(h2);
        end
    end
    close(f1);

    ChannelData = CD;
    clearvars CD testCh;
    Baseline = 0.12;

    f1 = figure('units','normalized','outerposition',[0 0 1 1]);
    plot(ChannelData);
    hold on;

plot([1,size(ChannelData,1)], repmat(Baseline,1,2), [1,size(ChannelDat
a,1)], repmat(ChargeLimit,1,2), 'LineWidth',4);
    set(gca,'FontSize',20);
    yyaxis right;
    plot(diff(DaqTS),'.r');
    title('Is Baseline OK');
    check = input('Is Baseline OK...');

```

```

while ~check
    Baseline = input('New Baseline...');
    yyaxis left;

plot([1, size(ChannelData,1)], repmat(Baseline,1,2), 'LineWidth',4);
    check = input('Is Baseline OK...');
end
close(f1);

%% Filtering Data

NaNcounter = zeros(r,1);
[LimRow, LimCol] = find(ChannelData <= Baseline | ChannelData >
ChargeLimit);

ProcessedChData =
bsxfun(@times, ChannelData(:,1:size(GainVector,2)), GainVector);
    Radiance = ProcessedChData;
% for plotting
    Radiance(Radiance<0) = 0;
    IntegratedIntensity = sum(Radiance(:,1:32),2);
% sum(Radiance(Radiance<0)=0) also gives same results
%     NormIntegIntensity =
cumsum(IntegratedIntensity)/sum(IntegratedIntensity);

    for i = 1:size(LimRow,1)
        ProcessedChData(LimRow(i), LimCol(i)) = NaN;
% get rid of all OR (Out of Range) data points
    end

    if checkMol
        ProcessedChData(:, checkMol) = NaN;
% for molecular emission
    end

    for i = 1:r
% Count the number of NaN in each row so as to know which were
removed
        if imp_d(r,3) == 1 || imp_d(r,4) == 1
            ProcessedChData(r,:) = NaN;
% If file shows Input Error or Out of Range
        end
        NaNcounter(i) = sum(isnan(ProcessedChData(i,:)));
    end

    ProcessedChData = [ProcessedChData DaqTS];
% need time stamp when getting rid of rows with NaN > threshold

    j = 1;
    for i = 1:r

```

```

        if NaNcounter(i)<21
% threshold of NaN's in array
            UpdatedProcessedChData(j,:) = ProcessedChData(i,:);
            j = j+1;
        end
    end

    ProcRow = size(UpdatedProcessedChData,1);
% updated size of ProcessedChData

    %% Temp measure Grey body fit

    TransposeTemp = zeros(ProcRow,1);
    GreyTemp = zeros(ProcRow,1);
    Error = zeros(ProcRow,2);
    GreyError = zeros(ProcRow,2);
    Residual = zeros(ProcRow,1);

    AbsIntensityData = zeros(ProcRow,NumChan);
%     IntensityDataNorm = zeros(ProcRow,NumChan);

    warning('off','all');
    for i = 1:ProcRow
        AbsIntensityData(i,:) =
UpdatedProcessedChData(i,1:NumChan)*CalibIntTime/(t_int*chWid);

% no diff if chWid is removed
%     AbsIntensityData(i,:) =
AbsIntensityData(i,:).*chWave(3,1:NumChan); % emisivitty
approximation (1/lamda)

        normCh = find(~isnan(UpdatedProcessedChData(i,1:32))==1,1);

        Output =
TempFit(AbsIntensityData(i,:),chWave(3,1:NumChan),normCh,2);

        GreyTemp(i) = Output.Greybody_temp;
        TransposeTemp(i) = Output.Transpose_temp;
        Residual(i) = Output.ResNorm;
        GreyError(i,1) = GreyTemp(i)-min(Output.Greybody_Error);
        GreyError(i,2) = max(Output.Greybody_Error)-GreyTemp(i);

        Error(i,1) = TransposeTemp(i)-min(Output.Error);
% Negative Error
        Error(i,2) = max(Output.Error)-TransposeTemp(i);
% Positive Error

% Output.Error is already formatted as [max,min]
        disp(i);
    end

```

```

warning('on','all');

GreyTemp(Residual > 0.5) = NaN;
% use only data if residual less than 0.5 (random)
GreyError(Residual > 0.5,:) = NaN;
SmoothGreyTemp = smooth(GreyTemp,3,'moving');
SelectTransposeTemp = TransposeTemp;
% Change smoothing parameter for temperature here
SelectTransposeTemp(Error(:,1)>350 | Error(:,2)>350) = NaN;

%% Finding Data Windows
%% Integrated Intensity
[IntMax,IntLoc] = max(IntegratedIntensity);

f1 = figure('units','normalized','outerposition',[0 0 1 1]);
plot(IntegratedIntensity);
title('Please select the point to end the noise window for
32Ch Integrated','FontSize',20);
[XLocs,~] = ginput(1);
close (f1);

XLocs = round(XLocs);
intThreshold =
round(1.1*max(IntegratedIntensity(1:XLocs)),3);
intStart = find(IntegratedIntensity>intThreshold,1);

%% Pressure
[~,PressureImportStart] = min(abs(P(:,1)-
DaqTS(1)+TimeBuffer)); % first light always precedes the
pressure signal
[~,PressureImportEnd] = min(abs(P(:,1)-DaqTS(end)-
TimeBuffer));
PressureImport =
[P_filt(PressureImportStart:PressureImportEnd),P(PressureImportStart
:PressureImportEnd,1)];

f1 = figure('units','normalized','outerposition',[0 0 1 1]);
plot(PressureImport(:,1));
title('Please select the point to end the noise window for
Pressure','FontSize',20);
[XLocs,~] = ginput(1);
close (f1);

XLocs = round(XLocs);
if sum(PressureImport(1:XLocs,1)>0)
    PressureThreshold =
round(1.1*max(PressureImport(1:XLocs,1)),4);
    PressStartLoc =
find(PressureImport(:,1)>PressureThreshold,1);
else

```

```

        PressureThreshold =
round(0.9*max(PressureImport(1:XLocs,1)),4);    % for negative
baseline
        PressStartLoc =
find(PressureImport(:,1)>PressureThreshold,1);
        end

    %% Diode/ PMT
        [~,DiodeImportStart] = min(abs(D(:,1)-DaqTS(1)+TimeBuffer));
        [~,DiodeImportEnd] = min(abs(D(:,1)-DaqTS(end)-TimeBuffer));
        DiodeImport =
fliplr(D(DiodeImportStart:DiodeImportEnd,1:2));    %
[Data,Time] format

        f1 = figure('units','normalized','outerposition',[0 0 1 1]);
        plot(DiodeImport(:,1));
        title('Please select the point to end the noise window for
Diode','FontSize',20);
        [XLocs,~] = ginput(1);
        close (f1);

        XLocs = round(XLocs);
        DiodeThreshold = round(1.1*max(DiodeImport(1:XLocs,1)),5);
% more significant digits since PMT signal is low
        DiodeStartLoc = find(DiodeImport(:,1)>DiodeThreshold,1);

    %% Grouping data, Burn Time and Pressure Metrics
        TempTime = UpdatedProcessedChData(:,NumChan+1);
% TempTime is measured from external trigger point
        intPressLag = PressureImport(PressStartLoc,2)-DaqTS(intStart);
        intDiodeLag = DiodeImport(DiodeStartLoc,2)-DaqTS(intStart);
        TempTime = (TempTime-DaqTS(intStart))*1000;
% make time zero to be the int start in ms
        RadianceTime = (DaqTS-DaqTS(intStart))*1000;
% Time for intensity data shifted to intstart
        pLag = min(85e-6,intPressLag);
        disp(['Effective Pressure Lag used: ',num2str(pLag),' s']);

% Pressure has a baseline correction incorporated
        DataGroup = {
% [P,D,Integ Int,Temp,Radiance,Press met,Burntime]
            [(PressureImport(:,1)-
mean(PressureImport(1:PressStartLoc,1)),(PressureImport(:,2)-pLag-
DaqTS(intStart))*1000),...
            [DiodeImport(:,1),(DiodeImport(:,2)-intDiodeLag-
DaqTS(intStart))*1000),...
            [IntegratedIntensity, RadianceTime],...

[TransposeTemp,SelectTransposeTemp,TempTime,Error,SmoothGreyTemp,Gre
yError],...

```

```

                                [Radiance,RadianceTime]...
% has the default smoothing from smoother loop
                                };
% Time in ms

    PeakPressure = max(DataGroup{1,1}(:,1));
    FiltMaxP = max(P_filt);
    P_filt = P_filt-mean(PressureImport(1:PressStartLoc,1));
    IntegratedPressure = trapz(P_filt(P_filt > 1))*ScopeSampleInt;
    PressProminence = PeakPressure/20;
    PeakHeight = 0.5*PeakPressure;

    f1 = figure('units','normalized','outerposition',[0 0 1 1]);

    findpeaks(smooth(DataGroup{1,1}(:,1),5,'moving'),'MinPeakProminence'
,PressProminence,'MinPeakHeight',PeakHeight);
    title('Is the first peak detected ? ','FontSize',20);

    check = input('Is the first peak detected ?');
    if check
        % For Fast thermites*****
        [~,pressLocs] =
    findpeaks(smooth(DataGroup{1,1}(:,1),5,'moving'),'MinPeakProminence'
,PressProminence,'MinPeakHeight',PeakHeight);
        close (f1);
    else
        % For Slow thermites*****
        [~,pressLocs] = max(DataGroup{1,1}(:,1));
        hold on;

    plot(pressLocs,DataGroup{1,1}(pressLocs,1),'r','MarkerSize',30);
        title('Does Peak Pressure Loc look OK (click on figure) ?
','FontSize',20);
        waitforbuttonpress;
        close (f1);
    end

    pressLocs = pressLocs(find(pressLocs>PressStartLoc,1));
% selecting the first prominent peak from ignition
    PressRate = (DataGroup{1,1}(pressLocs,1)-
DataGroup{1,1}(PressStartLoc,1))/...
        ((DataGroup{1,1}(pressLocs,2)-
DataGroup{1,1}(PressStartLoc,2))*1000);    % kPa/us

    DataGroup{1,6} = [PeakPressure;PressRate;IntegratedPressure];
% Pressure metrics

    disp(['Pressure starts:
',num2str(DataGroup{1,1}(PressStartLoc,2)),' ms from 32Ch int start;
Temperature point ',num2str(TempTime(1)),' ms after first light']);

```

```

disp(['Original Peak Pressure: ',num2str(OrigMaxP),'kPa; Max
filtered pressure: ',num2str(FiltMaxP),'kPa; PeakPressure w/ bkgnd
sub: ',num2str(PeakPressure),'kPa']);

BurnTime(1) =
(DiodeImport(find(DiodeImport(:,1)>(max(DiodeImport(:,1))/2),1,'last
'),2) -
DiodeImport(find(DiodeImport(:,1)>(max(DiodeImport(:,1))/2),1),2))*1
e6;
BurnTime(2) = (DaqTS(find(IntegratedIntensity >
max(IntegratedIntensity)/2,1,'last')) -
DaqTS(find(IntegratedIntensity >
max(IntegratedIntensity)/2,1)))*1e6;

DataGroup{1,7} = BurnTime;
% in us
DataGroup{1,8} = [intPressLag;intDiodeLag];
% in s
DataGroup{1,9} =
[intThreshold,0,PressureThreshold,0,DiodeThreshold];
DataGroup{1,10} = [DataGroup{1,1}(PressStartLoc,2);TempTime(1)];

%% Finding Prominent peak locations

ch3 = DataGroup{1,5}(:,3)/max(DataGroup{1,5}(:,3));
ch30 = DataGroup{1,5}(:,30)/max(DataGroup{1,5}(:,30));

[ch3MaxLocs(:,1),ch3MaxLocs(:,2)] =
findpeaks(ch3,'MinPeakProminence',0.05,'MinPeakDistance',25); %
minimum of 64 us between samples
ch3MaxLocs(:,2) = DataGroup{1,5}(ch3MaxLocs(:,2),33);
ch3MaxLocs = sortrows(ch3MaxLocs);

[ch30MaxLocs(:,1),ch30MaxLocs(:,2)] =
findpeaks(ch30,'MinPeakProminence',0.05,'MinPeakDistance',25); %
minimum of 64 us between samples
ch30MaxLocs(:,2) = DataGroup{1,5}(ch30MaxLocs(:,2),33);
ch30MaxLocs = sortrows(ch30MaxLocs);

DataGroup{1,11} = ch3MaxLocs;
DataGroup{1,12} = ch30MaxLocs;

[~,name,~] = fileparts(SpecFileName);
%% Plotting

f(1) = figure('units','normalized','outerposition',[0 0 1 1]);
% this figure is for time shifted data

subplot(2,1,1);
plot(DataGroup{1,1}(:,2),DataGroup{1,1}(:,1),'LineWidth',3);

```



```

set(gca, 'FontSize',15);
title('Pressure (kPa)');
xlabel('Time from Ignition (ms)','FontWeight','bold');

subplot(2,1,2);
yyaxis left;

plot(DataGroup{1,2}(:,2),DataGroup{1,2}(:,1)/max(DataGroup{1,2}(:,1)
));
ylim([0 1]);
yyaxis right;

plot(DataGroup{1,3}(:,2),DataGroup{1,3}(:,1)/max(DataGroup{1,3}(:,1)
));
ylim([0 1]);

set(gca, 'FontSize',15);
title('Norm. PMT vs Norm. Integrated Radiance');
xlabel('Time from Ignition (ms)','FontWeight','bold');

%% Pressure-Integrated Intensity-Temperature plots

f(2) = figure('units','normalized','outerposition',[0 0 1 1]);

limit = [-
0.1,DataGroup{1,4}(find(~isnan(DataGroup{1,4}(:,2))=1,1,'last'),3)+
0.5];

window(1) = find(DataGroup{1,1}(:,2)>limit(1),1);
window(2) = find(DataGroup{1,1}(:,2)<limit(2),1,'last');

window(3) = find(DataGroup{1,3}(:,2)>limit(1),1);
window(4) = find(DataGroup{1,3}(:,2)<limit(2),1,'last');

window(5) = find(DataGroup{1,4}(:,3)>limit(1),1);
window(6) = find(DataGroup{1,4}(:,3)<limit(2),1,'last');

[h3ax,h3lines] =
plotyyy(DataGroup{1,1}(window(1):window(2),2),DataGroup{1,1}(window(
1):window(2),1),...

DataGroup{1,3}(window(3):window(4),2),DataGroup{1,3}(window(3):windo
w(4),1),...

DataGroup{1,4}(window(5):window(6),3),DataGroup{1,4}(window(5):windo
w(6),2));

h3ax(1).YColor = 'b';
h3ax(2).YColor = 'r';
h3ax(3).YColor = 'k';

```

```

h3lines(1).LineStyle = '--';
h3lines(1).LineWidth = 0.5;
h3lines(1).Color = 'b';

h3lines(2).LineStyle = ':';
h3lines(2).LineWidth = 1.5;
h3lines(2).Color = 'r';

h3lines(3).LineStyle = 'none';
h3lines(3).Marker = '.';
h3lines(3).MarkerSize = 10;
h3lines(3).LineWidth = 1.5;
h3lines(3).Color = 'k';

xlabel(h3ax(1), 'Time from Ignition
(ms)', 'FontSize', 20, 'FontWeight', 'bold');
ylabel(h3ax(1), 'Pressure
(kPa)', 'FontSize', 20, 'FontWeight', 'bold');
ylabel(h3ax(2), 'Integrated
Intensity', 'FontSize', 20, 'FontWeight', 'bold');
ylabel(h3ax(3), 'Temperature
(K)', 'FontSize', 20, 'FontWeight', 'bold');

h3ax(1).YLim = [0 round(max(DataGroup{1,1}(:,1))+1)];
h3ax(1).YTick =
round(linspace(0, round(max(DataGroup{1,1}(:,1))+1), 5));

h3ax(2).YLim = [0, round(max(DataGroup{1,3}(:,1))+1)];
h3ax(2).YTick = 0:5:round(max(DataGroup{1,3}(:,1))+1);

% h3ax(3).YLim = [min(SmoothTransposeTemp)-100
max(SmoothTransposeTemp)+100];
% h3ax(3).YTick = round(min(SmoothTransposeTemp)-100,-
2):200:round(max(SmoothTransposeTemp)+100,-2);

set(h3ax, 'FontSize', 20);
% set(gca, 'FontSize', 20);

hLegend = legend('IntegratedIntensity', 'Pressure');
set(hLegend, 'FontSize', 20);
title({name, ['Peak Pressure ', num2str(DataGroup{1,6}(1,1)), ' kPa
& Press. Rate ', num2str(DataGroup{1,6}(2,1)), '
kPa/\mus']}, 'FontSize', 20);

%% Channel 3 and ALO Plot

f(3) = figure('position', [440 278 660 500]);

chALO = find(chWave(1,:) > 4.84e-7, 1, 'last')

```

```

yyaxis left;

plot(DataGroup{1,5}(:,33),DataGroup{1,5}(:,3)/max(DataGroup{1,5}(:,3)
)), 'LineStyle', '--', 'LineWidth',1, 'Color', 'b');
hold on;

plot(DataGroup{1,5}(:,33),DataGroup{1,5}(:,chAlO)/max(DataGroup{1,5}
(:,chAlO)), 'LineStyle', '--', 'LineWidth',0.2, 'Color', 'r');
ylim([0 1]);
xlabel('Time from Ignition
(ms)', 'FontSize',20, 'FontWeight', 'bold');
ylabel('Channel Norm
Intensity', 'FontSize',20, 'FontWeight', 'bold');

yyaxis right;

plot(DataGroup{1,4}(:,3),DataGroup{1,4}(:,2), 'LineStyle', 'none', 'Mar
ker', '.', 'Color', 'k', 'MarkerSize',10);
set(gca, 'ycolor', 'k');
ylabel('Temperature (K)', 'FontSize',20, 'FontWeight', 'bold');
ylim([min(DataGroup{1,4}(:,2))-100
max(DataGroup{1,4}(:,2))+100]);
yticks(round(min(DataGroup{1,4}(:,2))-100,-
2):250:round(max(DataGroup{1,4}(:,2))+100,-2));

legend(['NIR (' , num2str(round(chWave(2,3)*1e9)), '-
', num2str(round(chWave(1,3)*1e9)), ' nm) '], ['AlO
(' , num2str(round(chWave(2,chAlO)*1e9)), '-
', num2str(round(chWave(1,chAlO)*1e9)), ' nm) '], 'Temperature');
set(gca, 'FontSize',20);
set(gca, 'XLim', [-0.1,0.5]);
title(['AlO (' , num2str(round(chWave(2,chAlO)*1e9)), '-
', num2str(round(chWave(1,chAlO)*1e9)), ' nm) vs NIR
(' , num2str(round(chWave(2,3)*1e9)), ...
'-', num2str(round(chWave(1,3)*1e9)), ' nm)
', name], 'FontSize',20);

%% Spectra 3D

f(4) = figure('units', 'normalized', 'outerposition', [0 0 1 1]);

wavelengthArray = repmat(chWave(3,1:NumChan)*1e9,r,1);
for i = 1:NumChan

plot3(DataGroup{1,5}(:,33),wavelengthArray(:,i),DataGroup{1,5}(:,i))
;
hold on;
end
set(gca, 'FontSize',15);

```

```

view(-20,30);
xlabel('Time from Ignition
(ms)', 'FontSize',20, 'FontWeight', 'bold');
ylabel('Wavelength (nm)', 'FontSize',20, 'FontWeight', 'bold');
zlabel('Radiance', 'FontSize',20, 'FontWeight', 'bold');

h(1)=get(gca, 'xlabel');
h(2)=get(gca, 'ylabel');
h(3)=get(gca, 'zlabel');

x_tick=get(gca, 'xtick');
y_tick=get(gca, 'ytick');
z_tick=get(gca, 'ztick');

set(h(1), 'Position', [mean(x_tick) y_tick(1)-
(1.5*mean(diff(y_tick)))
z_tick(1)], 'HorizontalAlignment', 'center', 'rotation', 7);
set(h(2), 'Position', [x_tick(1)-(0.75*mean(diff(x_tick)))
y_tick(end)/2) z_tick(1)], 'HorizontalAlignment', 'center', 'rotation', -
37);
set(h(3), 'Position', [x_tick(1)-0.75*mean(diff(x_tick)) 900
mean(z_tick)], 'HorizontalAlignment', 'center', 'rotation', 90);
grid on;

%% Temp-Error plot
% Transpose Temp

f(5) = figure('position',[440 278 660 500]);

errorbar(DataGroup{1,4}(:,3),DataGroup{1,4}(:,1),DataGroup{1,4}(:,4)
,DataGroup{1,4}(:,5), 'o', 'MarkerSize',3, 'MarkerEdgeColor', 'red', ...
'MarkerFaceColor', 'red', 'Color', 'blue');
set(gca, 'FontSize',14);

title(['Error in Transpose Temp Estimate ',name], 'FontSize',20);
xlabel('Time from Ignition
(ms)', 'FontSize',20, 'FontWeight', 'bold');
ylabel('Temperature (K)', 'FontSize',20, 'FontWeight', 'bold');

%Greybody temp

f(6) = figure('position',[440 278 660 500]);

errorbar(DataGroup{1,4}(:,3),DataGroup{1,4}(:,6),DataGroup{1,4}(:,7)
,DataGroup{1,4}(:,8), 'o', 'MarkerSize',3, 'MarkerEdgeColor', 'red', ...
'MarkerFaceColor', 'red', 'Color', 'blue');
set(gca, 'FontSize',14);

```

```

title(['Error in GreyBody Temp Estimate ',name], 'FontSize',20);
xlabel('Time from Ignition
(ms)', 'FontSize',20, 'FontWeight', 'bold');
ylabel('Temperature (K)', 'FontSize',20, 'FontWeight', 'bold');

%% Unshifted norm data for checking the start points

f(7) = figure('units','normalized','outerposition',[0 0 1 1]);

plot(DaqTS, IntegratedIntensity/max(IntegratedIntensity), '-b');
hold on;

plot(DaqTS(intStart), IntegratedIntensity(intStart)/max(IntegratedInt
ensity), '.b', 'MarkerSize',30);

plot(DiodeImport(:,2), DiodeImport(:,1)/max(DiodeImport(:,1)), '-
r');

plot(DiodeImport(DiodeStartLoc,2), DiodeImport(DiodeStartLoc,1)/max(D
iodeImport(:,1)), '.r', 'MarkerSize',30);

plot(PressureImport(:,2), PressureImport(:,1)/max(PressureImport(:,1)
), '-g');

plot(PressureImport(PressStartLoc,2), PressureImport(PressStartLoc,1)
/max(PressureImport(:,1)), '.g', 'MarkerSize',30);

plot(PressureImport(pressLocs,2), PressureImport(pressLocs,1)/max(Pre
ssureImport(:,1)), '.k', 'MarkerSize',30);

xlabel('Time from Trigger (s)');
title(['Unshifted Norm Data ',name]);
legend('Integrated Int','Integrated Int
Threshold','Diode','Diode Threshold','Pressure','Pressure
Threshold');
set(gca, 'FontSize',20);

%% Analyze spectra

% check = input('Do you want to check spectra?');
%
% if check
%     f1 = figure;
%     plot(DataGroup{1,4}(:,1), '.r', 'MarkerSize',10);
%     hold on;
%     plot(DataGroup{1,4}(:,6), '.g', 'MarkerSize',10);
%     [Xindex,~] = ginput(3);
%     close(f1);

```

```

%
%       Xindex = round(Xindex);
%       Xindex(Xindex < 1) = 1;
%       f(8) = figure('units','normalized','outerposition',[0 0 1
1]);
%       f(9) = figure('units','normalized','outerposition',[0 0 1
1]);
%       f(10) = figure('units','normalized','outerposition',[0 0 1
1]);
%
%       SpectraShow(TransposeTemp(Xindex), GreyTemp(Xindex),
AbsIntensityData(Xindex,:), chWave(3,:), chWid, f(8), f(9), f(10));
%       end

%% Save Data and figures

name = [name, '-', num2str(Smoother), 'pt-Clean-ParUpdate-
', num2str(checkMol), ''];
check = input('Save ? ');

if check
%       savefig(f, [SaveFolderName, name], 'compact');
close all;
clear P f f1 ;
save([SaveFolderName, name]);
%
save([SaveFolderName, name], 'DataGroup', 'name', 'Smoother', 'Baseline',
'checkSmooth', 'CurrentLimit', 'PeakHeight', 'PressProminence', 'TimeBuf
fer');
    pause(1);
else
    break
end
end

function [chWavelength, chWidth] = channelWavelengthGen(spectCW,
grating, date)

    chWavelength = zeros(3,32);

    if grating == 150
        dispersion = 13;
% nm/mm

        if date == '09292017'
            spectCW = spectCW-2.58;
        elseif date == '11282016'
            spectCW = spectCW-4;
        else

```

```

        error('Wrong Turret rotation Date');
    end

    elseif grating == 600
        dispersion = 3;

    elseif grating == 1800
        dispersion = 0.9;
        spectCW = spectCW-0.42;
    else
        error('Enter correct grating density (1/mm)');
    end

    chWavelength(3,17) = spectCW;
    chWavelength(3,1:17) = (spectCW+16*dispersion):(-
dispersion):spectCW;
    chWavelength(3,18:32) = (spectCW-dispersion):(-
dispersion):(spectCW-15*dispersion);

    chWidth = 0.8*dispersion;
    % in nanometers

    for i = 1:32
        chWavelength(2,i) = chWavelength(3,i)-chWidth/2; % end (lower)
        chWavelength(1,i) = chWavelength(3,i)+chWidth/2; % start
(higher)
    end

    chWavelength = round(chWavelength,2)*1e-9;
    chWidth = round(chWidth,2)*1e-9;

    % chWavelength = round(chWavelength*1e-9,10);
    % chWidth = round(chWidth*1e-9,10);

end

function TempOutput = TempFit(AbsInt, lamda, normCh, check)

% check = 1 Ng Fit
% check = 2 NG and Greybody fit using norm 11 values

%% Radiation constants
lgt_c = 299792458;
h = 6.626e-34; %m2kgs-1
k_b = 1.38e-23; %m2kgs-2K-1
% sig = 5.67e-8; %kgs-3K-4
C1 = 2*pi*h*lgt_c^2; %m4kgs-3
C2 = h*lgt_c/k_b; % mK

```

```

AbsInt(AbsInt==0) = NaN;

if AbsInt(1,normCh)
    NormInt = AbsInt/AbsInt(1,normCh);
end

lamdaNorm = lamda(normCh);
[xData, yData, zData] = prepareCurveData(lamda, AbsInt, NormInt);

if nargin < 4
    check = 1;
end

%% Fit: 'Grey Body Non linear Temperature Fit'
if check ~= 1

    grayFit =
    @(T,x) ((C1./((x.^5).*exp(C2./(x.*T))))/(C1./((lamdaNorm.^5).*exp(C2./
    (lamdaNorm.*T)))));
    T0 = 2000;
    opts = optimoptions('lsqcurvefit','Display','off');
    [TempOutput.Greybody_temp,TempOutput.ResNorm,Res,~,~,~,J] =
    lsqcurvefit(grayFit,T0,xData,zData,[],[],opts);

    TempOutput.Greybody_Error = nlparci(TempOutput.Greybody_temp
    ,Res,'jacobian',J);

    NgTranspose = (log(C1./((xData).^5).*yData))./(C2./xData);
    [fitting,delta] = polyfit(xData,NgTranspose,1);
    [yFit,fitError] = polyval(fitting,xData,delta);
    fit1 = polyfit(xData,(yFit+2*fitError),1);
    fit2 = polyfit(xData,(yFit-2*fitError),1);
    % 95% confidence

    TempOutput.Transpose_temp = 1/fitting(1,2);
    TempOutput.Error = [1/fit2(1,2),1/fit1(1,2)];
    % TempOutput.Error =
    [1/(fitting(1,2)+2*mean(fitError)),1/(fitting(1,2)-
    2*mean(fitError))];

%% Fit: 'Transpose Fit'
else

    NgTranspose = (log(C1./((xData).^5).*yData))./(C2./xData);
    [fitting,delta] = polyfit(xData,NgTranspose,1);
    [yFit,fitError] = polyval(fitting,xData,delta);
    fit1 = polyfit(xData,(yFit+2*fitError),1);
    fit2 = polyfit(xData,(yFit-2*fitError),1);
    % 95% confidence

```



```

    TempOutput.Transpose_temp = 1/fitting(1,2);
    TempOutput.Error = [1/fit2(1,2),1/fit1(1,2)];
%     TempOutput.Error =
[1/(fitting(1,2)+2*mean(fitError)),1/(fitting(1,2)-
2*mean(fitError))];
    TempOutput.Greybody_temp = 0;
    TempOutput.Greybody_Error = 0;
    TempOutput.ResNorm = 0;

end

end

function temp_d = importfile(filename, startRow, endRow)

% IMPORTFILE Import numeric data from a text file as a matrix.
%   TEMP_D = IMPORTFILE(FILENAME) Reads data from text file FILENAME
for the default selection.
%
%   TEMP_D = IMPORTFILE(FILENAME, STARTROW, ENDROW) Reads data from
rows STARTROW through ENDROW of
%   text file FILENAME.
%
% Example:
%   temp_d = importfile('400-850nm-500-30-D-500sr.txt', [19, 450],
[45, 5496]);
%
%   See also TEXTSCAN.

%% Initialize variables.
delimiter = '\t';
if nargin<=2
    startRow = 19;
    endRow = inf;
end

%% Read columns of data as strings:
% For more information, see the TEXTSCAN documentation.
formatSpec =
'%s%s%s%s%s%s%s%s%s%s%s%s%s%s%s%s%s%s%s%s%s%s%s%s%s%s%s%s%s%s%
s%s%s%s%s%[\n\r]'; % reads 39 columns with last one empty

%% Open the text file.
fileID = fopen(filename,'r');

%% Read columns of data according to format string.
% This call is based on the structure of the file used to generate
this code. If an error occurs for
% a different file, try regenerating the code from the Import Tool.

```

```

textscan(fileID, '%[^\n\r]', startRow(1)-1, 'ReturnOnError', false);
%this order is important due to cursor location

dataArray = textscan(fileID, formatSpec, endRow(1)-startRow(1)+1,
'Delimiter', delimiter, 'ReturnOnError', false);
% number of times to apply formatSpec leads to the number of rows
that are read

for block=2:length(startRow) % adding individual blocks of rows if
need be, useful if multiple ranges of rows are input
    frewind(fileID); % go to beginning of file
    textscan(fileID, '%[^\n\r]', startRow(block)-1, 'ReturnOnError',
false); % going to the particular row
    dataArrayBlock = textscan(fileID, formatSpec, endRow(block)-
startRow(block)+1, 'Delimiter', delimiter, 'ReturnOnError', false);
    for col=1:length(dataArray)
        dataArray{col} = [dataArray{col};dataArrayBlock{col}];
    end
end

%% Close the text file.
fclose(fileID);

%% Convert the contents of columns containing numeric strings to
numbers.
% Replace non-numeric strings with NaN.
% can output the cell 'raw' if required

raw = repmat({''},length(dataArray{1}),length(dataArray)-1);
Data = zeros(length(dataArray{1}),length(dataArray)-1);

for col=1:length(dataArray)-1 % 1-38
    raw(1:length(dataArray{col}),col) = dataArray{col};
end

for
col=[1,2,3,4,5,6,7,8,9,10,11,12,13,14,15,16,17,18,19,20,21,22,23,24,
25,26,27,28,29,30,31,32,33,34,35,36,37,38]
    % Converts strings in the input cell array to numbers. Replaced
non-numeric strings with NaN.
    rawData = dataArray{col};
    Data(:,col) = str2double(rawData);
end

% convert any data with IE or OR into NaN; doing this in code
currently so
% as to allow for filtering OR data

% for i = 1:size(Data,1)

```

```
%     if Data(i,3) || Data(i,4) == 1
%         Data(i,6:38) = NaN;
%     end
% end
%% Create output variable
temp_d = Data;
```

Appendix B: Matlab Script for single particle modelling

```
m=800000;%steps
dp0=[21.7,46.1,66.1,82,94.7,109.4,121.9,131,145.9]';%peak size,nm
dp1=[18.72,30.51,39.64,46.33,51.5,57.17,61.8,65.1,70.38]';%size
after sintering,nm
bTi=[0.0247,0.0317,0.0404,0.0458,0.0511,0.0616,0.0675,0.0705,0.0753]
';%burn time for Ti,ms
vol = zeros(1,9);
m_initialTi = zeros(1,9);
s_area = zeros(1,9);
c_Ti=0;%heat capacity J/K mol
c_TiO2=0; %J/molK, variable assigned value through the function
heatTi=1233000;%heat of combustion j/mol,average of two sources

a=0.3;% EAC
pg=1.013e5;%gas pressure
kb=1.38e-23;%boltzmann constant
mg=4.8e-26;%air molecule weight
mTiO2=1.33e-25;%tio2 molec weight Kg
r=1.3; %1500K air heat ratio
hvTi=598712;%J/mole heat of vaporization tio2
nlossTiO2=zeros(1,9);%number of atom lost tio2
tg=1740;%gas temperature

dxTi=zeros(m,1);%create dx: vol ratio of unreacted Ti core
xTi=zeros(m,1);%create x: volume ratio of Ti unreacted at each step
dX_Ti = zeros(m,1);% create del_moles of reacting Ti
X_Ti = zeros(m,1);% create moles of Ti left
X_TiO2 = zeros(m,1);% create moles of TiO2 left
tempTi=zeros(m,1);%create particle temperature
intTi_correct=zeros(m,1);%corrected particle intensity
psTi=zeros(m,1);%create particle saturation pressure
zevTi=zeros(m,1);%create the evaporation rate of surface atoms
vTi=zeros(m,1);%create the heat loss of evaporation
dtempTi=zeros(m,1);%create dT
hgenTi= zeros(m,1);% heat generation
e=zeros(m,1);% emission loss T^4
r_k=zeros(m,1);

qTi=zeros(m,1);%create heat loss
rTi = zeros(m,1); % radiation heat loss
sigma = 5.67e-8;%W/m2K4

xTi(1)=0.999;%intial volume fraction of Ti
tempTi(1)=tg;%intial temperature of Ti,gas temperature
intTi_correct(1)=tg^4*0.1008;%e_avg(1) = 0.1008
e(1) = tg^4;
```

```

% mole calculations in a particle
for h = 1:9
    vol(h) = pi()*dp1(h)*1e-7)^(3)/6;% total volume calculation
(cc): remains fixed
    m_initialTi(h) = vol(h)*xTi(1)*4.11/48;
    s_area(h) = pi()*dp1(h)*1e-9)^(2);% m2
end

    flag =1;

for nTi = 2%change here for different sizes
    tTi=linspace(0,bTi(nTi,1)*1e-3,m)';%create time steps
    del_t = tTi(2) - tTi(1);

for i=1:(m-1)

    if xTi(i,1)==0
        r_k(i,1) = 0;

    else
        r_k(i,1) = del_t*(-3)*xTi(i,1)^(2/3)/(bTi(nTi,1)*1e-3);%
according to shrinking core model kinetic
        r_k(i,1) = del_t/(2*bTi(nTi,1)*1e-3*(1-xTi(i,1)^(-1/3)));%
according to shrinking core model diff
        r_k(i,1) = del_t*(-4)*xTi(i,1)*(-
1*log(xTi(i,1)))^0.75/(bTi(nTi,1)*1e-3);%A4
    end

    % use this whole 'if' section for the coupled model
%
%   if flag == 1
%
%       if (r_k(i,1) < r_ae(i,1))
%           dxTi(i,1) = r_k(i,1);
%           flag = 1;
%       else
%           dxTi(i,1) = r_ae(i,1);
%           flag = 2;           % to avoid switching back to
kinetic at later stages
%           end
%       else
%
%           dxTi(i,1) = r_ae(i,1);
%       end

%   if (i < 396041)
%       dxTi(i,1) = r_k(i,1);
%   else
%       if (r_k(i,1) < r_ae(i,1))

```

```

%           dxTi(i,1) = r_k(i,1); %uncomment this line if you
need to check only a single
%           model (kinetic)
%           else
%           dxTi(i,1) = r_ae(i,1); % or this line if you want
to check nucleation
%           end
%           end

xTi(i+1,1)=xTi(i,1)+dxTi(i,1);

if (xTi(i+1) < 0)
    xTi(i+1)=0;%get rid of complex numbers
end

dX_Ti(i) = dxTi(i) * vol(nTi) * (-4.11) / 48; %sign change to
make it a positive qty
X_Ti(i) = xTi(i) * vol(nTi) * (4.11) / 48; %moles of Ti left at
each step
X_TiO2(i) = (1-xTi(i)) * vol(nTi) * (4.11) / 48; %moles of TiO2
left at each step
%moles of Ti lost = moles of TiO2 formed
%total volume = vol of reacted Ti + vol if unreacted Ti
%mole fractions same as vol fractions

%density TiO2: 4.23g/cc, mol wt 80g/mol
%density Ti: 4.11 g/cc, At. wt 48g/mol

psTi(i)=10^(16.2-30361/tempTi(i)-0.000492*tempTi(i));%saturate
pressure

zevTi(i)=psTi(i)*s_area(nTi)/(2*kb*tempTi(i)*3.14*mTiO2)^0.5;%paper
125, evaporation rate s^-1
vTi(i)=zevTi(i)*hvTi/6.02e23;%heat loss of evaporation of one
particle (W)
nlossTiO2(nTi)=nlossTiO2(nTi)+zevTi(i)*del_t;

e_avg = xTi(i+1,1)*0.1 + (1 - xTi(i+1,1))*0.9;% vol fraction
equivalent to mole fraction Ti: 0.1 and TiO2 0.9

qTi(i,1)=a*3.14*(dp1(nTi,1)/2/1e9)^2*pg/2*(8*kb*tg/3.14/mg)^0.5*(r+1
)/(r-1)*(tempTi(i,1)-tg)/tg;%W, based on Kong's paper
rTi(i) = e_avg*sigma*s_area(nTi)*(tempTi(i)^4-tg^4);%W, radiation
loss
hgenTi(i) = dX_Ti(i)*heatTi;%heat generation, J

c_TiO2 = cTiO2(tempTi(i));
c_Ti = cTi(tempTi(i));
dtempTi(i,1)=1/(c_Ti*X_Ti(i)+c_TiO2*X_TiO2(i))*(hgenTi(i)-
del_t*(qTi(i,1)+rTi(i)+vTi(i)));%heat balance relation

```

```

tempTi(i+1,1)=tempTi(i,1)+dtempTi(i,1);
intTi_correct(i+1,1) = (tempTi(i+1,1)^4*e_avg);
e(i+1) = tempTi(i+1)^4;

end
end

max_i = max(intTi_correct(:,1));
intTi_correct = intTi_correct/max_i;

% max_i = max(e(:,1));
% intTi_correct = e/max_i;
% plot(tTi, tempTi);
% ylabel('Temperature (K)', 'FontSize',16);
% xlabel('Time (us)', 'FontSize',16);
% title('AE and shrink Kin', 'FontSize',16);

%figure ();
hold on;
plot(tTi,intTi_correct);
% ylabel('Intensity', 'FontSize',20);
% xlabel('Time (us)', 'FontSize',20);
% title('Model Fit to Observed Streak', 'FontSize',18);
% legend({'0.01', '0.05', '0.1', '0.2', '0.3', '0.5', '1'}, 'FontSize',12);

%loss=nlossTiO2/6.02e23;
% end
% legend({'kin', 'streak', 'diff', 'ae', 'comb'}, 'FontSize',12);
%%
%Reaction models
    %r_k(i,1)=del_t*(-4)*xTi(i,1)*(-
1*log(xTi(i,1)))^0.75/(bTi(nTi,1)*1e-3);% according to Avrami
Erofeev A4 kinetic
    %r_k(i,1)=del_t*(-3)*xTi(i,1)*(-
1*log(xTi(i,1)))^0.66/(bTi(nTi,1)*1e-3);% according to Avrami
Erofeev A3 kinetic
    %r_k(i,1)=del_t*(-2)*xTi(i,1)*(-
1*log(xTi(i,1)))^0.5/(bTi(nTi,1)*1e-3);% according to Avrami Erofeev
A2 kinetic
    %r_k(i,1)=del_t*(-1)*xTi(i,1)*(1-xTi(i,1))/(bTi(nTi,1)*1e-3);%
Prout Tompkins Autocat B1

    %r_k(i,1) = del_t*(-1)*(xTi(i,1))/(bTi(nTi,1)*1e-3);% first order
F1
    %r_k(i,1) = del_t*(-1)*(xTi(i,1))^2/(bTi(nTi,1)*1e-3);% second
order F2
    %r_k(i,1) = del_t*(-1)*(xTi(i,1))^3/(bTi(nTi,1)*1e-3);% third
order F3

```

```

    %r_k = del_t*(-3)*(xTi(i,1))^(.66)/(2*(1-
(xTi(i,1))^(.33))*bTi(nTi,1)*1e-3); %3D diffusion D3
    %r_k = del_t*(-1.5)/(bTi(nTi,1)*1e-3*(xTi(i,1)^(-.33)-1)); % D4
Ginstsling
    %r_k = del_t*(-0.5)/((1-xTi(i,1))*bTi(nTi,1)*1e-3); %D1 Diffusion
1D
    %r_k = del_t/(log(xTi(i,1))*bTi(nTi,1)*1e-3); %D2 Diffusion 2D

    %r_k = del_t/(2*bTi(nTi,1)*1e-3*(1-xTi(i,1)^(-1/3)));% according
to shrinking core model diff
    %r_k=del_t*(-3)*xTi(i,1)^(2/3)/(bTi(nTi,1)*1e-3);% according to
shrinking core model kinetic

```

```

function f = cZrO2(T)
t = T/1000;
if (T > 2950)
    f = 87.86370 + 0.000141*(t) - 0.000027*(t)^2 + 0.000002*(t)^3 +
0.000393*(t)^(-2);%liq
elseif T > 1478 && T < 2950
    f = 74.47520;
else
    f= 69.20001 + 8.548290*t - 0.862921*(t)^2 + 0.246374*(t)^3 -
1.382767*(t)^(-2);%solid
end
end

```

```

function f = cZr(T)
t = T/1000;
if (T > 2125)
    f = 41.84000 + 3.954064e-8*(t) - 9.195094e-9*(t)^2 + 7.208698e-
10*(t)^3 + 4.577756e-8*(t)^(-2);%liq
else
    f= 22.00069 + 2.211893*t + 0.410633*(t)^2 + 0.705368*(t)^3 -
2.927135*(t)^(-2);%solid
end
end

```

```

function f = cTiO2(T)
t = T/1000;
if (T > 2000)
    f = 100.416 + 5.991573e-8*(t) - 1.796728e-8*(t)^2 + 1.839876e-
9*(t)^3 + 3.592186e-8*(t)^(-2);% Anatase liq
else
    f = 67.2983 + 18.7094*t - 11.579*(t)^2 + 2.449561*(t)^3 -
1.485471*(t)^(-2);% rutile solid
end
end

```


end

```
function f = cTi(T)
t = T/1000;
if (T > 1939)
    f = 47.23694 + 1.975192e-8*t - 5.335145e-9*(t)^2 + 4.904109e-
10*(t)^3 + 1.564855e-8*(t)^(-2);
else
    f = 23.05660 + 5.541331*t - 2.055881*(t)^2 + 1.611745*(t)^3 -
0.056075*(t)^(-2);
end
end
```

Appendix C: Matlab Script for Color Camera Pyrometry

```
clear variables;
%% Path declarations
s = genpath('D:\4_Pyrometry\Phantom MATLAB SDK');
addpath(s);
load('D:\4_Pyrometry\Color Camera Pyrometry\SDK based
code\tempLookupTable.mat');

% LoadPhantomLibraries();
% RegisterPhantom(true);

%% File location, handle creation and image range check
% change for every specific experiment
fileName = 'D:\4_Pyrometry\Bing Samples\RGO Si 051117\500mA550ms-EXP-
25us-FR-23015.cine';

imageNo = input('Enter the image range for the video... (0 for all
images) ');

%% Get image stack

% [bpp16AlignedStack, unshiftedStack, IH, FR,
Exp,firstCineIm,lastCineIm] = ReadRawCineFileImageUpdate(fileName,
imageNo);
[~, unshiftedStack, IH, FR, Exp,firstCineIm,lastCineIm] =
ReadRawCineFileImageUpdate(fileName, imageNo);
stackSize = size(unshiftedStack(:,:,:),3);
FR = double(FR);
firstCineIm = double(firstCineIm);

%% Display RAW images
%
% check = input('Want to display RAW images ?...');
% if check
%     for i = 1:stackSize
%         figure,
image(unshiftedStack(:,:,i), 'CDataMapping', 'scaled'), colormap(gray(2
^12));
%     end
% end

%% RGB extraction
calibFactors = [1.007 0.966 0.972]; % GR, BG, BR for no window and
wide angled lens
% calibFactors = [0.952 0.888 0.847]; % for macro lens with window
heightI = IH.biHeight;
widthI = IH.biWidth;
blackLevel = 200; %IH.BlackLevel;
```

```

whiteLevel = 4000; % IH.WhiteLevel = 4064

% bppOrigStack = unshiftedStack; % store for RAW data if 16 bpp was
selected in cine save then this is 12 bit otherwise is 8 bit

% redChannel = uint16(zeros(heightI,widthI,stackSize));
% greenChannel = uint16(zeros(heightI,widthI,stackSize));
% blueChannel = uint16(zeros(heightI,widthI,stackSize));
%
% for k = 1:stackSize
%     for i = 1:heightI % Row
%         for j = 1:widthI % Column
%             if unshiftedStack(i,j,k)>0 % can change here for
thresholding
%                 if (mod(i,2)==0 && mod(j,2)==1)
%                     redChannel(i,j,k) = unshiftedStack(i,j,k);
%                 elseif (mod(i,2)==1 && mod(j,2)==0)
%                     blueChannel(i,j,k) = unshiftedStack(i,j,k);
%                 else
%                     greenChannel(i,j,k) = unshiftedStack(i,j,k);
%                 end
%             end
%         end
%     end
% end

%% Demosiacing

RinterpGradC = zeros(heightI,widthI,stackSize);
GinterpGradC = zeros(heightI,widthI,stackSize);
BinterpGradC = zeros(heightI,widthI,stackSize);

tempStackFinal = zeros(heightI,widthI,stackSize);
errorStackGradC = zeros(heightI,widthI,stackSize);
tempAvg = zeros(stackSize,2); % temp and time

% check = input('option 1 = Bilinear Interp OR option = 2 gradient
corrected Bilinear');

tic;
for k = 1:stackSize

    demosaicIm = demosaic(unshiftedStack(:,:,k), 'gbrg');
    RinterpGradC(:,:,k) = double(demosaicIm(:,:,1));
    GinterpGradC(:,:,k) = double(demosaicIm(:,:,2));
    BinterpGradC(:,:,k) = double(demosaicIm(:,:,3));

%% Temperature Extraction

```

```

    dmG_RGradC =
    (GinterpGradC(:, :, k) ./ RinterpGradC(:, :, k)) / calibFactors(1);
    dmB_GGradC =
    (BinterpGradC(:, :, k) ./ GinterpGradC(:, :, k)) / calibFactors(2);
    dmB_RGradC =
    (BinterpGradC(:, :, k) ./ RinterpGradC(:, :, k)) / calibFactors(3);

    tempGradC = zeros(heightI, widthI);

    for i = 1:heightI
        for j = 1:widthI
            if unshiftedStack(i, j, k) > blackLevel &&
unshiftedStack(i, j, k) < whiteLevel
                if (dmG_RGradC(i, j) > 0.61 && dmB_GGradC(i, j) > 0.33 &&
dmB_RGradC(i, j) > 0.22 && dmG_RGradC(i, j) < 1.2 && dmB_GGradC(i, j) < 0.94
&& dmB_RGradC(i, j) < 0.83) % takes care of NaNs as well
                    ratioMat = [dmG_RGradC(i, j), dmB_GGradC(i, j),
dmB_RGradC(i, j)];
                    diff =
bsxfun(@minus, tempLookupTable(:, 2:4), ratioMat);
                    [errorStackGradC(i, j, k), loc] =
min(sum(abs(diff), 2));
                    tempGradC(i, j) = tempLookupTable(loc, 1);
                end
            end
        end
    end

    satMask = unshiftedStack(:, :, k) > whiteLevel;
    satMask = imfilter(satMask, [1 1 1; 1 1 1; 1 1 1]); % logicals
hence even if the sum is 2 the value in mask is 1
    tempGradC(satMask) = 5001;
    tempGradC(errorStackGradC(:, :, k) > 0.05) = 5001;
    tempStackFinal(:, :, k) = tempGradC;
toc;

%% Average temperature
tempAvg(k, 1) = mean(tempGradC(tempGradC < 3000 & tempGradC > 1000));
tempAvg(k, 2) = (firstCineIm / FR + (k - 1) / FR) * 1000;
end

% errorStack = round(errorStack * 100); % for scaling the error data
accordingly

%% Convert into images or AVI
[~, name, ~] = fileparts(fileName);

tic;
folderName = uigetdir('D:\', 'Enter location to save video');
cd(folderName);

```

```

figure('units','normalized','outerposition',[0 0 1 1]);
cmap1 = cat(1, repmat([0 0 0],1000,1), jet(2500), repmat([0 0
0],1500,1), [0.5 0.5 0.5]); % 5001 for grey pixel
cmap2 = hot(4100);
v = VideoWriter([name, '1.avi']);
v.FrameRate = 10;
open(v);

for k = 1:stackSize
    ax1 = subplot(1,2,1);
    image(tempStackFinal(:,:,k));
    colormap(ax1, cmap1);
    c = colorbar;
    c.Label.String = 'Temperature (K)';
    title('Temperature');

    ax2 = subplot(1,2,2);
    image(unshiftedStack(:,:,k));
    colormap(ax2, cmap2);
    title('RAW Pixels');

    frame = getframe(gcf);
    writeVideo(v, frame);
end
toc;
close;
close(v);

save 'tempAvg';
%% Unload Libraries
% UnregisterPhantom(); %Use this function when you finished your
work
% UnloadPhantomLibraries();

function [matlabIm, unshiftedIm, imgHeader, frameRate,
Exposure, firstIm, lastIm] = ReadRawCineFileImageUpdate(fileName,
imageNo)
%Read an image specified by imageNo from a cine located at the path
specified by fileName parameter.
% RETURNS:
% matlabIm - 1D Gray/3D RGB matrix. For 16bpp images the pixel
values are aligned to 16bits
% unshiftedIm - 1D Gray/3D RGB matrix with image pixel values
unshifted

% Usage:
% LoadPhantomLibraries();
% RegisterPhantom(true); %Register the Phantom dll's ignoring
connected cameras.

```

```

%                               %Use this function once at the begining of
your work
% [matlabIm, origIm] = ReadRawCineFileImage('D:\Cine\test.cine', -
3000, true);
% other work with cine files
% .....
% UnregisterPhantom(); %Use this function when you finished your
work
% UnloadPhantomLibraries();

%% Create the cine handle from the cine file.
%Is recomended that cine handle creation should be done once for a
batch of image readings.
%This will increase speed.
currentCine = Cine(fileName);

%% Get information about cine
%read the saved range
firstIm = currentCine.GetFirstImageNumber;
totalRange = currentCine.GetImageCount;
lastIm = int32(double(firstIm) + double(totalRange) - 1);

if (length(imageNo)==1 || imageNo(1) == 0)
    imageNo(1) = firstIm;
    imageNo(2) = lastIm;
end

if (imageNo(1)<firstIm || imageNo(end)>lastIm)
    error(['Image number must be in saved cine range ['
num2str(firstIm) ';' num2str(lastIm) ']']);
end

widthI = currentCine.GetImWidth;
heightI = currentCine.GetImHeight;
imgSize = currentCine.GetMaxImageSizeInBytes; % results in creating
a buffer to read the image into
frameRate = currentCine.GetFrameRate;
Exposure = currentCine.GetExposure;

%% Prepare a "destination" for images (Cine RAW, unpacked) without
processing, with CSR

currentCine.SetUseCase(PhFileConst.UC_SAVE); % Set use case to SAVE
(=2)
currentCine.SetSaveParams % savefiletype to cineraw; save16bit true;
savepacked true; savexml, savetimestamp: false
currentCine.SetNoProcessing; % only CSR and bad pixel repair
currentCine.SetUncalibrated; % valueis currently true

stack = imageNo(end)-imageNo(1) + 1;

```

```

matlabIm = uint16(zeros(heightI,widthI,stack));
unshiftedIm = uint16(zeros(heightI,widthI,stack));
%Create the image range to be read
imgRange = get(libstruct('tagIMRANGE'));
%take one image at imageNo
imgRange.Cnt = 1;

%% Get image

for i = 1:stack

imgRange.First = imageNo(1)+i-1;
[HRES, unshiftedImBuffer, imgHeader] =
currentCine.GetCineImage(imgRange,imgSize);
PhGetErrorMessage(HRES)

% Read image information from header
isColorImage = IsColorHeader(imgHeader); % functions available in
utils
% is16bppImage = Is16BitHeader(imgHeader);

% Transform 1D image pixels to 1D/3D image pixels to be used with
MATLAB
if (HRES >= 0)
    [extractedIm] =
ExtractImageMatrixFromImageBuffer(unshiftedImBuffer, imgHeader); %
overwrite the unshiftedIm as it is just cropping the unused bits
    if (isColorImage)
        samplespp = 3;
    else
        samplespp = 1;
    end
    bps = GetEffectiveBitsFromIH(imgHeader);
    [matlabIm(:, :, i), unshiftedIm(:, :, i)] =
ConstructMatlabImage(extractedIm, imgHeader.biWidth,
imgHeader.biHeight, samplespp, bps);
end
end

%% Destroy Cine

currentCine.delete;

classdef Cine < handle
%A class that encapsulates a cine handle.

    %% Properties
    properties (Constant)
        PREVIEW_NAME = 'Preview';

```

```

end

properties(Access = private)
    CineHandle = [];
end

properties(SetAccess = private)
    IsLive;
end

%% Constructor
methods (Access = public)
    function cine = Cine(varargin)
        if (nargin == 1)
            arg1 = varargin{1};
            %file cine constructor
            if (ischar(arg1))
                [HRES cine.CineHandle] =
PhNewCineFromFile(arg1);
                cine.IsLive = false;
            elseif (isa(arg1, 'Cine'))
                %COPY CONSTRUCTOR
                cineObj = arg1;
                cine.CineHandle = 0;
                if (cineObj.CineHandle~=0)
                    if (cineObj.IsLive)
                        cine.CineHandle = cineObj.CineHandle;
                    else
                        [HRES, cine.CineHandle] =
PhDuplicateCine(cineObj.CineHandle);
                    end
                end
                cine.IsLive = cineObj.IsLive;
            else
                error('Bad parameter type');
            end
        elseif (nargin == 2)
            %camera cine constructor
            arg1 = varargin{1};
            arg2 = varargin{2};
            if (isfinite(arg1) && isfinite(arg2) &&
isscalar(arg1) && isscalar(arg2))
                cameraNumber = uint32(arg1);
                cineNumber = int32(arg2);
                if (cineNumber == PhConConst.CINE_PREVIEW ||
cineNumber < PhConConst.CINE_CURRENT)
                    error('Bad cine number');
                end
                if (cineNumber == PhConConst.CINE_CURRENT)
                    %Live cine case

```



```

        [HRES cine.CineHandle] =
PhGetCineLive(cameraNumber);
        cine.IsLive = true;
    else
        [HRES cine.CineHandle] =
PhNewCineFromCamera(cameraNumber, cineNumber);
        cine.IsLive = false;
    end
    else
        error('Bad parameter type');
    end
    else
        error('Arguments number mismatch');
    end
end
end

%% Methods
methods (Access = public)
    %% CineHandle manipulation
    function delete(this)
        if (this.CineHandle~=0 && ~this.IsLive)
            PhDestroyCine(this.CineHandle);
        end
    end

    %% GeneralInfo
    %First saved image number.
    function retVal = GetFirstImageNumber(this)
        pInfVal = libpointer('int32Ptr',0);
        PhGetCineInfo(this.CineHandle,
PhFileConst.GCI_FIRSTIMAGENO, pInfVal);
        retVal = pInfVal.Value;
    end

    %The number of images a cine contains.
    function retVal = GetImageCount(this)
        pVal = libpointer('uint32Ptr',0);
        PhGetCineInfo(this.CineHandle,
PhFileConst.GCI_IMAGECOUNT, pVal);
        retVal = pVal.Value;
    end

    %The number of frames after the trigger.
    function retVal = GetPostTriggerFrames(this)
        pInfVal = libpointer('uint32Ptr',0);
        PhGetCineInfo(this.CineHandle,
PhFileConst.GCI_POSTTRIGGER, pInfVal);
        retVal = pInfVal.Value;
    end
end

```

```

function retVal = GetLastImageNumber(this)
    retVal = int32(double(this.GetFirstImageNumber()) +
double(this.GetImageCount()) - 1);
end

%Trigger delay in frames.
%Setting postrigger frames larger than cine partition image
%capacity will work as a trigger delay.
function retVal = GetTriggerDelay(this)
    if (this.GetPostTriggerFrames() <= this.GetImageCount())
        retVal = 0;
    else
        retVal = this.GetPostTriggerFrames() -
this.GetImageCount();
    end
end

function retVal = GetCameraSerial(this)
    pInfVal = libpointer('int32Ptr',0);
    PhGetCineInfo(this.CineHandle,
PhFileConst.GCI_CAMERASERIAL, pInfVal);
    retVal = pInfVal.Value;
end

function retVal = GetCameraVersion(this)
    pInfVal = libpointer('int32Ptr',0);
    PhGetCineInfo(this.CineHandle,
PhFileConst.GCI_CAMERAVERSION, pInfVal);
    retVal = pInfVal.Value;
end

function retVal = GetFileType(this)
    pInfVal = libpointer('int32Ptr',0);
    PhGetCineInfo(this.CineHandle,
PhFileConst.GCI_FROMFILETYPE, pInfVal);
    retVal = pInfVal.Value;
end

function retVal = IsFileCine(this)
    pInfVal = libpointer('int32Ptr',0);
    PhGetCineInfo(this.CineHandle,
PhFileConst.GCI_ISFILECINE, pInfVal);
    retVal = pInfVal.Value;
end

function retVal = HasMetaWB(this)
    pInfVal = libpointer('int32Ptr',0);
    PhGetCineInfo(this.CineHandle, PhFileConst.GCI_WBISMETA,
pInfVal);

```

```

        retVal = (pInfVal.Value~=0);
    end

    %% UseCase
    function cineUseCaseID = GetUseCase(this)
        [HRES cineUseCaseID] = PhGetUseCase(this.CineHandle);
    end

    function SetUseCase(this, CineUseCaseID)
        PhSetUseCase(this.CineHandle, CineUseCaseID);
    end

    %% Cine Metadata
    function retVal = IsColor(this)
        pInfVal = libpointer('int32Ptr',0);
        PhGetCineInfo(this.CineHandle,
        PhFileConst.GCI_ISCOLORCINE, pInfVal);
        retVal = pInfVal.Value;
    end

    function retVal = Is16Bpp(this)
        pInfVal = libpointer('int32Ptr',0);
        PhGetCineInfo(this.CineHandle,
        PhFileConst.GCI_IS16BPPCINE, pInfVal);
        retVal = pInfVal.Value;
    end

    function retVal = GetBppReal(this)
        pInfVal = libpointer('int32Ptr',0);
        PhGetCineInfo(this.CineHandle, PhFileConst.GCI_REALBPP,
        pInfVal);
        retVal = pInfVal.Value;
    end

    function retVal = GetImWidth(this)
        pInfVal = libpointer('int32Ptr',0);
        PhGetCineInfo(this.CineHandle, PhFileConst.GCI_IMWIDTH,
        pInfVal);
        retVal = pInfVal.Value;
    end

    function retVal = GetImHeight(this)
        pInfVal = libpointer('int32Ptr',0);
        PhGetCineInfo(this.CineHandle, PhFileConst.GCI_IMHEIGHT,
        pInfVal);
        retVal = pInfVal.Value;
    end

    function retVal = GetFrameRate(this)
        pInfVal = libpointer('uint32Ptr',0);

```

```

        PhGetCineInfo(this.CineHandle,
PhFileConst.GCI_FRAMERATE, pInfVal);
        retValue = pInfVal.Value;
    end

    %Note: retValueurns exposure in ns
    function retValue = GetExposure(this)
        pInfVal = libpointer('uint32Ptr',0);
        PhGetCineInfo(this.CineHandle,
PhFileConst.GCI_EXPOSURENS, pInfVal);
        retValue = pInfVal.Value;
    end

    function retValue = GetEDRExposureNs(this)
        pInfVal = libpointer('uint32Ptr',0);
        PhGetCineInfo(this.CineHandle,
PhFileConst.GCI_EDREXPOSURENS, pInfVal);
        retValue = pInfVal.Value;
    end

    %% ImageProcessing
    function retValue = GetBrightness(this)
        pInfVal = libpointer('singlePtr',0);
        PhGetCineInfo(this.CineHandle, PhFileConst.GCI_BRIGHT,
pInfVal);
        retValue = pInfVal.Value;
    end

    function SetBrightness(this, value)
        pInfVal = libpointer('singlePtr',value);
        PhSetCineInfo(this.CineHandle, PhFileConst.GCI_BRIGHT,
pInfVal);
    end

    function retValue = GetContrast(this)
        pInfVal = libpointer('singlePtr',0);
        PhGetCineInfo(this.CineHandle, PhFileConst.GCI_CONTRAST,
pInfVal);
        retValue = pInfVal.Value;
    end

    function SetContrast(this, value)
        pInfVal = libpointer('singlePtr',value);
        PhSetCineInfo(this.CineHandle, PhFileConst.GCI_CONTRAST,
pInfVal);
    end

    function retValue = GetGamma(this)
        pInfVal = libpointer('singlePtr',0);

```

```

        PhGetCineInfo(this.CineHandle, PhFileConst.GCI_GAMMA,
pInfVal);
        retValue = pInfVal.Value;
    end

    function SetGamma(this, value)
        pInfVal = libpointer('singlePtr',value);
        PhSetCineInfo(this.CineHandle, PhFileConst.GCI_GAMMA,
pInfVal);
    end

    function retValue = GetSaturation(this)
        pInfVal = libpointer('singlePtr',0);
        PhGetCineInfo(this.CineHandle,
PhFileConst.GCI_SATURATION, pInfVal);
        retValue = pInfVal.Value;
    end

    function SetSaturation(this, value)
        pInfVal = libpointer('singlePtr',value);
        PhSetCineInfo(this.CineHandle,
PhFileConst.GCI_SATURATION, pInfVal);
    end

    function retValue = GetHue(this)
        pInfVal = libpointer('singlePtr',0);
        PhGetCineInfo(this.CineHandle, PhFileConst.GCI_HUE,
pInfVal);
        retValue = pInfVal.Value;
    end

    function SetHue(this, value)
        pInfVal = libpointer('singlePtr',value);
        PhSetCineInfo(this.CineHandle, PhFileConst.GCI_HUE,
pInfVal);
    end

    function retValue = GetSensitivity(this)
        pInfVal = libpointer('singlePtr',0);
        PhGetCineInfo(this.CineHandle, PhFileConst.GCI_GAIN16_8,
pInfVal);
        retValue = pInfVal.Value;
    end

    function wbValue = GetWhiteBalanceGain(this)
        wbValue = libstruct('tagWBGAIN');
        pInfVal = libpointer('tagWBGAIN', wbValue);
        if(this.HasMetaWB())

```

```

        PhGetCineInfo(this.CineHandle, PhFileConst.GCI_WB,
pInfVal);%get the WB applied before image interpolation (on raw
image)
        else
            PhGetCineInfo(this.CineHandle,
PhFileConst.GCI_WBVIEW, pInfVal);%get the WB applied on already
interpolated images
        end
        wbValue = pInfVal.Value;
    end

    function SetWhiteBalanceGain(this, wbValue)
        pWBVal= libpointer('tagWBGAIN', wbValue);
        if (this.HasMetaWB())
            PhSetCineInfo(this.CineHandle, PhFileConst.GCI_WB,
pWBVal);%will be set before image interpolation (on raw image)
        else
            PhSetCineInfo(this.CineHandle,
PhFileConst.GCI_WBVIEW, pWBVal);%will be set on already interpolated
images
        end
    end

    function retVal = GetRotation(this)
        pInfVal = libpointer('singlePtr',0);
        PhGetCineInfo(this.CineHandle, PhFileConst.GCI_ROTATE,
pInfVal);
        retVal = pInfVal.Value;
    end

    function SetRotation(this, value)
        pInfVal = libpointer('singlePtr',value);
        PhSetCineInfo(this.CineHandle, PhFileConst.GCI_ROTATE,
pInfVal);
    end

    function SetSaveParams(this)
        pInfVal = libpointer('uint32Ptr',0);
        PhSetCineInfo(this.CineHandle,
PhFileConst.GCI_SAVEFILETYPE, pInfVal);
        %
        pInfVal = libpointer('tagIMRANGE',imrange);
        %
        PhSetCineInfo(this.CineHandle,
PhFileConst.GCI_SAVERANGE, pInfVal);
        pInfVal = libpointer('int32Ptr',true);
        PhSetCineInfo(this.CineHandle,
PhFileConst.GCI_SAVE16BIT, pInfVal);
        pInfVal = libpointer('int32Ptr',false);
        PhSetCineInfo(this.CineHandle,
PhFileConst.GCI_SAVEPACKED, pInfVal);
        pInfVal = libpointer('int32Ptr',false);

```

```

        PhSetCineInfo(this.CineHandle, PhFileConst.GCI_SAVEXML,
pInfVal);
        pInfVal = libpointer('uint32Ptr',0);
        PhSetCineInfo(this.CineHandle,
PhFileConst.GCI_SAVESTAMPTIME, pInfVal);
        end

        function SetNoProcessing(this)
            pInfVal = libpointer('int32Ptr',true);
            PhSetCineInfo(this.CineHandle,
PhFileConst.GCI_NOPROCESSING, pInfVal);
        end

        function SetUncalibrated(this)
            pInfVal = libpointer('int32Ptr',false);
            PhSetCineInfo(this.CineHandle,
PhFileConst.GCI_UNCALIBRATEDIMAGE, pInfVal);
        end

        function SetNoBadPixelRepair(this)
            pInfVal = libpointer('int32Ptr',true);
            PhSetCineInfo(this.CineHandle,
PhFileConst.GCI_BADPIXELREPAIR, pInfVal);
        end

        %% GetImage
        function [HRES, pixels, IH] = GetCineImage(this, imgRange,
bufferSize)
            [HRES, pixels, IH] = PhGetCineImage(this.CineHandle,
imgRange, bufferSize);
        end

        function imgSizeInBytes = GetMaxImageSizeInBytes(this)
            pInfVal = libpointer('uint32Ptr',0);
            PhGetCineInfo(this.CineHandle,
PhFileConst.GCI_MAXIMGSIZE, pInfVal);
            imgSizeInBytes = pInfVal.Value;
        end

        function SetVFlipView(this, flipV)
            pInfVal = libpointer('int32Ptr',flipV);
            PhSetCineInfo(this.CineHandle,
PhFileConst.GCI_VFLIPVIEWACTIVE, pInfVal);
        end

        function dlgRes = GetSaveCineName(this)
            %%will show the dialog to browse for a file where the
            cine will be saved.
            dlgRes = (PhGetSaveCineName(this.CineHandle) ~= 0);
        end

```

```

function [HRES] = StartSaveCineAsync(this)
    HRES = PhWriteCineFileAsync(this.CineHandle);
end

function [HRES] = StopSaveCineAsync(this)
    [HRES] = PhStopWriteCineFileAsync(this.CineHandle);
end

function [HRES progress] = GetSaveCineFileProgress(this)
    [HRES progress] =
PhGetWriteCineFileProgress(this.CineHandle);
end

function [error] = GetSaveCineError(this)
    pInfVal = libpointer('int32Ptr',0);
    PhGetCineInfo(this.CineHandle, PhFileConst.GCI_WRITEERR,
pInfVal);
    error = pInfVal.Value;
end
end

%% Utils
methods (Access = public, Static)
    function cineNo = ParseCineNo(cineStr)
        if (strcmp(cineStr,Cine.PREVIEW_NAME))
            cineNo = PhConConst.CINE_PREVIEW;
        elseif (strcmp(cineStr(1), 'F'))
            %the cine is from flash
            cineNo =
int32(str2double(cineStr(2:length(cineStr))));
            cineNo = int32(PhConConst.FIRST_FLASH_CINE) + cineNo
- 1;%flash cine number
        else
            %the cine is from ram
            cineNo =
int32(str2double(cineStr(1:length(cineStr))));
        end
    end

    function cineStr = GetStringForCineNo(cineNo)
        if (cineNo == PhConConst.CINE_PREVIEW)
            cineStr = Cine.PREVIEW_NAME;
        elseif(cineNo >= PhConConst.FIRST_FLASH_CINE)
            cineStr = ['F' num2str(cineNo -
PhConConst.FIRST_FLASH_CINE + 1)];
        else
            cineStr = num2str(cineNo);
        end
    end
end

```


end

end

Bibliography

- [1] Muller RA. Energy and Power and the physics of explosions, 2008.
- [2] Rossi C, Estève A, Vashishta P. Nanoscale energetic materials. *J Phys Chem Solids* 2010;71:57–8. doi:10.1016/j.jpics.2009.10.015.
- [3] Brânzei M, Coman T. Structure Improvement of Aluminothermic Welding Joints by Using Modifiers. *World Acad Sci Eng Technol Int J Mater Metall Eng* 2012;6:745–8.
- [4] Rossi C. Two Decades of Research on Nano-Energetic Materials. *Propellants Explos Pyrotech* 2014;39:323–7. doi:10.1002/prop.201480151.
- [5] Yetter RA, Risha GA, Son SF. Metal particle combustion and nanotechnology. *Proc Combust Inst* 2009;32:1819–38. doi:10.1016/j.proci.2008.08.013.
- [6] Armstrong RW, Baschung B, Booth DW, Samirant M. Enhanced Propellant Combustion with Nanoparticles. *Nano Lett* 2003;3:253–5.
- [7] Dokhan A, Price EW, Seitzman JM, Sigman RK. The effects of bimodal aluminum with ultrafine aluminum on the burning rates of solid propellants. *Proc Combust Inst* 2002;29:2939–46. doi:10.1016/s1540-7489(02)80359-5.
- [8] Danen WC, Martin JA. Energetic Composites. 5266132, 1991.
- [9] Aumann CE, Skofronick GL, Martin JA. Oxidation Behaviour of Aluminum Nanopowders. *J Vac Sci Technol B* 1995;13:1178–83. doi:10.1116/1.588232.
- [10] Martirosyan KS, Wang L, Luss D. Novel nanoenergetic system based on iodine pentoxide. *Chem Phys Lett* 2009;483:107–10. doi:10.1016/j.cplett.2009.10.038.
- [11] Jian GQ, Chowdhury S, Sullivan K, Zachariah MR. Nanothermite reactions: Is gas phase oxygen generation from the oxygen carrier an essential prerequisite to ignition? *Combust Flame* 2013;160:432–7. doi:10.1016/j.combustflame.2012.09.009.
- [12] Wang HY, Jian GQ, Yan S, DeLisio JB, Huang C, Zachariah MR. Electrospray Formation of Gelled Nano-Aluminum Microspheres with Superior Reactivity. *ACS Appl Mater Interfaces* 2013;5:6797–801. doi:10.1021/am401238t.
- [13] Tillotson TM, Gash AE, Simpson RL, Hrubesh LW, Satcher JH, Poco JF. Nanostructured energetic materials using sol-gel methodologies. *J Non Cryst Solids* 2001;285:338–45. doi:10.1016/s0022-3093(01)00477-x.
- [14] Menon L, Patibandla S, Ram KB, Shkuratov SI, Aurongzeb D, Holtz M, et al. Ignition studies of Al/Fe₂O₃ energetic nanocomposites. *Appl Phys Lett* 2004;84:4735–7. doi:10.1063/1.1759387.
- [15] Kwon J, Ducere JM, Alphonse P, Bahrami M, Petrantonio M, Veyan J-F, et al. Interfacial Chemistry in Al/CuO Reactive Nanomaterial and Its Role in Exothermic Reaction. *ACS Appl Mater Interfaces* 2013;5:605–13. doi:10.1021/am3019405.

- [16] Prakash A, McCormick A V, Zachariah MR. Tuning the reactivity of energetic nanoparticles by creation of a core-shell nanostructure. *Nano Lett* 2005;5:1357–60. doi:10.1021/nl0506251.
- [17] Séverac F, Alphonse P, Estève A, Bancaud A, Rossi C. High-energy Al/CuO nanocomposites obtained by DNA-directed assembly. *Adv Funct Mater* 2012;22:323–9. doi:10.1002/adfm.201100763.
- [18] Tanguay V, Goroshin S, Higgins AJ, Zhang F. Aluminum Particle Combustion in High-Speed Detonation Products. *Combust Sci Technol* 2009;181:670–93. doi:10.1080/00102200802643430.
- [19] Chakraborty P, Zachariah MR. Do nanoenergetic particles remain nano-sized during combustion? *Combust Flame* 2014;161:1408–16. doi:10.1016/j.combustflame.2013.10.017.
- [20] Bazyn T, Krier H, Glumac N. Evidence for the transition from the diffusion-limit in aluminum particle combustion. *Proc Combust Inst* 2007;31 II:2021–8. doi:10.1016/j.proci.2006.07.161.
- [21] Ivanov YF, Osmonoliev MN, Sedoi VS, Arkhipov VA, Bondarchuk SS, Vorozhtsov AB, et al. Productions of Ultra-Fine Powders and Their Use in High Energetic Compositions. *Propellants, Explos Pyrotech* 2003;28:319–33. doi:10.1002/prop.200300019.
- [22] Chowdhury S, Sullivan K, Piekielek N, Zhou L, Zachariah MR. Diffusive vs Explosive Reaction at the Nanoscale. *J Phys Chem C* 2010;114:9191–5. doi:10.1021/jp906613p.
- [23] Park K, Lee D, Rai A, Mukherjee D, Zachariah MR. Size-Resolved Kinetic Measurements of Aluminum Nanoparticle Oxidation with Single Particle Mass Spectrometry 2004.
- [24] Ermoline A, Dreizin EL. Equations for the Cabrera-Mott kinetics of oxidation for spherical nanoparticles. *Chem Phys Lett* 2011;505:47–50. doi:10.1016/j.cplett.2011.02.022.
- [25] Lynch P, Fiore G, Krier H, Glumac N. Gas-phase reaction in nanoaluminum combustion. *Combust Sci Technol* 2010;182:842–57. doi:10.1080/00102200903341561.
- [26] Rai A, Park K, Zhou L, Zachariah MR. Understanding the mechanism of aluminium nanoparticle oxidation. *Combust Theory Model* 2006;10:843–59. doi:10.1080/13647830600800686.
- [27] Ermoline A, Yildiz D, Dreizin EL. Model of heterogeneous combustion of small particles. *Combust Flame* 2013;160:2982–9. doi:10.1016/j.combustflame.2013.06.018.
- [28] Trunov MA, Schoenitz M, Dreizin EL. Effect of polymorphic phase transformations in alumina layer on ignition of aluminium particles. *Combust Theory Model* 2006;10:603–23. doi:10.1080/13647830600578506.
- [29] Firmansyah DA, Sullivan K, Lee KS, Kim YH, Zahaf R, Zachariah MR, et al.

- Microstructural behavior of the alumina shell and aluminum core before and after melting of aluminum nanoparticles. *J Phys Chem C* 2012;116:404–11. doi:10.1021/jp2095483.
- [30] Rufino B, Boule'h F, Coulet M V, Lacroix G, Denoyel R. Influence of particles size on thermal properties of aluminium powder. *Acta Mater* 2007;55:2815–27. doi:10.1016/j.actamat.2006.12.017.
- [31] Sullivan KT, Kuntz JD, Gash AE. The role of fuel particle size on flame propagation velocity in thermites with a nanoscale oxidizer. *Propellants, Explos Pyrotech* 2014;39:407–15. doi:10.1002/prop.201400020.
- [32] Weismiller MR, Malchi JY, Lee JG, Yetter RA, Foley TJ. Effects of fuel and oxidizer particle dimensions on the propagation of aluminum containing thermites. *Proc Combust Inst* 2011;33:1989–96. doi:10.1016/j.proci.2010.06.104.
- [33] Sanders VE, Asay BW, Foley TJ, Tappan BC, Pacheco AN, Son SF. Reaction Propagation of Four Nanoscale Energetic Composites (Al/MoO₃, Al/WO₃, Al/CuO, and B₁₂O₃). *J Propuls Power* 2007;23:707–14. doi:10.2514/1.26089.
- [34] Sullivan KT, Chiou WA, Fiore R, Zachariah MR. In situ microscopy of rapidly heated nano-Al and nano-Al/WO₃ thermites. *Appl Phys Lett* 2010;97. doi:10.1063/1.3490752.
- [35] Zhou L, Piekiet N, Chowdhury S, Zachariah MR. Time-Resolved Mass Spectrometry of the Exothermic Reaction between Nanoaluminum and Metal Oxides: The Role of Oxygen Release. *J Phys Chem C* 2010;114:14269–75. doi:10.1021/jp101146a.
- [36] Beckstead MW. Correlating aluminum burning times. *Combust Explos Shock Waves* 2005;41:533–46. doi:10.1007/s10573-005-0067-2.
- [37] Lynch P, Krier H, Glumac N. A correlation for burn time of aluminum particles in the transition regime. *Proc Combust Inst* 2009;32 II:1887–93. doi:10.1016/j.proci.2008.06.205.
- [38] Badiola C, Gill RJ, Dreizin EL. Combustion characteristics of micron-sized aluminum particles in oxygenated environments. *Combust Flame* 2011;158:2064–70. doi:10.1016/j.combustflame.2011.03.007.
- [39] Bazyn T, Krier H, Glumac N. Combustion of nanoaluminum at elevated pressure and temperature behind reflected shock waves. *Combust Flame* 2006;145:703–13. doi:10.1016/j.combustflame.2005.12.017.
- [40] Sullivan K, Zachariah MR. Simultaneous Pressure and Optical Measurements of Nanoaluminum Thermites: Investigating the Reaction Mechanism. *J Propuls Power* 2010;26:467–72. doi:10.2514/1.45834.
- [41] Sullivan KT, Cervantes O, Densmore JM, Kuntz JD, Gash AE, Molitoris JD. Quantifying Dynamic Processes in Reactive Materials: An Extended Burn Tube Test. *Propellants Explos Pyrotech* 2015;40:394–401. doi:10.1002/prop.201400267.

- [42] Sullivan KT, Piekielec NW, Wu C, Chowdhury S, Kelly ST, Hufnagel TC, et al. Reactive sintering: An important component in the combustion of nanocomposite thermites. *Combust Flame* 2012;159:2–15. doi:10.1016/j.combustflame.2011.07.015.
- [43] Bazyn T, Glumac N, Krier H, Ward TS, Schoenitz M, Dreizin EL. Reflected shock ignition and combustion of aluminum and nanocomposite thermite powders. *Combust Sci Technol* 2007;179:457–76. doi:10.1080/00102200600637261.
- [44] Levitas VI, Pantoya ML, Dean S. Melt dispersion mechanism for fast reaction of aluminum nano- and micron-scale particles: Flame propagation and SEM studies. *Combust Flame* 2014;161:1668–77. doi:10.1016/j.combustflame.2013.11.021.
- [45] Levitas VI. Mechanochemical mechanism for reaction of aluminium nano- and micrometre-scale particles. *Philos Trans A Math Phys Eng Sci* 2013;371:20120215. doi:10.1098/rsta.2012.0215.
- [46] Watson KW, Pantoya ML, Levitas VI. Fast reactions with nano- and micrometer aluminum: A study on oxidation versus fluorination. *Combust Flame* 2008;155:619–34. doi:10.1016/j.combustflame.2008.06.003.
- [47] Childs PRN, Greenwood JR, Long CA. Review of temperature measurement. *Rev Sci Instrum* 2000;71:2959–78. doi:10.1063/1.1305516.
- [48] McNesby KL, Homan BE, Benjamin RA, Boyle VM, Densmore JM, Biss MM. Invited Article: Quantitative imaging of explosions with high-speed cameras. *Rev Sci Instrum* 2016;87. doi:10.1063/1.4949520.
- [49] Maun JD, Sunderland PB, Urban DL. Thin-filament pyrometry with a digital still camera. *Appl Opt* 2007;46:483–8. doi:10.1364/AO.46.000483.
- [50] Lewis WK, Rumchik CG, Smith MJ, Fernando KAS, Crouse CA, Spowart JE, et al. Comparison of post-detonation combustion in explosives incorporating aluminum nanoparticles: Influence of the passivation layer. *J Appl Phys* 2013;113. doi:10.1063/1.4790159.
- [51] Lewis WK, Rumchik CG. Measurement of apparent temperature in post-detonation fireballs using atomic emission spectroscopy. *J Appl Phys* 2009;105:23–6. doi:10.1063/1.3089251.
- [52] Goroshin S, Frost DL, Levine J, Yoshinaka A, Zhang F. Optical pyrometry of fireballs of metalized explosives. *Propellants Explos Pyrotech* 2006;31:169–81. doi:10.1002/prop.200600024.
- [53] Bassett WP, Dlott DD. High dynamic range emission measurements of shocked energetic materials: Octahydro-1,3,5,7-tetranitro-1,3,5,7-tetrazocine (HMX). *J Appl Phys* 2016;119. doi:10.1063/1.4953353.
- [54] Crepeau J. A Brief History of the T. Vol. 1 Heat Transf. Energy Syst. Thermophys. Prop. Heat Transf. Equipment; Heat Transf. Electron. Equip., ASME; 2009, p. 59–65. doi:10.1115/HT2009-88060.

- [55] Khatami R, Levendis YA. On the deduction of single coal particle combustion temperature from three-color optical pyrometry. *Combust Flame* 2011;158:1822–36. doi:10.1016/j.combustflame.2011.01.007.
- [56] Levendis YA, Estrada KR, Hottel HC. Development of multicolor pyrometers to monitor the transient response of burning carbonaceous particles. *Rev Sci Instrum* 1992;63:3608–22. doi:10.1063/1.1143586.
- [57] Fu T, Tan P, Pang C, Zhao H, Shen Y. Fast fiber-optic multi-wavelength pyrometer. *Rev Sci Instrum* 2011;82. doi:10.1063/1.3596567.
- [58] Lynch P, Krier H, Glumac N. Emissivity of Aluminum-Oxide Particle Clouds: Application to Pyrometry of Explosive Fireballs. *J Thermophys Heat Transf* 2010;24:301–8. doi:10.2514/1.43853.
- [59] Kalman J, Allen D, Glumac N, Krier H. Optical Depth Effects on Aluminum Oxide Spectral Emissivity. *J Thermophys Heat Transf* 2015;29:74–82. doi:10.2514/1.T4260.
- [60] Weismiller MR, Lee JG, Yetter RA. Temperature measurements of Al containing nano-thermite reactions using multi-wavelength pyrometry. *Proc Combust Inst* 2011;33:1933–40. doi:10.1016/j.proci.2010.06.094.
- [61] Glumac NG, Krier H, Bazyn T, Eyer R. TEMPERATURE MEASUREMENTS OF ALUMINUM PARTICLES BURNING IN CARBON DIOXIDE. *Combust Sci Technol* 2005;177:485–511. doi:10.1080/00102200108952170.
- [62] Wilkinson J, Lightstone JM, Boswell CJ, Carney JR. Emission Spectroscopy of Aluminum in Post- Detonation Combustion. *Time* 2007;1271:1271–4.
- [63] Wang R, Li S, Zhou W, Luo Z-X, Meng J, Tian J, et al. A high-speed, eight-wavelength visible light-infrared pyrometer for shock physics experiments. *AIP Adv* 2017;7:095014. doi:10.1063/1.4996927.
- [64] Bassett WP, Dlott DD. Multichannel emission spectrometer for high dynamic range optical pyrometry of shock-driven materials. *Rev Sci Instrum* 2016;87. doi:10.1063/1.4964386.
- [65] Ng D, Fralick G. Use of a multiwavelength pyrometer in several elevated temperature aerospace applications. *Rev Sci Instrum* 2001;72:1522–30. doi:10.1063/1.1340558.
- [66] Fu T, Wang Z, Cheng X. Temperature Measurements of Diesel Fuel Combustion With Multicolor Pyrometry. *J Heat Transfer* 2010;132:051602. doi:10.1115/1.4000467.
- [67] DeWitt DP, Nutter GD, editors. *Theory and Practice of Radiation Thermometry*. Hoboken, NJ, USA: John Wiley & Sons, Inc.; 1988. doi:10.1002/9780470172575.
- [68] Vision Research. PHANTOM V21X / V31X / V41X / V61X / V12.1 / V71X / Miro310 / Miro110 Color & Spectral Response Curve n.d.
- [69] Densmore JM, Biss MM, McNesby KL, Homan BE. High-speed digital color

- imaging pyrometry. *Appl Opt* 2011;50:2659–65.
- [70] Ma H, Stevens R, Stone R. In-Cylinder Temperature Estimation from an Optical Spray-Guided DISI Engine with Color-Ratio Pyrometry (CRP). 2006. doi:10.4271/2006-01-1198.
- [71] Connelly BC, Kaiser SA, Smooke MD, Long MB. Two-Dimensional Soot Pyrometry with a Color Digital Camera. *Jt Meet US Sect Combust Insitiute* 2005;2.
- [72] Wyatt C. Radiometric calibration: theory and methods. Elsevier; 2012.
- [73] Mcnesby KL, Biss MM, Homan BE, Benjamin RA, Sr VMB, John M. *Imaging Detonations of Explosives*. 2015.
- [74] Pautin S, Giovannini A, Bédard B. Thin filament infrared pyrometry: instantaneous temperature profile measurements in a weakly turbulent hydrocarbon premixed flame. *Exp Fluids* 1994;17:397–404. doi:10.1007/BF01877042.
- [75] Tsyba GA, Salamatov VG, Polyakov VL. A Video Pyrometer. *Instruments Exp Tech* 2003;46:480–3. doi:10.1023/A:1025173830105.
- [76] Kuhn PB, Ma B, Connelly BC, Smooke MD, Long MB. Soot and thin-filament pyrometry using a color digital camera. *Proc Combust Inst* 2011;33:743–50. doi:10.1016/j.proci.2010.05.006.
- [77] Fu T, Cheng X, Shi C, Zhong M, Liu T, Zheng X. The set-up of a vision pyrometer. *Meas Sci Technol* 2006;17:659–65. doi:10.1088/0957-0233/17/4/008.
- [78] Simonini S, Elston SJ, Stone CR. Soot temperature and concentration measurements from colour charge coupled device camera images using a three-colour method. *Proc Inst Mech Eng Part C J Mech Eng Sci* 2001;215:1041–52. doi:10.1177/095440620121500905.
- [79] Densmore JM, Homan BE, Biss MM, McNesby KL. High-speed two-camera imaging pyrometer for mapping fireball temperatures. *Appl Opt* 2011;50:6267–71.
- [80] Densmore JM, Biss MM, Homan BE, McNesby KL. Thermal imaging of nickel-aluminum and aluminum-polytetrafluoroethylene impact initiated combustion. *J Appl Phys* 2012;112:5. doi:10.1063/1.4762009.
- [81] Densmore JM, Sullivan KT, Gash AE, Kuntz JD. Expansion behavior and temperature mapping of thermites in burn tubes as a function of fill length. *Propellants, Explos Pyrotech* 2014;39:416–22. doi:10.1002/prop.201400024.
- [82] Morton DC. Atomic Data for Resonance Absorption Lines. III. Wavelengths Longward of the Lyman Limit for the Elements Hydrogen to Gallium. *Astrophys J Suppl Ser* 2003;149:205–38. doi:10.1086/377639.
- [83] Miyata K, Kubota N. Combustion of Ti and Zr particles with KNO₃. *Propellants Explos Pyrotech* 1996;21:29–35. doi:10.1002/prop.19960210107.
- [84] Zong YC, Li SQ, Niu F, Yao Q. Direct synthesis of supported palladium

- catalysts for methane combustion by stagnation swirl flame. *Proc Combust Inst* 2015;35:2249–57. doi:10.1016/j.proci.2014.06.114.
- [85] Cashdollar KL, Zlochower IA. Explosion temperatures and pressures of metals and other elemental dust clouds. *J Loss Prev Process Ind* 2007;20:337–48. doi:10.1016/j.jlp.2007.04.018.
- [86] Wei HY, Yoo CS. Kinetics of small single particle combustion of zirconium alloy. *J Appl Phys* 2012;111. doi:10.1063/1.3677789.
- [87] Trunov MA, Hoffmann VK, Schoenitz M, Dreizin EL. Combustion of boron-titanium nanocomposite powders in different environments. *J Propuls Power* 2008;24:184–91. doi:10.2514/1.30483.
- [88] Molodetsky IE, Vicenzi EP, Dreizin EL, Law CK. Phases of titanium combustion in air. *Combust Flame* 1998;112:522–32. doi:10.1016/s0010-2180(97)00146-6.
- [89] Badiola C, Dreizin EL. Combustion of micron-sized particles of titanium and zirconium. *Proc. Combust. Inst.*, vol. 34, The Combustion Institute; 2012, p. 2237–43. doi:10.1016/j.proci.2012.05.089.
- [90] Yuan CM, Amyotte PR, Hossain MN, Li C. Minimum ignition temperature of nano and micro Ti powder clouds in the presence of inert nano TiO₂ powder. *J Hazard Mater* 2014;275:1–9. doi:10.1016/j.jhazmat.2014.04.047.
- [91] Young G, Sullivan K, Zachariah MR, Yu K. Combustion characteristics of boron nanoparticles. *Combust Flame* 2009;156:322–33. doi:10.1016/j.combustflame.2008.10.007.
- [92] Bidabadi M, Fereidooni J. Modelling ignition temperature and burning time of a single aluminium nanoparticle. *Micro Nano Lett IET* 2013;8:783–7. doi:10.1049/mnl.2013.0417.
- [93] Jian G, Piekielek NW, Zachariah MR. Time-Resolved Mass Spectrometry of Nano-Al and Nano-Al/CuO Thermite under Rapid Heating: A Mechanistic Study. *J Phys Chem C* 2012;116:26881–7. doi:10.1021/jp306717m.
- [94] Buckmaster J, Jackson TL. Modelling the combustion of a sub-micron aluminium particle. *Combust Theory Model* 2014;18:242–60. doi:10.1080/13647830.2014.883086.
- [95] Sundaram DS, Yang V, Zarko VE. Combustion of nano aluminum particles (Review). *Combust Explos Shock Waves* 2015;51:173–96. doi:10.1134/S0010508215020045.
- [96] Huang Y, Risha GA, Yang V, Yetter RA. Combustion of bimodal nano/micron-sized aluminum particle dust in air. *Proc Combust Inst* 2007;31:2001–9. doi:10.1016/j.proci.2006.08.103.
- [97] Sundaram DS, Yang V, Huang Y, Risha GA, Yetter RA. Effects of particle size and pressure on combustion of nano-aluminum particles and liquid water. *Combust Flame* 2013;160:2251–9. doi:10.1016/j.combustflame.2013.04.025.
- [98] Bojko BT, DesJardin PE, Washburn EB. On modeling the diffusion to

- kinetically controlled burning limits of micron-sized aluminum particles. *Combust Flame* 2015;161:3211–21. doi:10.1016/j.combustflame.2014.06.011.
- [99] Egan GC, LaGrange T, Zachariah MR. Time-Resolved Nanosecond Imaging of Nanoscale Condensed Phase Reaction. *J Phys Chem C* 2015;119:150127145402000. doi:10.1021/jp5084746.
- [100] Egan GC, Sullivan KT, Lagrange T, Reed BW, Zachariah MR. In situ imaging of ultra-fast loss of nanostructure in nanoparticle aggregates. *J Appl Phys* 2014;115. doi:10.1063/1.4867116.
- [101] Lee KC, Taira T, Mo Koo G, Young Lee J, Yoh JJ. Ignition characteristics of laser-ablated aluminum at shock pressures up to 2 GPa. *J Appl Phys* 2014;115. doi:10.1063/1.4861153.
- [102] Guha S, Li MD, Tarlov MJ, Zechariah MR. Electrospray-differential mobility analysis of bionanoparticles. *Trends Biotechnol* 2012;30:291–300. doi:10.1016/j.tibtech.2012.02.003.
- [103] Collins DR, Cocker DR, Flagan RC, Seinfeld JH. The scanning DMA transfer function. *Aerosol Sci Technol* 2004;38:833–50. doi:10.1080/027868290503082.
- [104] Electrostatic Classifiers Series 3080. 2009.
- [105] Tsai D-H, Hawa T, Kan H-C, Phaneuf RJ, Zachariah MR. Spatial and size-resolved electrostatic-directed deposition of nanoparticles on a field-generating substrate: theoretical and experimental analysis. *Nanotechnology* 2007;18:365201. doi:10.1088/0957-4484/18/36/365201.
- [106] Kong CD, Yao Q, Yu D, Li SQ. Combustion characteristics of well-dispersed aluminum nanoparticle streams in post flame environment. *Proc Combust Inst* 2015;35:2479–86. doi:10.1016/j.proci.2014.06.127.
- [107] Kim SH, Woo KS, Liu BYH, Zachariah MR. Method of measuring charge distribution of nanosized aerosols. *J Colloid Interface Sci* 2005;282:46–57. doi:10.1016/j.jcis.2004.08.066.
- [108] Fristrom RM, Westenberg A. A. *Flame Structure*. 1965.
- [109] Allen D, Krier H, Glumac N. Heat transfer effects in nano-aluminum combustion at high temperatures. *Combust Flame* 2014;161:295–302. doi:10.1016/j.combustflame.2013.07.010.
- [110] Sorensen CM. The mobility of fractal aggregates: A review. *Aerosol Sci Technol* 2011;45:755–69. doi:10.1080/02786826.2011.560909.
- [111] Khawam A, Flanagan RD. Solid-State kinetic Models: Basic and Mathematical Fundamentals. *JPhysChemB* 2006;110:17315–28. doi:10.1021/jp062746a.
- [112] Levenspiel O. *Chemical reaction engineering*. 3rd ed. New York: Wiley; 1999.
- [113] Allen D, Krier H, Glumac N. Nano-alumina accommodation coefficient measurement using time-resolved laser induced incandescence. *J Heat Transfer* 2016. doi:10.1115/1.4033642.
- [114] Mukherjee D, Sonwane CG, Zachariah MR. Kinetic Monte Carlo simulation of

- the effect of coalescence energy release on the size and shape evolution of nanoparticles grown as an aerosol. *J Chem Phys* 2003;119:3391–404. doi:10.1063/1.1580098.
- [115] Zong Y, Jacob RJ, Li S, Zachariah MR. Size Resolved High Temperature Oxidation Kinetics of Nano-Sized Titanium and Zirconium Particles. *J Phys Chem A* 2015;119:6171–8. doi:10.1021/acs.jpca.5b02590.
- [116] Rai A, Lee D, Park KH, Zachariah MR. Importance of phase change of aluminum in oxidation of aluminum nanoparticles. *J Phys Chem B* 2004;108:14793–5. doi:10.1021/jp0373402.
- [117] Levitas VI, Asay BW, Son SF, Pantoya M. Mechanochemical mechanism for fast reaction of metastable intermolecular composites based on dispersion of liquid metal. *J Appl Phys* 2007;101. doi:10.1063/1.2720182.
- [118] Henz BJ, Hawa T, Zachariah MR. On the role of built-in electric fields on the ignition of oxide coated nanoaluminum: Ion mobility versus Fickian diffusion. *J Appl Phys* 2010;107. doi:10.1063/1.3247579.
- [119] Puri P, Yang V. Thermo-mechanical behavior of nano aluminum particles with oxide layers during melting. *J Nanoparticle Res* 2010;12:2989–3002. doi:10.1007/s11051-010-9889-2.
- [120] Stamatis D, Ermoline A, Dreizin EL. A multi-step reaction model for ignition of fully-dense Al-CuO nanocomposite powders. *Combust Theory Model* 2012;16:1011–28. doi:10.1080/13647830.2012.694480.
- [121] Dikici B, Dean SW, Pantoya ML, Levitas VI, Jouet RJ. Influence of aluminum passivation on the reaction mechanism: Flame propagation studies. *Energy and Fuels* 2009;23:4231–5. doi:10.1021/ef801116x.
- [122] Levitas VI, Pantoya ML, Chauhan G, Rivero I. Effect of the Alumina Shell on the Melting Temperature Depression for Aluminum Nanoparticles. *J Phys Chem C* 2009;113:14088–96. doi:10.1021/jp902317m.
- [123] Williams RA, Patel J V., Ermoline A, Schoenitz M, Dreizin EL. Correlation of optical emission and pressure generated upon ignition of fully-dense nanocomposite thermite powders. *Combust Flame* 2013;160:734–41. doi:10.1016/j.combustflame.2012.11.021.
- [124] Drew CM, Gordon AS, Knipe RH. Study of Quenched Aluminum Particle Combustion, 1964, p. 17–39. doi:10.1016/B978-1-4832-2730-6.50007-5.
- [125] Sippel TR, Son SF, Groven LJ. Aluminum agglomeration reduction in a composite propellant using tailored Al/PTFE particles. *Combust Flame* 2014;161:311–21. doi:10.1016/j.combustflame.2013.08.009.
- [126] Poda AR, Moser RD, Cuddy MF, Doorenbos Z, Lafferty BJ, Weiss, Jr. CA, et al. Molecular Nanotechnology Nano-Aluminum Thermite Formulations : Characterizing the Fate Properties of a Nanotechnology during Use. *J Nanomater Mol Nanotechnol* 2013;2:1–9. doi:10.4172/2324-8777.1000105.
- [127] Puszynski JA. Processing and characterization of aluminum-based

- nanothermites. *J Therm Anal Calorim* 2009;96:677–85. doi:10.1007/s10973-009-0037-0.
- [128] Zhou L, Piekiet N, Chowdhury S, Zachariah MR. T-Jump/time-of-flight mass spectrometry for time-resolved analysis of energetic materials. *Rapid Commun Mass Spectrom* 2009;23:194–202. doi:10.1002/rcm.3815.
- [129] ACerS-NIST Phase Equilibria Diagrams Database 2017.
- [130] Zheng HD, Ou JZ, Strano MS, Kaner RB, Mitchell A, Kalantar-Zadeh K. Nanostructured Tungsten Oxide - Properties, Synthesis, and Applications. *Adv Funct Mater* 2011;21:2175–96. doi:10.1002/adfm.201002477.
- [131] Kappagantula K, Crane C, Pantoya M. Determination of the spatial temperature distribution from combustion products: A diagnostic study. *Rev Sci Instrum* 2013;84. doi:10.1063/1.4822118.
- [132] Friedlander SK. *Smoke, Dust, and Haze: Fundamentals of Aerosol Dynamics*. Oxford University Press; 2000.
- [133] Schoenitz M, Ward TS, Dreizin EL. Fully dense nano-composite energetic powders prepared by arrested reactive milling. *Proc Combust Inst* 2005;30:2071–8. doi:10.1016/j.proci.2004.08.134.
- [134] Ohkura Y, Rao PM, Zheng XL. Flash ignition of Al nanoparticles: Mechanism and applications. *Combust Flame* 2011;158:2544–8. doi:10.1016/j.combustflame.2011.05.012.
- [135] Jacob RJ, Jian G, Guerieri PM, Zachariah MR. Energy release pathways in nanothermites follow through the condensed state. *Combust Flame* 2015;162:258–64. doi:10.1016/j.combustflame.2014.07.002.
- [136] Fischer SH, Grubelich MC, Iit RI. Theoretical energy release of thermites, intermetallics, and combustible metals. *Twenty-Fourth Int Pyrotech Semin* 1998:231–86.
- [137] Fischer SH, Grubelich MC. A SURVEY OF COMBUSTIBLE METALS, THERMITES, AND INTERMETALICS FOR PYROTECHNIC APPLICATIONS. 32nd AIAA/ASME/SAE/ASEE Jt. Propuls. Conf., 1996.
- [138] Price EW, Sigman RK. Combustion of aluminized solid propellants. *CPIA Publ* 1999;691:227–48.
- [139] Pantoya ML, Granier JJ. Combustion behavior of highly energetic thermites: Nano versus micron composites. *Propellants Explos Pyrotech* 2005;30:53–62. doi:10.1002/prop.200400085.
- [140] Thiruvengadathan R, Bezmelnitsyn A, Apperson S, Staley C, Redner P, Balas W, et al. Combustion characteristics of novel hybrid nanoenergetic formulations. *Combust Flame* 2011;158:964–78. doi:10.1016/j.combustflame.2011.02.004.
- [141] Parimi VS, Tadigadapa SA, Yetter RA. Control of nanoenergetics through organized microstructures. *J Micromechanics Microengineering* 2012;22:055011. doi:10.1088/0960-1317/22/5/055011.

- [142] Jacob RJ, Wei B, Zachariah MR. Quantifying the enhanced combustion characteristics of electrospray assembled aluminum mesoparticles. *Combust Flame* 2016;167:472–80. doi:10.1016/j.combustflame.2015.09.032.
- [143] Egan GC, Zachariah MR. Commentary on the heat transfer mechanisms controlling propagation in nanothermites. *Combust Flame* 2015;162:2959–61. doi:10.1016/j.combustflame.2015.04.013.
- [144] Son SF, Asay BW, Foley TJ, Yetter RA, Wu MH, Risha GA. Combustion of nanoscale Al/MoO₃ thermite in microchannels. *J Propuls Power* 2007;23:715–21. doi:10.2514/1.26090.
- [145] Zhang S, Dreizin EL. Reaction Interface for Heterogeneous Oxidation of Aluminum Powders. *J Phys Chem C* 2013;117:14025–31. doi:10.1021/jp402990v.
- [146] Zhou W, DeLisio JB, Wang X, Egan GC, Zachariah MR. Evaluating free vs bound oxygen on ignition of nano-aluminum based energetics leads to a critical reaction rate criterion. *J Appl Phys* 2015;118. doi:10.1063/1.4930889.
- [147] Piekielec NW, Zhou L, Sullivan KT, Chowdhury S, Egan GC, Zachariah MR. Initiation and reaction in Al/Bi₂O₃ nanothermites: Evidence for the predominance of condensed phase chemistry. *Combust Sci Technol* 2014;186:1209–24. doi:10.1080/00102202.2014.908858.
- [148] Martirosyan KS. Nanoenergetic Gas-Generators: principles and applications. *J Mater Chem* 2011;21:9400. doi:10.1039/c1jm11300c.
- [149] Conny JM. Internal Composition of Atmospheric Dust Particles from Focused Ion-Beam Scanning Electron Microscopy. *Environ Sci Technol* 2013;47:8575–81. doi:10.1021/es400727x.
- [150] Altmann F, Young RJ. Site-specific metrology, inspection, and failure analysis of three-dimensional interconnects using focused ion beam technology. *J Micro/Nanolithography, MEMS, MOEMS* 2014;13:011202. doi:10.1117/1.JMM.13.1.011202.
- [151] Grandfield K, Engqvist H. Focused ion beam in the study of biomaterials and biological matter. *Adv Mater Sci Eng* 2012;2012. doi:10.1155/2012/841961.
- [152] Phaneuf MW. Applications of focused ion beam microscopy to materials science specimens. *Micron* 1999;30:277–88. doi:10.1016/s0968-4328(99)00012-8.
- [153] Wixom RR, Tappan AS, Brundage AL, Knepper R, Ritchey MB, Michael JR, et al. Characterization of pore morphology in molecular crystal explosives by focused ion-beam nanotomography. *J Mater Res* 2010;25:1362–70. doi:10.1557/jmr.2010.0167.
- [154] Shuck CE, Frazee M, Gillman A, Beason MT, Gunduz IE, Matou?? K, et al. X-ray nanotomography and focused-ion-beam sectioning for quantitative three-dimensional analysis of nanocomposites. *J Synchrotron Radiat* 2016;23:990–6. doi:10.1107/S1600577516007992.

- [155] Qiu HW, Stepanov V, Chou TM, Surapaneni A, Di Stasio AR, Lee WY. Single-step production and formulation of HMX nanocrystals. *Powder Technol* 2012;226:235–8. doi:10.1016/j.powtec.2012.04.053.
- [156] Overdeep KR, Weihs TP. Design and functionality of a high-sensitivity bomb calorimeter specialized for reactive metallic foils. *J Therm Anal Calorim* 2015;122:787–94. doi:10.1007/s10973-015-4805-8.
- [157] Jacob RJ, Jian G, Guerieri PM, Zachariah M. Gas vs. Condensed Phase Reactions in Nano-Thermites. 52nd Aerosp. Sci. Meet., Reston, Virginia: American Institute of Aeronautics and Astronautics; 2014, p. 1–8. doi:10.2514/6.2014-0816.
- [158] McBride BJ, Gordon S. Computer Program for Calculation of Complex Chemical Equilibrium Compositions and Applications II. User's Manual and Program Description. 1996.
- [159] Granier JJ, Pantoya ML. Laser ignition of nanocomposite thermites. *Combust Flame* 2004;138:373–83. doi:10.1016/j.combustflame.2004.05.006.
- [160] Puszynski JA, Bulian CJ, Swiatkiewicz JJ. Processing and ignition characteristics of aluminum-bismuth trioxide nanothermite system. *J Propuls Power* 2007;23:698–706. doi:10.2514/1.24915.
- [161] Parr T, Johnson C, Hanson-parr D, Higa K, Wilson K. Evaluation of Advanced Fuels for Underwater Propulsion. Proc. 39th JANNAF Combust. Subcomm. Meet., 2003. doi:JSC CD-24.
- [162] Bucher P, Yetter RA, Dryer FL, Parr TP, Vicenzi EP. Flame Structure Measurement of Single , Isolated Aluminum Particles Burning in Air 1996:1899–908.
- [163] Lynch P, Krier H, Glumac N. Micro-alumina particle volatilization temperature measurements in a heterogeneous shock tube. *Combust Flame* 2012;159:793–801. doi:10.1016/j.combustflame.2011.07.023.
- [164] Wang H, Jian G, Egan GC, Zachariah MR. Assembly and reactive properties of Al/CuO based nanothermite microparticles. *Combust Flame* 2014;161:2203–8. doi:10.1016/j.combustflame.2014.02.003.
- [165] Jacob RJ, Ortiz-Montalvo DL, Overdeep KR, Weihs TP, Zachariah MR. Incomplete reactions in nanothermite composites. *J Appl Phys* 2017;121. doi:10.1063/1.4974963.
- [166] Dlott DD. Thinking big (and small) about energetic materials. *Mater Sci Technol* 2006;22:463–73. doi:10.1179/174328406X83987.
- [167] Zachariah MR. NanoEnergetics: Hype, reality and future. *Propellants, Explos Pyrotech* 2013;38:7. doi:10.1002/prop.201380131.
- [168] Sundaram D, Yang V, Yetter RA. Metal-based nanoenergetic materials: Synthesis, properties, and applications. *Prog Energy Combust Sci* 2017;61:293–365. doi:10.1016/j.pecs.2017.02.002.
- [169] Wang H, Jacob RJ, DeLisio JB, Zachariah MR. Assembly and encapsulation of

- aluminum NP's within AP/NC matrix and their reactive properties. *Combust Flame* 2017;180:175–83. doi:10.1016/j.combustflame.2017.02.036.
- [170] Kim SB, Kim KJ, Cho MH, Kim JH, Kim KT, Kim SH. Micro- and Nanoscale Energetic Materials as Effective Heat Energy Sources for Enhanced Gas Generators. *ACS Appl Mater Interfaces* 2016;8:9405–12. doi:10.1021/acsami.6b00070.
- [171] Zhou X, Torabi M, Lu J, Shen RQ, Zhang KL. Nanostructured Energetic Composites: Synthesis, Ignition/Combustion Modeling, and Applications. *ACS Appl Mater Interfaces* 2014;6:3058–74. doi:10.1021/am4058138.
- [172] Jacob RJ, Zachariah MR. Quantifying the Combustion Characteristics of Nano-aluminum Based Microstructures 2016.
- [173] Bockmon BS, Pantoya ML, Son SF, Asay BW, Mang JT. Combustion velocities and propagation mechanisms of metastable interstitial composites. *J Appl Phys* 2005;98:1–7. doi:10.1063/1.2058175.
- [174] Kappagantula K, Crane C, Pantoya M. Factors influencing temperature fields during combustion reactions. *Propellants, Explos Pyrotech* 2014;39:434–43. doi:10.1002/prop.201300154.
- [175] Perry WL, Tappan BC, Reardon BL, Sanders VE, Son SF. Energy release characteristics of the nanoscale aluminum-tungsten oxide hydrate metastable intermolecular composite. *J Appl Phys* 2007;101:064313. doi:10.1063/1.2435797.
- [176] Bucher P, Yetter RA, Dryer FL, Parr TP, Hanson-Parr DM. PLIF species and ratiometric temperature measurements of aluminum particle combustion in O₂, CO₂ and N₂O oxidizers, and comparison with model calculations. *Twenty-Seventh Symp Combust Vols 1 2* 1998:2421–9.
- [177] Jacob RJ, Kline DJ, Zachariah MR. High speed 2-dimensional temperature measurements of nanothermite composites: Probing thermal vs. Gas generation effects. *J Appl Phys* 2018;123:115902. doi:10.1063/1.5021890.
- [178] Pokhil PF. *Combustion of Powdered Metals in Active Media*. 1973.
- [179] Geisler RL. A Global View of the Use of Aluminum Fuel in Solid Rocket Motors 2002:3748. doi:10.2514/6.2002-3748.
- [180] Trunov MA, Schoenitz M, Dreizin EL. Ignition of aluminum powders under different experimental conditions. *Propellants Explos Pyrotech* 2005;30:36–43. doi:10.1002/prop.200400083.
- [181] Beckstead MW. A Summary of Aluminum Combustion. RTO/VKI Spec. Course “Internal Aerodyn. Solid Rocket Propulsion,” vol. RTO-EN-023, 2002.
- [182] Washburn EB, Webb JA, Beckstead MW. The simulation of the combustion of micrometer-sized aluminum particles with oxygen and carbon dioxide. *Combust Flame* 2010;157:540–5. doi:10.1016/j.combustflame.2009.11.005.
- [183] Gill RJ, Badiola C, Dreizin EL. Combustion times and emission profiles of micron-sized aluminum particles burning in different environments. *Combust*

- Flame 2010;157:2015–23. doi:10.1016/j.combustflame.2010.02.023.
- [184] Huang Y, Risha GA, Yang V, Yetter RA. Effect of particle size on combustion of aluminum particle dust in air. *Combust Flame* 2009;156:5–13. doi:10.1016/j.combustflame.2008.07.018.
- [185] Jacob R, Zong Y, Yang Y, Li S, Zachariah MR. Size-Resolved Burn Rate Measurements of Metal NanoParticles. 54th AIAA Aerosp Sci Meet 2016:1–9. doi:10.2514/6.2016-0687.
- [186] Babuk V, Dolotkazin I, Gamsov A, Glebov A, De Luca LT, Galfetti L. Nanoaluminum as a Solid Propellant Fuel. *J Propuls Power* 2009;25:482–9. doi:10.2514/1.36841.
- [187] Pang WQ, Fan XZ, Zhao FQ, Zhang W, Xu HX, Yu HJ, et al. Effects of Different Nano-Metric Particles on the Properties of Composite Solid Propellants. *Propellants Explos Pyrotech* 2014;39:329–36. doi:10.1002/prop.201300172.
- [188] Maggi F, Dossi S, Paravan C, DeLuca LT, Liljedahl M. Activated aluminum powders for space propulsion. *Powder Technol* 2015;270:46–52. doi:10.1016/j.powtec.2014.09.048.
- [189] Dossi S, Paravan C, Maggi F, Lorenzo M Di, Gibertoni S, Ardalic J, et al. Novel Activated Metal Powders for Improved Hybrid Fuels and Green Solid Propellants 2016:1–14. doi:10.2514/6.2016-4596.
- [190] Sippel TR, Son SF, Groven LJ. Modifying aluminum reactivity with poly(carbon monofluoride) via mechanical activation. *Propellants, Explos Pyrotech* 2013;38:321–6. doi:10.1002/prop.201200202.
- [191] Sippel TR, Son SF, Groven LJ. Altering reactivity of aluminum with selective inclusion of polytetrafluoroethylene through mechanical activation. *Propellants, Explos Pyrotech* 2013;38:286–95. doi:10.1002/prop.201200102.
- [192] Sippel TR, Son SF, Groven LJ, Zhang SS, Dreizin EL. Exploring mechanisms for agglomerate reduction in composite solid propellants with polyethylene inclusion modified aluminum. *Combust Flame* 2015;162:846–54. doi:10.1016/j.combustflame.2014.08.013.
- [193] Cheng JL, Hng HH, Ng HY, Soon PC, Lee YW. Synthesis of Sub-Micron Nickel Particles Coated onto Aluminum Powders via a Modified Polyol Process. *Met Mater Int* 2008;14:583–7. doi:10.3365/met.mat.2008.10.583.
- [194] Aly Y, Hoffman VK, Schoenitz M, Dreizin EL. Reactive, Mechanically Alloyed Al center dot Mg Powders with Customized Particle Sizes and Compositions. *J Propuls Power* 2014;30:96–104. doi:10.2514/1.b35031.
- [195] Kim SH, Zachariah MR. Enhancing the rate of energy release from nanoenergetic materials by electrostatically enhanced assembly. *Adv Mater* 2004;16:1821–+. doi:10.1002/adma.200306436.
- [196] Clayton NA, Kappagantula KS, Pantoya ML, Kettwich SC, Iacono ST. Fabrication, Characterization, and Energetic Properties of Metallized Fibers.

- ACS Appl Mater Interfaces 2014;6:6049–53. doi:10.1021/am404583h.
- [197] Yan S, Jian GQ, Zachariah MR. Electrospun Nanofiber-Based Thermite Textiles and their Reactive Properties. ACS Appl Mater Interfaces 2012;4:6432–5. doi:10.1021/am3021125.
- [198] Li X, Guerieri P, Zhou W, Huang C, Zachariah MR. Direct Deposit Laminate Nanocomposites with Enhanced Propellant Properties. ACS Appl Mater Interfaces 2015;7:9103–9. doi:10.1021/acsami.5b00891.
- [199] Quann RJ, Neville M, Janghorbani M, Mims CA, Sarofim AF. MINERAL MATTER AND TRACE-ELEMENT VAPORIZATION IN A LABORATORY-PULVERIZED COAL COMBUSTION SYSTEM. Environ Sci Technol 1982;16:776–81. doi:10.1021/es00105a009.
- [200] Xie JW, Jiang J, Davoodi P, Srinivasan MP, Wang CH. Electrohydrodynamic atomization: A two-decade effort to produce and process micro-/nanoparticulate materials. Chem Eng Sci 2015;125:32–57. doi:10.1016/j.ces.2014.08.061.
- [201] Cloupeau M, Prunetfoch B. ELECTROSTATIC SPRAYING OF LIQUIDS IN CONE-JET MODE. J Electrostat 1989;22:135–59.
- [202] Tsai DH, Zangmeister RA, Pease LF, Tarlov MJ, Zachariah MR. Gas-phase ion-mobility characterization of SAM-functionalized Au nanoparticles. Langmuir 2008;24:8483–90. doi:10.1021/la7024846.
- [203] Yarrington CD, Son SF, Foley TJ, Obrey SJ, Pacheco AN. Nano aluminum energetics: The effect of synthesis method on morphology and combustion performance. Propellants, Explos Pyrotech 2011;36:551–7. doi:10.1002/prop.201000156.
- [204] Young G, Wang H, Zachariah MR. Application of nano-aluminum/nitrocellulose mesoparticles in composite solid rocket propellants. Propellants, Explos Pyrotech 2015;40:413–8. doi:10.1002/prop.201500020.
- [205] Price WE. Combustion of Metalized Propellants. Fundam Solid-Propellant Combust 1984:479–513. doi:doi:10.2514/5.9781600865671.0479.0513.
- [206] Wang HY, DeLisio JB, Jian GQ, Zhou WB, Zachariah MR. Electro spray formation and combustion characteristics of iodine-containing Al/CuO nanothermite microparticles. Combust Flame 2015;162:2823–9. doi:10.1016/j.combustflame.2015.04.005.
- [207] Wang H, Jian G, Zhou W, DeLisio JB, Lee VT, Zachariah MR. Metal Iodate-Based Energetic Composites and Their Combustion and Biocidal Performance. ACS Appl Mater Interfaces 2015;7:17363–70. doi:10.1021/acsami.5b04589.
- [208] Huang C, Jian G, DeLisio JB, Wang H, Zachariah MR. Electro spray Deposition of Energetic Polymer Nanocomposites with High Mass Particle Loadings: A Prelude to 3D Printing of Rocket Motors. Adv Eng Mater 2015;17:95–101. doi:10.1002/adem.201400151.
- [209] Hill KJ, Warzywoda J, Pantoya ML, Levitas VI. Dropping the hammer:

- Examining impact ignition and combustion using pre-stressed aluminum powder. *J Appl Phys* 2017;122:125102. doi:10.1063/1.5003632.
- [210] Granier JJ, Plantier KB, Pantoya ML. The role of the Al₂O₃ passivation shell surrounding nano-Al particles in the combustion synthesis of NiAl. *J Mater Sci* 2004;39:6421–31. doi:10.1023/B:JMASC.0000044879.63364.b3.
- [211] Chintersingh K-L, Schoenitz M, Dreizin EL. Combustion of boron and boron-iron composite particles in different oxidizers. *Combust Flame* 2018;192:44–58. doi:10.1016/j.combustflame.2018.01.043.
- [212] Epshteyn A, Weismiller MR, Huba ZJ, Maling EL, Chaimowitz AS. Optimization of a High-Energy Ti-Al-B Nanopowder Fuel. *Energy and Fuels* 2017;31:1811–9. doi:10.1021/acs.energyfuels.6b02321.
- [213] Yao Y, Huang Z, Xie P, Lacey SD, Jacob RJ, Xie H, et al. Carbothermal shock synthesis of high-entropy-alloy nanoparticles. *Science* (80-) 2018;359:1489–94. doi:10.1126/science.aan5412.
- [214] Kappagantula KS, Pantoya ML, Horn J. Effect of surface coatings on aluminum fuel particles toward nanocomposite combustion. *Surf Coatings Technol* 2013;237:456–9. doi:10.1016/j.surfcoat.2013.08.035.
- [215] Helmich RJ, Suslick KS. Chemical aerosol flow synthesis of hollow metallic aluminum particles. *Chem Mater* 2010;22:4835–7. doi:10.1021/cm101342r.
- [216] McCollum J, Smith DK, Hill KJ, Pantoya ML, Warzywoda J, Tamura N. A slice of an aluminum particle: Examining grains, strain and reactivity. *Combust Flame* 2016;173:229–34. doi:10.1016/j.combustflame.2016.09.002.
- [217] Bachmaier A, Pippin R. Effect of oxide particles on the stabilization and final microstructure in aluminium. *Mater Sci Eng A* 2011;528:7589–95. doi:10.1016/j.msea.2011.06.071.
- [218] Levitas VI, Dikici B, Pantoya ML. Toward design of the pre-stressed nano- and microscale aluminum particles covered by oxide shell. *Combust Flame* 2011;158:1413–7. doi:10.1016/j.combustflame.2010.12.002.
- [219] Parigger CG, Hornkohl JO. Computation of AlO B₂Σ⁺ X₂Σ⁺ + emission spectra. *Spectrochim Acta - Part A Mol Biomol Spectrosc* 2011;81:404–11. doi:10.1016/j.saa.2011.06.029.
- [220] Dikici B, Pantoya ML, Levitas V. The effect of pre-heating on flame propagation in nanocomposite thermites. *Combust Flame* 2010;157:1581–5. doi:10.1016/j.combustflame.2010.04.014.
- [221] Nicholas A, Finne T, Galysh I, Mai A, Yen J, Sawka W, et al. SpinSat Mission Overview SpinSat Mission Overview. 27th Annu. AIAA/USU Conf. Small Satell., 2013, p. SSC13-I-3.
- [222] Row SL, Groven LJ. Smart Energetics: Sensitization of the Aluminum-Fluoropolymer Reactive System. *Adv Eng Mater* 2018;20:1700409. doi:10.1002/adem.201700409.
- [223] Shirinov AV, Schomburg WK. Pressure sensor from a PVDF film. *Sensors*

- Actuators A Phys 2008;142:48–55. doi:10.1016/j.sna.2007.04.002.
- [224] OSBORNE DT, PANTOYA ML. Effect of Al Particle Size on the Thermal Degradation of Al/Teflon Mixtures. *Combust Sci Technol* 2007;179:1467–80. doi:10.1080/00102200601182333.
- [225] Kappagantula KS, Farley C, Pantoya ML, Horn J. Tuning Energetic Material Reactivity Using Surface Functionalization of Aluminum Fuels. *J Phys Chem C* 2012;116:24469–75. doi:10.1021/jp308620t.
- [226] Yang H, Huang C, Chen H. Tuning reactivity of nanoaluminum with fluoropolymer via electrospray deposition. *J Therm Anal Calorim* 2017;127:2293–9. doi:10.1007/s10973-016-5801-3.
- [227] DeLisio JB, Hu X, Wu T, Egan GC, Young G, Zachariah MR. Probing the Reaction Mechanism of Aluminum/Poly(vinylidene fluoride) Composites. *J Phys Chem B* 2016;120:5534–42. doi:10.1021/acs.jpcc.6b01100.
- [228] Pantoya ML, Dean SW. The influence of alumina passivation on nano-Al/Teflon reactions. *Thermochim Acta* 2009;493:109–10. doi:10.1016/j.tca.2009.03.018.
- [229] Galfetti L, Luca LT De, Severini F, Meda L, Marra G, Marchetti M, et al. Nanoparticles for solid rocket propulsion. *J Phys Condens Matter* 2006;18:S1991–2005. doi:10.1088/0953-8984/18/33/S15.
- [230] MEDA L, MARRA G, GALFETTI L, INCHINGALO S, SEVERINI F, DELUCA L. Nano-composites for rocket solid propellants. *Compos Sci Technol* 2005;65:769–73. doi:10.1016/j.compscitech.2004.10.016.
- [231] Meda L, Marra G, Galfetti L, Severini F, De Luca L. Nano-aluminum as energetic material for rocket propellants. *Mater Sci Eng C* 2007;27:1393–6. doi:10.1016/j.msec.2006.09.030.
- [232] Fleck TJ, Murray AK, Gunduz IE, Son SF, Chiu GTC, Rhoads JF. Additive manufacturing of multifunctional reactive materials. *Addit Manuf* 2017;17:176–82. doi:10.1016/j.addma.2017.08.008.
- [233] Sullivan KT, Zhu C, Duoss EB, Gash AE, Kolesky DB, Kuntz JD, et al. Controlling Material Reactivity Using Architecture. *Adv Mater* 2016;28:1934–9. doi:10.1002/adma.201504286.
- [234] Murray AK, Isik T, Ortalan V, Gunduz IE, Son SF, Chiu GTC, et al. Two-component additive manufacturing of nanothermite structures via reactive inkjet printing. *J Appl Phys* 2017;122:1–6. doi:10.1063/1.4999800.
- [235] Dlott DD. Shock compression dynamics under a microscope. *AIP Conf Proc* 2017;1793. doi:10.1063/1.4971456.
- [236] Wang H, DeLisio JB, Holdren S, Wu T, Yang Y, Hu J, et al. Mesoporous Silica Spheres Incorporated Aluminum/Poly (Vinylidene Fluoride) for Enhanced Burning Propellants. *Adv Eng Mater* 2018;20:1700547. doi:10.1002/adem.201700547.
- [237] Guerieri PM, DeLisio JB, Zachariah MR. Nanoaluminum/Nitrocellulose

- microparticle additive for burn enhancement of liquid fuels. *Combust Flame* 2017;176:220–8. doi:10.1016/j.combustflame.2016.10.011.
- [238] Chen B, Zheng H, Riehn M, Bok S, Gangopadhyay K, Maschmann MR, et al. In Situ Characterization of Photothermal Nanoenergetic Combustion on a Plasmonic Microchip. *ACS Appl Mater Interfaces* 2018;10:427–36. doi:10.1021/acsami.7b13226.